R85-5

OSP 91857

ENTRAINMENT IN DIFFUSIVE THERMOHALINE SYSTEMS: APPLICATION TO SALT GRADIENT SOLAR PONDS

by
JOSEPH F. ATKINSON
E. ERIC ADAMS
W. KENDALL MELVILLE
and
DONALD R.F. HARLEMAN

RALPH M. PARSONS LABORATORY
HYDRODYNAMICS AND COASTAL ENGINEERING

Report No. 300

Prepared for
Civil and Environmental Engineering Division
National Science Foundation
and
Solar Energy Research Institute
U.S. Department of Energy

December 1984

MIT

DEPARTMENT
OF
CIVIL
ENGINEERING

SCHOOL OF ENGINEERING
MASSACHUSETTS INSTITUTE OF TECHNOLOGY
Cambridge, Massachusetts 02139

R85-5 OSP 91857

ENTRAINMENT IN DIFFUSIVE THERMOHALINE SYSTEMS: APPLICATION TO SALT GRADIENT SOLAR PONDS

by

Joseph F. Atkinson
E. Eric Adams
W. Kendall Melville
and
Donald R.F. Harleman

RALPH M. PARSONS LABORATORY
HYDRODYNAMICS AND COASTAL ENGINEERING

Report No. 300

Prepared for
Civil and Environmental Engineering Division
National Science Foundation
and
Solar Energy Research Institute
U.S. Department of Energy

December 1984

ABSTRACT

The development of a numerical model for simulating the temporal evolution of vertical temperature and salinity profiles in a salt gradient solar pond is described. The model uses a mixed-layer approach and a general entrainment relation is derived for predicting the growth of the upper mixed layer. A major part of the research involves an experimental study of the process of mixed-layer deepening in a strongly stratified "diffusive" double-diffusive system. Two different experiments are described. In the first, a vertically oscillating grid was used to drive interfacial mixing in a two-layer system in which the temperature and salinity differences between the layers were varied over a large range of values. Results for single stratification (temperature or salinity) were found to agree with those of earlier researchers, but it was found that for a given $Ri = g'\hat{\ell}/\hat{u}^2$, where g' = reduced gravity, and $\hat{\ell}$ and $\hat{u}$ are turbulence length and velocity scale, respectively, an increase in the destabilizing temperature difference would cause an increase in the rate of entrainment over the value for salinity stratification alone. This effect is modeled by defining a velocity scale which includes the buoyancy-induced velocity resulting from the temperature distribution.

The second experiment looked at wind-induced mixing in a laboratory wind/wave tank. Tests were done using several different mean wind speeds ranging from 4 m/s to 11 m/s. Two-layer systems were again considered, with either salt or diffusive double-diffusive stratification. Two separate fetch lengths were also considered in an attempt to find a fetch

dependence on the entrainment rates. No differences could be seen in the results for the two different kinds of stratification, with the entrainment rate following roughly an inverse Richardson number law. However, the mixed layer deepening was somewhat faster for the longer fetch and this result is explained in terms of an increased return flow along the interface, leading to increased shear-induced mixing.

A series of experiments was also conducted in the wind/wave tank to test the effect of placing floating plastic netting or floating plastic pipes on the water surface. This has been suggested as a possible means of helping to reduce wind-induced mixing in solar ponds. The results obtained here indicate that both the nets and pipes can be at least partially effective in reducing wind-mixing, with the nets generally performing better than the pipes. Some increased mixing may be present directly beneath a floating net or pipe, but the areally averaged effect of the nets or pipes is to decrease the turbulence levels in the surface water layer.

Experimental data, along with suggested values obtained from previous researchers, are used to define suggested values for the coefficients in the entrainment model which is incorporated into the full numerical simulation model. Sensitivity of the model to several of the parameters is examined and a calibration run is shown, using field data from a small solar pond. Unfortunately, wind-mixing was apparently not very important in this pond and a full calibration test of the wind-mixing model will have to wait until data from a much larger pond becomes available.

ACKNOWLEDGEMENTS

This report essentially constitutes the doctoral dissertation of Joseph F. Atkinson.

We acknowledge the assistance of Professor Keith D. Stolzenbach who participated in many of the technical discussions. Thanks are due to Roy Milley and Jack Crocker, who helped build some of the experimental apparatus. Larry Deschaine and Jeff Munic participated in various aspects of the research under the M.I.T. Undergraduate Research Opportunity Program. In particular, Mr. Munic is responsible for much of Table 1. We would also like to thank R. Peter Fynn of the Ohio Agricultural Research and Development Center for providing field data from their solar pond and Dr. Gad Assaf of Solmat Systems, Ltd., for providing samples of netting used for controlling wind-mixing in the Israeli solar ponds. Beth Quivey, Ellen Campbell and Claudia Gale produced the typed text.

The research reported here has been supported by the National Science Foundation, grant no. CEE-8119384, and the Department of Energy, through the Solar Energy Research Institute, subcontract no. XX-3-03066-1. In addition, Dr. Joseph F. Atkinson was partially supported during a portion of this study as a Paul Rappaport Fellow of the American Solar Energy Society.

Table of Contents

FIGURES

20) Calibration of $\hat{\kappa}$ with measured values for ΔT as a function of time.

21) Calculated values of $\hat{\kappa}$ as a function of ΔT_0

22) Horizontal locations for measurement of vertical velocity profiles in grid-mixing tank

23) Experimental set-up for laser velocity measurements

24) Power spectrum for accelerometer data, showing energy at around 20 Hz

25) Power spectra calculated for the grid-induced velocity signal as a function of h_g (distance from the grid)

26) Noise spectrum for measurements shown in Figure 25

27) Velocity profiles for grid experiment

28) Autocorrelation for signal at h_g = 9.6 cm

29) Time scale profile

30) Variation of $\hat{\ell}$ with h_g for $h_g \leq 10$ cm (from Thompson and Turner, 1975)

31) Mixed-layer deepening in the grid experiment.

32) u_e/u vs. Ri for the grid experiments

33) u_e/σ vs. Ri_σ for the grid experiments

34) Wind/wave facility

35) Surface drift currents

36) Vertical wind speed profiles for $\bar{W}$ = 7.8 m/s and X = 3.3 m, measured at 5 different lateral positions

37) Lateral air velocity profiles for $\bar{W}$ = 7.8

38) Calculation of u_{*a}

39) Variation of u_{*a} with fetch

40) Average friction velocities for the two test sections

41) Stratification during wind test, showing intermediate wedge-shaped layer.

42) Comparison of salinity profiles measured at different fetches

43) Example of change of mixed layer depth with time

44) Temporal development of salinity profile measured at the center of the 3.5 m test section

45) Plan view of return flow patterns along the interface, showing the three observed modes

46) Wind entrainment results, using u_* as the scaling velocity

47) Wind entrainment results, using $\hat{u}$ = rms horizontal component for scaling

48) Ratio of rms velocity to u_* (rms value obtained by averaging along length of test section)

49) Comparison of average water velocities in the two test sections, with a density interface present

50) Average velocities near the interface for the two test sections

51) Wind entrainment results, using u_r as the scaling velocity

52) Sketch of net material used for reducing wind-mixing

53) Velocity measurements directly underneath a (a) pipe or (b) net, compared with measurements at the same locations but with an open surface

54) Visualization of effect of floating pipe on flow beneath the pipe

55) Visualization of effect of floating net on flow beneath the net

56) Comparison of velocity measurements between two nets and at the same locations without the nets in place

57) Salinity effect on evaporation

58) Comparison of radiation attenuation models

59) Entrainment model, u_e/σ vs. Ri and Rf vs. Ri

60) Estimates for $C_1 = u_d/u_*$

TABLES

CHAPTER 1

Introduction

1.1 Salt gradient solar ponds

1.1.1 Physical Description

There has been growing interest in recent years in the use of salt gradient solar ponds (SGSP) for collecting and storing solar energy. Tabor (1963, 1980, 1981) has described the general characteristics and operation of a solar pond and the reader is referred to these papers for a more complete description. Briefly, the SGSP is a relatively shallow body of water in which a stable salinity gradient is established to counteract the buoyancy induced by absorption of solar radiation. The increase in density due to the added salt more than compensates for the density reduction due to radiative heating, thus enabling hot water to be generated and stored in the lower depths of the pond. Temperatures close to boiling have been observed in a number of ponds and one pond has been reported as having reached the boiling point (Weeks et al., 1981). A number of natural solar ponds, or heliothermic lakes, have also been reported, some of them exhibiting surprisingly high temperatures (Tabor, 1980; Kirkland et al., 1980).

The vertical stratification of a SGSP is illustrated in Figure 1, where the basic three-layer structure can be seen. The bottom layer, known as the lower convecting zone (LCZ) or storage zone, is well-mixed and acts as the collector and storage unit for thermal energy. Heat may be extracted from the LCZ for direct use as low temperature thermal energy or for driving an organic Rankine cycle turbine for electricity

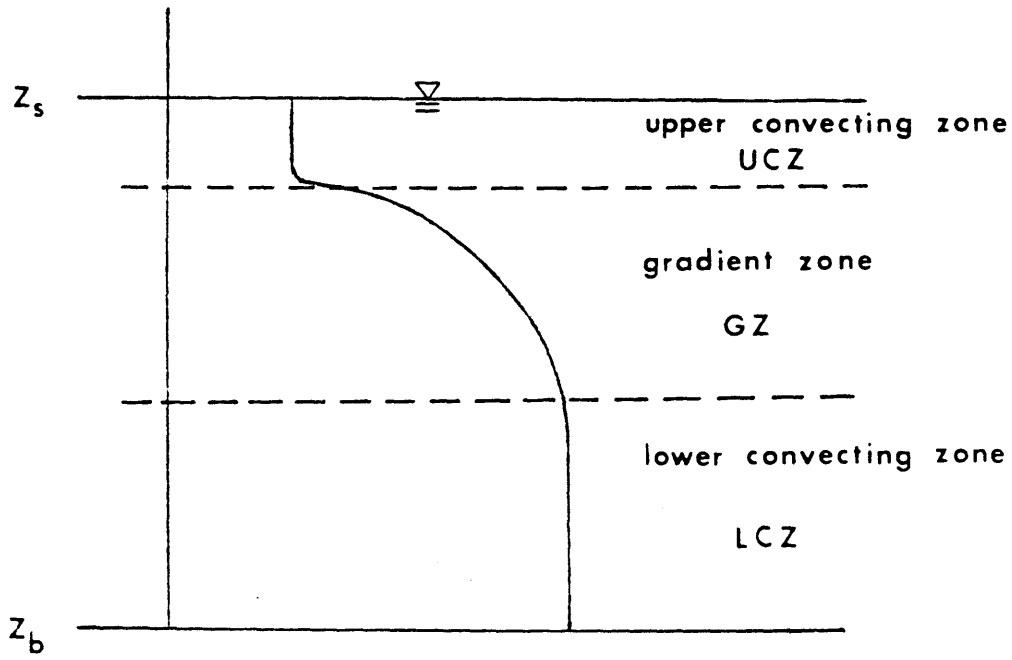

FIGURE 1 Typical Stratification in a SGSP; The Curve Represents Temperature, Salinity or Density

production, as has been demonstrated in Israel (Bronicki et al., 1980). A gradient zone (GZ) overlies the storage zone. This is a stably stratified non-convecting region which serves as an insulator for the stored heat, separating the LCZ from direct contact with the atmosphere. Heat (and salt) flux through the GZ is limited by molecular diffusion. An upper mixed layer, or upper convecting zone (UCZ) is also present, due to various processes including wind-mixing, penetrative convection and diffusion. It is desirable to minimize the depth of this UCZ, as it has a pronounced negative effect on the thermal efficiency of the pond (Kooi, 1979; Wang and Akbarzadeh, 1983).

One means of heat extraction is accomplished by pumping working fluid through tubing laid out on the bottom of the pond. However, this may become inefficient for very large ponds because of the large amount of tubing required. An alternative method is to pump fluid from the LCZ through an external heat exchanger and then return it to the opposite end of the pond, as illustrated in Figure 2. For example, the pond at Ein Bokek in Israel has been used to generate electrical power for a resort hotel since 1979.

One other aspect of solar pond operation that should be mentioned is that of gradient maintenance. Due to various physical processes such as diffusion, mechanical mixing by wind, mean shear or penetrative convection, and internal convective instabilities, the stabilizing salt gradient can be eroded. This causes an increased upward heat flux and, therefore, the thermal efficiency of the pond is reduced. In order to insure optimal operation of a pond some means of maintaining the salt gradient is necessary. The most promising method of doing this is with

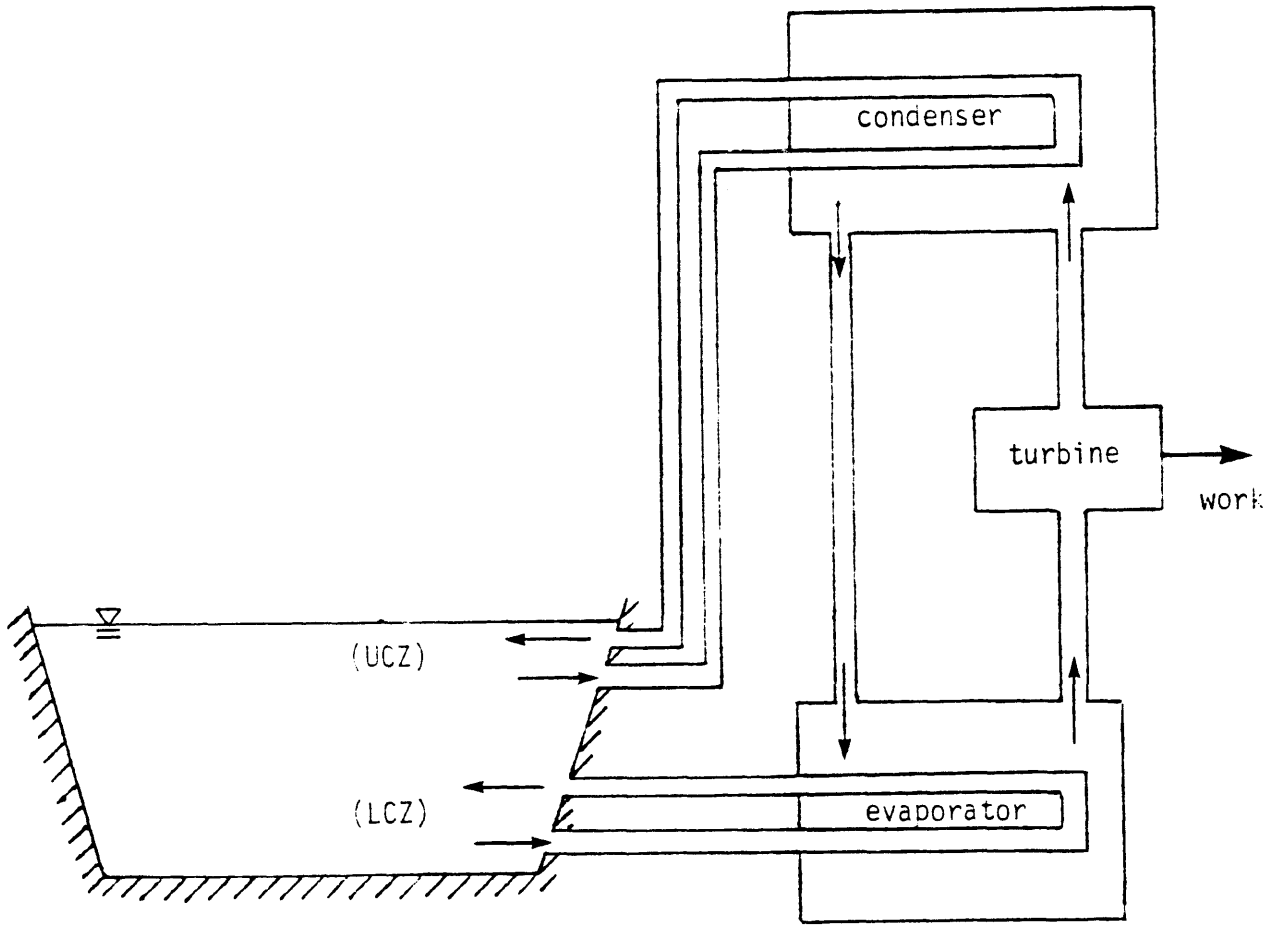

FIGURE 2 Schematic Diagram of Heat Extraction From a SGSP for Power Generation

the use of a scanning diffuser which can inject or withdraw fluid at precisely determined locations in order to eliminate internal convecting zones or to extend the GZ region back into one of the convecting zones (see Atkinson et al., 1984).

It is important to be able to predict the performance of a solar pond in order to determine its cost-effectiveness in providing useful energy. One of the major results of the present study is the development of a model that may be used for predicting vertical temperature and salinity profiles in a thermohaline system, with a particular application to solar ponds. The model is based on a mixed-layer formulation, as described in the following section, and calculates mixed-layer deepening using an entrainment relation developed from a parameterization of the turbulent kinetic energy budget in the mixed layer (UCZ). The main purpose of the present research was to study the possible influence of double-diffusive stratification on the entrainment mechanism and to develop data with which the entrainment model could be calibrated. A general entrainment model is derived in Chapter 3 and Chapters 4 and 5 describe the experiments performed. Results are summarized in Chapter 7.

1.1.2 Models for temperature and salinity distributions in water bodies

Considerable research effort has been reported in the literature dealing with the problem of gaining an understanding of the various transport processes in the water environment. In particular, there is great interest in modeling the distributions of temperature and dissolved constituents. A knowledge of the temperature distribution is one of the most basic bits of information needed in the study of a given water body

and a hydrothermal model often forms an integral part of more complicated biological and chemical models. In some cases the distribution of dissolved salts may also be important to consider, as in the oceans, estuaries, inland saline lakes and in SGSP's.

A three dimensional numerical formulation will generally provide the most accurate and detailed model for the relevant physical processes of interest in a given modeling situation. However, this approach can become unwieldy and overly expensive to run. Most studies have been primarily concerned with the vertical structure of water bodies with relatively large horizontal extent so that horizontal variations could be ignored. Not only are there great simplifications involved with a one-dimensional model over a multi-dimensional one, but also in many instances a predominantly vertical stratification is observed in the field, suggesting the simpler approach. Of course, care must be taken when applying a one-dimensional model to make certain that the assumption of negligible horizontal variations is justified. This research is concerned primarily with one-dimensional processes.

Earlier models of temperature stratification in natural water bodies used a heat conservation equation employing an eddy diffusivity which could be varied as a function of depth and time to account for greater mixing near the surface due to shear stress associated with wind. Due to difficulties in determining appropriate values for the diffusivity, which requires detailed shear measurements, and also due to observations that a relatively well-mixed surface layer bounded below by a sharp thermocline is often found in oceans and lakes, the concept of a mixed-layer model was introduced. For instance, Niiler and Kraus (1977) argue in favor of

the mixed-layer formulation since it avoids much of the difficulty of the variable eddy diffusivity formulation by assuming that the upper layer is fully mixed. Harleman (1982) presents a good discussion of some of the history of the development of mixed layer models. Since the upper layer is assumed to be fully mixed, specification of the diffusivity becomes unimportant in that layer. In order to close these models conditions at the upper and lower boundaries of the mixed layer must be accounted for, as well as the evolution of the layer. The growth of the layer may be evaluated with the use of a turbulent kinetic energy (TKE) budget, as discussed in Chapter 3.

The basic structure of a SGSP (Figure 1) is well-suited for adopting the one-dimensional mixed-layer approach for modeling the vertical stratification which is idealized as shown in Figure 3. Note that concern here is primarily for processes occurring at the UCZ/GZ boundary. A well-mixed surface layer is bounded below by a thin interface across which there is a finite density step $\Delta\rho$. There is an arbitrary density gradient below the interface, $\Gamma = d\rho/dz$ as a result of both temperature and salinity gradients. A one-dimensional structure is assumed and this is checked following criteria listed by Bloss and Harleman (1979). First, mixing may be associated with horizontal flows. A densimetric Froude number is defined for the inflow (or outflow) as

$$Fr = \frac{u}{\sqrt{g'D}} \quad , \tag{1.1}$$

where u = horizontal flow velocity, $g' = g\,\Delta\rho/\rho_o$, $\Delta\rho$ = density step at

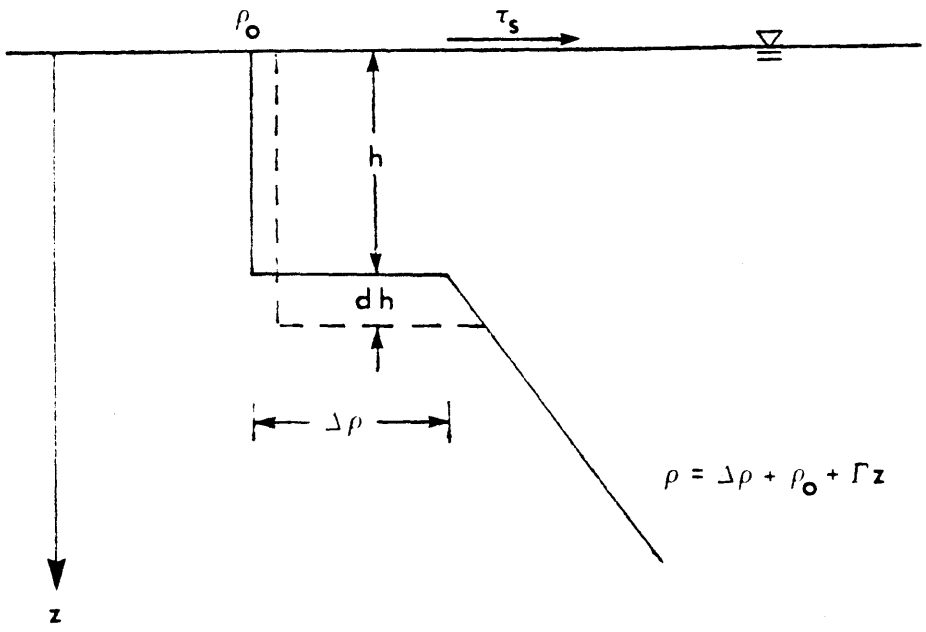

FIGURE 3 Idealized Stratification Considered in the Mixed-Layer Approach

thermocline (pycnocline) and D = mean depth. (Appendix A contains a listing of nomenclature used.) If Fr << 1, then horizontal isotherms may be expected. Also, strong winds may cause set-up and result in part of the hypolimnion being uncovered at one end. The one-dimensional approach is no longer valid if the wind speed W (in m/s) is such that $W \gtrsim 2\times10^{3}\ (hD\Delta\rho/X\rho_o)^{1/2}$ (Bloss and Harleman, 1979), where h = upper layer depth and X = total length. Now consider a small solar pond with the following properties: X = 100 m, D = 3m, h = .3 m, u = .01 m/s and $\Delta\rho$ = 140 kg/m^3. Then Fr = 4.9 x 10^{-3} and W would have to be greater than 71 m/s. For a large pond, let X = 1000 m. Then Fr = 4.9 x 10^{-3} and W would have to be greater than 23 m/s. Thus it is seen that for the representative conditions considered here the one-dimensional approach is valid.

Therefore, horizontal variations are neglected, though finite horizontal extent must be considered to allow for inflows and outflows which may be associated with various aspects of pond operation, such as heat extraction and gradient maintenance. Considering a long, thin horizontal slab of fluid as sketched in Figure 4, the quasi-one-dimensional equations expressing the balances for thermal energy and salt mass content are the advection-diffusion equations,

$$\frac{\partial H}{\partial t} + \frac{1}{A}\frac{\partial}{\partial z}(wAH) = \frac{1}{A}\frac{\partial}{\partial z}\left(A\kappa_T \frac{\partial T}{\partial z}\right) + \frac{B(u_i H_i - u_o H)}{A} + \frac{1}{A}\frac{\partial}{\partial z}(A\phi_S) \quad (1.2)$$

and

$$\frac{\partial \rho_s}{\partial t} + \frac{1}{A}\frac{\partial}{\partial z}(wA\rho_S) = \frac{1}{A}\frac{\partial}{\partial z}\left(Ak_S \frac{\partial \rho_s}{\partial z}\right) + \frac{B(u_i \rho_{Si} - u_o \rho_S)}{A} \quad , \quad (1.3)$$

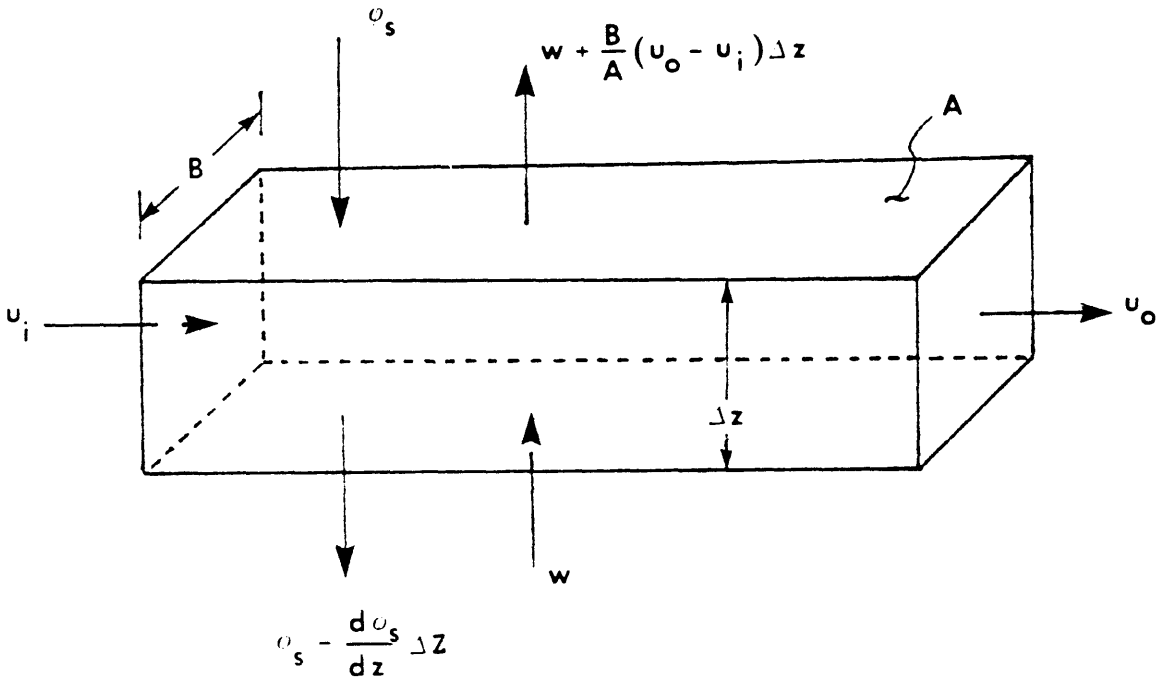

FIGURE 4 Definition Sketch For Heat and Salt Balances (Diffusive Fluxes Not Shown)

where $H = \rho c_p T$, A = horizontal area, w = vertical velocity, ρ = density, c_p = specific heat, κ_T = thermal conductivity, T = temperature, B = width (lateral scale), u = horizontal flow, ϕ_S = solar radiation flux, $\rho_S = \rho S$, S = salinity, k_S = salt diffusivity and the subscripts i and o refer to inflow and outflow quantities, respectively. The vertical velocity w arises when inflow and outflow are not equal at a given level and is solved from continuity:

$$w = \frac{1}{A} \int_{z_b}^{z} (u_i - u_o) B dz \quad , \tag{1.4}$$

where z_b is the bottom. Boundary and initial conditions must also be specified for solution of the equations and these are discussed in Chapter 6, which includes a description of the entire numerical model.

The change in the mixed layer depth with time is calculated from an energy budget as follows. Referring to Figure 3, when a small amount of fluid, Δh, from below the interface is mixed into the upper layer, the change in potential energy of the system is

$$\Delta PE = \frac{1}{2} gA[\Delta\rho h \Delta h + \Gamma h \Delta h^2] \quad , \tag{1.5}$$

where $\Delta\rho$ = density step across interface and h = upper layer depth. (Note that a general expression for the change in potential energy of the layer would also contain a term for buoyancy fluxes through the boundaries - this is ignored for now.) Assuming that the friction

velocity and drift velocity are proportional, the rate at which kinetic energy is added to the layer is estimated as

$$\frac{\Delta KE}{\Delta t} = \tau_s u_s A = C_1 \rho_s A u_*^3 \tag{1.6}$$

where τ_s = surface shear stress = $\rho_s u_*^2$, ρ_s = surface layer density, u_* = friction velocity, u_s = surface drift velocity and C_1 = constant. When there is an unstable buoyancy flux (eg., surface cooling) ΔKE will also have a contribution from buoyancy-induced flow (i.e., penetrative convection). This is discussed further in Chapter 3. Neglecting the nonlinear term in (1.5), a flux Richardson number may be defined as the ratio of the change in potential energy due to entrainment to the input of kinetic energy,

$$Rf = \frac{\Delta PE}{\Delta KE} = \frac{1}{2C_1} u_e g \frac{\Delta\rho}{\rho_s} \frac{h}{u_*^3} \quad , \tag{1.7}$$

where $u_e = \Delta h/\Delta t$. This expression may be simplified by defining a bulk Richardson number,

$$Ri_* = g \frac{\Delta\rho}{\rho_s} \frac{h}{u_*^2} \quad , \tag{1.8}$$

so that

$$Rf = \frac{1}{2C_1} \frac{u_e}{u_*} Ri_* \tag{1.9}$$

Then, as long as u_e may be found, Rf may be evaluated and the change in upper layer depth is calculated from (1.5). This approach is more convenient than using u_e directly when incorporating the entrainment algorithm into a numerical code which uses fixed element sizes.

It is interesting to note that a common assumption in many mixed-layer models is that Rf is constant. That is, a constant fraction of input wind energy is used for mixed-layer deepening. Then, from (1.9), it is easily seen that the entrainment function would be of the form

$$\frac{u_e}{u_*} \propto Ri_*^{-1} \tag{1.10}$$

and there is some experimental support for this result. Chapter 2 provides a review of previous entrainment models and experiments.

1.2 Double-diffusive effects

When dealing with systems having both temperature and salinity gradients it is necessary to consider possible double-diffusive processes. An essential feature of such systems is that instability and convection may occur even when there is gravitational stability. The concept of double-diffusion has been reviewed extensively in the literature (Turner, 1973, 1974, 1975, 1981; Sherman et al., 1978; Huppert and Turner, 1981; Chen and Johnson, 1984) and only the main features are repeated here. Huppert and Turner (1981) define necessary conditions for

double-diffusive convection to occur as the presence of two or more components in the fluid with different molecular diffusivities and stratified in such a way that they make opposing contributions to the vertical density gradient. The form of the convection depends on which of the components provides the destabilizing force. Figure 5 illustrates the two possible orientations which can lead to double-diffusive convection in a thermohaline system. In Figure 5a both temperature and salinity decrease with depth, so that the temperature distribution provides the stabilizing contribution to the density gradient. In this case, the instability takes the form of long, thin convection cells known as "salt fingers". Stommel et al. (1956) were the first to describe the possibility of salt fingering and this is now recognized as being an important transport mechanism in the oceans. The second type of instability arises in systems where both temperature and salinity increase with depth, as in Figure 5b. This is known as the "diffusive" case (Turner, 1973) and the instability is in the form of overstable oscillations. It is this latter case that this research will be primarily concerned with, as a SGSP pond represents an example of a diffusive thermohaline system.

One of the more interesting features observed in experiments with double-diffusive systems is that when a stable salinity gradient is heated from below, a series of well-mixed layers will form, separated by relatively thin interfaces (see Turner, 1965, 1968b; Shirtcliffe, 1969; Huppert, 1971; Linden, 1976; Mancini et al., 1976; Huppert and Linden, 1979). The mechanism for this behavior is due to the much faster diffusion of heat than that of salt. That is, both heat and salt will

a) finger regime

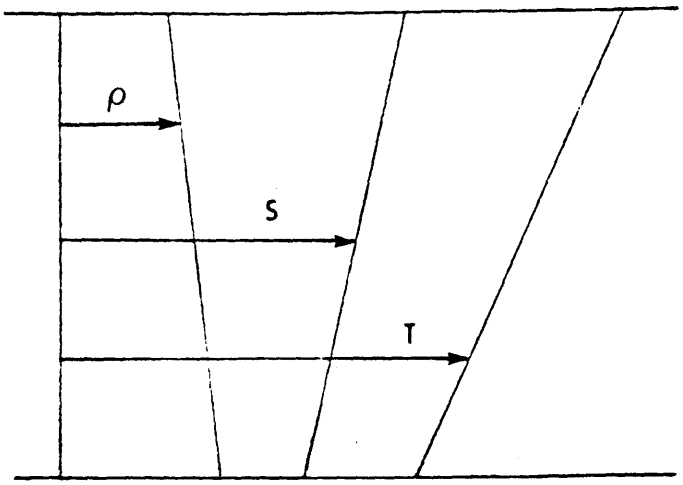

b) diffusive regime

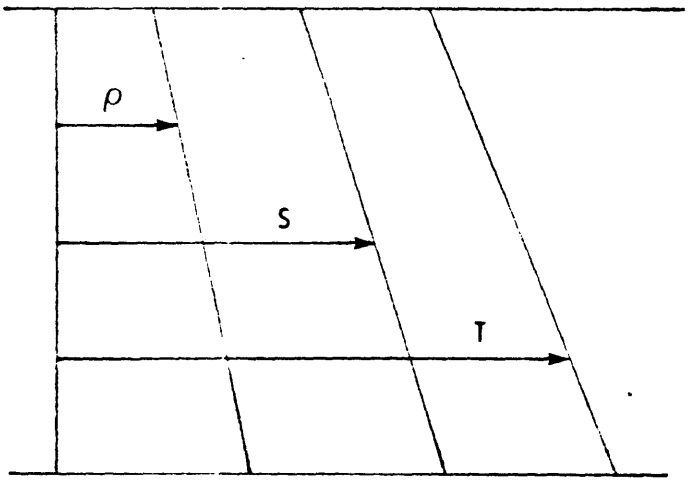

FIGURE 5 Illustration of Thermohaline Double-Diffusive Systems

diffuse across an interface, but while the salt makes a stabilizing contribution to the growing diffusive boundary layer, the heat diffuses so much more quickly that the boundary layer becomes unstable and begins to convect. A well-mixed layer then forms, with another interfacial region ahead of it. With time, these layers have been observed to merge, when the buoyancy difference across the adjoining interface approaches zero. Layer formation has also been observed for salt-finger systems, where relatively thin salt finger interfaces separate well-mixed layers. This has been recognized as an important transfer mechanism in the oceans, as the fingers are able to transport salt and heat much more effectively than molecular diffusion.

There has been much interest in measurements of the fluxes of heat and salt across a double-diffusive interface. As noted above, salt fingers represent a very efficient transport mechanism, compared with molecular diffusion, for both heat and salt. However, there is greater interest here in the diffusive regime where experiments have indicated that salt flux is enchanced while heat flux is somewhat reduced in comparison to the fluxes that would be expected by molecular diffusion alone. This point is discussed further in section 3.2.2 and Appendix C. It is felt that double-diffusive experiments and results in general have been well reviewed elsewhere (see papers by Turner, cited above), but section 2.3. provides a more detailed review of several experiments more directly applicable to the present study.

1.2.1 Stability analysis

The stability of a double-diffusive system may be analyzed by a linear perturbation analysis of the thermohaline Raleigh-Jeffreys problem (Veronis, 1964; Nield, 1967; Baines and Gill, 1969). If we consider a gradient region of depth D, bounded above and below by infinite horizontal planes and having temperature and salinity steps, ΔT and ΔS, as shown in Figure 6, then there are four non-dimensional parameters needed to describe the system (Turner, 1973):

$$\begin{aligned} Ra &= \frac{g\alpha_T \Delta T D^3}{\nu k_T} & Pr &= \nu/k_T \\ \tau &= k_S/k_T & R_\rho &= \frac{\alpha_S \Delta S}{\alpha_T \Delta T} \end{aligned} \qquad (1.11)$$

where Ra is the thermal Rayleigh number, Pr is the Prandtl number, ν is kinematic viscosity, τ is the ratio of salt to thermal diffusivity, R_ρ is the stability parameter and α_S and α_T are the saline and thermal expansion coefficients, respectively. It will also be convenient to define a saline Rayleigh number, $Ra_S = R_\rho\ Ra$, and the Schmidt number, $Sc = \nu/k_S$.

The following development is condensed from the treatment of Baines and Gill (1969). The governing equations for this system are written with the Boussinesq approximation (tensor notation):

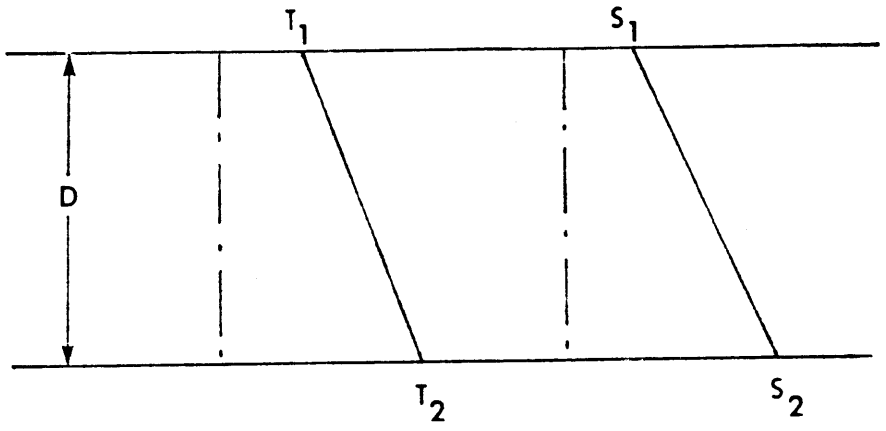

FIGURE 6 Definition Sketch for Stability Analysis

$$\frac{\partial u_i}{\partial x_i} = 0 \tag{1.12}$$

$$\frac{\partial u_i}{\partial t} + u_j \frac{\partial u_i}{\partial x_j} = -\frac{\rho}{\rho_o} g - \frac{1}{\rho_o} \frac{\partial p}{\partial x_i} + \nu \nabla^2 u_i \tag{1.13}$$

$$\frac{\partial T}{\partial t} + u_j \frac{\partial T}{\partial x_j} = k_T \nabla^2 T \tag{1.14}$$

$$\frac{\partial S}{\partial t} + u_j \frac{\partial S}{\partial x_j} = k_S \nabla^2 S \tag{1.15}$$

The salt and heat equations are linked through an equation of state:

$$\rho = \rho_o (1 - \alpha_T \Delta T_o + \alpha_S \Delta S_o) \tag{1.16}$$

where $\rho_o = \rho(T_o, S_o)$ and $\Delta T_o = T - T_o$ and $\Delta S_o = S - S_o$ (see eq. 4.1). The initial steady state is given by $u_i = 0$ (all i) and this results in linear gradients for T and S. The system is then subjected to infinitesimal perturbations (in u_i, T, S, p and ρ) and equations for the perturbation quantities are derived by subtracting the equations for the initial state from the equations for the perturbed state and linearizing. Pressure terms are eliminated by cross-differentiation and subtraction of the momentum equations. After some further manipulations and non-dimensionalizing, the resulting set of equations is:

$$(\frac{\partial}{\partial t} - \nabla^2)\nabla^2 w' = -Ra\nabla_1^2 T' - \frac{1}{\tau} Ra_S \nabla_1^2 S' \tag{1.17}$$

$$(Pr \frac{\partial}{\partial t} - \nabla^2)T' = w' \tag{1.18}$$

$$(Sc \frac{\partial}{\partial t} - \nabla^2)S' = w' \quad , \tag{1.19}$$

where primes denote non-dimensional perturbation quantities, and $\nabla_1^2 = \partial^2/\partial x^2 + \partial^2/\partial y^2$.

By assuming wave-like solutions it can be shown that for free, conducting boundaries the equations representing marginal stability for this system are:

$$Ra - \frac{1}{\tau} Ra_S \leq \frac{27}{4} \pi^2 \tag{1.20}$$

and

$$\frac{Sc^2}{(Pr+Sc)(Sc+1)} Ra - \frac{Pr^2}{(Pr+Sc)(Pr+1)} (\frac{1}{\tau}) Ra_S \leq \frac{27}{4} \pi^2 \quad . \tag{1.21}$$

These stability curves may be affected slightly by rotation (Worthem et al., 1983) or the Soret effect (Hurle and Jakeman, 1971), but these effects are neglected here. The factor $27/4\ \pi^4 = 657$ results from the determination of the fastest growing (most unstable) mode. The above criterion (1.21) can be written in a more convenient form as

$$Ra_e = Ra - \frac{Pr+\tau}{Pr+1} Ra_S \leq \frac{27}{4} \pi^2 \ [(1+\tau)(1 + \frac{\tau}{Pr})] \quad , \tag{1.22}$$

where Ra_e is defined as an "effective" Rayleigh number (Turner, 1973; Delnore, 1980). Ra_e plays the same role in double-diffusive convection

as Ra does in thermal convection. Eqs. (1.20) and (1.22) are plotted in Figure 7, along with the line for static gravitational stability, where $Ra = Ra_S$. Conditions in solar ponds or other "diffusive" systems fall within the upper right hand quadrant of this figure, where (1.22) provides the appropriate stability criterion. It can be seen that these systems may become unstable while they are still gravitationally stable and this is an important point to remember when modeling this type of system.

It is interesting to note that only a very small salt gradient is required to establish conditions where the oscillatory mode becomes possible. Hurle and Jakeman (1969, 1971) recognized this fact and showed that the Soret effect could produce gradients large enough to cause oscillatory behavior. The Soret effect refers to the diffusive transport of a solute due to a temperature gradient. (The analogous transport of heat due to a solute gradient is known as the Dufour effect.) These effects are discussed in Appendix B.

As mentioned above stability of the system must be considered carefully in a numerical model for a thermohaline system, since gravitational stability is not a guarantee of overall stability. For this purpose a simplified form of (1.22) may be derived for solar pond conditions. It is easily shown that both Ra and Ra_S are of order 10^{10} or larger for typical solar pond conditions. Since the r.h.s. of (1.22) is of order 10^3 it may be ignored and we have

$$Ra - \frac{Pr+\tau}{Pr+1} Ra_s \leq 0$$

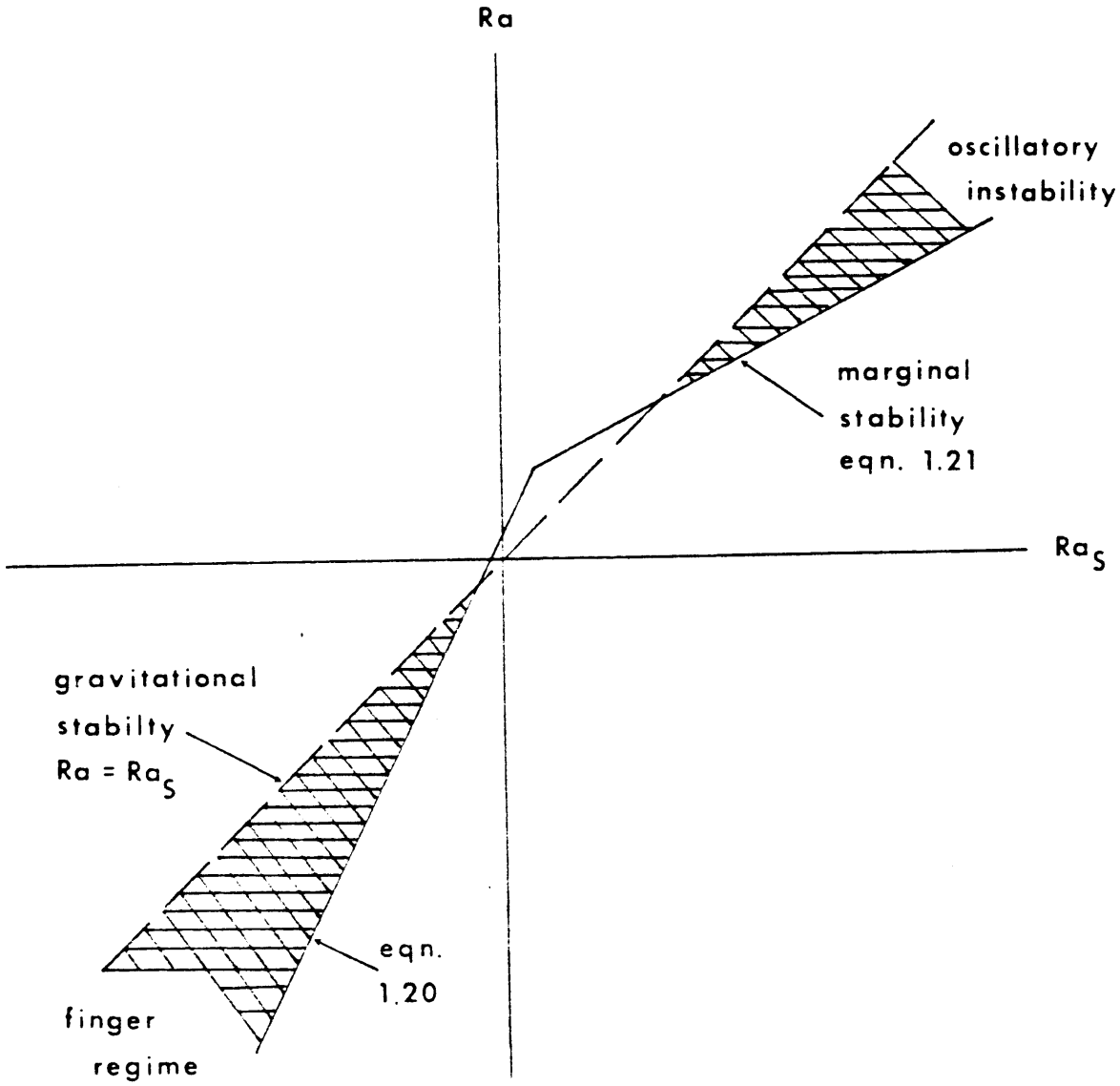

FIGURE 7 Thermohaline Stability Diagram

$$\frac{gD^4}{\nu k_T \rho_o} \left[- \frac{\partial \rho}{\partial T} \frac{\partial T}{\partial z} - \frac{\nu + k_S}{\nu + k_T} \frac{\partial \rho}{\partial S} \frac{\partial S}{\partial z} \right] \leq 0$$

$$\frac{\partial S}{\partial z} \geq - \left(\frac{\nu + k_T}{\nu + k_S} \right) \frac{\partial \rho}{\partial T} \frac{\partial T}{\partial z} \Big/ \frac{\partial \rho}{\partial S} \quad . \tag{1.23}$$

This stability criterion was first described by Weinberger (1964). A typical value of the quantity in parentheses is ~ 1.14, though Elwell et al. (1977) have shown that it can vary somewhat due to the temperature and salinity dependence of the diffusivities. (A value of unity would correspond with the gravitational stability criterion.)

It is interesting to note that the above analysis assumes a length scale equal to the layer depth so that an instability in a solar pond would be predicted to extend the entire depth of the GZ. This is contrary to observations in ponds where the instability typically occurs over several cm. Walton (1982) has shown that (1.23) may be applied on a local level when modeling ponds (i.e., using local values for the gradients) and this is the approach used in the numerical model, described in Chapter 6.

1.3 Outline of experimental work

Two separate experiments were performed. In the first a small laboratory tank was used with a vertically oscillating grid to provide mixing energy. This experiment, described in Chapter 4, was designed as a relatively simple test of whether double-diffusive stratification would have any effect on entrainment. It was also chosen because there has been considerable interest in grid-mixing experiments and a number of

papers have appeared in the literature (Section 2.2.1). Therefore, it was felt that a good comparison could be made between the present results and those of previous research dealing with singly stratified systems.

It is believed that grid-mixing experiments provide a reasonable model for mixed layer deepening where the mixing energy is input with a length scale much less than the layer depth, as with turbulence associated with wave breaking. However, it should be noted that these tests have zero mean shear so that it is difficult to apply the results directly to field conditions where appreciable shear is present. When energy is transferred to the water body by surface shear stress larger scale eddies will be present (scaling on upper layer depth), resulting in more kinetic energy being transported downward. This is more efficient than the turbulent diffusive transport of the grid experiments. With mean shear present shear production of turbulence must also be considered.

A second set of experiments used wind-mixing in order to obtain data under conditions where mean shear was present. Chapter 5 describes these experiments, which were conducted in a laboratory wind/wave flume. It is felt that the results of these experiments are more directly applicable for calibrating the entrainment model for solar ponds. Tests were done at higher Ri than have been reported in previous work and the possible influence of "diffusive" stratification was looked at. Both of these points are of concern in solar pond modeling and neither has been addressed in the literature.

In addition to the wind-induced entrainment experiments, a series of tests was performed to look at the effectiveness of using a floating grid

of wind-wave suppressors on the surface of a solar pond to reduce deepening of the UCZ. This method has been used with some success in the field (Assaf, personal communication), though there has not been any serious testing of the effect of having the suppressors in place. While this was not a major objective in the present research, the tests described in Section 5.3 provide a first look at the effect the suppressors have on the wind-induced flow in the wind/wave flume.

CHAPTER 2

Literature Review

2.1 Mixed-layer models

A large number of one-dimensional mixed layer models have been reported in the literature. They are all similar in treating the upper layer as a well-mixed region, but there are differences in the way the deepening of the layer is calculated. Early mixed layer models were developed by Kitaigorodskii (1960) and Kraus and Rooth (1961). Kitaigorodskii's model assumed a balance between the mean work done by wind stress and the work needed to mix heat downward from the surface, while Kraus and Rooth balanced the tendency for layer deepening by penetrative convection with upwelling from below. Both of these models assumed steady state conditions and were thus somewhat limited in their modeling capability. Kraus and Turner (1967) formulated the first transient mixed layer model of the seasonal thermocline by solving a coupled set of equations governing the surface layer temperature and mechanical energy budgets. They considered the main force for entrainment as penetrative convection during the cooling season, suggesting that wind-mixing was important only during the warming season.

Most mixed layer models may be seen as variations and/or improvements in the formulation of Kraus and Turner (see Niiler and Kraus, 1977). Denman (1973) looked at the upper layer response to meteorological inputs on a time scale on the order of several days (rather than the seasonal scales of interest to Kraus and Turner) and concluded that wind-mixing could be important in the mixed layer dynamics

for analyses carried out on these shorter time scales. This was also the conclusion of Pollard et al. (1973), who included a momentum equation in their formulation and solved for the mean mixed layer velocity. They argued that the real fluid velocity solved in this manner provided a more appropriate scaling velocity than the friction velocity associated with wind stress, suggesting that interfacial shear was primarily responsible for entrainment. Niiler (1975) expanded on this model by considering in greater detail the strong shear zones at the upper and lower boundaries of the mixed layer. Miller (1976) made a valuable contribution by including a salt balance for the mixed layer in addition to the thermal energy balance. He showed that a stable salinity step would result in a shallower mixed layer depth and warmer surface temperature since not as much cool water is entrained from below.

One of the main differences in various mixed layer models is in the way the mechanical energy budget is treated. This is an important point since this is how entrainment is calculated. The two main sources of kinetic energy in the upper layer are buoyancy-driven convection and surface wind stress. Mean currents from other sources may also be important in some cases. The simplest model is to assume that a constant fraction of the input kinetic energy is transformed to potential energy by entrainment. This corresponds to a constant value for Rf and is consistent with observations reported by Turner (1969). Denman (1973) was one of the first to use this assumption in a mixed layer model and it has also been incorporated in more recent models (eg., Niiler, 1975; Stefan and Ford, 1975; Miller, 1976; Hurley-Octavio et al., 1977; Steinhorn et al., 1979), with values assumed for Rf ranging from unity to

less than five percent. From (1.8), this implies that $u_e/u_* \propto Ri_*^{-1}$ and it is shown in Chapter 3 that this result is obtained only by ignoring the temporal and production terms in the TKE budget and by assuming that there is no leakage of energy below the interface and that dissipation is either negligible or a constant fraction of the input energy.

There is some experimental support for the inverse Richardson number entrainment law, but a more general model which includes the various terms of the TKE budget would be expected to be applicable over a wider range of conditions. In other words, the entrainment is no longer simply proportional to Ri^{-1} and Rf then becomes a varying function of the existing stratification. Tucker and Green (1977) calculated the energy available for mixing as the net difference between input wind energy in the form of shear or surface wave breaking, convectively produced turbulence and dissipation, but their energy balance neglects the temporal storage and leakage terms (see Chapter 3) and they do not parameterize their budget in a convenient manner. Zeman and Tennekes (1977) developed a parameterization of the TKE budget evaluated at the entrainment interface and their resulting entrainment relation was later incorporated into the mixed layer models of Bloss and Harleman (1979) and Atkinson and Harleman (1983a). However, it is shown in Chapter 3 that several assumptions and simplifications were made in deriving this entrainment model which are not appropriate for solar pond conditions. Sherman et al. (1978) derived an entrainment model which is slightly more general than the Zeman and Tennekes model, particularly in their treatment of the possible stratification existing beneath the mixed

layer. They reviewed a number of experiments and suggested coefficient values which gave a best fit for their model (Table 4). Imberger and Patterson (1981) also developed a parameterization scheme to calculate entrainment in a reservoir model. This formulation includes some quite detailed parameterizations of various processes of importance in reservoirs. The model developed in Chapter 3 is designed to be as simple as possible while still retaining essential features for modeling solar ponds. The result is similar to that of Sherman et al. (1978), with several modifications.

2.2 Entrainment experiments in singly-diffusive systems

2.2.1 Oscillating grids

Oscillating grid experiments provide a means of studying mixing in stratified systems in a relatively controlled manner. They are particularly useful in modeling mixed layer behavior under conditions of negligible mean shear and where the length scale of the input energy is considerably less than the layer depth, as with wave-induced mixing (breaking). Grids have also been used to gain insight into the entrainment process in general, though comparison of grid results with results from other systems has been difficult due to differences in the turbulence generation mechanism and to the presence or absence of mean shear. A large amount of effort has been spent in studying grid-mixing experiments in order to better understand the process of turbulent mixing across a density interface. For the most part, these studies have been concerned with singly-diffusive systems, with the two exceptions noted below (section 2.3). Partial reviews of the various oscillating grid

experiments have been given by Turner (1973), Denton (1978), McDougall (1979) and Fernando and Long (1983). The present review includes these previous reports and also some more recent papers. Table 1 summarizes the grid experiments which are described in greater detail below.

Rouse and Dodu (1955) performed the first oscillating grid experiments as a laboratory analog to wave-breaking turbulent mixing in the oceans. They noted and described the entrainment process for the first time and observed that there appeared to be a finite rate of interfacial mixing for any combination of Froude and Reynolds numbers (see Table 1 for their definitions of Fr and Re). A two-layer configuration was used with the grid in the upper layer and the mixed layer depth was kept constant by adding solution to the bottom layer and withdrawing from the top (stirred) layer at a rate chosen to balance the rate at which fluid was entrained across the interface. An interfacial mixing coefficient, or diffusivity, was defined as the product of the velocity (assumed to be proportional to fh), and h:

$$\varepsilon = C\ fh^2\ , \tag{2.1}$$

where C = proportionality constant. A dimensional argument was used to suggest that the normalized entrainment rate should depend on the Froude and Reynolds numbers, i.e., $E = u_e h/\varepsilon = f(Fr,Re)$. Variations in viscosity were obtained by using solutions of varying concentrations of dissolved salt and sugar. It is not clear whether combinations of solutions used were such that double-diffusive effects may have been present, but this is a possible explanation for their reported results,

$$E = 5 \times 10^4 \, Fr^{5/2} Re \qquad (2.2)$$

which does not agree with more recent findings (see (2.4)). They noted that if a constant fraction of the input kinetic energy were used for entrainment, then E should be proportional to Fr^2 and there would be no effect of viscosity.

Experiments by Cromwell (1960) and Turner and Kraus (1967) provided some interesting qualitative observations of the entrainment process, though Turner and Kraus were more concerned with the process of penetrative convection. Both experiments showed that the entrainment velocity was initially fast, but slowed gradually with time and approached a constant value which depended on the density difference across the interface. The decrease in u_e was also probably due to the movement of the interface away from the grid, so the mixing energy becomes weaker. Turner and Kraus also suggested that E should be a function of a Richardson number, $Ri = Fr^{-2}$, but noted that Re might be important in some cases.

Turner (1968a) performed experiments using salt and heat (separately) to produce the necessary stratification. Two-layer systems were considered, with either one grid only at the middle of the lower layer or with one grid at the middle of both layers. The results were independent of whether the upper layer was stirred or not. This result was explained by the observation that mixing events were relatively sparse and there was negligible interaction between the turbulence in the two layers. The interface remained at a constant level when both layers were stirred, but for the single grid experiments it was maintained at a

constant level using the same withdrawal/addition technique as Rouse and Dodu (1955).

These experiments provided the first qualitative results for grid-induced entrainment. Turner found that for weak stratification the entrainment rate u_e was the same for both the heat and salt stratified systems. However, for stronger stratification the heat results showed that the entrainment was approximately proportional to the inverse of a parameter related to a Richardson number. For salt stratification the entrainment varied more closely with the negative three-halves power of this parameter, i.e.,

$$u_e \tilde{\propto} Ri_l^{-1} \qquad \text{(heat stratification)} \qquad (2.3)$$

and

$$u_e \tilde{\propto} Ri_l^{-3/2} \qquad \text{(salt stratification)} \qquad (2.4)$$

where

$$Ri_l = g \frac{\Delta\rho}{\rho_o} \frac{\ell}{(\ell f)^2}$$

and ℓ is a length scale. A characteristic stirring velocity was defined as $\hat{u} = f\ell$. However, since ℓ was undetermined, the results were plotted as (u_e/f) vs. $(\Delta\rho/\rho_o f^2)$ using arbitrary scales. Turner (1973)

later replotted these results using the turbulent length and velocity scales measured in non-stratified fluid and reported by Thompson and Turner (1975). It was assumed that the velocity and length scales measured under the non-stratified conditions would be applicable to the experiments with a density interface. This point is discussed further in Section 2.2.1.1. The basic relationships (2.3) and (2.4) were unchanged using the new scaling and these results are shown in Figure 8.

In order to explain the differences observed for the heat and salt stratified systems, Turner (1968a) suggested that differences in the molecular diffusivities of the components could account for the change in the exponent. In particular, since the inverse Ri relationship could be interpreted in terms of an energy argument (i.e., a constant fraction of input kinetic energy used to increase the potential energy by entrainment - see Equation 1.10), he assumed that (2.3) represented some sort of limiting condition and that the much lower diffusivity of salt (roughly two orders of magnitude less than heat) caused an entrained fluid element to be incorporated into its surroundings at a much slower rate. This argument was supported by observations of the interface obtained by successively dyeing the upper and lower layers which indicated that entrained saline fluid might return to the interface before an appreciable amount of salt could diffuse out and be mixed throughout the stirred layer. It should also be noted that the effect of molecular diffusivity would be greater for stronger stratification since the turbulence becomes increasingly damped. In contrast to Rouse and Dodu (1955), viscosity was discarded as a possible influence on the entrainment rate, for two reasons: (i) first, the viscosity did not vary

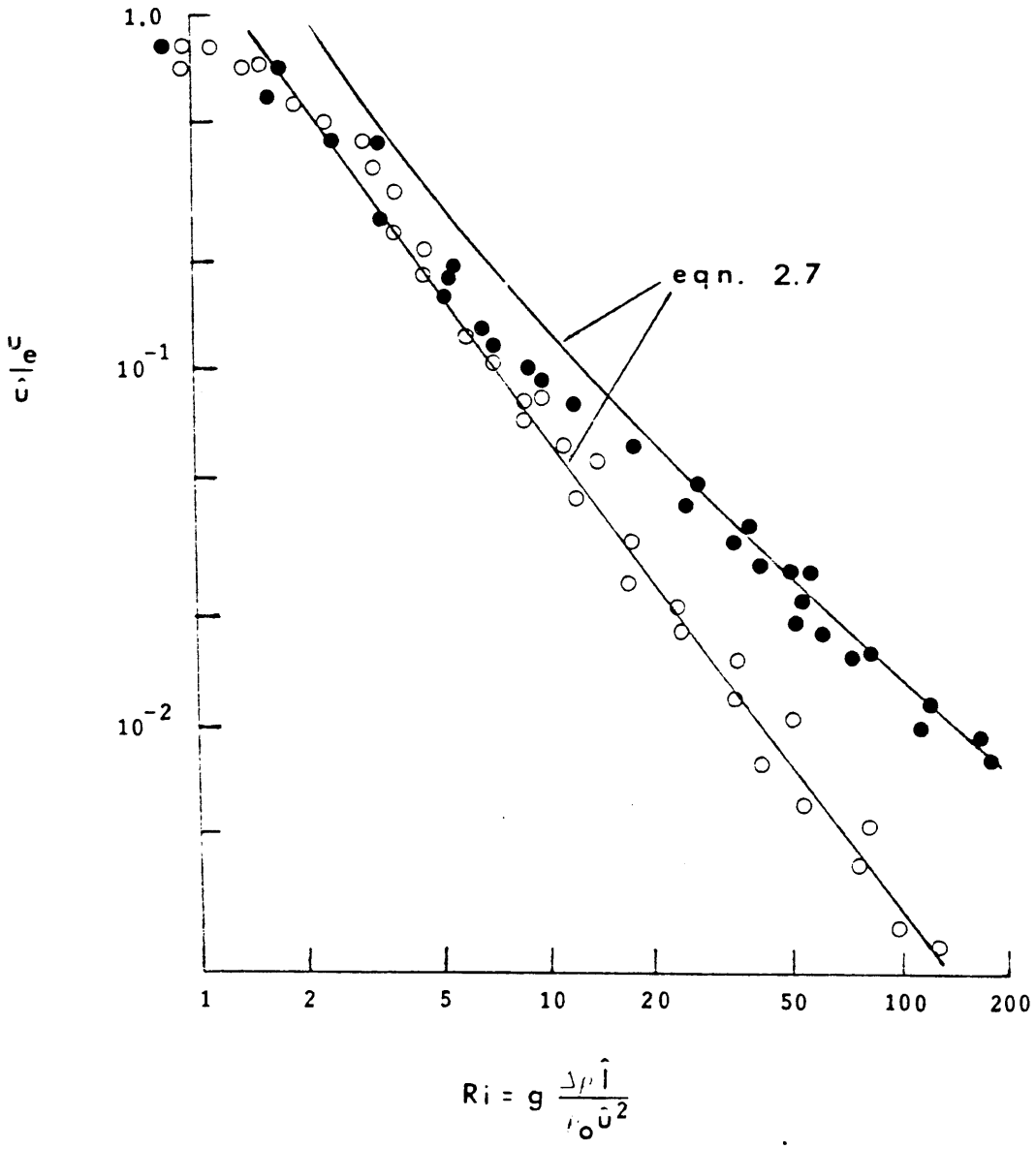

FIGURE 8 Grid-Mixing Results for Singly-Stratified Systems (from Turner, 1973)

enough in these experiments to account for the difference, and (ii) it was noted that viscosity would play a role in the generation of turbulence near the grid and in its subsequent decay as it progressed away from the grid towards the interface, but there was no need to invoke viscosity as long as the velocity and length scales of the turbulence near the interface were specified. Therefore, neither the Reynolds number nor Prandtl number (Pr) were needed and a Peclet number (Pe) was chosen to describe the molecular effects. Here, Pr is defined as $Pr = \nu/k_T$ and $Pe = \hat{u}\,\hat{\ell}/\hat{k}$, where k is the diffusivity of the stratified component and $\hat{u}$ and $\hat{\ell}$ are the turbulent velocity and length scales. Pe expresses the relative strength of turbulent diffusion compared with molecular diffusion. Turner further argued that modification of (2.3) by a function of Pe alone was not appropriate since this would affect results over the entire range of Ri values, while the data showed that the entrainment was similar for both heat and salt at low Ri (Figure 8). He suggested a relationship of the form

$$\frac{u_e}{\hat{u}} = Ri^{-1}(C + RiPe)^{-1/2} \quad , \tag{2.5}$$

where C is a constant. This had the desired characteristics to describe the experimental results.

The effect of molecular diffusivity on entrainment was also demonstrated by Wolanski and Brush (1975), who used heat, salt, sugar, suspensions of idealized sediment (silica spheres) or suspensions of natural kaolinite clay to provide stratification in a two-layer system with either one or both layers stirred. Based on the experimental range

of the parameters in their tests, they showed that there was a negligible dependence of u_e on Re for given Ri and Pe and argued that Re and Pe entered strongly into the entrainment relationship only as the combination Pr = Re/Pe so that $u_e/\hat{u} = f(Ri, Pr)$. (Note that this implies that viscosity is important in the entrainment process, which is inconsistent with the findings of other researchers, as noted above.) Their results are summarized by

$$E = C\, Ri^{-n} \quad , \tag{2.6}$$

where C depends on the various length scales of the problem (mesh spacing, oscillation stroke, mixed layer depth) and n is a function of Pr. In contrast to (2.3) and (2.4), values of n as high as 3 to 4 were found. However, these high values were obtained when the suspensions were used and Hopfinger and Toly (1976) have suggested that non-Newtonian effects may have been responsible. Denton (1978) offered an explanation for these very low entrainment rates as being an effect of the fall velocity of the suspended particles.

Linden's (1973) analysis supported the result (2.4) for high Ri and Pe conditions. He performed experiments in a two-layer salt-stratified tank in which a vortex ring was projected at the interface. The vortex ring was used as a model for a turbulent eddy impinging at an entrainment interface. Movie film was used to record and measure the characteristic length and velocity of the ring and observations of the interaction of the ring with the interface showed that the interface is first deflected downward and mixing occurs as it recoils and fluid is thrust into the

upper layer. Entrainment in a grid-mixing experiment was then supposed to consist of a combination of similar events. The result $E \propto Ri^{-3/2}$ was derived by assuming that the fluid is ejected upwards a distance approximately equal to the length scale of the ring and that the rate at which kinetic energy is released by the recoil (estimated as the natural response time scale for the deflected interface) is equal to the rate at which potential energy is increased by the lifting of fluid across the interface. At low values of Ri the interface becomes less stable and more distorted and the above model is not applicable. At low Pe molecular diffusion becomes more important and the interfacial flux increases as diffusion is significant during the initial depression of the interface.

Based on Linden's work and also citing some unpublished experiments by Rooth, Turner (1973) revised his earlier argument and suggested that the basic entrainment law was given by (2.4). Rooth performed temperature-stratified experiments with high values of Pe obtained by increasing $\hat{u}$ and found that $E \propto Ri^{-3/2}$, where $E = u_e/\hat{u}$. Turner noted, "As Pe is reduced, the curves break away from the $Ri^{-3/2}$ line at successively lower values of Ri, rising above it with decreased slope as molecular diffusion increases the transfer rate.". He also cited the study by Fortesque and Pearson (1967) of gas absorption into a water surface as an example of a very high Ri situation. This study showed that E was independent of Ri, but proportional to $Pe^{-1/2}$, where Pe was defined with the gas diffusivity in water and with the length and velocity scales of the large eddies in the water. Turner suggested that

this limit might also apply for a water-water interface.

Further experiments relating to the dependence of E on Pe were conducted by Crapper and Linden (1974), using the same apparatus as Turner (1968a). Two-layer systems using either temperature or salt stratification were considered and the emphasis of these experiments was to examine the detailed structure of the interface separating the layers. Ri, Pe, and Re were defined using actual turbulence measurements (reported in Thompson and Turner, 1975) and variations with Ri and Pe were examined while Re was approximately constant. For temperature stratification interfacial thickness was found to increase with decreasing Pe and there was a relatively undisturbed central core region, while for Pe $>$ 200 eddies apparently were able to penetrate completely across the interface. No significant trend was found with Ri. For salt stratification there was little variation in interface thickness with either Ri or Pe. They noted that under low Pe, quasi-steady conditions, the interface thickness is determined by a balance between a diffusive flux through the central core and an entrainment flux at the edges of the core region; i.e., the gradient within the core region will adjust to obtain this balance. For Pe $\tilde{>}$ 200 direct mechanical mixing was needed to explain the interfacial fluxes and this result was shown to be consistent with Turner's (1968a, 1973) data since Pe $\tilde{<}$ 200 corresponded roughly to Ri $\tilde{<}$ 7, which is the region where salt and temperature entrainment results were similar (see Figure 8).

Hopfinger and Toly (1976) also performed salt-stratified experiments where Pe was varied by changing the velocity and length scales of the turbulence. They concluded that $E \propto Ri^{-3/2}$, but the coefficient of

proportionality was dependent on values of $\hat{u}$ and $\hat{\ell}$. An alternative to (2.5) was proposed as

$$\frac{u_e}{\hat{u}} = C_1 Ri^{-3/2} + C_2 (RiPe^{1/2})^{-1} \quad , \tag{2.7}$$

where C_1 and C_2 are constants. In other words, as Pe becomes small (i.e., corresponding with temperature stratification), the second term on the right hand side provides the dominant contribution and $E \tilde{\propto} Ri^{-1}$. For larger Pe (e.g., salinity stratification), $E \tilde{\propto} Ri^{-3/2}$, as the first term dominates. This relation attempts to incorporate a Pe dependence (i.e., a dependence on molecular diffusivity) into one equation that explains both the temperature-stratified (generally low Pe) and salt-stratified (high Pe) results. The form of the equation was chosen to fit the data trends as reported by Turner (1973) and shown in Figure 8. The curves drawn in Figure 8 were calculated from (2.7) using $C_1 = 2.18$ and $C_2 = 11.2$, with Pe estimated using values of $\hat{u}$ and $\hat{l}$ reported by Thompson and Turner (1975).

Long (1978a, 1978b, 1978c) has developed a theory for grid-induced entrainment in a strongly stable salt-stratified system which predicts that $u_e/\hat{u} \propto Ri_1^{-7/4}(z/h)$, where z is defined as the distance between the interface and a virtual source of energy. (see Section 2.2.1.1) and $Ri_1 = \Delta b h^3/(z\hat{u})^2$. The Richardson number exponent of -7/4 is very close to the value of -3/2 previously suggested. Fernando and

Long (1983) performed experiments in a two-layer salt-stratified system to check the earlier theoretical results and showed that the data was well represented by the above relation. However, it could be argued that a curve corresponding to $Ri_l^{-3/2}$ would also fit the data reasonably well and it would be difficult to choose which curve was a closer fit due to the small difference in the exponents. Long's model appears to be supported by the data presented by Fernando and Long, but it does not have any provision for varying the diffusivity of the stratified component and would not, for instance, reproduce Turner's (1973) heat-stratified results. There is also no provision for very weakly stratified conditions, where Ri (Ri_l) approaches zero (of course, this is also true for Equation 2.7).

In contrast to the above grid-mixing experiments which were concerned with two-layer systems, Linden (1975) examined the effect of having a continuous stratification in the unmixed layer. He used the same tank as Turner (1968a) and performed experiments with an initial linear density stratification (using salt) as well as two-layer tests in order to compare E in the two systems at comparable Ri. Internal waves were observed in the stratified experiments, radiating energy away from the interface which might otherwise be used for entrainment. The reduction in the entrainment rate from the two-layer case was found to have approximately the same value as the ratio of the maximum rate at which energy could be radiated away by internal waves to the rate of change of potential energy. This ratio was defined by

$$R = Ri_G^{3/2}/Ri^2 \quad , \tag{2.8}$$

where $Ri_G = (N\lambda/\hat{u})^2$, $N = [(-g/\rho_o)\Gamma]^{1/2}$ is the Brunt-Vaisala frequency and λ = wavelength of the internal wave. Ri_G is seen to be a kind of gradient Richardson number, expressing the ratio of internal wave energy to the energy level in the mixed layer. A simple relationship between E and Ri was not found, though a function of the form of (2.6) seemed to be appropriate, with n varying between 0.7 and 1.5, depending on the strength of the gradient and the mixed layer depth. Linden concluded that E could not be determined uniquely by a local interfacial parameter when there was a density gradient in the unstirred layer and suggested that $E = f(Ri, Ri_G)$. The general entrainment relation developed in Chapter 3 includes a term of account for internal wave generation.

Experiments by Kantha and Long (1980) and Hopfinger and Linden (1982) have followed Turner and Kraus (1967) in considering mixed layer deepening in the presence of a surface buoyancy flux. Kantha and Long modeled this effect by adding lighter or heavier fluid at the surface of the tank and withdrawing fluid at the bottom in order to maintain a constant buoyancy flux without a net addition of water. They characterized each experiment in terms of the input flux of energy by the grid and the input surface buoyancy flux and found that the mixed layer depth was of the same order as the Monin-Obukhov length, defined as proportional to the cube of a representative r.m.s. velocity in the mixed layer divided by the surface buoyancy flux. Hopfinger and Linden modeled a buoyancy flux by adding fresh water to a salt solution and also by heating. They noted that

$$h \propto \frac{\hat{u}^3}{B_f}$$

implies that a constant fraction of input kinetic energy (by buoyant convection) is used to increase the potential energy by entrainment (first noted by Kraus and Turner, 1967). However, they also suggest that this relationship is not well proven and that the global energetics implied in this argument does not predict the temporal evolution of the mixed layer depth well. The interaction of the eddies in the mixed layer with the stratification is an essentially local process and the available energy may not be a constant fraction of the energy input. They found that h scaled better on the local turbulence level and that this result was equivalent to the global energy argument only for approximately uniform turbulence in the mixed layer (i.e., shallow layers, strong convection or shear flow).

2.2.1.1 Turbulence Models and Measurements

The mechanism of turbulence generation by an oscillating grid has been previously discussed by Thompson and Turner (1975) and Hopfinger and Toly (1976). The flow development is described in terms of three regions: i) the generation of quasi-steady jet flow near the grid bars, dependent on grid cross-section, oscillation amplitude and viscosity; ii) jet interaction and break-down into turbulence which is advected by the jets and iii) viscous decay of turbulence. The quasi-steady motions associated with the grid oscillation have been found to persist up to one or two mesh spacings away from the grid and this was also found in the

present experiments (Figure 25). In this region the fluid motion is dominated by the movement of the grid and true turbulence is not very significant.

The spatial decay law for turbulence may be derived from the steady-state turbulent energy equation under non-stratified conditions,

$$\frac{d}{dz}\,(\overline{w' q^2/2} + \overline{w'p'/\rho}) + \varepsilon = 0 \qquad (2.9)$$

(see Section 3.1 for a discussion of the terms in the TKE equation). Assuming the flux of TKE is proportional to $\hat{u}^3$ and $\varepsilon \propto \hat{u}^3$, we have $d(\hat{u}^3)/dz = C_1\hat{u}^3/\hat{l}$, where C_1 is a proportionality constant. As shown below, the r.m.s. turbulent horizontal velocity is used to estimate $\hat{u}$ and $\hat{l}$ is the turbulent (integral) length scale. Now, if $\hat{l} \propto z$, (2.9) may be solved to obtain

$$\hat{u} = u_0(z/z_0)^{-C_2} \qquad (2.10)$$

where $C_3 = \hat{l}/z$ and $C_2 = C_1/3C_3$. u_0 is the velocity at the virtual origin z_0 and is assumed to be proportional to fs, where f = oscillation frequency and s = stroke. Hopfinger and Toly found that the values for C_1 and C_3 changed individually with different grid geometries, but the ratio C_2 remained approximately constant with a value close to unity. Thompson and Turner (1975) also derived (2.10) from an inertial decay model proposed as an analog to the temporal decay model of Batchelor (1953).

Several experiments have been reported in which turbulence levels in grid-mixing tanks were measured. The purpose of these tests was to define appropriate velocity and length scales for interpreting entrainment results. That is, data was needed to find the values for the constants in (2.10). Thompson and Turner (1975) used a rotating hot film probe to obtain values for $\hat{u}$ and $\hat{l}$ as functions of depth from the stirring grid and these results were used to scale the earlier entrainment experiments of Turner (1968a) (the scaled data was reported in Turner, 1973). $\hat{u}$ was defined as the r.m.s. horizontal velocity component and $\hat{l}$ was defined as the integral length scale, determined from autocovariance calculations. (These definitions will be used for the remainder of this section.) Measurements were made in a non-stratified system and it was assumed that they would provide appropriate values under conditions where a density interface was present. Their results indicated that, for a given value of h_g (distance from the grid), $\hat{u}$ was proportional to f and to $h_g^{-1.5}$. They also found that $\hat{l} \propto h_g$.

Long (1975) suggested that the measurements made under homogeneous conditions were in fact not relevant to the experiments with a density interface present and his analysis implied that $\hat{u}$ should depend slightly on Ri. In other words, the presence of an interface would tend to inhibit the turbulence. In addition it was proposed that a weak density gradient in the nominally homogeneous layer would cause a decrease in $\hat{u}$ which depended on Ri. (Note that Wolanski and Brush (1975) found very weak density gradients in the supposedly mixed layer in their grid-mixing experiments.) Assuming that there is an Ri dependence, $\hat{u}$ would no longer

be simply proportional to the stirring frequency f (a result from dimensional analysis for a homogeneous system), but instead depends on $f^{4/3}$ (Long, 1975). It was suggested that this dependency of $\hat{u}$ on Ri might account for the different power laws reported by Turner (1968a, 1973) for temperature and salinity stratified experiments (Eqs. 2.3 and 2.4). Although not explicitly stated, Long's argument must also take into account the differences in molecular diffusivity between salt and heat since different values of $u_e/\hat{u}$ were found at the same Ri for the two kinds of stratification in Turner's experiment. It is more likely that there would be stronger density fluctuations in the stirred layer with salt stratification since fluid entrained across the interface would not tend to be mixed into the layer as readily as with heat stratification. More of the input energy would then be used in maintaining the homogeneity of the layer, leaving less for entrainment.

However, more recent experimental results discussed below have shown that Long's argument is incorrect and the measurements made in a homogeneous system provide the proper scaling quantities for the entrainment tests. Hopfinger and Toly (1976) measured the horizontal velocities produced by an oscillating grid using a hot film probe both with and without a density interface present. Variations in grid geometry, oscillation frequency and amplitude were examined and $\hat{u}$ was found to be proportional to f whether a density interface was present or not. A laser anemometer was also used as a check on the hot film results, but only for homogeneous conditions. The integral length scale was calculated and their results showed that $\hat{l} \propto h_g$ and $\hat{u} \propto h_g^{-1}$ and it was suggested that the results of Thompson and Turner

(1975) were also well represented by $\hat{u} \propto h_g^{-1}$ instead of a -1.5 exponent, as they had reported. In order to check the implicit assumption that $\hat{u}^2$ is a good estimate of the turbulent kinetic energy available near an interface, Hopfinger and Toly also measured the vertical velocity component and showed that at distances greater than about one mesh spacing from the grid the turbulence was very close to being isotropic (the horizontal r.m.s. velocity was at least 90% of the vertical r.m.s. velocity at corresponding points). Measurements of $\hat{u}$ near a salinity interface were compared with measurements made at the same distance from the grid but without an interface and little difference could be seen. They concluded that the homogeneous values of $\hat{u}$ and $\hat{l}$ were representative of values near an interface.

Further support for this conclusion was provided by McDougall (1979). He performed a comprehensive set of turbulence measurements using a laser anemometer with a tank built to reproduce Turner's (1968a) apparatus. He was able to obtain data near an interface since the density step was produced using a combination of solutes such that the refractive index of the solution remained constant. He showed that a small density difference across the mixed layer was not dynamically important and that $\hat{u}$ did not depend significantly on Ri. Therefore, the turbulence in the stirred layer is relatively unaffected by the entrainment of fluid across the interface. Measurements of the r.m.s. vertical velocities $\hat{v}$ in homogeneous fluid showed that at corresponding points $\hat{v}$ was slightly greater than $\hat{u}$. However, $\hat{v}$ decreased near an interface whereas $\hat{u}$ remained nearly unaffected until right at the edge of the interface, where some increase in $\hat{u}$ was observed and this was

attributed to the distortion of the eddies as they impact.

Long (1978a, 1978b, 1978c) later revised his earlier argument (discussed above) and developed a theory of turbulence in stratified fluid for the zero-mean-shear conditions of the grid-mixing experiments. He showed that the eddy viscosity $\hat{u}\,\hat{l}$ should be constant in a homogeneous stirred layer, so that $\hat{l} \propto h_g$ implies that $\hat{u} \propto h_g^{-1}$, as found in the above-mentioned experiments. He also proposed that $\hat{u}$ near an interface should be approximately the same as it would be without an interface present but that $\hat{v}$ would decrease with increasing interfacial stability. Some experimental evidence for Long's theory is shown by McDougall (1979) and Fernando and Long (1983). A mixing parameter $K = \hat{u}\, h_g$ was defined to characterize the turbulent energy source and a Richardson number $Ri' = \Delta b h^3/K^2$, where $\Delta b = g\Delta\rho/\rho_o$, was suggested as being the most appropriate choice for this problem. It is noted that if h_g corresponds with h then Ri' is the same as Ri defined in (1.7), where $\hat{u}$ is substituted for u_*.

The integral length scale $\hat{l}$ was obtained from autocorrelation calculations. Both Thompson and Turner (1975) and Hopfinger and Toly (1976) assumed a Taylor hypothesis in relating their measurements in time to measurements in space (this assumes that the probe is moving much faster than the turbulence). Therefore the autocorrelation estimates result in a direct calculation of length scale. Single-point measurments taken in time are somewhat more difficult to interpret in terms of spatial characteristics, especially under conditions of zero mean flow. This is the case with LDA measurements for grid-induced motion. (Note, for instance, that McDougall, 1979, did not calculate length scales.) A

possible procedure is to calculate the integral time scale from the time series of data and multiply by the velocity scale to define a length scale. This is the procedure followed in the present experiments (section 4.3.1), but it is not clear how the present results relate to the results obtained with the rotating probe.

Summary

As seen in the review above, there has been considerable interest in grid-induced mixing in stratified fluid. The grid entrainment experiments are listed in Table 1 and several conclusions are summarized below:

(1) For low Pe conditions the entrainment relation appears to follow $u_e/\hat{u} \propto Ri^{-1}$, while for high Pe, $u_e/\hat{u} \propto Ri^{-3/2}$ or $u_e/\hat{u} \propto Ri^{-7/4}$.

(2) Measurements of grid-induced horizontal length and velocity scales obtained under non-stratified conditions provide appropriate scaling quantities for entrainment results in stratified systems.

(3) When the quiescent layer is stratified a second parameter must be included in the entrainment relation to account for loss of entrainment energy due to internal waves.

(4) The Pe dependence of u_e may be incorporated into a single equation to describe entrainment in either temperature stratified (low Pe) or salt-stratified (high Pe) systems, as shown by Equation (2.7) (see Figure 8).

(5) Previous experiments have looked primarily at singly-stratified systems and have not considered systematically the effect of a

Table 1. Summary of oscillating grid entrainment experiments.

Reference	Apparatus	Experimental Conditions	Basic Results	Comments
Rouse and Dodu (1955)	plastic cylinder, 50 cm long x 20 cm diameter; grid made at 1 cm wide metal strips spaced 5 cm on center	mean grid position 8 cm below surface and 10 cm above the interface; h kept constant by adding solution at the bottom and withdrawing at top; density and viscosity differences obtained by using solutions of varying concentrations of salt and sugar; $\Delta\rho/f_o \lesssim 3\%$; two-layer systems	from a dimensional analysis, assumed entrainment was a function of Fr and Re: $E = 5 \cdot 10^4 \, Fr^{5/2} \, Re = 5 \cdot 10^4 \, Ri^{-5/4} \, Re$	a "mixing coefficient" was defined as $\varepsilon = Cfh^2$ (which implicitly assumes $\hat{u} = Cfh$ and $\hat{\ell} = h$); then, $E = u_e h/\varepsilon$, $Fr = \varepsilon/(h^3 g')^{1/2}$ and $Re = \varepsilon/\nu$; Re was not varied much; noted that $E \propto Fr$ would imply that a constant fraction of input KE was used for entrainment (changing the PE), but their results did not support this; one possible reason for this may be due to double-diffusive effects
Cromwell (1960)	27 cm long x 17 cm wide x 14 cm deep tank; grid made of 1/4" galvanized mesh	initial stratified (salt) conditions, with maximum density like that of sea water	qualitative results; u_e was found to gradually slow with time, approaching a constant value, but initially was quite fast	provided good observation of the structure of the interface using dye; noted that some large-scale circulation was observed; suggested that there may be a critical dissimilarity in the turbulence spectra of the tank and the ocean, so that there was some uncertainty in applying results directly

Table 1. Summary of oscillating grid entrainment experiments (continued).

Reference	Apparatus	Experimental Conditions	Basic Results	Comments
Turner and Kraus (1967)	plexiglass tank, 25.4 cm x 23 cm x 44 cm deep; 1 cm x .15 cm plexiglass strips spaced 4.5 cm on center formed the grid	a ~ 1 cm, grid just below surface; started with initial uniform density, then simulated heating or cooling by adding solutions of greater or lesser salinity at the surface	noted slowing of u_e with time, approaching constant value depending on $\Delta\rho$; showed by dimensional argument that E shoud be E = f(Ri), but suggested that Re may also be important in some cases; concluded that much of the mixed layer growth could be modeled by proper consideration of the heating/cooling cycle	primary emphasis was to find "how much of the observed time dependence of the mixed layer depth and the surface temperature can be explained . . . with a fixed stirring rate and a correct modeling of the surface heat input alone"
Bouvard and Dumas (1967)	box 80 cm x 80 cm x 1 m high; grid made of a perforated plate	homogenous fluid	turbulence measurements	developed hot wire technique for measuring turbulence
Turner (1968a)	Perspex tank, 25.4 cm x 25.4 cm x 40 cm deep; grid formed with	two-layer system, each layer 18 cm deep; some experiments with both layers stirred by grids at middle of layers, some experiments with	temperature stratification => $u_e \tilde{\alpha}$ Ri^{-1}; this relationship also true for salt stratification at low Ri, but at	Ri was not well-defined since the proper length scale was unknown, though it was suggested that the length and velocity scales of the turbulence near the

Table 1. Summary of oscillating grid entrainment experiments (continued).

Reference	Apparatus	Experimental Conditions	Basic Results	Comments
Turner (1968a) cont.	1 cm square Perspex strips, space 5 cm on center	only bottom layer stirred, but interface maintained at constant level by withdrawal/ addition technique similar to Rouse and Dodu (1955); 1 cm stroke f = 166-333 cpm, $\Delta\rho/\rho_o \cong$ 0.005 (temperature or salinity)	higher Ri, $u_e \tilde{\propto} Ri^{-3/2}$; concluded that molecular diffusion becomes more important at high Ri and affects the entrainment law; suggested that $u_e/\hat{u} = Ri^{-1}\ (c + RiPe)^{-1/2}$	interface would be the proper scales to use; assumed that the -1 law was fundamental because of its convenient interpretation in terms of an energy balance, and the slower rate for salt was due to the much lower diffusivity, so that an entrained element was incorporated into its surroundings at a slower rate; viscosity discarded as possible cause of differences observed
Linden (1971)	same as Turner (1968a)	considered two-layer "finger" system; 1 cm stroke, f = 0-5 Hz	suggested that $\lambda_1 = w^2/u_g^2$ could be used as a measure of the effect of turbulence, where w = velocity in fingers without grid motion and u_g = grid-induced motion	this experiment is of interest since it considers both double-diffusive and turbulence effects; however, it is not of direct use in the present experiments because of the different stratification
Crapper and Linden (1974)	same as Turner (1968a)	used two-layer stratification with either ΔT or ΔS; looked at variations in interface thickness	conclude that there is a dependence of u_e on Pe and results are consistent	these results supply additional evidence that Pe is important in the entrainment mechanism

Table 1. Summary of oscillating grid entrainment experiments (continued).

Reference	Apparatus	Experimental Conditions	Basic Results	Comments
Crapper and Linden (1974) cont.		with Ri and Pe (Re ~ constant); measured detailed interfacial structure with thermocouple and conductivity probes	with Turner's (1973) results--Pe affects the interface thickness and determines whether molecular diffusion or mechanical entrainment is more important in the interfacial flux	
Wolanski and Brush (1975)	same as Turner (1968a)	used two-layer stratification with heat, salt, sugar and suspensions of natural kaolinite clay and idealized sediment	$E = CRi^{-n}$, where n = n(Pr) and C depends on geometry and varies from ~1-4; noted existence of weak density gradient in supposedly mixed layer	the high values of n obtained here have been explained by Denton (1978) as a direct result of the settling of the particles in the suspensions
Linden (1975)	same as Turner (1968a)	used both two-layer and linearly stratified systems, with the grid stirring near the top; compared values of u_e obtained with the two kinds of stratification under similar conditions	$E \propto Ri^{-n}$, where n depended on the stratification in the quiescent layer and varied between 0.7 and 1.5; suggested that $E = f(Ri_G, Ri)$, where $Ri_G = (N\lambda/\hat{u})^2$ is a gradient Richardson number and λ = internal wave length	note that it was difficult to define h in the linearly stratified case; suggests that an approximately constant fraction of kinetic energy near the interface is converted to potential energy by entrainment, but the available energy may not be a constant fraction of the energy input near the surface

Table 1. Summary of oscillating grid entrainment experiments (continued).

Reference	Apparatus	Experimental Conditions	Basic Results	Comments
Thompson and Turner (1975)	same as Turner (1968a), but used several different kinds of grids (square cross-section, round rods) and also considered data from Bouvard and Dumas (1967), using perforated plate	measured turbulence velocity (r.m.s. value) and length (integral scale) scales under non-stratified conditions using a rotating hot film probe; looked at spatial variation (vertically); f = 2-5 Hz, s = 1 cm	$\hat{\ell} \propto z^{-1}$ (z = distance from virtual origin, assumed to be at z_o = s = stroke, to measurement point); $\hat{u} \cong 1.4\ f\ s^{2.5}\ z^{-1.5}$	good discussion of turbulence generation by oscillating grid; relation for $\hat{u}$ describes data to within ±50%; these measurements were used by several of the investigators listed in this table to scale entrainment results
Hopfinger and Toly (1976)	same as Bouvard and Dumas (1967) except grid was made of square bars	obtained turbulence measurements both with and without a density interface present--f = 2-6 Hz, s = 4 and 9 cm, and m = mesh spacing = 5 and 10 cm; rotating hot film probe used for most measurements, though laser anemometer was also used to check results; two-	$\hat{\ell} \propto z$, where z measured from virtual origin z_o = 3 cm below grid; $\hat{u} = .25\ fs^{3/2}\ m^{1/2}\ z^{-1}$ (within 20%); for high Pe conditions, found that $u_e/\hat{u} \propto Ri^{-3/2}$, with coefficient depending on geometry; suggested that $u_e/\hat{u}$	concluded from their data obtained both with and without a density interface that the values of $\hat{u}$ and $\hat{\ell}$ calculated for non-stratified conditions were representative of values that would be present near an interface; this work compliments that of Thompson and Turner (1975)

Table 1. Summary of oscillating grid entrainment experiments (continued).

Reference	Apparatus	Experimental Conditions	Basic Results	Comments
Hopfinger and Toly (1976) cont.		layer salt stratification used	= $Ri^{-1}(C_1 Pe^{-1/2} + C_2 Ri^{-1/2})$ would adequately model the Pe dependence of u_e	
Crapper (1976)	same as Turner (1968a)	used two-layer diffusive double-diffusive stratification; s = 1 cm, f = 50-300 r.p.m., initially, Δs = 0.75% and R_ρ = $\tilde{=}$ 2 for all runs (i.e., not strongly stratified); obtained fluxes by measuring T and S in each layer	defined $\lambda_e = u_s/u_d$ as the parameter showing the relative importance of grid motion and double-diffusive effects ($u_s = \hat{u}$ = grid-induced velocity associated with double-diffusive convection and measured in absence of grid motion); found that $\lambda_1 \to 0 \Rightarrow$ results were the same as for experiments with heating only (no grid), in terms of the flux ratio; for $\lambda_c \tilde{>} 1$ mechanical mixing dominated; showed that increasing ΔT caused an increase in salt flux	this is the only previous experiment to look at externally imposed entrainment in a diffusive system, but the stratification used here is too weak for application of the results to solar pond conditions; noted that the transport across a diffusive interface at high λ_1 was probably similar to the transport across an unstirred diffusive interface with R_ρ just slightly > 1, where turbulence is produced by an unstable buoyancy flux

Table 1. Summary of oscillating grid entrainment experiments (continued).

Reference	Apparatus	Experimental Conditions	Basic Results	Comments
McDougall (1979)	replica of Turner (1968a)	f = 1-10 Hz, s = 1 cm; used laser anemometer to measure horizontal and vertical velocities 10 cm from the grid both with and without a density interface; avoided refractive index problems by using a combination of solutes (sugar and Epsom salts) so that a density interface could be created without changes in the refractive index of the solution	significant mean motion found for $f \gtrsim 7$ Hz; measurements at various horizontal locations indicate no obvious patterns (depending on whether the measurement point is directly below a grid bar or not); for $f < 7$ Hz, $\hat{u} \propto f$, as shown by Hopfinger and Toly (1976)	also concluded that turbulence scales measured in non-stratified fluid provide relevant scaling parameters at the base of a mixed layer; noted that the entrainment process must change with Ri since a significant fraction of the buoyancy flux is due to molecular diffusion (see also Crapper and Linden, 1974)
Fernando and Long (1983)	57.2 x 57.2 cm^2 area x 61 cm high plexiglass tank; grid made of plexiglass bars with cross section .95 cm x .95 cm and	s = 5 cm, f = 1.2-2.2 Hz; two-layer salt stratification; deepening of the layer was monitored by observations on a shadowgraph and interfacial layer thickness was determined by vertically traversing a laser beam; conductivity probe also traversed	$E = u_e/\hat{u} \propto Ri^{-7/4}$ where $Ri = \Delta z^3/K^2$ and z = distance from interface to virtual origin and $K = \hat{u}z$ is defined as "action", or a mixing coefficient	this experiment was designed to test the theoretical results of Long (1978a, 1978b, 1978c) and the agreement is quite good; however, no allowance is made for different diffusivity and Turner's (1973) result for thermal stratification $E \tilde{\propto} Ri^{-1}$, would not be reproduced

Table 1. Summary of oscillating grid entrainment experiments (continued).

Reference	Apparatus	Experimental Conditions	Basic Results	Comments
Fernando and Long (1983) cont.	arranged in array with 4.76 cm spacing (on centers)	to obtain salinity profiles		

destabilizing temperature difference in a salt-stabilized system. Section 2.3 reviews grid experiments which have consided double-diffusive conditions.

2.2.2 Shear flow

Entrainment due to a shear flow has been studied by a number of investigators including Ellison and Turner (1959), Lofquist (1960) and Moore and Long (1971). Many of these studies have been reviewed by Bo Pederson (1980) and Gartrell (1979). Using the mean layer velocity $\bar{u}$ and depth h as scaling parameters, the entrainment rate has been usually found to be proportional to the inverse Richardson number, i.e., $u_e/\bar{u} \propto Ri^{-1}$, where $Ri = g'h/\bar{u}^2$. These experiments generally used two-layer salt stratification. However, Moore and Long also looked at heat stratification and obtained the same basic result as with salt. Ellison and Turner established the flow by allowing a salty layer to flow down an incline under a fresh water layer or floated a fresh water layer over a salty layer. Lofquist considered density flows and Moore and Long added a momentum flux at the upper and lower boundaries through a system of jets. Their experiment was conducted in an annular flume and they were able to establish flow in opposite directions for the two layers in this way.

The main source of energy for entrainment in these experiments is interfacial shear production and the inverse Ri entrainment result is in agreement with the constant Rf assumption discussed previously. This also implies that it may be important to solve a momentum budget to estimate $\bar{u}$ in a mixed layer model, as originally proposed by

Pollard et al. (1973).

2.2.3 Surface shear-stress-driven entrainment

A number of surface shear-stress-driven entrainment experiments have been performed in order to gain some insight into the process of mixed-layer deepening in stratified fluid. Some of these experiments have used annular flumes while others have used rectangular tanks. An advantage of the annular apparatus is that end effects (finite fetch) are avoided, but there is also the problem of possible secondary motion due to rotation and tilting. Figure 9 shows a sketch of the general apparatus used in these experiments. Results from several of the more pertinent experiments are summarized in Table 2 and Figure 10.

Surface shear stress driven entrainment experiments provide the most directly applicable results for developing a wind-mixing model. Perhaps the best known of these experiments are the ones performed by Kato and Phillips (1969) and Kantha et al. (1977). Both sets of experiments used the same apparatus, an annular tank holding salt-stratified fluid with a rotating screen providing shear stress at the upper surface. The only essential difference was that Kato and Phillips considered linearly stratified fluid while Kantha et al. looked at a two-layer system. Therefore, internal wave radiation in the bottom layer was not present in the latter study, but was probably able to reduce the entrainment rate in the former case. Internal wave energy generated in the two-layer system would be confined to the interfacial region and this has been observed by Wyatt (1978), who watched films of the experiment and reported small amplitude interfacial wave breaking. Kantha et al. obtained entrainment

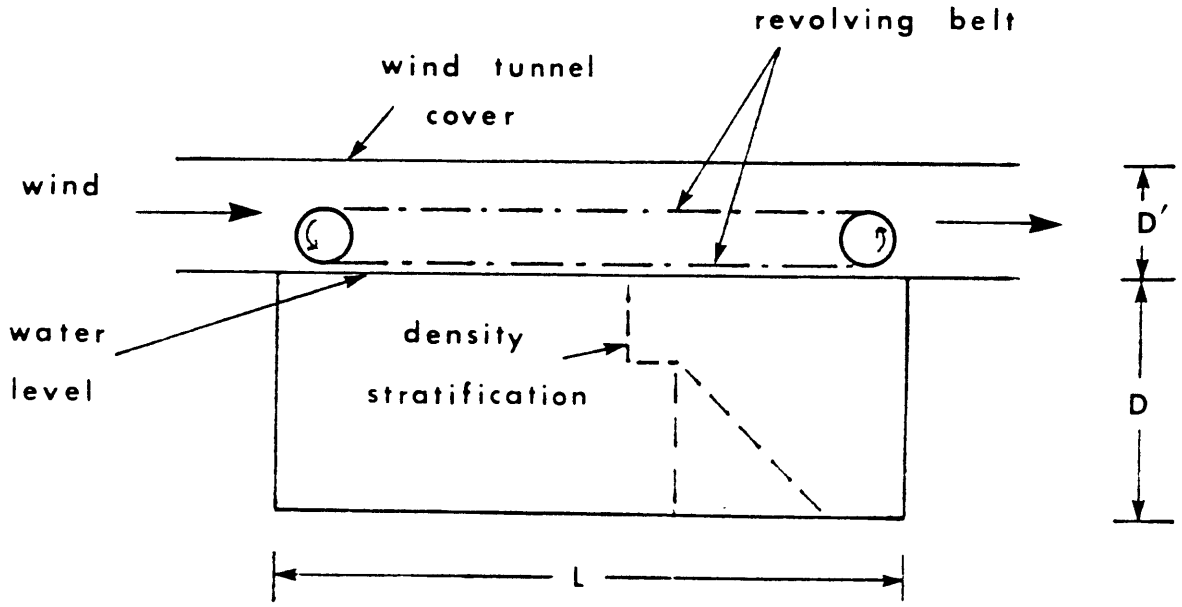

FIGURE 9 General Set-Up for Surface Shear Stress Driven Mixing Experiments

Table 2
Summary of Previous Surface Shear Stress Driven Entrainment Experiments (see notes below)

Reference	Tank Dimensions[1] (cm) L	D	D[1]	W	Stratification[2]	Shear Stress[3]	Approximate Parameter Range Ri[4]	U_w or U_B[5] (m/s)	Results[6] a	b
Wu (1973)	232	28	9.5	20.5	2	W	60-450	4.5 - 14	0.234	1
Chashechkin (1980)	40	30	-	15	L	B	[0.01 - 1.8]	max 0.18	?	3/2
Kit et al. (1980)	500	35	-	15	2, L[9]	B	10 - 100	?	0.13	3/2[7]
			-			B[8]	1 - 15[8]	0.05 - 0.2[8]	4.7 x 10^{-38}	3/2[8]
			15			W	25 - 500	3.8 - 12.5	1.5	3/2
Shelkornikov & Alyardin (1982)	710	60	11.5	37.5	2	W	100 - 500	4 - 6.5	0.17-0.31 (0.24)	1.2
Kato & Phillips (1969)	Annular tank, inside diameter = 107, outside diameter = 152				L	B[10]	30 - 300	.1 - .32	2.5	1
Kantha et al. (1977)	D = 28				2	B[10]	30 - 1100	.1 - .32	X"	1"

NOTES for Table 2

1. refer to Figure 9
2. "2" => two -layer system; "L" => linearly stratified (all of the experiments listed here used salt stratification)
3. "W" => wind; "B" => belt
4. Ri_* defined as in eq. (1.8), except for Chashechkin, where u_B = belt speed replaces u_*
5. u_W = wind speed, usualy the maximum; u_B = belt speed
6. see eq. (2.18)
7. note that the $Ri^{-3}/^2$ result was not found for the belt tests in Kit et al., but this was a best fit using the -3/2 relationship (see also note 8)
8. in this series of tests u_r = return current velocity near interface was used in place of u_* and a good collapse of data was obtained
9. no significant difference is reported between the linearly-stratified and two-layer tests
10. a rotating screen was used, rather than a belt
11. an inverse Ri law was found only for $90 \lesssim Ri \lesssim 400$; outside of this range a single exponent entrainment law was not found to be applicable; note that the model of Zeman and Tennekes (1977) reproduces much of this data well

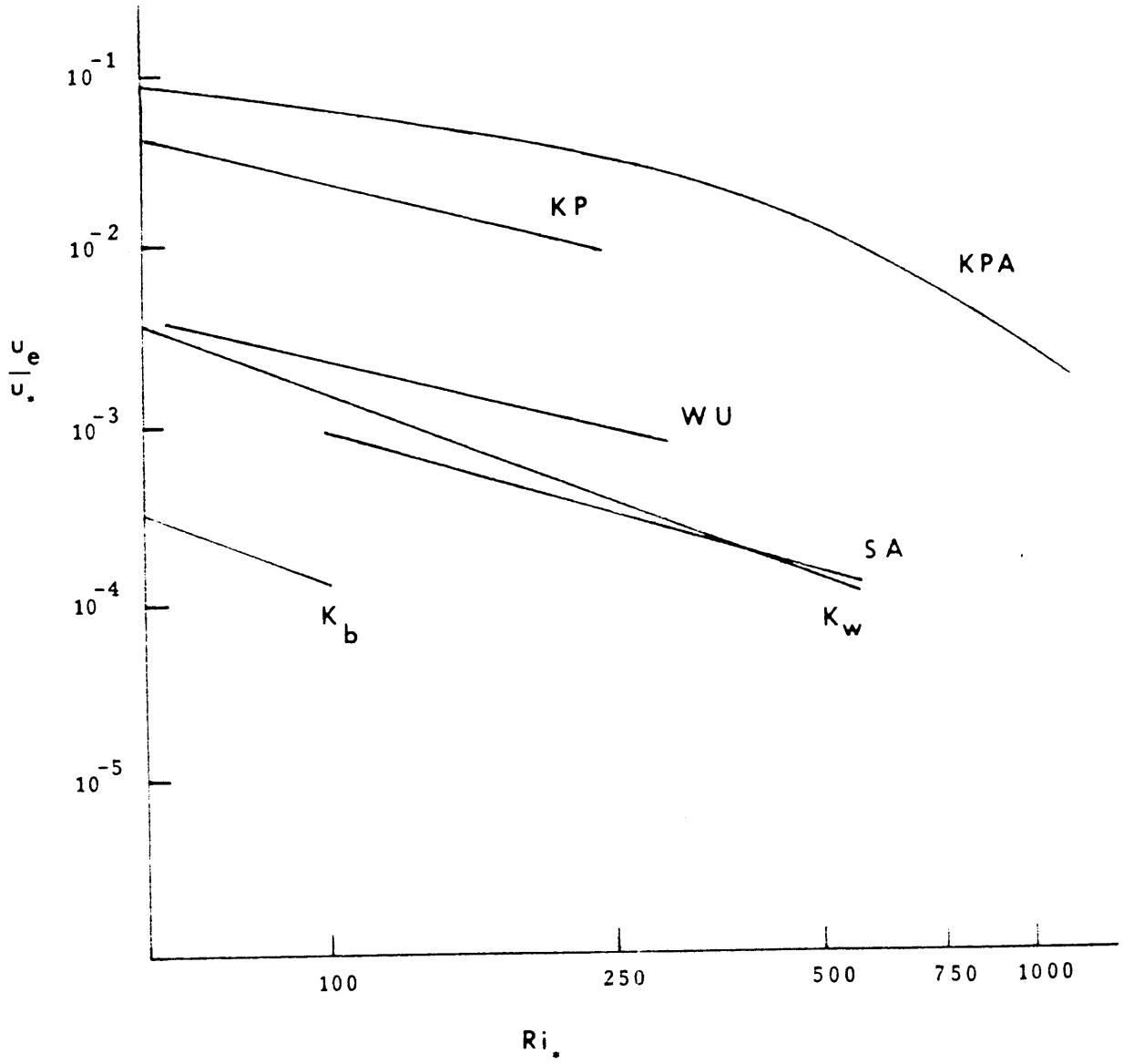

FIGURE 10 Entrainment Results from Previous Surface Shear Stress Driven Experiments; KP = Kato and Phillips (1969); WU = Wu (1973); SA = Shelkovnikov and Alyavdin (1982); K_w = Kit et al. (1980) Using Wind; K_b = Kit et al. (1980) Using a Belt - Also See Notes in Table 2

rates approximately twice those reported by Kato and Phillips and postulated that the difference was due to internal wave radiation. This agrees with calculations of Kranenburg (1981), which predict an entrainment rate for a linearly stratified bottom layer to be roughly half that for one with constant density.

The friction velocity for these experiments was determined by measuring the torque applied to the rotating wheel. The result $u_e/u_* \propto Ri_*^{-1}$ was found by Kato and Phillips and also by Kantha et al. over a limited range of Ri_*. Actually, Kantha et al. found that no single-exponent Ri_* entrainment law would adequately describe their results over the range of Ri_* considered in their experiments ($30 < Ri_* < 1100$).

Experiments in rectangular flumes have used both wind and revolving belts at the surface to provide shear stress. Salt has been used to provide the density stratification and both two-layer and linearly stratified systems have been considered. In general a friction velocity was defined to characterize the surface stress and used to define a bulk Richardson number as in (1.8). For wind experiments the air friction velocity is usually determined by fitting a logarithmic curve to the vertical wind speed data points. The water friction velocity can then be estimated with an assumption for the stress continuity across the surface. For belt experiments the shear stress is determined by torque and angular velocity measurements. E (normalized by u_*) has been found to be related to Ri_* in a manner similar to (2.6):

$$E = u_e/u_* = a\ Ri_*^{-b} \quad , \tag{2.11}$$

where a and b are experimentally determined constants.

Wu (1973) first observed wind-induced entrainment in a two-layer system by dyeing the upper layer and determined u_e by timing the descent of the dyed layer. He described the interface structure as "...wavy and rough, with high frequency disturbances superimposed on short-crested irregular waves. The interface was also observed to be bombarded by low frequency vortices, appearing as blue puffs which penetrated deeply into the clear (lower) layer and then retreated. Wisps of fluid often developed during penetration and were detached from the crests of disturbances.... The blue layer, always homogeneous in color, undoubtedly marked the turbulent mixing zone with a rather sharp density jump at its lower bound." This description also applies to the present experiments (section 5.2), except that the upper layer was not always homogeneous in color and the interface was not always sharp. Wu also observed a slight tilting of the interface and a weak return current along the interface, but he suggested that this current probably produced negligible entrainment. He added that the return current serves merely to smooth out longitudinal variations in the mixed layer.

Wu compared his results with those of Kato and Phillips (1969) (see Table 2) where a = 2.5 and b = 1 (equation 2.11). He noted that the order-of-magnitude difference in the results was probably due to the distribution of currents near the interface since his tank had end walls and, therefore, recirculation. Wu also noted that when wind was used to produce the surface stress the portion of the stress that is used for

wave drag should be subtracted from the total before computing the friction velocity of the induced current. His result listed in Table 2 has this correction already applied and it implies that only about 11% of the input kinetic energy was used for entrainment.

Chashechkin (1980) performed experiments in a small tank using linearly-stratified salt solutions and a rubber belt to provide surface stress. Although some of his results are of interest, this experiment is not of great use since he does not even report a value for the coefficient in (2.11). A value of b = 3/2 was, however, reported. The descent of the interface was observed using a Schlieren method and Chashechkin noted that the interface was relatively sharp at its upper edge, but had a more diffuse bottom. The interfacial thickness appeared to be greater with lower values of u_e. u_e was observed to be relatively large when the belt was first set in motion, then slowed to almost zero for several minutes as the initially entrained fluid was mixed throughout the mixed layer. The entrainment then proceeded at a somewhat slower pace than in the initial period. As in Wu's experiment, u_e was approximately constant for each test.

Kit et al. (1980) performed tests using both wind and a circular screen in two-layer and linearly stratified systems, with salinity differences providing the density stratification. Interestingly, results for the two kinds of stratification were found to be very similar. One might expect the entrainment in the linearly-stratified case to be somewhat less than in the two-layer case since there is a possibility of leakage of energy by internal waves. This effect was demonstrated by

Linden (1975) for oscillating grid experiments and may also be seen by comparing the results of Kato and Phillips (1969) with those of Kantha et al. (1977). Significant differences were, however, found between the wind and belt tests, with wind entrainment approximately an order of magnitude greater than that produced by the belt (see Figure 10). This difference was explained by the extra turbulence in the upper layer due to the presence of waves when wind was used. The upper layer was dyed in these experiments and the descent of the interface was recorded by visual observation at the center of the flume. The development of an intermediate wedge-shaped layer at the upwind end of the interface was also observed and it was supposed that the return flow structure in this intermediate layer was in the opposite direction to the recirculating flow in the upper mixed layer.

For the moving screen results a relationship of the type expressed by (2.11) was not found, though a result of this form was reported as showing "satisfactory agreement" (see Table 2, note 7). Assuming that the entrainment is produced primarily by shear production, u_r = return flow near the interface was defined as the proper scaling velocity and was substituted for u_* in (2.11). A reasonably good collapsing of data then resulted except for the wind results, where the entrainment was still about an order of magnitude higher. They concluded that there was a different mechanism involved and there was a major source of mixing energy associated with the wind waves so that shear alone was not responsible. Furthermore, they suggested that oscillating grid experiments were more comparable to wind experiments since the turbulence structure is more similar.

Kit et al. also attempted to explain differences in experimental results for annular and rectangular channels (eg., they note that Wu's relationship predicts entrainment to be about one order of magnitude less than the Kato and Phillips results at similar Ri_* values). However, it should be noted that a more direct comparison would have been with Kantha et al.'s results since they also used two-layer stratification. Kantha et al. found greater values of u_e than Kato and Phillips, so the differences between their results and those of Kit et al. are even more dramatic. Kit et al. suggested that the reduction in the entrainment in rectangular channels is due to the presence of the end walls, so that the surface shear force is balanced by the end wall pressure force (obtained from a momentum balance for the upper layer). Then the influence of u_e is negligible on the shear stresses and pressure distribution. However, u_e still depends strongly on the velocity distribution in the upper layer. The reduction in u_e with end walls present is then attributable to a reduced (negligible) interfacial shear, since the force balance is predominantly between the surface shear and end wall pressure forces.

Shelkovnikov and Alyavdin (1982) also used wind to study entrainment in a two-layer system. A conductivity probe was used to monitor salinity profiles, but it is not clear where the probe was located, or if profiles were taken at several locations and then averaged. They report an interfacial layer thickness of 2 - 3 cm and, as with the previous experiments, found that u_e was approximately constant for each test run. In addition, they measured the mean horizontal velocity in the water using a hot wire anemometer, though their results are scaled with u_*. They found that the entrainment was proportional to $Ri_*^{-1.2}$

and interpreted this result as implying that the entrainment mechanism derived energy from a combination of both shear production and turbulent diffusion from the surface. They suggested that shear production alone would result in a -1 exponent while turbulent diffusion alone would result in a -3/2 exponent (as shown by the oscillating grid experiments). The lower value for entrainment found here as compared with the annular experiments is explained as being due to the greater complexity of the flows produced, which implies greater dissipation of kinetic energy and a lower value for the effective shear stress.

In addition to the experimental studies noted above, Kullenberg (1977) reports data obtained from measurements in coastal waters which support the inverse Richardson number entrainment law. This data is valuable in that it was obtained under natural conditions and also because values of Ri_* as high as 0 (10^4) were obtained. He showed that both field and experimental entrainment data could be represented reasonably well by a single curve and the Ri_*^{-1} result at high Ri_* is consistent with the model developed in Chapter 3 (see also Figure 59).

Summary

Several points may be concluded about the surface shear stress driven entrainment studies reviewed above:

(1) The exponent in the entrainment relation (i.e., b in (2.11)), has been found to lie somewhere between 1 and 1.5, inclusive, but there is little evidence to suggest that a single-exponent entrainment law is really applicable over a large range of Ri values.

(2) The coefficient a (equation (2.11)) has been found to have values ranging from 4.7×10^{-3} (when u_r is used as the scaling velocity) to 1.5 (using u_*).

(3) In general, the entrainment in the rectangular flume tests has been found to be significantly lower than in the annular tests; this result is explained as being due to the presence of the end walls and the flow structure is considerably more complicated. There is also a significant difference between the entrainment in wind-driven and belt-drive tests and the presence of wind waves appears to help increase u_e.

(4) After an initial transient period, u_e is approximately constant in the rectangular flume experiments. u_e decreases slightly with time (distance from the belt) for the annular tests, but this is probably due to the increasing effect of side-wall friction as the mean current develops.

(5) A small fraction ($\tilde{<}10\%$) of the input energy by surface shear stress is converted to potential energy by entrainment.

(6) The entrainment mechanism apparently derives energy from both interfacial shear production and turbulent diffusion from the surface.

2.3 Double-diffusive experiments with stirring

Several experiments have considered double-diffusive effects in oscillating grid-induced mixing. Linden (1971) looked at salt fingers in the presence of grid turbulence while Crapper (1976) looked at the diffusive case. Both experiments were conducted in the same tank as

Turner (1968a) and used the turbulence measurements reported by Thompson and Turner (1975). The primary purpose of these experiments was to see how the double-diffusive fluxes of salt and heat were affected by the grid turbulence and to try to determine regimes where either double-diffusion or turbulence dominated the interfacial transports.

In Linden's experiments the same initial conditions were used for each run: $\alpha_T \Delta T = 0.07$ and $\alpha_S \Delta S = 0.08$. The turbulence strength was varied by changing the grid oscillation frequency f from 0 to 5 Hz. Fluxes were determined by measuring temperature and salinity in the lower layer over the course of the experiment. As f was increased he found that the ratio of heat flux to salt flux (expressed in buoyancy units, i.e, $\alpha_T H_f / \rho c_p$ and α_S g f_S) also increased and approached a constant value approximately equal to the initial value of the ratio of temperature difference to salinity difference (also expressed in buoyancy units), implying that the transport was dominated by mechanical mixing across the interface. Linden argued that instead of a Richardson number, a better measure of the effects of turbulence is given by a parameter $\lambda_L = w^2/u_g^2$, where w is the velocity in the fingers (a function of the temperature and salinity steps) and u_g is the grid-induced velocity. As the turbulence level is increased, λ_L decreases and a minimum value for salt flux was found at f = 2.2 Hz. This was explained as the result of a disruption of the ordered finger transport as the grid turbulence is first felt. As f is increased further mechanical mixing becomes dominant and the salt flux starts increasing again.

Crapper's results were also expressed in terms of a parameter indicating the relative importance of the grid-generated velocity and the

convective velocity associated with the double-diffusive conditions: $\lambda_c = u_g/u_d$, where u_d is the velocity associated with double-diffusive convection, measured in the absence of grid motion. His experiments were limited to relatively weakly stabilized conditions. An initial salinity difference of 0.75% was used, with a temperature difference chosen so that the initial value of the stability parameter was $R_\rho = 2$. f was varied between 50 and 300 rpm. As in Linden's experiment, the flux ratio was found to approach a value of about 0.15 for low λ_c, which agrees with Turner's (1965) result. The effectiveness of the double-diffusive transport relative to the grid-induced transport was shown to be especially important as the stirring rate decreased. For a given overall density difference and stirring rate the salt transport was also shown to be an increasing function of the temperature difference. Finally, Crapper noted that the transport across a diffusive interface at high stirring rate was similar to the transport across an unstirred interface at low values of R_ρ (slightly greater than 1), where turbulence is produced by the unstable buoyancy flux and the interface is not strongly stable.

2.4 Solar ponds

The general concept of a SGSP has already been discussed in section 1.3.1. Previous research has been concerned with various aspects of pond operation, such as the stability of the NCZ (Zangrando, 1979; Walton, 1982), heat extraction (Zangrando and Bryant, 1977; Wittenberg and Etter, 1982; Nielsen, 1983), bottom heat loss (Hull et al., 1983; Hull et al., 1981), and gradient maintenance (Chinery et al., 1983; Nielsen, 1976,

Table 3

Solar Pond Listing

Location	Operator	Dates	Size	Purpose	Operating Notes	Comments	Refs.
Major Natural Solar Ponds:							
Antilles Venezuela					unlined		7,2
Hot Lake Oroville, WA			2 m deep		unlined	situated in a depression on the top of a mountain	2,7,10
Medue Lake Szovata, Transylvania		described 1910	1.32 m deep		unlined	first natural solar lake described in literature	7,10
Red Sea Eilat, Israel			80 x 40 m elliptical pool		unlined		3,7,10
Lake Vanda Antarctica					unlined	surface covered with ice	10,2
Man-Made Ponds:							
Albuquerque New Mexico	Univ. of N.M.	1975 -	100 m^2	research & heating a house	hypalon liner; cost $5700; liner $1500, salt $1400	highest temp. ever recorded for solar pond 220°F	2,4,10

Location	Operator	Dates	Size	Purpose	Operating Notes	Comments	Refs.
Man-Made Ponds (cont'd.):							
Albuquerque, New Mexico	Univ. of N.M.			research		saturated solar pond, potassium nitrate used	2,4,10
Alice Springs, Australia		1981	2000 m^2 2 m deep	research		torrential rain problems	2,4
Argonne, Illinois	Argonne Nat. Lab.	1980	1000 m^2	research			2,4
Aspendale, Australia	CSIRO	1964-66	100 m^2		lined with rivaseal	wind mixing problems, turbid water, algae problems, poor efficiency	2,10
Aspendale, Australia			small research pond			filled backwards, denser layers added after lighter layers to float them	7,10
Atlit, Israel (near Haifa)		filled April '64	25 x 50 m area 1.5 m deep			filled above salt marsh an underground aquifer rich in CO_2 modified the structure beneath the pond	2,6,7, 10
Basancon, France		1872	5 m		unlined	first man-made heliothermic lake reported, created accidentally	6

Location	Operator	Dates	Size	Purpose	Operating Notes	Comments	Refs.
Man-Made Ponds (cont'd.):							
Boulder City Nevada	Desert Research Institute					saturated solar pond, borax used	2
Brazil			small research pond				2
Chattanooga, Tennessee	T.V.A.	Spring 1982	4000 m^2 3 m deep	extracts 140 kwt	$1,640,00 total; copper sulfate	largest U.S. pond	2,4
Chile						have considered conversion of salt flats to solar ponds	10
Columbus, Ohio	Ohio State U.	completed 1975	200 m^2 2.5 m deep	research provides heat for drying crops	$7500, salt $2400, liner $2500; copper sulfate, chlorine & acid	has been operating continuously longer than any other pond	2,4,10
Columbus, Ohio	Ohio State U.	1980	400 m^2	research			12
Dead Sea Potash Works	Sci. Res. Found.	completed 1960	600 m^2	research		first experimental solar pond, highest temp. 205°F	2

Location	Operator	Dates	Size	Purpose	Operating Notes	Comments	Refs.
Man-Made Ponds (cont'd.):							
Dead Sea Potash Works		1975	1100 m^2	heat extraction		first time heat was extracted	2,7,10
New Dead Sea I	Solmat Systems Ltd.	spring '83	10 acres	research energy prod.		5 MW peaking	4
New Dead Sea II	Solmat Systems Ltd.	1984	60 acres	research energy prod.		5 MW peaking	4
Ein Bokek, Israel	Solmat Systems, Ltd.	Dec. 1979	7000 m^2 3 m deep	power output, 35 kw summer, 15 kw winter		operates at temperatures in the region of 90°C	1,2,4, 10,11
Flagstaff, Arizona		summer 1982	800 m^2	heats 1500 m^2 storage bldg.			2
India		Feb. 1980	100 m^2		suspended porous bags of sodium hypochlorite	first pond in hot, humid climate	2,10
Jerusalem, Israel		1958-	1 m^2 area				6

Location	Operator	Dates	Size	Purpose	Operating Notes	Comments	Refs.
Man-Made Ponds (cont'd):							
Living History Farms, Desmoines, Iowa			9.8 m diameter, 3.7 m deep				5
Los Alamos, N.M.	Los Alamos Nat. Lab.	1982	185 m^2	research			12
Los Banos, CA	Calif. Dept. Water Resources	1984	2 ponds, each 1/2 acre	provide heat for driving desalin-			
Miamisburg, Ohio	Monsanto	1978	2000 m^2 3 m deep	provided 144 gigajoules (total) to heat municipal pool	lined	liner leaked	2,4,10
Nevada	Desert Res. Inst.	1983	1000 m^2	research			12
Saudi Arabia				small research pond			2

Location	Operator	Dates	Size	Purpose	Operating Notes	Comments	Refs.
Man-Made Ponds (cont'd.):							
Sedom, Israel		1959	625 m^2 area, 0.8 m deep			evaporation pond converted to heliothermic lake, peak temp 96°C, solution became dirty because of disintegration of walls	6
Turkey				precipitates anhydrous sodium sulfate		sodium sulfate pond, less costly than producing sodium sulfate by conventional means	2
Utah State Univ.	Utah State U.	1982	232 m^2	research			12
Yavne, Israel	Solmat Systems - Pond, Ormat Turbines	completed 1977	1500 m^2 area	produced 6 kwe power using a Rankine cycle engine			2,4,10
Wooster, Ohio	Ohio Agricultural R & D Ctr.	completed 1975	150 m^2	to heat greenhouse	lined	liner leaked	

Location	Operator	Dates	Size	Purpose	Operating Notes	Comments	Refs.
Proposed Ponds:							
Salton Sea, California			1 km^2 5 m deep	5 MWe demonstration pond	25×10^6 - $\$30 \times 10^6$		4,11
Salton Sea, California			~0.4 $mile^2$	energy generation, 600 MWe	$\$1.1 \times 10^9$	could supply enough energy for 1 million people	4, 11
Truscott Brine Lake, Texas			80000 m^2	to supply energy for Red River chloride control project, 1.9 MWe at 15% plant capacity factor	$\$5 \times 10^6$		4,11

References for Table 3

1. Clark (1980)
2. Edesess (1982)
3. Por (1970)
4. Harleman et al. (1983)
5. Hull (1980a)
6. Kirkland and Bradbury (1980)
7. Kreider and Kreith (1981)
8. N.T.I.S., U.S. Dept. of Commerce, "Solar Ponds: 1970-November, 1981 (Jan. 1982).
9. Solar Energy Information Bank, "Solar Ponds, a Selected Bibliography (Nov. 1981).
10. Tabor (1981)
11. Winsburg (1980)
12. International Solar Pond Letters, 1 (3,4), sponsored by A.S.E.S.

1979, 1983; Atkinson et al. 1984). Basic physics of the SGSP have been discussed (eg., Weinberger, 1964) and a number of feasibility studies have been performed (WESTEC, 1981; Lin, 1982; Battelle, 1982, 1983).

The number of ponds established in the world is growing slowly, but still relatively small. Table 3 summarizes many of the current installations, though it may already be out of date. It seems that interest in ponds is growing rapidly around the world.

2.4.1 Previous modeling efforts

In addition to the studies mentioned above there have been a number of models proposed for predicting the performance of a SGSP. Weinberger (1964) developed a one-dimensional analytical model for calculating expected operating temperatures using a heat diffusion equation with constant (molecular) diffusivity and involving a heat source term due to sinusoidally time varying radiation input. His model assumed that the pond surface temperature was equal to ambient air temperature and that the thermal properties of the ground below the pond were similar to those of the pond water. He was able to derive relationships between optimum temperatures, pond depth, collection efficiency and energy withdrawal rates. The assumptions of constant molecular thermal diffusivity, sinusoidal radiation input and average water surface temperature equal to average air temperature were also used by Rabl and Nielsen (1974), who developed a pond model in which the lower convecting zone was physically separated from the gradient zone by a transparent partition. They considered the possibility of using the ground beneath the pond as additional thermal storage space and also the effect of edge losses on ponds

of finite horizontal area.

Although analytical models are useful in obtaining first-order predictions, a number of simplifying assumptions are necessary to obtain solutions. A numerical formulation of the problem avoids many of these difficulties and boundary conditions may be more accurately incorporated. This was first recognized by Tybout (1966) and several numerical schemes have been devised for studying SGSP's. For instance, Akbarzadeh and Ahmadi (1980) have implemented Weinberger's (1964) model in a computer code. Shah et al. (1981) have recently presented a simplified computer model used for predicting storage zone temperatures in the Ohio Agricultural Research and Development Center's (OARDC) pond in Wooster, Ohio. This is a lumped parameter model based on an energy balance for the storage zone in which linear heat transfer functions are assumed for the various heat loss terms. Other simplified models which consist primarily of a heat budget for the LCZ are described by Henderson and Leboeuf (1980) and Panahi et al. (1982). Hull (1980) has used a numerical formulation to check some of the assumptions of the earlier model of Rabl and Nielsen (1975), and several investigators have studied the problem of pond stability (Hull, 1980; Hull et al., 1981; Meyer, 1982). Other modelers have incorporated more realistic meteorological forcing and surface boundary conditions into their codes, but essentially neglect the stability problem (Chepurniy and Savage, 1974; Hawlader and Brinkworth, 1981).

Very few models presented so far have attempted to incorporate both the short term meteorology and the physics governing the pond in a very complete manner. Although wind-mixing has been recognized as being an important problem, this effect has not been considered in great detail

and many models assume a constant depth upper mixed layer.

Meyer (1982) made a valuable contribution to the solar pond modeling literature by including both wind-induced mixing (entrainment) and double-diffusive effects and he attempted to model the growth of the UCZ. However, the fluxes due to double-diffusion (calculated according to "effective" diffusivities - see Appendix C) and wind-mixing were added linearly and it will be shown that this procedure is incorrect, since wind effects will usually dominate mixing across the interface. Cha et al. (1981) developed a model for the UCZ of a SGSP following the oceanic model described by Delnore (1980). Their model uses depth-dependent eddy diffusivities to account for wind-mixing, but the equations were derived for oceanic conditions and it is not clear that the method is applicable for much shallower solar ponds. Atkinson and Harleman (1983a) described a mixed-layer model for SGSPs, but there is some uncertainty in the entrainment relation they used since it was developed for much less strongly stratified systems.

Chapter 6 discusses the formulation of a transient one-dimensional numerical model for predicting temperature and salinity profiles in a SGSP. The model is based on the mixed layer approach as described in Chapter 1 and is an extension of the model described by Atkinson and Harleman (1983a). An important feature of this formulation is the inclusion of an entrainment algorithm so that the thickness of the UCZ may be calculated. As previously indicated, this informatin will be useful in the design of large-scale SGSP's.

CHAPTER 3

Development of Entrainment Model

In this chapter a model for entrainment is discussed. The model arises primarily from energy arguments relating the energy used by the entrainment process to the total supply of energy. The following section develops a general entrainment relation from a parameterization of the turbulent kinetic energy (TKE) budget in the upper mixed layer. The formulation is a synthesis of the models described by Niiler (1975) and Zeman and Tennekes (1977) and is similar to the relation derived by Sherman et al. (1978), although the conclusions are different. Section 3.2 then discusses a localized model for grid induced entrainment including the mechanisms responsible for the mixing. Section 3.3 discusses application of the model to wind-induced mixing.

3.1 Parameterization of the turbulent kinetic energy budget

Referring to Figure 3, consider that there is an input of energy to the mixed layer at the surface due to wind shear or some other source of energy. This energy supply may lead to an increase in the storage of TKE in the mixed layer, some may be used to maintain the homogeneity of the layer and a certain fraction will be dissipated. At the interface there may be an additional source of TKE from shear production and also a possible sink as energy is transferred to internal wave motion radiating through the stratified lower layer. The net TKE left over is then available for increasing the potential energy of the system through entrainment. These various processes are accounted for in the TKE

equation. Assuming that viscous transport of TKE is negligible and also neglecting all horizontal gradients, the TKE equation is written as

$$\frac{\partial q}{\partial t} = -\frac{g}{\rho_o}\overline{w'\rho'} - \frac{\partial}{\partial z}\overline{(w'q + w'p'/\rho_o)} - \overline{u'w'}\frac{\partial u}{\partial z} - \frac{1}{2}\nu\,\overline{(\frac{\partial u'}{\partial z})^2}, \quad (3.1)$$

(I) (II) (III) (IV) (V)

where q = TKE per unit mass ($1/2\ \overline{u_i'^2}$), primes denote fluctuating quantities and overbars indicate a time-averaged quantity. Term (I) expresses the time rate of change of TKE, term (II) is the work done against gravity, term (III) is the flux divergence, term (IV) expresses the mechanical production of energy by the working of the Reynolds stress on the mean shear and term (V) is the viscous dissipation, which will be denoted by ε_1 in the following. The relative orders of magnitude for each of these terms must be determined in order to relate u_e to the parameters describing the turbulence.

It is convenient to work with an averaged form of (3.1). For this we integrate (3.1) over h and then divide by h to obtain averaged quantities. Vertical gradients then disappear for the averaged terms except near the upper and lower boundaries of the layer. For instance, the flux divergence term provides the main source for mixing energy due to surface wind stress and the shear production term may be important at the lower boundary. If σ is defined as the velocity scale for turbulence in the mixed layer, then the flux divergence source term is estimated as

being proportional to σ^3/h. The mean viscous dissipation will also be proportional to this quantity.

At the bottom of the mixed layer there is a possible sink of energy by internal wave radiation into an underlying gradient region. That is, perturbations at the interface (thermocline) caused by turbulence in the mixed layer may generate internal waves which would radiate energy away from the interfacial region which might otherwise be used for entrainment. Note that in the case of a two-layer system ($\Gamma = 0$) waves would be confined to the interface. This leakage of energy will not in general scale with h and for now it will be denoted as ε_2. Therefore, we set

$$- \frac{\partial}{\partial z} \overline{\overline{(w'q + w'p'/\rho_o)}} - \overline{\overline{\varepsilon_1}} = C_F \frac{\sigma^3}{h} - \overline{\overline{\varepsilon_2}} \quad , \tag{3.2}$$

where C_F is a proportionality coefficient and the double overbar indicates spatial averaging. The r.h.s. of (3.2) is the net input of TKE to the layer by pressure and velocity fluctuations at the surface, after subtracting viscous dissipation. ε_2 then further reduces the net input by allowing leakage of energy by internal wave radiation away from the layer.

The shear production term was parameterized by Zeman and Tennekes (1977) as

$$- \overline{\overline{u'w'}} \frac{\partial \bar{u}}{\partial z} = C_{SH} u_e \frac{\bar{u}^2}{h} \quad , \tag{3.3}$$

where C_{SH} is a proportionality coefficient. (An alternative parameterization of the shear production term is discussed in Section 3.3.1.) The partially parameterized TKE budget for the upper layer is now

$$\frac{\partial \bar{q}}{\partial t} = -\frac{g}{\rho_o}\overline{w'\rho'} + C_F \frac{\sigma^3}{h} - \bar{\varepsilon}_2 + C_{SH}\, u_e \frac{\bar{u}^2}{h} \quad . \tag{3.4}$$

In other words, the change in storage of TKE in the layer is determined by the net balance between input of TKE by wind working on the surface and shear production and loss of energy by viscous dissipation, internal wave radiation and work against buoyancy. Following Zilitinkevich (1975), the temporal term is parameterized as

$$\frac{\partial \bar{q}}{\partial t} = C_t\, u_e \frac{\sigma^2}{h} \tag{3.5}$$

where C_t is a proportionality constant. We now consider the remaining two terms.

The leakage of energy by internal wave radiation will depend on the amplitude of the waves generated and their period, which in turn depends on the stratification (i.e., Brunt-Vaisala frequency). The amplitude a can be estimated by equating the kinetic energy of an eddy impinging on the interface with the potential energy associated with the maximum displacement of the interface. Again referring to Figure 3, if Γ is very small (relative to $\Delta\rho$) then $a \propto \rho_o\sigma^2/g\Delta\rho$. However, if there is a negligible density step then $a \propto \sigma/N$, where $N = (g\Gamma/\rho_o)^{1/2}$ is the buoyancy frequency. Zeman and Tennekes (1977) assumed this latter relation and wrote $\varepsilon_2 \propto \sigma^3/a$ or $\varepsilon_2 = C_D\sigma^2 N$, where C_D is a

proportionality constant. Sherman et al. (1978) used an interpolation between the two extremes to define a and assumed that $\varepsilon_2 \propto a^2N^3$, which is a more direct estimate of the energy transported by internal waves. Their relation is

$$\varepsilon_2 = C_D\sigma^2 N \left(\frac{\rho_o \sigma N}{\rho_o \sigma N + g\Delta\rho}\right)^2 \qquad (3.6)$$

However, following Kantha (1977), a can be estimated more directly in the case of neither Γ nor $\Delta\rho$ vanishing, again by equating kinetic and potential energies. Then, $g(\Delta\rho/\rho_o)a + N^2a^2/2 \sim \sigma^2/2$, or $a \sim [(g'^2 + N^2\sigma^2)1/2 - g']/N^2$, where $g' = g\,\Delta\rho/\rho_o$. Assuming $\varepsilon_2 \propto a^2N^3$ then gives

$$\varepsilon_2 = \frac{C_D}{N}\left[2g'^2 + N^2\sigma^2 - 2g'(g'^2 + N^2\sigma^2)1/2\right] \quad . \qquad (3.7)$$

This expression approaches the same limits as (3.6) for the cases where either $\Delta\rho$ or N approach zero. (Note that l'Hopital's Rule must be applied for N approaching zero.)

The final term to be evaluated is the buoyancy term, which accounts for the transfer of kinetic to potential energy. Allowing for both temperature and salinity stratification, the buoyancy flux across the interface due to entrainment is $-u_e\Delta b = -u_e g(\alpha_T\Delta T - \alpha_S\Delta S)$ and this will usually be the dominant contribution to the buoyancy term. However, in the limit of very strong stratification (high Ri) diffusion becomes increasingly important. Consider a situation where there is a

well-mixed but quiescent layer of depth h bounded below by a sharp density interface as shown in Figure 11. Since there is no stirring action in the layer diffusion will tend to spread the interface out, decreasing the depth of the well-mixed region. Now let the turbulence level in the mixed layer be slowly increased. A point will be reached where there is just enough energy to mix the mass diffused upward, so that h neither increases nor decreases. In other words, the diffusive boundary layer is scoured at the same rate it is trying to develop and spread into the mixed region. As the turbulence level is further increased (Ri is decreased) the diffusive boundary layer becomes eroded and h increases. Diffusion, then, plays a major role in determining a critical value for Ri at which u_e becomes zero and beyond which u_e can become negative. This mechanism is the probable explanation for the observed interfacial movement in a series of mean shear entrainment experiments using very low bulk velocities (Zangrando, 1984, personal communication). It also explains the observed growth and decay of the mixed regions in a recent experiment conducted by Newell (1984).

The buoyancy flux by diffusion is $-k_b(\partial b/\partial z)$, where k_b is a buoyancy diffusion coefficient (either salt or thermal diffusivity) and $\partial b/\partial z$ is the buoyancy gradient in the boundary layer. This gradient is estimated as $\partial b/\partial z \tilde{=} \Delta b/\ell_d$, where Δb is the buoyancy difference over a diffusive boundary layer thickness ℓ_d. Again allowing for the possible presence of both salinity and temperature gradients, assume $k_b(\partial b/\partial z) \tilde{=} g(\alpha_T \Delta T\, k_T/\ell_T - \alpha_S \Delta S\, k_S/\ell_S)$ where $\ell_T \propto \sqrt{k_T \hat{t}}$ and $\hat{\ell}_S \propto \sqrt{k_S t}$ are the temperature and salinity boundary layer

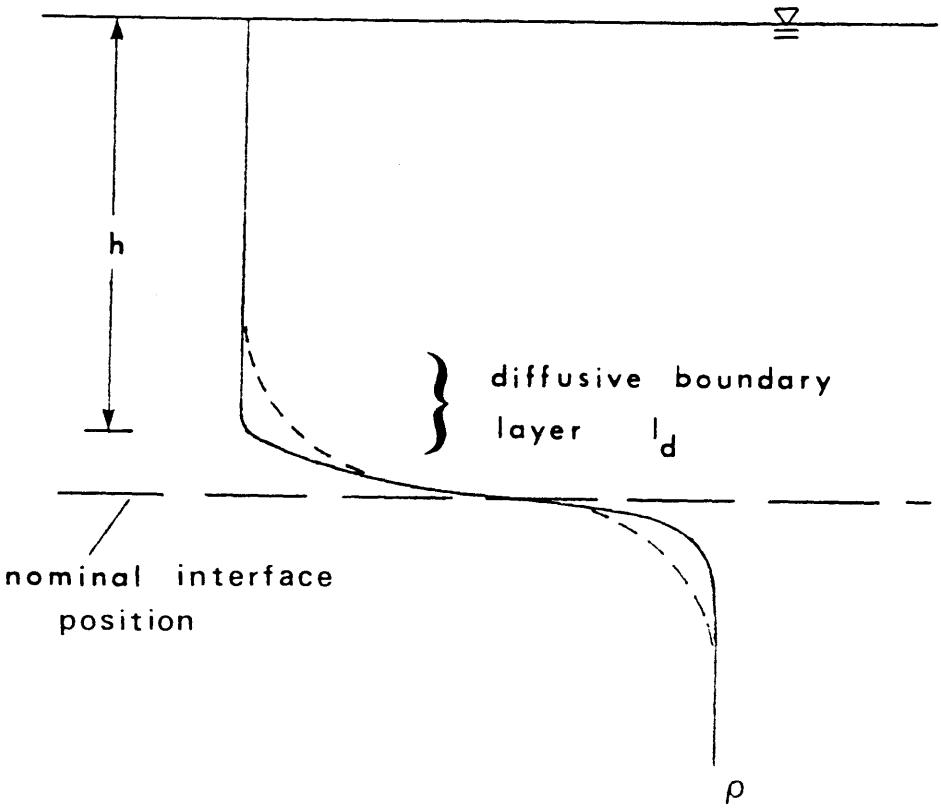

FIGURE 11 Illustration of Diffusive Limit For Entrainment
(See Discussion in Text)

thicknesses, respectively. $\hat{t}$ is a time scale over which the boundary layers are allowed to develop. For the case of singly stratified systems without stirring $\hat{t}$ would be indefinitely large. When turbulence is present the boundary layer will be scoured by eddies at a rate related to σ/h, so that $\hat{t} \sim h/\sigma$. For double-diffusive stratification without externally imposed stirring $\hat{t}$ will be controlled by the time scale for the double boundary layer to become unstable (due to the much more quickly diffusing heat). In this case $\hat{t}$ will be a function of the stability parameter R_ρ. When both double-diffusive stratification and external stirring are present the time scales for the two processes must be compared to determine the proper choice for $\hat{t}$. For now it is assumed that $\hat{t} \sim h/\sigma$ and it will be shown below (Section 3.2.2) that this is valid for the present experiments. Inserting proportionality coefficients, the diffusive flux is then

$$-g\ [C_T\alpha_T\Delta T(k_T \frac{\hat{u}}{\ell})^{1/2} - C_S\alpha_S\Delta S(k_S \frac{\hat{u}}{\ell})^{1/2}].$$

Finally, combining the entrainment and diffusive fluxes gives

$$\frac{g}{\rho_o}\overline{w'\rho'} = u_e g(\alpha_S\Delta S - \alpha_T\Delta T) + g[C_S\alpha_S\Delta S(k_S \frac{\hat{u}}{\ell})^{1/2} - C_T\alpha_T\Delta T(k_T \frac{\hat{u}}{\ell})^{1/2} \quad (3.8)$$

Upon substituting (3.5), (3.7), and (3.8) into (3.4) and rearranging, the following entrainment relation is derived:

$$\frac{u_e}{\sigma} = \frac{C_F - \varepsilon'_2 + C_T Ri_T Pe_T^{-1/2} - C_S Ri_S Pe_S^{-1/2}}{C_t + Ri - C_{SH}\bar{u}^2/\sigma^2} \quad , \tag{3.9}$$

where

$$\varepsilon'_2 = \frac{C_D}{N}\left[2Ri\ g'/\sigma + \frac{N^2 h}{\sigma} - 2\,\frac{Ri}{\sigma}\,(g'^2 + N^2\sigma^2)^{1/2}\right] \tag{3.10}$$

and $Ri = g'h/\sigma^2$, $Ri_T = g\alpha_T \Delta T\ h/\sigma^2$, $Ri_S = g\alpha_S \Delta S\ h/\sigma^2$ ($Ri = Ri_S - Ri_T$), and $Pe_T = \sigma h/k_T$ and $Pe_S = \sigma h/k_S$ are the thermal and salinity Peclet numbers, respectively. If (3.6) is used to estimate the leakage term, then

$$\varepsilon'_2 = C_D R_S^3 (R_S + Ri)^{-2} \quad , \tag{3.11}$$

where $R_S = Nh/\sigma$ is similar to an inverse Froude number. When (3.11) is used to define ε'_2 in (3.9) and the diffusive terms are neglected, the entrainment relation derived by Sherman et al. (1978) is obtained. Zeman and Tennekes (1977) assumed that shear production was negligible and that Γ could be approximated as $\Gamma \sim 2\ \Delta\rho/h$ (this is true only if the entire water column was initially linearly stratified). Their entrainment function used

$$\varepsilon_2' = C_D \sqrt{2Ri} \tag{3.12}$$

and this has been used in the most recent versions of the wind-mixing model developed at M.I.T. (Bloss and Harleman, 1979; Atkinson and Harleman, 1983a). However, this formulation is less general than (3.10) or (3.11). Zeman and Tennekes also suggested that in cases where shear production becomes important, it serves to balance the dissipation loss expressed by ε_2, and a modified relation includes neither ε_2 nor shear production (see Eq. 3.15).

In order to apply (3.9) the scaling velocity σ must be evaluated. In general σ will be a function of both the friction velocity u_* resulting from surface shear stress and a buoyancy velocity w_* arising from an unstable buoyancy flux:

$$\tilde{w}_* = (B_f h)^{1/3} \tag{3.13}$$

The rate at which energy is supplied by surface shear stress depends on u_*^3 ; similarly, the rate at which buoyancy forces supply energy is related to w_*^3. In other words, if $u_* = 0$ then entrainment would proceed by penetrative convection. Therefore, we follow Sherman et al. (1978) in defining σ in terms of the powers associated with the energy supply mechanisms:

$$\sigma = (w_*^3 + C_v^3 u_*^3)^{1/3} \quad , \tag{3.14}$$

where C_v is a proportionality coefficient.

It now remains to determine the values of the various proportionality coefficients in (3.9) in order to evaluate u_e. There is a large degree of uncertainty in the coefficient values. Zeman and Tennekes used the results of the thermal convection experiments of Willis and Deardorff (1974) to find C_F and C_D and also the salt-stratified shear experiments of Kato and Phillips (1969) to find C_V. C_t was obtained by noting that a turbulent front entraining into neutrally stratified fluid moves at a rate $u_e/\sigma = 0.3$. However, these experiments used relatively low Ri values (a maximum of ~ 400) and it is not clear that the values obtained are valid for a larger range of Ri. (Solar pond conditions may correspond with Ri as high as 10^3 - 10^4.) Sherman et al. reviewed a number of entrainment experiments and suggested coefficient values that gave a best fit for their model. These experiments were either thermally or salt-stratified, but again the maximum Ri value was about 1100. Table 4 lists values for the various coefficients, except C_T and C_S which are discussed below. Figure 12a shows plots of (3.9) using different coefficient values and different expressions for ε_2'. It is interesting to note that although the curves for u_e/u_B do not show a large degree of variation, the corresponding curves for Rf may be quite different.

As previously mentioned, the diffusive terms in (3.9) become important only for large Ri and provide a limiting value of Ri for entrainment to occur. Note that ε'_2 tends to vanish as Ri becomes increasingly large (using either 3.10 or 3.11), implying that the eddies

Table 4

Summary of Coefficient Values for Entrainment Relation

Parameter	Range of Values Reported by Sherman	Suggested Values from Sherman et al. (1978)	Suggested Values from Zeman and Tennekes (1977)
C_v	1.0 - 2.2	1.8	2.0
C_F	0.2 - 1.0	0.38	0.5
C_D	0 - 0.04	0.04	0.024
C_t	0 - 3.6	2.25	3.55
C_{SH}	0 - 1.0	0.3	0

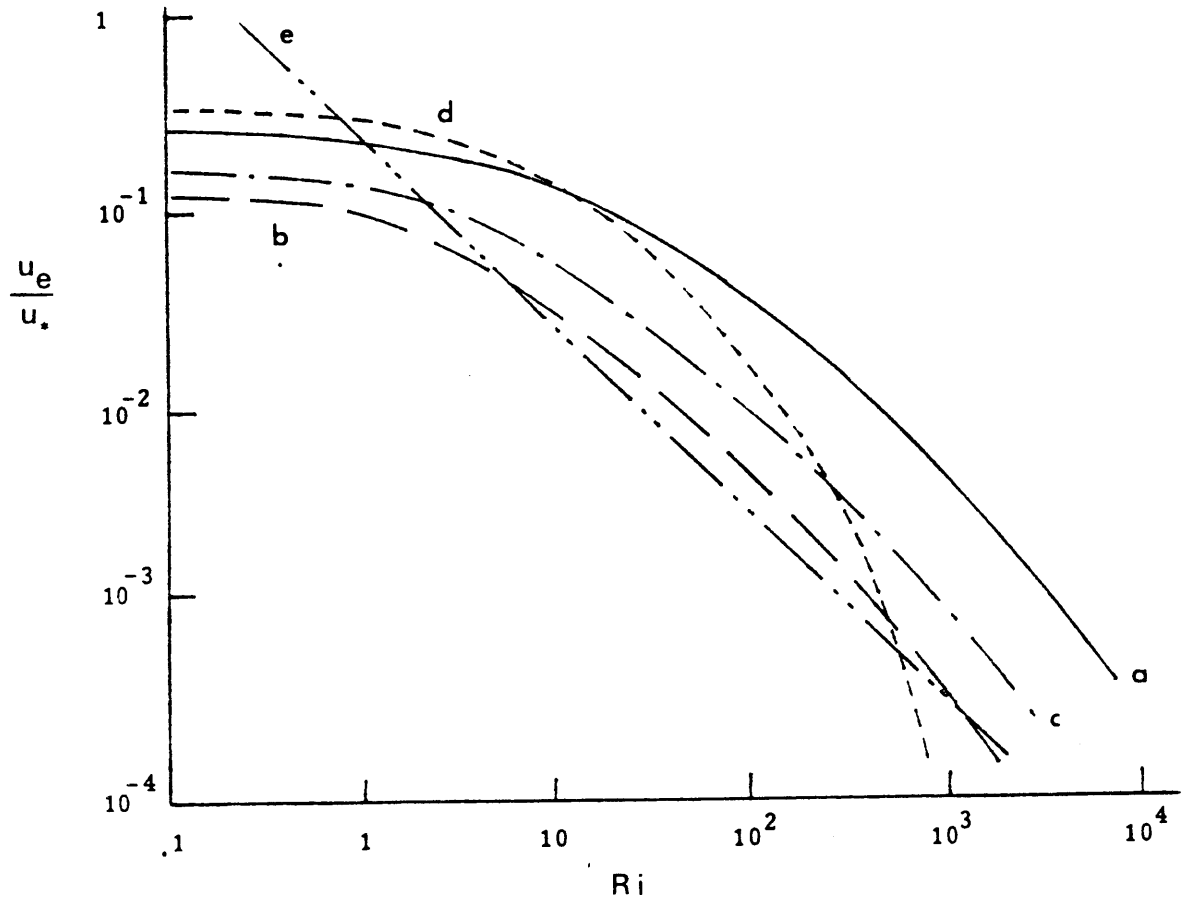

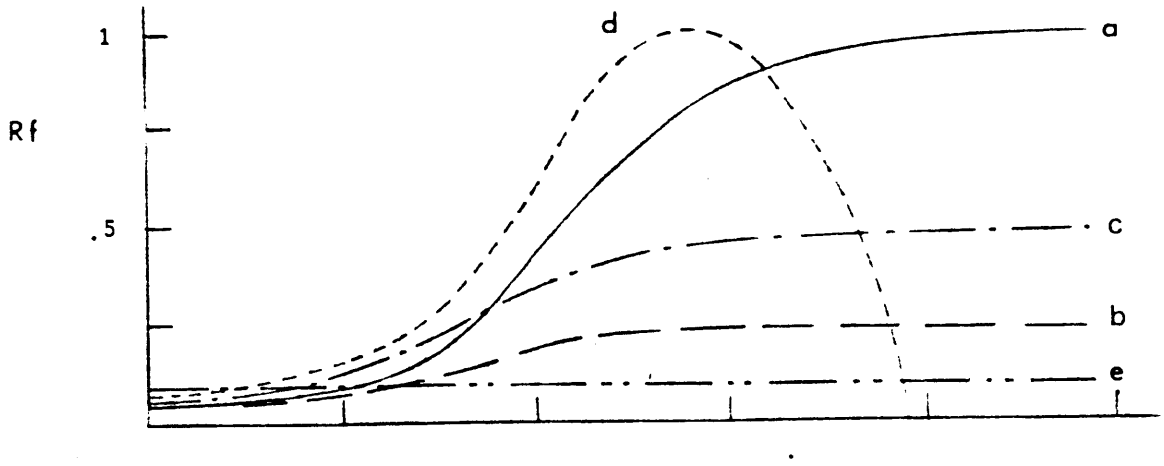

FIGURE 12 Comparison of Entrainment Models (See Notes)

NOTES FOR FIGURE 12

All curves assume $w_* = 0$ and use eqn. (3.9) with $C_1 = 1$ and $C_T = C_S = 3 \times 10^{-4}$

Curve	Reference	Parameter Values					
		eqn. for ε_2	C_F	C_D	C_V	C_t	C_{SH}
a)	Sherman et al. (1978)	3.11	.38	.04	1.8	2.25	0
b)	-	3.11	.38	.04	1	1.67	0
c)	-	3.11	.38	.04	1.23	2.08	0
d)	Bloss and Harleman (1979)	3.12	.5	.024	2	3.55	0
e)	Wu (1973)	-	.234	0	1	0	0

are less able to deform the highly stable interface to provide perturbations for internal wave generation. Then u_e goes to zero when $C_F = C_T Ri_T Pe_T^{-1/2} - C_S Ri_S Pe_S^{-1/2}$ (this is approximately true since ε'_2 is not exactly zero except in two-layer stratification.) Unfortunately, there is little data available to evaluate C_T or C_S. Both coefficients are probably small since they include a factor $1/2\pi$ (from the estimates for ℓ_T and ℓ_S) and also because they are used to account for the difference between the temperature and salinity steps across the boundary layer (the values desired) and the bulk steps across the entire interface (the known values). Turner's (1973) grid-mixing data may be used to obtain an upper bound for the values of C_T and C_S separately, since his data are for singly stratified systems (see Figure 8). Note that for a stable thermally stratified system Ri_T becomes negative. At the highest value of Ri used in his experiments there does not appear to be any effect of the diffusive term for either salt or temperature. Then if it is assumed that the magnitude of the diffusive term is at most about one tenth of the value of $\hat{u}_e/u$ at that point, then we find $\tilde{C}_T = 5 \times 10^{-3}$ and $C_S \tilde{=} 10^{-2}$. Using results from Newell's (1984) experiment (raw data received by personal communication) conditions may be identified where u_e is about zero. u_e was found to vanish at $Ri \tilde{=} 4 \times 10^4$ and this implies values for C_T and C_S between $1 - 5 \times 10^{-4}$. As expected, we see that these diffusive terms are usually negligible when calculating the entrainment; however, at large Ri they become important and are needed to allow u_e to become zero and even negative, as observed in several laboratory experiments. This will also be true in the field,

since under no mixing conditions diffusion will cause the mixed layer to become thinner as the interface grows into the mixed region.

One further note should be made concerning the entrainment relation (3.9). If the diffusive terms are neglected, as well as the leakage and shear production terms (or, assume that these processes balance in some way), then (3.9) becomes

$$\frac{u_e}{\sigma} \sim \frac{C_F}{C_t + Ri} \quad . \tag{3.15}$$

This is the relation suggested by Zeman and Tennekes (1977) for conditions of strong shear production and it is also of the same form as the relation proposed by Bo Pederson (1980). Furthermore, at large Ri the temporal term becomes insignificant (C_t is of order one) and we have

$$\frac{u_e}{\sigma} \sim C_F \, Ri^{-1} \quad . \tag{3.16}$$

This result is supported by a number of experiments of mixing in stratified fluids (see Turner, 1973) and implies that a constant fraction of the input energy is used for entrainment (see eq. 1.10). This is a common assumption in earlier oceanic mixed-layer models. However, it has been shown that a single-exponent Richardson number law is not adequate for modeling entrainment over a large range of Ri (Kantha et al., 1977) and it is not applicable as $Ri \to 0$ or $Ri \to \infty$. It has also been pointed out that a relationship of this type can only apply if the entrainment is independent of molecular diffusion, which becomes more

important with increasing Ri (Phillips, 1977). It is possible to account for variations in u_e with different stratifying substances by letting the coefficients in the entrainment relation vary with molecular diffusivity, as suggested by Sherman et al. (1978). This would have to be done, for instance, to explain the differences between salt-stratified and temperature-stratified grid-induced entrainment (see eqs. 2.3 and 2.4).

The mixing efficiency of the input energy is evaluated by substituting (3.9) into (1.9), where σ is used in place of u_*. The shape of the functions depends on which formulation is used for ε'_2 and on the coefficient values. Figure 12b shows plots for Rf corresponding to entrainment functions shown in Figure 12a.

3.2 Grid-induced entrainment

The analysis of entrainment in a grid-mixing experiment is somewhat easier since there is no mean motion and the shear production term can be ignored in the TKE budget. In order to simplify matters the following development will be concerned with two-layer systems only, so that $\varepsilon_2 = 0$. A more localized approach is taken here than in the previous section, though the end result will be related to the previous model. In fact, both approaches stem from energy arguments and should lead to the same result. A detailed look at the processes occurring at the interface also sheds some light on various factors which may influence the entrainment, such as diffusion, double-diffusive effects or mean shear in the mixed layer. The following mechanistic model follows Linden's (1973) description closely, though the conclusions here are different.

3.2.1 The case of zero diffusion

We first consider grid-induced entrainment for the case where diffusion is negligible. The effect of diffusion is then discussed in the following section. Consider the simplified entrainment relation expressed by (3.16). Recall that the assumptions inherent in this equation are neglect of diffusion, shear production, internal wave leakage and temporal storage. From experimental results, for thermal stratification $u_e/\sigma \tilde{\propto} Ri^{-1}$ but $u_e/\sigma \tilde{\propto} Ri^{-3/2}$ for salt stratification (Figure 8). It appears then that $C_F \tilde{\propto} Ri^{-1/2}$ for for salt but is approximately constant for heat. From the studies reviewed in Section 2.2 the difference in entrainment between the two types of stratification is related to the Peclet number and Hopfinger and Toly's (1976) empirical result (eq. 2.7) implies that $C_F \sim (Ri^{-1/2} + Pe^{-1/2})$. It is now shown that this type of dependence is indeed plausible.

Following Linden (1973), consider the situation sketched in Figure 13. A sharp density interface separates two density homogeneous regions. An eddy with characteristic dimension $\hat{\ell}$ and velocity $\hat{u}$ approaches the interface from above. As the eddy impacts on the interface its kinetic energy is transferred to potential energy as the interface becomes distorted and buoyancy forces act to try to restore it to its initial equilibrium position. The eddy becomes flattened slightly, with a length scale $\hat{\ell}'$. After the forward motion of the eddy has been arrested and the energy has been stored as potential energy the interface begins to recoil and the original eddy collapses. According to Linden mixing occurs as lower layer fluid is thrust upwards during this recoil and incorporated

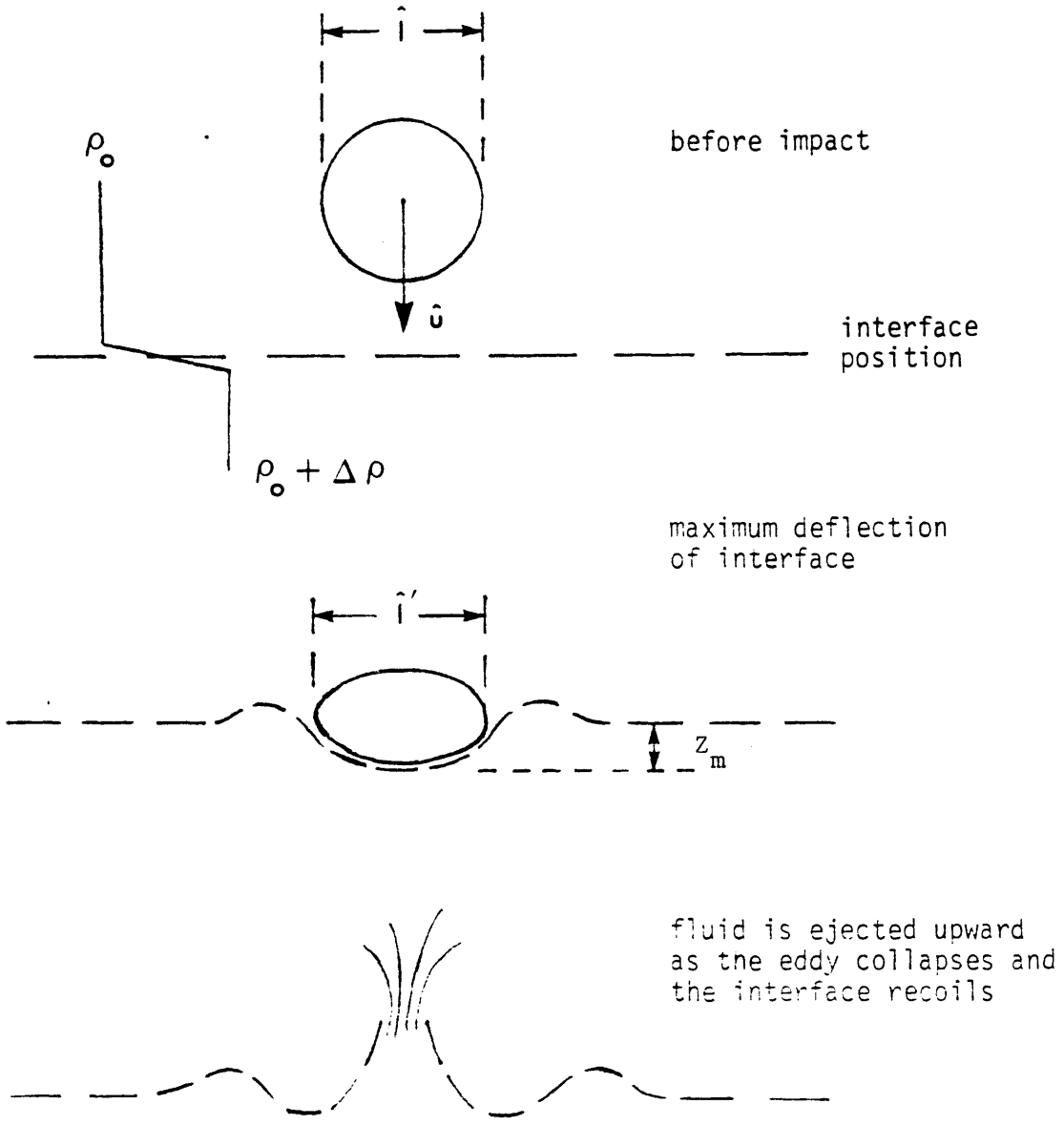

FIGURE 13 Mechanistic Model for Entrainment Caused By An Eddy Impinging at the Interface of a Two-Layer System

into the upper layer, thus resulting in a slight deepening of that layer. Since Linden also neglected diffusion (high Pe assumed), he suggested that the fluid thrust upwards by the recoil was mixed into the upper layer by additional eddies. It is shown below that this contradicts the experimental conditions which Linden assumed, and in fact, molecular diffusion must be invoked to mix ejected fluid into the upper layer.

Before impact, the kinetic energy of the system is $KE_i \propto \rho_o \hat{u}^2$. If Z_m is the maximum displacement of the interface after impact, then $KE_i \approx PE \propto g\Delta\rho Z_m$, which implies

$$\frac{Z_m}{\hat{\ell}} \propto Fr^2 \tag{3.17}$$

where $Fr = \hat{u}/(g \frac{\Delta\rho}{\rho_o} \hat{\ell})^{1/2}$ is the Froude number defined with the local eddy scales. This result was also derived by Linden in a somewhat more rigorous manner and is supported by his measurements.

The rate at which potential energy of the system is increased by direct mechanical entrainment is

$$\frac{dE_e}{dt} \propto g \frac{\Delta\rho}{\rho_o} u_e \tag{3.18}$$

and the rate at which energy is supplied is

$$\frac{dE_k}{dt} \propto \hat{u}^3/\hat{\ell} \quad . \tag{3.19}$$

If the energy balance is primarily between these two terms then $\frac{dE_e}{dt} = \frac{dE_k}{dt}$ gives

$$\frac{u_e}{\hat{u}} \propto Fr^2 = Ri^{-1}. \tag{3.20}$$

Note that this is essentially the same argument and result as was obtained from the parametrization of the TKE budget (Eq. 3.15), which implies that a constant fraction of the input energy is used for entrainment. Linden assumed that this was the basic energy balance as entrainment proceeded by the ejection of fluid from the interfacial recoil. However, he evaluated the entrainment differently, assuming that it was controlled by the time scale of the recoil of the interface. The recoil time was estimated as the natural response time of the interface being forced by a distance $\hat{\ell}$: $t_r \propto (\hat{\ell}\rho_o/g\Delta\rho)^{1/2}$. If entrainment is primarily controlled by the recoil mechanism then a better choice for the forcing distance is Z_m. With this simple substitution in the definition of t_r, Linden's result is changed from $u_e/\hat{u} \propto Ri^{-3/2}$ to $u_e/\hat{u} \propto Ri^{-1}$ which is consistent with (3.20).

Consider now in greater detail what happens to the fluid which is ejected by the recoil of the interface. If the energy balance is primarily between the initial kinetic energy of the eddy and the increase in potential energy due to entrainment as discussed above, then at least some of the fluid raised into the upper layer must be mixed into the layer before it has a chance to fall back to the interface. There are two basic processes by which this may occur. First, if molecular diffusion proceeds quickly enough then the ejected fluid will diffuse into its surroundings before it has a chance to drop back to the interface. Recall that Turner (1968a) used this type of argument to explain the slower entrainment of salt compared with heat as a result of its much lower diffusivity. The second mechanism by which the fluid may be mixed is due to a scouring effect of the motions in the stirred

layer. For instance, Linden assumed that the fluid raised by the recoil was swept away by eddies not in direct contact with the interface. This implies, however, that the time scale of the recoil must be at least as large as the time scale for the eddies, or $(Z_m/g')^{1/2} \geq \hat{l}/\hat{u}$. Using (3.17), this implies $Fr \geq 1$, which contradicts Linden's argument since he assumed that Fr was always less than unity. If this recoil mechanism is primarily responsible for entrainment, then for these relatively less stable conditions u_e should not depend on molecular diffusivity since the incorporation of the ejected fluid is accomplished by mechanical turbulent mixing.

Now, if the ejected fluid does in fact fall back to the interface before being mixed into the upper layer there must be another sink for the energy of the eddy. This consists of the generation of interfacial waves and dissipation. Note that even during the initial impact of the eddy there will be some ripple formation, and additional ripples will be generated as fluid falls back to the interface after the initial recoil. In the limit of zero diffusivity and relatively strong stability ($Fr < 1$) and under steady conditions the rate at which energy arrives will be the same as the rate at which energy is generated as interfacial waves, which is estimated as

$$\frac{dE}{dt} \propto a^2/t_w^3 \quad , \tag{3.21}$$

where a = amplitude and t_w = period of the waves generated. Z_m gives a good estimate for a and t_w can be estimated as the period of deep

water waves of wavelength $\hat{\ell}$, $t_w \propto (\ell\rho_o\hat{}/g\Delta\rho)^{1/2}$ is made. Therefore, (3.21) becomes

$$\frac{dE_w}{dt} \propto \frac{Z_m^2}{(\hat{\ell}/g')^{3/2}} = Fr^3 g' \hat{u} \qquad (3.22)$$

As the interface is excited by the impact of eddies of scale $\hat{\ell}$ wave motion will be generated. Some of the energy in these waves will be dissipated but a fraction may be liberated as the waves interact and break, causing some mixing across the interface and leading to entrainment. This mechanism was indirectly suggested by Linden (1973) and more recently invoked (qualitatively) by Asaeda and Tamai (1980) in explaining their observed entrainment. Fernando and Long (1983) have also argued that this is the dominant entrainment mechanism for salt-stratified grid-mixing systems. It is also reasonable for explaining the current results, since under strongly stable conditions the disturbed interface appeared to support small-scale wave-like motion, while large excursions of eddies from the mixed layer into the lower layer were usually not observed (see Figure 17). Assuming that entrainment results as a fraction of internal wave energy is transferred to potential energy, equating (3.18) and (3.22) then results in

$$\frac{u_e}{\hat{u}} \propto Fr^3 = Ri^{-3/2} \quad . \qquad (3.23)$$

This result may be compared with the relation derived by Long (1978a),

$u_e/\hat{u} \propto Ri^{-7/4}$. The difference between the slopes of -3/2 and -7/4 (on a log-log plot of $u_e/\hat{u}$ vs. Ri, as in Figure 8) will probably not be easily distinguishable, so it is difficult to decide which relation is better supported by data.

3.2.2 Effect of diffusion

The net entrainment will in general consist of both the fluid recoil/ejection and interfacial wave breaking mechanisms so that both Ri^{-1} and $Ri^{-3/2}$ terms will appear in evaluating $u_e/\hat{u}$. The relative contributions of each of these terms depends on the strength of the stability of the interface and on diffusivity. These effects become important in determining how much of the fluid raised by the recoil of the interface becomes incorporated into the stirred layer. This may be evaluated by considering the fraction of the total mass of the fluid raised by the recoil which may be expected to be mixed before it falls back to the interface. This is done by comparing the bulk transfer coefficients associated with these two processes. That is, the transport of mass by the recoil is compared with the transport of mass out of the raised fluid parcel by diffusion or mixing by an eddy.

For diffusion the transfer is estimated by k/l_d, where k = diffusivity and l_d = diffusive length scale as before, and following the arguments leading to the definition of the diffusive terms in (3.8), $l_d \propto (k\hat{l}/\hat{u})^{1/2}$. For the recoil the transfer coefficient will be related to Z_m/t_r, where t_r is defined with Z_m as the forcing distance, i.e., $t_r \sim (Z_m/g')^{1/2}$. By taking the ratio of these two quantities we find $(k\,\hat{u}/\hat{l})^{1/2}(Z_m/g')^{1/2} / Z_m \propto P_e^{-1/2}$,

which is a measure of the fraction of the mass raised by the recoil which diffuses into the upper layer and does not fall back to the interface. This is interpreted as being related to the fraction of energy which is converted to potential energy through diffusive mixing during the recoil. As mentioned above, mixing of the raised fluid by additional eddies in the upper layer will only occur for very weakly stratified conditions (Fr $\geq$ 1) and this mechanism is neglected here. The fraction of input energy transferred directly to potential energy by entrainment is then estimated as $Pe^{-1/2}$. With the additional contribution by interfacial wave breaking (3.23) we have

$$\frac{u_e}{\hat{u}} = Ri^{-1}(C_1 Pe^{-1/2} + C_2 Ri^{-1/2}) \quad . \tag{3.24}$$

This result is in fact precisely the empirical relation suggested by Hopfinger and Toly (1976) and on comparing with (3.9) we see that $C_F = C_1\ Pe^{-1/2} + C_2\ R_i^{-1/2}$. That is, C_F depends both on molecular diffusivity and Ri. The coefficients C_2 and C_3 may be evaluated by fitting the equation to Turner's (1973) data for salinity or temperature stratified conditions. This has already been done in Figure 8, where $\hat{u}$ = 0.28 cm/s and $\hat{\ell}$ = 0.9 cm (Thompson and Turner, 1975). Then Pe_T = 180 and $Pe_S = 1.7 \times 10^4$. A reasonable fit of the data for Ri > 10 was found for C_1 = 2.18 and C_2 = 11.2. The model appears to reproduce the salinity-stratified data slightly better than the

temperature-stratified conditions, especially at lower Ri. However, it has already been pointed out that the model is not expected to hold for weakly stratified conditions since the neglect of the temporal term is then not justified.

To summarize the results obtained in this section so far, an entrainment model (3.24) has been developed for singly-stratified grid-mixing systems. It is a simplified case of the more general model derived in (3.9). The expression is the same as the empirical relation suggested by Hopfinger and Toly (1976) and it accounts for differences in the diffusivity of the stratified component. Assumptions inherent in this development include neglect of the shear production and energy leakage terms. Ri was also assumed to be large enough so that C_t could be neglected, but not so large that the "diffusive limit" terms had to be included. We now consider the possible effects that double-diffusive stratification may have on this model.

3.2.3 Double-diffusive effects

Several experiments have looked at the effect of double-diffusive stratification on interfacial fluxes in a grid-mixing system (see Section 2.3). In particular, Crapper (1976) showed that the interfacial salt flux was increased by raising the destabilizing temperature difference across the interface. Murota and Michioku (1983) also showed that the entrainment relationship is affected by double-diffusive stratification and found that $u_e/u_d \propto Ri^{-n}$, where n was between 1 and 1.5 and u_d was the buoyancy induced velocity associated with double-diffusive instability (they were heating a salt gradient from below). The current

research was designed to explore this effect more fully. Since the fluxes across a double-diffusive interface had been shown to be different than would be expected by molecular diffusion alone, it was originally thought that the effect of double-diffusive stratification on entrainment might be modeled by changing Pe in (3.24) by defining an "effective" diffusivity as a function of R_ρ. However, as shown below, a closer examination reveals that this approach is not well founded on a physical basis. It was found that a result of double-diffusive stratification was to cause an unstable heat flux across the interface. The effect of this unstable buoyancy flux is to add more kinetic energy to the layer and increase the entrainment rate over what it would be for the same conditions but without a temperature gradient. This mechanism of entrainment driven by convectively-produced turbulence in a double-diffusive system has been suggested previously by Linden (1974a) and Crapper (1976).

"Effective" diffusivities for heat and salt may be defined so that the measured fluxes of heat or salt can be equated to the product of the respective diffusivity and interfacial gradient. This is done in Appendix C where it is seen that in general the modified thermal diffusivity is somewhat less than the molecular value, but the salt diffusivity may be greater or less than the molecular value. It should be kept in mind, however, that these "effective" double-diffusive diffusivities are defined in terms of the interfacial heat and salt fluxes as determined by measurements of the bulk quantities in the layers. If we envision a stably salt-stratified experiment, the resulting effective salt diffusivity would be zero since diffusion would

only act to thicken the interface, and measurements of salinity on either side of the interface would show no change with time (i.e., zero flux).

The mechanism responsible for a salt flux greater than zero is the growth, eventual instability and resulting convection of the double boundary layer when an unstable temperature gradient is imposed on the salt interface. As the boundary layer becomes unstable a thermal plume arises and salt is carried into the upper (or lower) layer and mixed by the turbulence generated by the plumes (see Linden and Shirtcliffe, 1978). On the other hand, the salinity gradient and developing boundary layer provide a stabilizing influence which inhibits the thermal convection and this must be why the "effective" thermal diffusivity is less than the molecular value (except at very low R_ρ).

It is now desired to evaluate the possible effects on entrainment of imposing an unstable temperature gradient on a two-layer salt-stratified system. That is, for a given value of Ri what would be the effect of increasing the temperature of the lower layer? From the above discussion it is not appropriate to invoke double-diffusive fluxes unless conditions are such that boundary layer instability occurs. Diffusion from the fluid parcel lifted by the interfacial recoil into the stirred layer will still be controlled by molecular processes.

Double-diffusive fluxes will be important only when the time scale for the development of boundary layer instability is less than the time scale for the turbulence. In other words, the time between arrivals of successive eddies must be long enough so that the boundary layer is allowed to become unstable. Otherwise the boundary layer is scoured by the eddies and unstable conditions will not be reached. The time scale

for the eddies is simply $\hat{t} \sim \hat{l}/\hat{u}$. The time scale for boundary layer instability is estimated following the model described by Linden and Shirtcliffe (1978). Their model considers a double-diffusive interface separating two well-mixed layers. The interface consists of a central diffusive core, where fluxes are controlled by molecular diffusion along linear gradients, with growing double boundary layers on either side of this core (Figure 14). In the following only the top half of the interface is considered, as the process described is symmetrical on the lower half.

Consider an initial condition at $t = 0$ where there is no boundary layer development. For $t > 0$ both heat and salt diffuse into the mixed region, with heat diffusing at a much faster rate. Eventually the temperature gradient becomes strong enough to cause instability and fluid in the diffusive boundary layers is lifted as a "thermal" into the upper layer. After the instability occurs the interface is restored to its initial condition. (Note that this is a steady-state model - Newell (1984) has discussed the unsteady case where the interfacial thickness is allowed to grow with time). Figure 14 illustrates this process. Linden and Shirtcliffe define an effective Rayleigh number for the boundary layer region as $Ra_e = g\delta\rho d_T^3/\rho_o \nu\kappa_T$, where d_T = position of the maximum density inversion and $\delta\rho$ = density anomaly. This definition is similar to the quantity in (1.20). The boundary layer becomes unstable when Ra_e exceeds a critical value Ra_c and for the situation considered here $Ra_e \sim 0\ (10^3)$. This development can be traced in the $Ra - Ra_s$ plane as shown in Figure 15. Using their expressions for d_T and $\delta\rho$, the time t_c at which instability will occur is estimated by setting $Ra_e = Ra_c$:

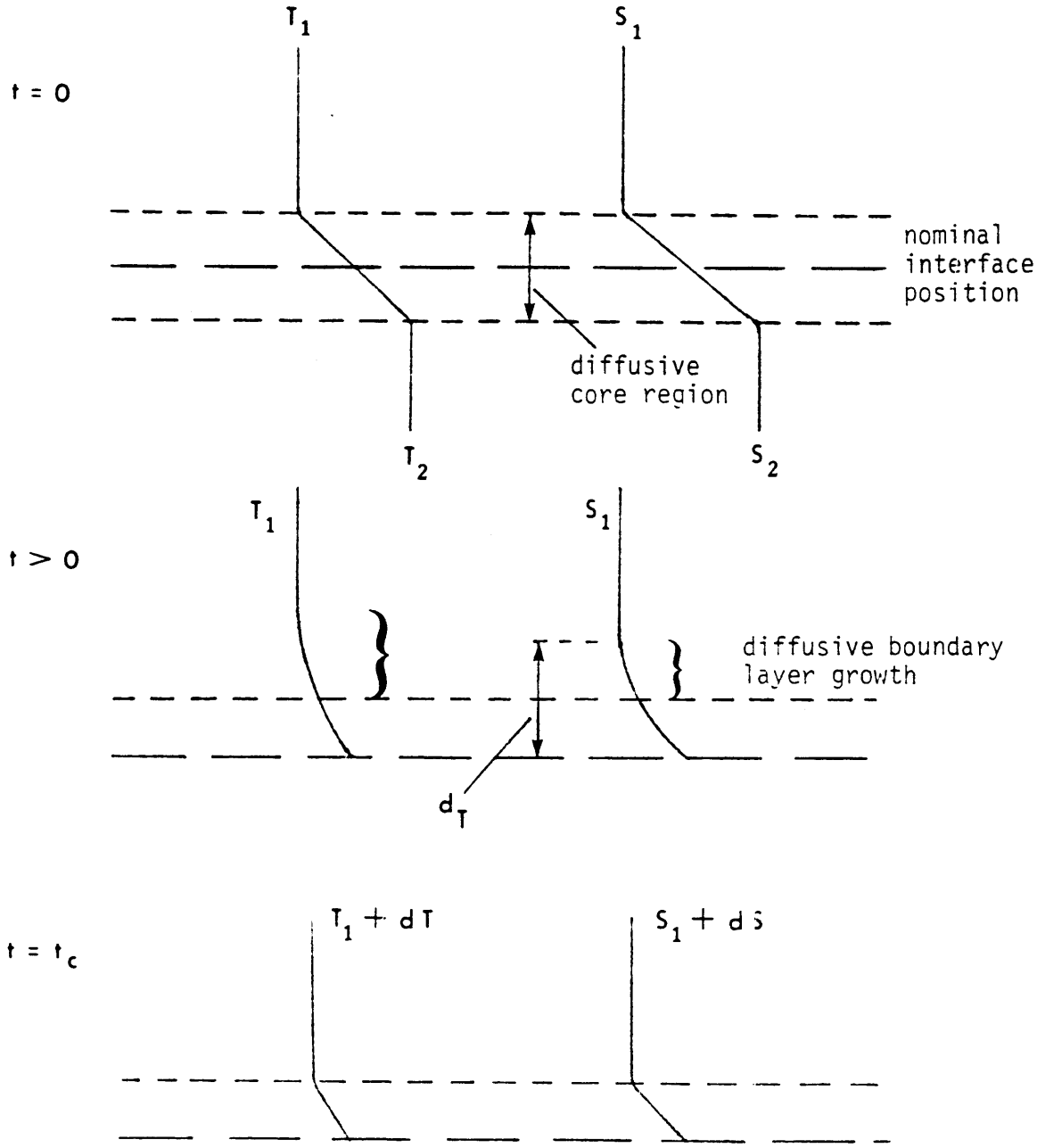

(at t = t_c thermals form and carry fluid away from the boundary layer into the mixed layer, effectively scouring the interface and restoring initial conditions, approximately)

FIGURE 14 Illustration of Double-Diffusive Boundary Layer Instability

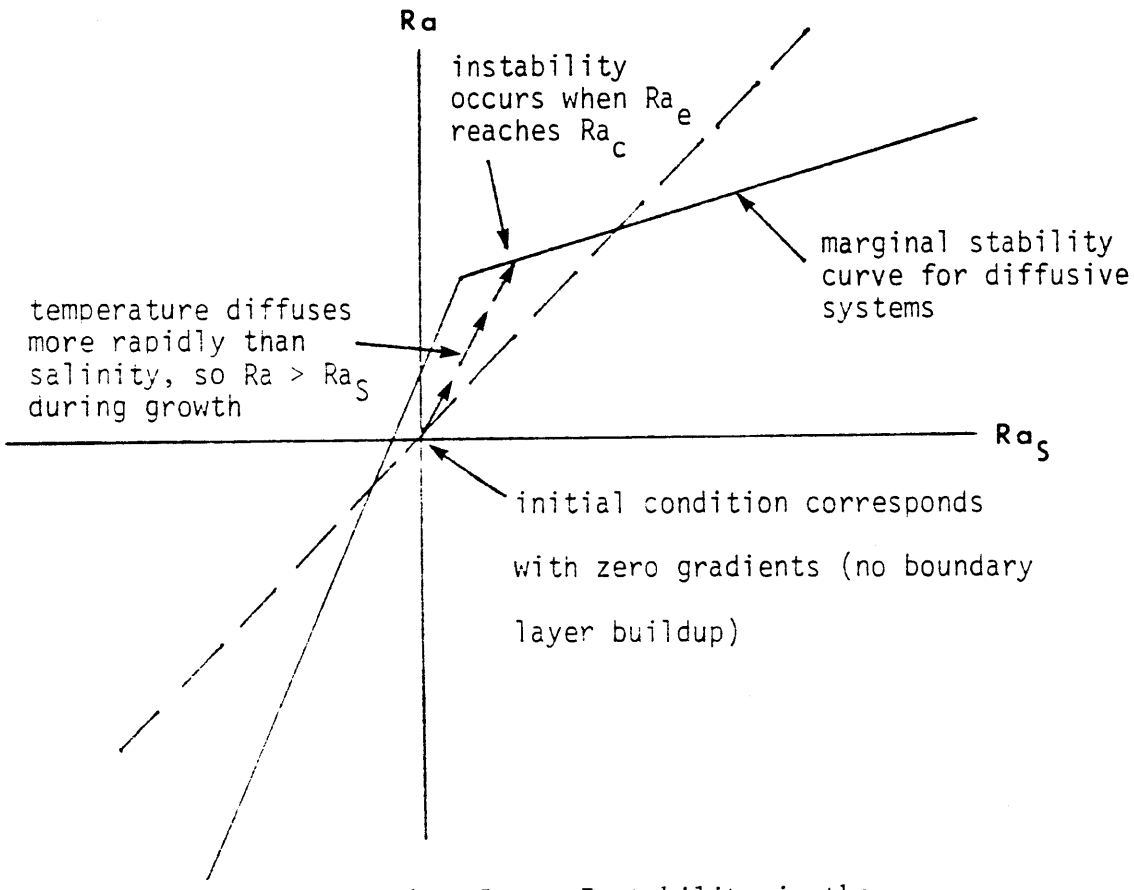

FIGURE 15 Development of Boundary Layer Instability in the Ra - Ra_s Plane

$$t_c = \frac{1}{\pi k_T} \left\{ \frac{\pi \nu k_T Ra_c}{g\alpha_T \Delta T (1-\tau^{1/2})^3} \right\}^{2/3} \qquad (3.25)$$

t_c may then be compared with $\hat{t}$ and this is done in Section 4.3.

This time scale comparison provides a criterion for deciding whether double-diffusive fluxes will be important in the interfacial transport. For a given stirring rate and ΔS across the interface heating of the bottom layer will cause double-diffusion to become increasingly important and will begin to dominate the interfacial fluxes when $t_c < \hat{t}$. Crapper's (1976) experiment (reviewed in Section 2.3.2) provides a test for this criterion. First, using (3.25) with representative values for ν, k_T and τ, we set $\hat{t} = \hat{\ell}/\hat{u} = t_c \Rightarrow \alpha\Delta T = 0.21\ (\hat{u}/\hat{l})^{1.5}$, assuming that $Ra_c = 1000$. Crapper used $R_\rho = 2$ and $\Delta S = 0.75\%$, so $\alpha_T \Delta T = 2.9 \times 10^{-3}$. If we assume that $\hat{l} = 0.9$ cm (Thompson and Turner, 1975) then $\hat{u} = 5.2 \times 10^{-2}$ cm/s. Then Crapper's parameter $\lambda_c = \hat{u}/u_d = 0.22$, where $u_d = 0.24$ cm/s was the convective velocity measured in the absence of grid-stirring. This value falls easily in the range found by Crapper corresponding to conditions where both grid-mixing and double diffusion were important (his results show that $\lambda_c \sim 0.1 - 0.6$ corresponds with this condition).

It may be concluded then that double-diffusive effects do not play a dominant role in the entrainment process except for conditions where $t_c \leq t$. It will be shown in Chapter 4 that the interfacial salt flux is accomplished almost entirely by entrainment, at least under the conditions of the present experiments. On the other hand, the heat flux

is somewhat greater than can be explained by entrainment alone. An additional convective flux term must be included which is consistent with the grid-mixing model discussed above. It appears that the growth of the mixed layer is inhibited primarily by the strongly stable salinity interface, but that significant heat conduction across the interface occurs in addition to the entrainment. The effect of this heat flux is to provide a buoyancy source at the bottom of the mixed layer which leads to an additional source of kinetic energy in the layer. The strength of this buoyant convection depends on the magnitude of the driving temperature difference, so that increasing the temperature of the lower layer (and also the salinity slightly to maintain a constant $\Delta\rho$) should result in an increased rate of entrainment. This effect is accounted for by including both the grid-induced velocity and the buoyancy-induced velocity in defining the scaling velocity, as in (3.14). The results of Section 4.3.2 support this idea.

Therefore, we conclude that double-diffusive diffusivities (as defined in Appendix C) do not apply to the grid-mixing model, but that the influence of the double-diffusive stratification may be accounted for by incorporating a buoyancy-induced velocity in defining the velocity scale. This velocity arises because heat conducts across the interface, which advances relatively slowly because of the resistance provided by the stabilizing salt gradient. The effect of the temperature gradient is not to change the diffusivity, since salt diffusion will still be controlled by the molecular value, but to change the scaling velocity in the entrainment model. In other words, (3.24) may still be used, but in a slightly modified form:

$$\frac{u_e}{\sigma} = Ri^{-1}(C_1 Pe_5^{-1/2} + C_2 Ri^{-1/2}) \quad , \tag{3.26}$$

where $Ri = g'\hat{\ell}/\sigma^2$, and $Pe_S = \sigma\hat{\ell}/k_S$ and σ is defined as in (3.14). Again, the assumptions inherent in (3.24) and summarized at the end of the previous section should also be kept in mind.

3.3 Wind-Induced Entrainment

The input of TKE to the water column by surface wind shear stress is $u_S\tau_S$ and (3.9) is used to evaluate the resulting entrainment. Energy may be transferred downward to an interface as wind-generated surface waves break and also as a mean current develops in the upper layer. It has been suggested that oscillating grid experiments provide a reasonable model for entrainment induced by surface wave breaking turbulence (Turner, 1981), while surface shear-stress-driven experiments such as those of Kato and Phillips (1969) and Kantha, et al. (1977) more closely model the entrainment resulting from the development of the drift current. Wind-mixing experiments probably exhibit effects of both wave-induced mixing and mean shear instabilities leading to entrainment. Shelkovnikov and Alyavdin (1982) made this suggestion to explain their experimental results, which followed an entrainment law $u_e/u* \propto Ri*^{-1.2}$. Since they used salt stratification they expected to find an exponent of -1.5 if the entrainment were primarily accomplished by eddies associated with surface waves (i.e., similar to the grid model and results), while an exponent of -1 should have resulted if mean shear were primarily responsible for the mixing, as found in experiments with mean flow (see the review in Section 2.2.2). Their

value between these two extremes then seems to imply that both processes may be important.

It should be remembered that a single-exponent Ri law will not be valid over a large range of Ri values, as shown by Kantha, et al. (1977) and demonstrated by the form of the entrainment relation (3.9). However, we may consider the possible influence of mean shear on the mechanistic model discussed in Section 3.2 and explain how the exponent might change.

3.3.1 Effect of Shear

Recall that under conditions of zero mean shear there is a Ri^{-1} and a $Ri^{-3/2}$ term in the entrainment relation and the relative importance of each term depends on the ability of molecular diffusion to cause the fluid raised by the recoil of the interface to be incorporated into the stirred layer before it has a chance to drop back to the interface (see discussion leading to eq. 3.24). If a weak mean flow in the stirred layer is now superimposed, the effect will be to increase the tendency of the raised fluid to be mixed into the layer. The velocity gradient near the interface will cause the raised fluid to be sheared in the direction of the flow, effectively increasing the surface area for diffusion. With stronger flows turbulence shear production may become significant enough to cause additional mixing of the raised fluid. Thus, the contribution of the Ri^{-1} term is increased and it is not unlikely that experimental data may be fitted best by a model with an exponent value between -3/2 and -1.

Under conditions where the entrainment is not driven primarily by the interfacial bombardment of small-scale eddies as in the grid

experiments, but rather by interfacial instability caused by mean flow in the mixed layer, experimental results have shown that $u_e \propto Ri^{-1}$, where Ri is defined with the mean flow velocity (see Section 2.2.2). In this case fluid is mixed across the interface by means of interfacial wave instabilities (Browand and Wang, 1972; Wyatt, 1978; Bo Pedersen, 1980). Imberger and Patterson (1981) have also discussed this type of mixing in terms of a "billowing" mechanism.

A model for shear-induced entrainment may be obtained by applying the TKE budget to a two-layer system with a mean velocity difference between the two layers. Then, neglecting the temporal, leakage and diffusive terms (i.e., Ri is neither very low nor very high) and assuming that interfacial stress is the main source of TKE, the main balance is between the buoyancy (entrainment) and shear production terms, or

$$\frac{g}{\rho_o} \overline{w'\rho'} \simeq - \overline{u'w'} \frac{\partial \bar{u}}{\partial z} \quad . \tag{3.27}$$

Following Buch (1982), define a vertical momentum transfer coefficient K_m such that $u_{*_i}^2 = -K_m \, \partial\bar{u}/\partial z$, where u_{*_i} is the friction velocity associated with interfacial shear. Also, $\bar{u}'\bar{w}' \sim u_{*_i}^2$, so

$$\frac{g}{\rho_o} u_e \Delta\rho \propto u_{*_i}^4 / K_m \text{ -> or } \frac{u_e}{u_{*_i}} \propto Ri_i^{-1} \frac{u_{*_i} h}{K_m} \quad . \tag{3.28}$$

where Ri_i is defined as in (1.8) except with $u*_i$ instead of $u*$. An inverse Ri entrainment law is then obtained if K_m is proportional to $u*_i h$. This expression may also be written in terms of the mean velocity by noting that τ_i = interfacial stress = $\rho_o u*_i^2 = \rho_o C_i(\bar{u}-u_i)^2$, where C_i is an interfacial drag coefficient and u_i is the velocity at the interface. Assuming $u_i/\bar{u} \ll 1$,

$$\frac{u_e}{\bar{u}} \propto C_i^{1/2} \; Ri^{-1} \frac{\bar{u}h}{K_m} \quad , \tag{3.29}$$

where Ri is now defined using $\bar{u}$ as the scaling velocity. A similar relationship may be derived by assuming that the input energy is primarily by surface shear, so that the balance in the TKE equation is between buoyancy (as above) and the flux divergence term (see eq. 3.1). Following a similar procedure as above it is easily shown that an inverse Ri relationship results, using either $\bar{u}$ or u_* as the scaling velocity. As previously mentioned there is experimental evidence to support this relationship so that the assumption $K_m \propto \bar{u}h$ appears to be justified.

The above discussion provides an alternative parameterization for the shear production term in (3.9). Again assuming $u_i/\bar{u} \ll 1$ and with $K_m \propto \bar{u}h$, (3.27) gives

$$\frac{g}{\rho_o} \; u_e \, \Delta\rho \propto \overline{-u'w'} \frac{\partial \bar{u}}{\partial Z} \propto \frac{\bar{u}^3}{h} \quad . \tag{3.30}$$

With this parameterization of the shear production term, the entrainment relation (3.9) is changed to

$$\frac{u_e}{\sigma} = \frac{C_F + C_{SH}\bar{u}^3/\sigma^3 - \varepsilon_2' + C_T Ri_T Pe_T^{-1/2} - C_S Ri_S Pe_S^{-1/2}}{C_t + Ri} \qquad (3.31)$$

This expression is more consistent with the results of shear entrainment experiments. For instance, if two-layer shear flow is considered and the diffusive and temporal terms are neglected, $\sigma \propto \bar{u}$ and $u_e/\sigma \propto Ri^{-1}$. This is not an obvious result when using the former parameterization (3.3) which led to (3.9). The entrainment relation should also reduce to the form $u_e/\sigma \propto Ri^{-1}$ as indicated in (3.30) when the main balance in the TKE equation is between shear production and buoyancy and this is the case for (3.31), but not for (3.9).

CHAPTER 4

Grid-Mixing Experiment

An oscillating grid entrainment experiment was designed to check some of the ideas arising from the literature review (Section 2.2.1) and developed in Chapter 3. The main purpose of the experiment was to see if double-diffusive stratification (i.e., imposing an unstable temperature distribution on a salt-stabilized system) would have any effect on the entrainment rate measured for a system with salinity stratification only at the same value of Ri. Much stronger density differences than in previous studies were also considered here. The grid-mixing tests provide a first indication that u_e can be influenced by double-diffusive stratification, though it will be seen in Chapter 5 that there was no double-diffusive effect observed in the wind-mixing experiment. The experimental apparatus and procedure for the grid-mixing tests are presented in Sections 4.1 and 4.2 and results are given in Section 4.3

4.1 Apparatus

The grid-mixing experiments were conducted in a rectangular tank made of 1.27 cm thick plate glass with 10.2 cm of styrofoam insulation on all sides to minimize heat losses. Windows were cut in the front and back which could be removed for flow visualization. During an experiment the mean position of the grid was usually 4-5 cm below the water surface and insulation was floated on the surface to reduce heat transfer there. The inside dimensions of the tank were 41.3 x 41.3 cm^2 in area and 50.1 cm high. The grid was designed on the basis of descriptions of grids used in many of the earlier grid-mixing experiments. It was composed of

square plexiglass strips, 0.96 cm on a side and 40.5 cm long, joined together in an array with a 5.0 cm (on center) spacing. The middle of the grid was reinforced to make the connection with the driving rod as rigid as possible. The overall geometrical solidity of the grid was 39%. The driving rod passed up through bearings in the lid of the tank and was coupled to an eccentric arm connected to a rotating wheel driven by an electric motor. The motor and wheel were suspended above the tank and the only physical connection to the tank was through the rod and the bearings in the top of the tank. The tank and grid are sketched in Figure 16.

The frequency of the grid motion could be adjusted by controlling the voltage supplied to the motor with a variac and was checked independently using a strobe light. The oscillation stroke was determined by the eccentric connection of the driving rod to the rotating wheel. Throughout these experiments, however, the stroke and frequency were maintained at 1.0 cm and 5.0 Hz, respectively.

This procedure was followed because the main purpose of the experiment was to look at the effect of changing the temperature and salinity stratification on u_e and it was desired to maintain constant conditions for as many of the other variables as possible. In addition, previous oscillating grid experiments have already looked at the effect of changing f and s (see Section 2.2). For instance, it has been shown that $\hat{u} \propto f$ ($\hat{u}$ = r.m.s. horizontal velocity) and u_e results for varying f are represented by a single curve when $\hat{u}$ is used as the scaling velocity (i.e., the effect of changing f is accounted for by scaling in this manner). Therefore, it is assumed that different values of f would

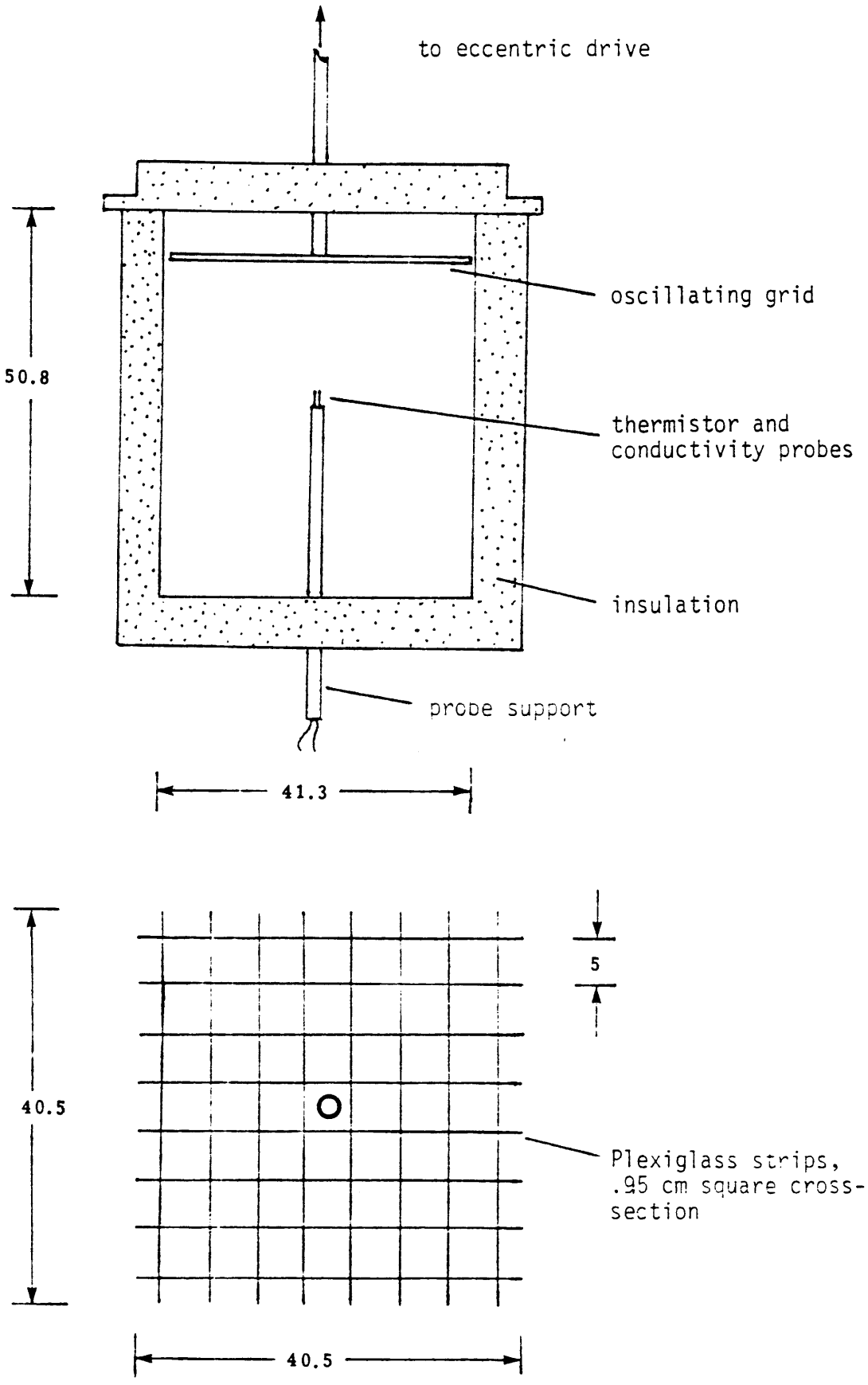

FIGURE 16 Apparatus for Grid-Mixing Experiment Showing Laboratory Tank and Oscillating Grid (All Dimensions in cm)

produce the same results as shown here. The exception to this might be for values of f low enough that the time scale for the grid-generated eddies would become comparable to the time scale for double-diffusive instability (see discussion in Section 3.2.3). A separate set of experiments might be conducted to examine this limit.

Temperature and salinity values were measured with a thermistor and microconductivity probe mounted at the tip of a stainless steel tube which passed up through a hole in the bottom of the tank. The two probe tips were spaced about 0.8 cm apart in the horizontal plane. This arrangement provided good data for either of the mixed layers but there is greater uncertainty for data taken in the interfacial region where fluctuations were stronger (see Figure 18). The tube was connected to a point gauge and could be moved vertically to record profiles. The point gauge was connected to a potentiometer so that probe position could be monitored electronically. Descriptions and calibrations of the probes are provided in Appendix D.

Two basic types of experiments were conducted with this apparatus, as explained below. Entrainment experiments were designed to provide data with which u_e could be related to Ri and compared for thermal, salinity and double-diffusive stratification. The second set of experiments consisted of taking grid-induced velocity measurements under non-stratified conditions using a laser-Doppler anemometer in order to define appropriate velocity and length values to scale the entrainment results. Data collection and analysis was accomplished primarily with a computer data acquisition system, though an X-Y plotter was used for some of the singly-stratified entrainment tests and flow visualization was also used.

4.1.1 Entrainment Tests

Two-layer stratification was used for the entrainment tests, with the density step created in three different ways: (i) a warm layer over a cooler layer (no salt); (ii) a fresh water layer over a salty layer (no temperature difference), and (iii) a cool fresh layer over a warm salty layer (double-diffusive stratification). As noted above, the purpose of these tests was to compare the entrainment rates found for the three types of stratification at comparable Ri (i.e., for the same overall density step) and determine if there was any appreciable effect of imposing a destabilizing temperature gradient on salt-stratified entrainment. The entrainment rate u_e was determined by noting the position of the interface as a function of time after the grid was started. This was done by moving the probes through the interfacial region at various times and recording the position of the maximum density gradient. Flow visualization was also used to observe the mean interfacial position and when one of the layers was heated the windows on the tank were removed only briefly for each observation. An initial series of salt-stratified experiments were run in which dye was added to either the upper or lower layer and it was assumed that the dye interface corresponded to the density interface. (This assumption was later checked using the conductivity probe - it was found that there was a small systematic bias in the visually obtained interface positions but this was approximately constant and the values for u_e obtained by either method were virtually the same.) An additional series of runs was performed using a shadowgraph technique. A small collimated light source was used and this procedure produced very clear pictures of the position of the interface

(Figure 17). u_e was evaluated by looking at a series of photographs taken as the experiment proceeded and noting the interface position as a function of time.

The largest set of experiments relied on temperature and salinity gradient measurements to obtain the interfacial position. It should be noted that within the accuracy of the present experiments there was no appreciable difference between the salinity and temperature interface thicknesses. An example of the temperature and salinity profiles measured through the interface is shown in Figure 18. Some increased fluctuations may be seen just above the interface, but the interface itself is generally quite clear and sharp. This is typical for the mesurements obtained in this set of tests.

In addition to the thermistor and conductivity probe measurements the temperature of each layer was measured with a mercury thermometer at the beginning and end of each run. Salinity values were also determined by taking several small samples from each layer for gravimetric analysis, described in Appendix D. This procedure allowed an additional calibration of the probes and also provided a check on the total heat and salt contents of the system at the beginning and end of each run.

Once temperature and salinity are known it is necessary to use an equation of state to calculate density and, therefore, density differences. The variation of density with temperature may be modeled by a parabolic curve with a maximum at T = 4°C. An examination of data listed in the C.R.C. Handbook and also data reported by the Office of Saline Water (Kellogg, 1965), led to the conclusion that the dependence of

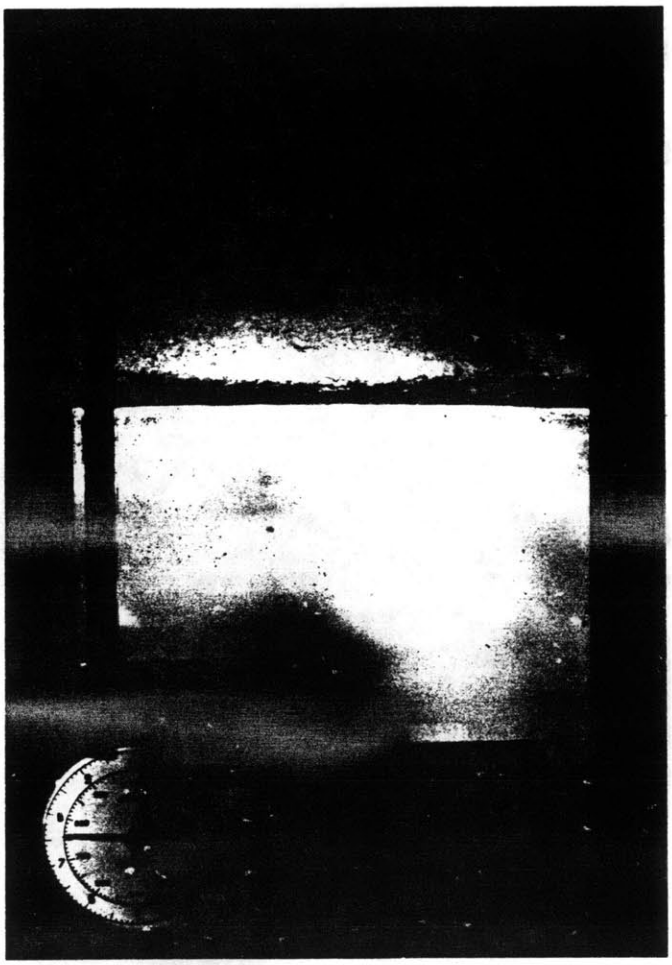

FIGURE 17 Photographs of Grid Entrainment Interface As Seen Using the Shadowgraph, For Different Density Steps. Note that There was Some Shading, So That the Interface Appears to be Slightly Thicker Than It Really Is

a) $\Delta\bar{\rho}/\rho_o = .085$

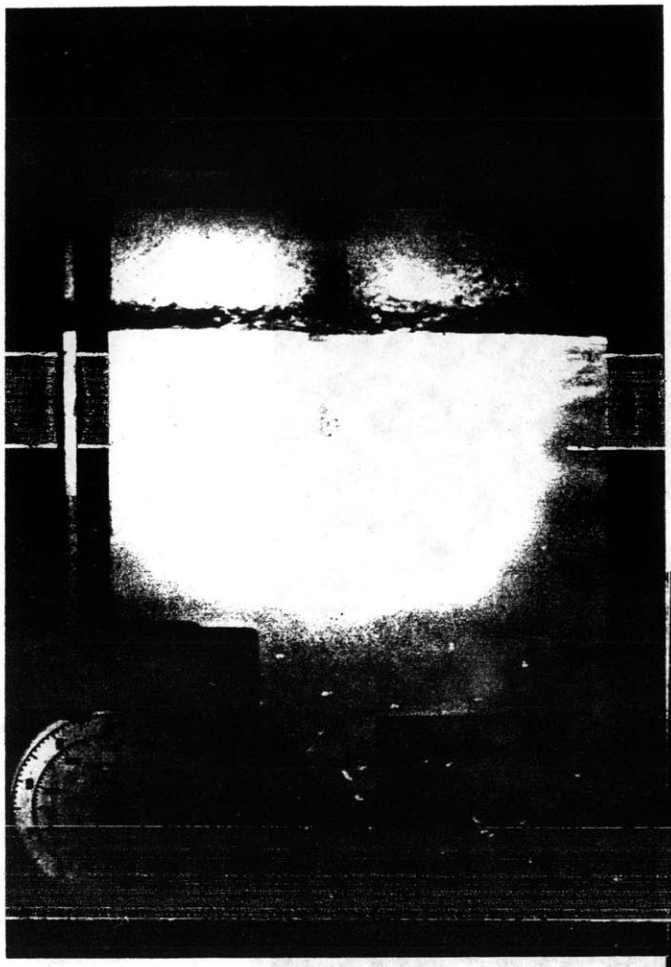

b) $\Delta\bar{\rho}/\rho_o = .039$

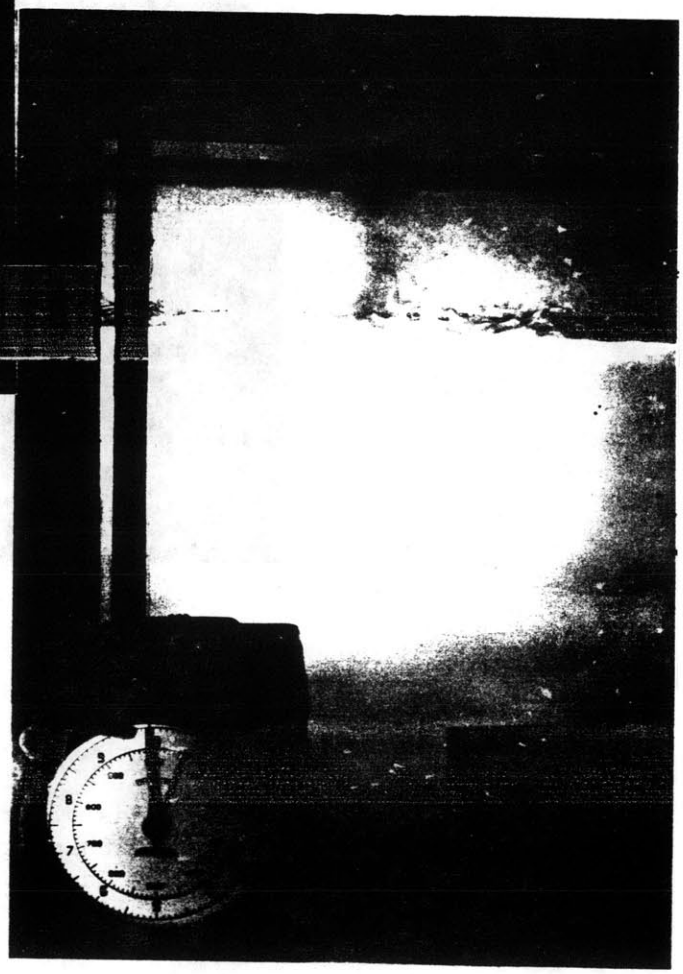

c) $\Delta\bar{\rho}/\rho_o = .007$

FIGURE 17 (continued)

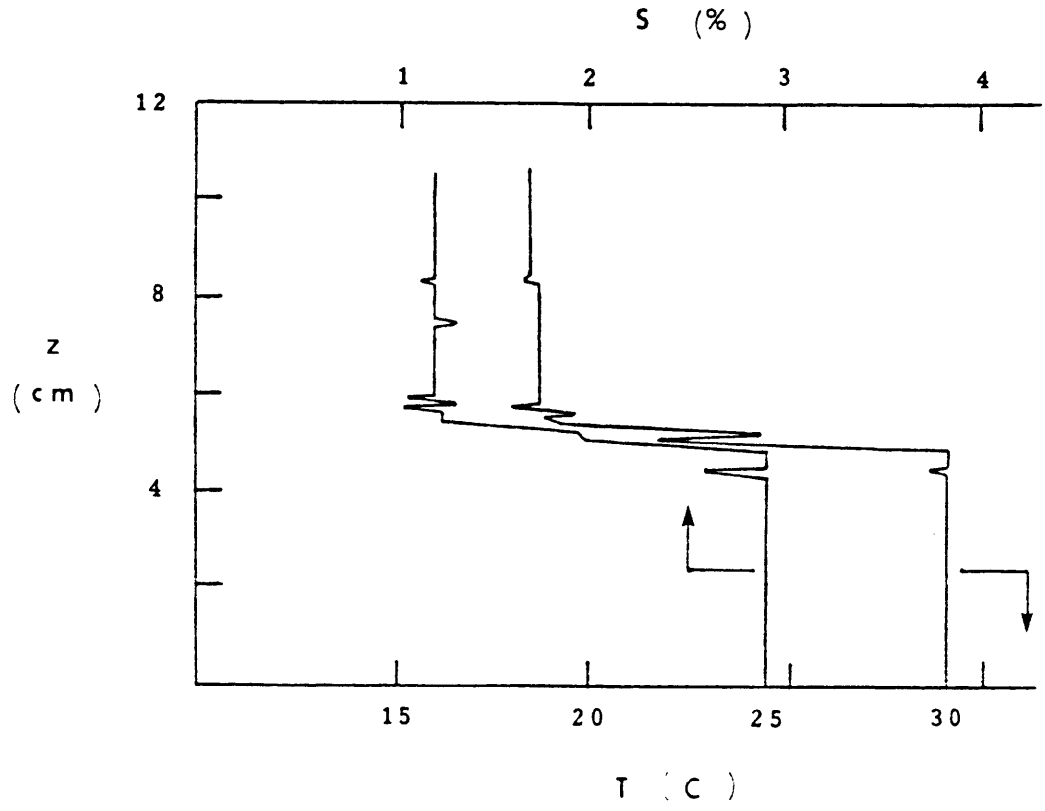

FIGURE 18 Example of Temperature and Salinity Profiles Measured In Grid-Mixing Tests

density on salinity would be well-represented by a simple linear function. Assuming that the effects of temperature and salinity are independent allows superposition, and the equation of state used in the present experiments was

$$\rho(kg/m^3) = 999.97 - 0.00663\ (T-4)^2 + 7.615\ S\ , \qquad (4.1)$$

where T is measured in °C and S is weight percent and the linear dependence on S was determined by a least-squares fit to the data mentioned above. Crapper (1976) used a least-squares technique to define a multiple-coefficient relation to fit data from the International Critical Tables for $10°C < T < 50°C$ and $0 < S < 6\%$. Over these ranges the difference between Crapper's values and those computed by (4.1) is less than 0.5%. In addition, several tests were made to compare density measurements of a solution (obtained with a hydrometer) with calculated values and it was found that for $T < 50°C$ and $S < 10\%$ the density values calculated by (4.1) were usually within 1% of the measurements and always within about 2%. For higher T and S the accuracy decreased to about 2 to 5%.

It was necessary to know $\Delta\rho$ for each measurement. Temperature and salinity values were obtained from the probe outputs (see Appendix D) and density was calculated from (4.1). Also, the changes in ΔT and ΔS across the interface as functions of time can be analyzed as follows. First consider the situation sketched in Figure 19, where two well-mixed reservoirs are in thermal contact with each other and isolated from the environment. A thin conducting surface separates the two reservoirs and a small flow is allowed from reservoir 1 to reservoir 2

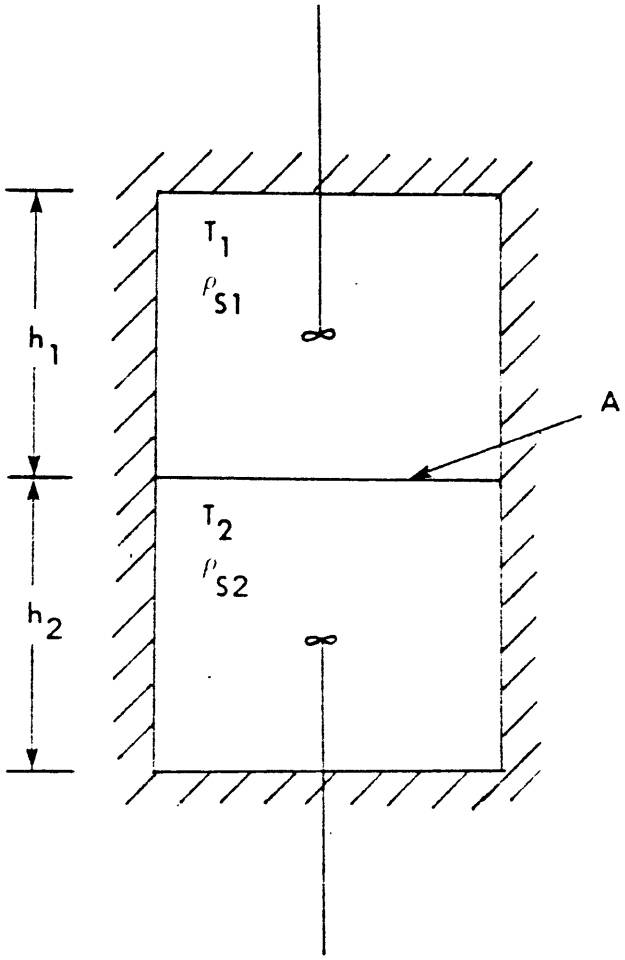

FIGURE 19 System Configuration Assumed For Derivation of Equations (4.4) and (4.5)

(i.e., fluid from reservoir 2 is entrained into the upper layer). Assuming that the only heat transfer in the system is done by interfacial conduction or entrainment, and that $dh/dt > 0$ the bulk heat balances for the two reservoirs may be written

$$\frac{d(V_1 H_1)}{dt} = A\hat{\kappa}\Delta T + AH_2 \frac{dh_1}{dt}$$

and

$$\frac{d(V_2 H_2)}{dt} = -A\hat{\kappa}\Delta T - AH_2 \frac{dh_1}{dt} = -\frac{d(V_1 H_1)}{dt} \quad , \tag{4.2}$$

where V = volume, $H = \rho C_p T$ = heat content, $\Delta T = T_2 - T_1$ and $\hat{\kappa}$ is a heat transfer coefficient which includes both molecular and turbulent conductivity. Then with A constant and noting that $dh_1/dt = -dh_2/dt$,

$$\frac{dH_1}{dt} = \frac{1}{h_1}\left[\hat{\kappa}\,\Delta T + (H_2 - H_1)\frac{dh_1}{dt}\right]$$

and

$$\frac{dH_2}{dt} = \frac{1}{h_2}\left[-\hat{\kappa}\,\Delta T\right] \quad . \tag{4.3}$$

Furthermore, assume that $\rho_1 c_1 \sim \rho_2 c_2 \sim \rho_0 c_p$ (constant), so

$$\frac{d(\Delta T)}{dt} = \frac{1}{\rho_0 c_p}\left[\frac{dH_2}{dt} - \frac{dH_1}{dt}\right]$$

$$\Rightarrow \quad \frac{d(\Delta T)}{dt} = -\left[\frac{\hat{\kappa}}{\rho_0 c_p}\left(\frac{h_1 + h_2}{h_1 h_2}\right) + u_e/h_1\right]\Delta T \quad , \tag{4.4}$$

where $u_e = dh_1/dt$. Note that if $u_e = 0$, (4.4) may be solved to obtain $\Delta T = \Delta T_o \exp(-\kappa\gamma t/\rho_o C_p)$, where $\gamma = (h_1 + h_2)/h_1 h_2$ and ΔT_o = initial temperature difference. A similar analysis for salt

stratification results in

$$\frac{d(\Delta\rho_S)}{dt} = -\left[\kappa_S\left(\frac{h_1 + h_2}{h_1\ h_2}\right) + u_e/h_1\right]\Delta\rho_S \qquad (4.5)$$

where $\rho_S = \rho S$ = salt concentration, $\Delta\rho_S = \rho_{S2} - \rho_{S1}$ and κ_S is a salt transfer coefficient.

Equations (4.4) and (4.5) can predict the changes in ΔT and $\Delta\rho_S$ quite well for the experiments provided that $\hat{\kappa}$ and κ_S are evaluated. This was done following a numerical iterative procedure with input values of u_e (measured during the experiment) and initial values of h_1, h_2 and ΔT ($\Delta\rho_S$) to choose $\hat{\kappa}$ (κ_S) so that (4.4) and (4.5) would reproduce the final value of ΔT ($\Delta\rho_S$). It was found that values for κ_S were small, of order $0(10^{-9}m/s)$ and the diffusive flux expressed by κ_S was neglible when compared with the entrainment flux. However, values for $\hat{\kappa}$ were calculated which showed that there was a considerable interfacial conductive heat flux. The procedure for calculating $\hat{\kappa}$ was very successful, as shown in the example of Figure 20. It can be seen that Eqn. (4.4) modeled the change in ΔT with time reasonably well. Eqs. (4.4) and (4.5) were then used to evaluate ΔT and $\Delta\rho_S$ at intermediate times for the flow visualization tests, using the measured initial and final values of ΔT and $\Delta\rho_S$ for calibration. The probes were used to check the calculations for several of the flow visualization tests and good agreement was found (as in Figure 20). Evaluation of $\hat{\kappa}$ and κ_S was also useful in calculating any additional (other than could be explained by entrainment) heat or salt flux.

As mentioned above, calculated values for κ_S tended to be very

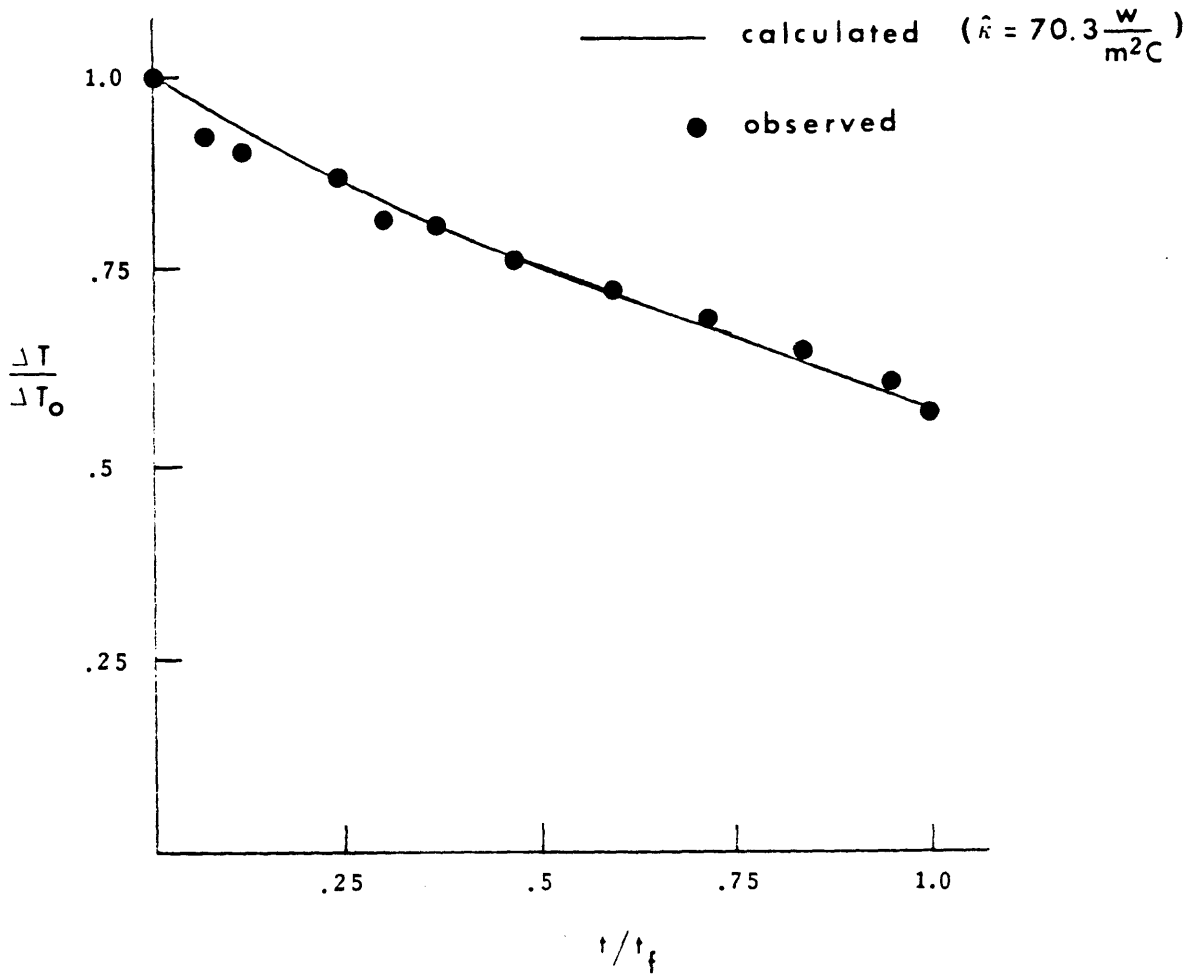

FIGURE 20 Calibration of $\hat{\kappa}$ With Measured Values of ΔT as a Function of Time

small, sometimes even taking very small negative values (approximately $0(\pm\ 10^{-9})$m/s). There was no discernable pattern in the variation of κ_S values with changes in ΔT or $\Delta\sigma_S$ and it was concluded that for all tests run here the interfacial salt flux was accomplished primarily by mechanical entrainment. That is, the change in salinity of the upper layer could be found for any time after beginning mixing by a simple dilution calculation and the salinity of the (undisturbed) lower layer remained approximately constant. On the other hand, values of $\hat{\kappa}$ were large enough that the conductive heat flux was in many cases of the same order of magnitude as the entrainment heat flux. There appeared to be some dependence of $\hat{\kappa}$ on ΔT_0 , as shown in Figure 21. However, the scatter in the data is quite large and the only conclusion to be made at this point is that $\hat{\kappa}$ appears to increase with increasing ΔT_o. It should be noted that the data in Figure 21 represent double-diffusively stratified tests. Also, when using (4.4) to evaluate$\hat{e}$ κ it should be remembered that heat loss to the surroundings is neglected. As previously mentioned, total heat and salt contents were checked at the beginning and end of each run and the data in Figure 21 are all from runs where less than 3% of the initial heat content was lost.

4.1.2 Velocity Measurements

The velocity measurements were made with a DISA Type 55L Laser Doppler Aneometer Mark II system using a Spectra Physics Stabilite Model 124B He-Ne laser. The analog voltage output was monitored on an oscilloscope display and fed into the computer data acquisition system which digitized and stored the data on hard disk. Measurements were

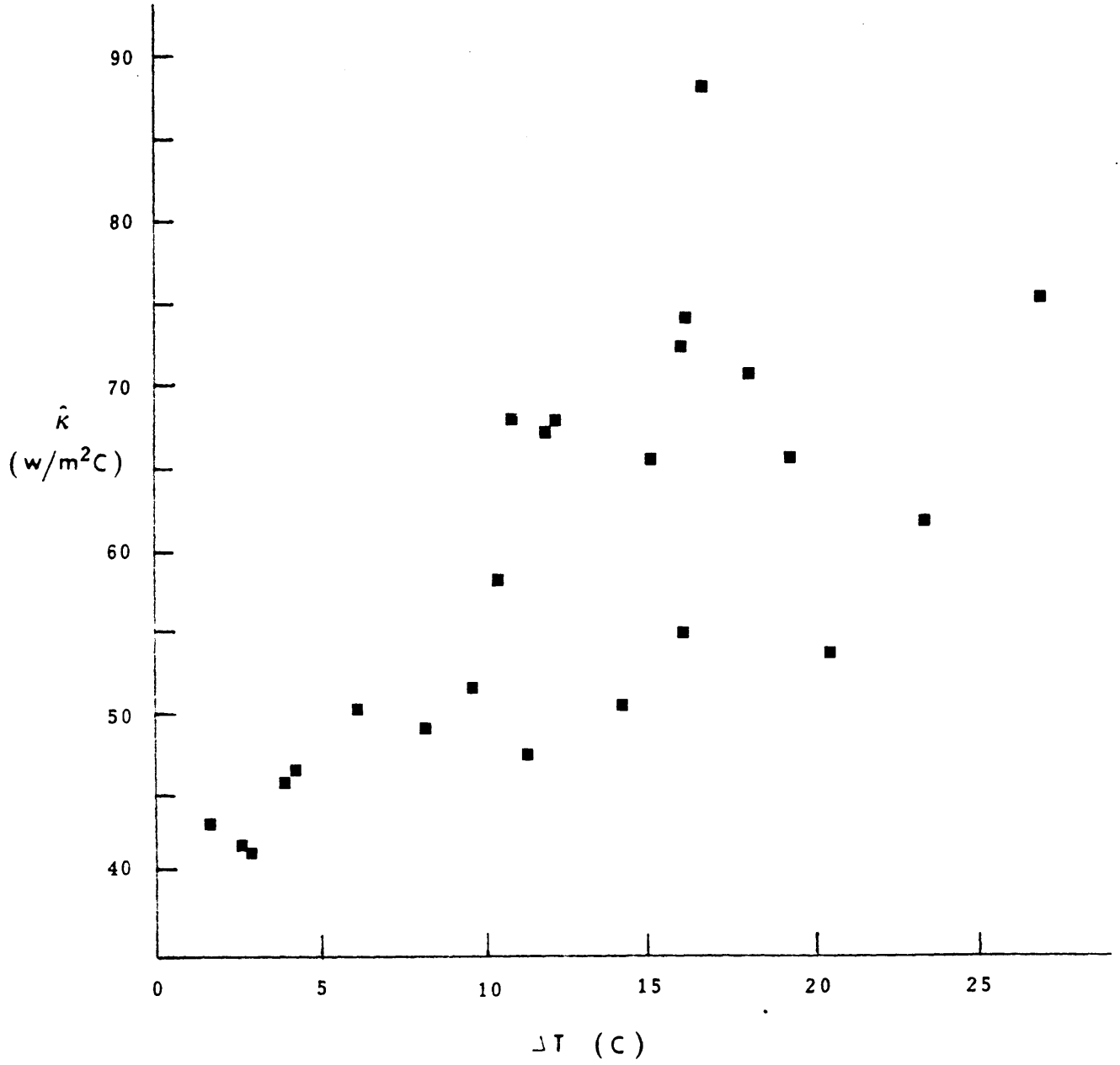

FIGURE 21 Calculated Values of $\hat{\kappa}$ as a Function of ΔT_o

taken of the vertical profile of the horizontal velocity component at several locations within the tank, as shown in Figure 22. No density stratification was used for these tests, as it was desired to avoid problems associated with index of refraction fluctuations. The use of similar measurements in previous experiments has been reviewed in Section 2.2.1.1. The laser and photomultiplier were mounted on a frame which could be raised and lowered so that vertical profiles could be measured. Different measuring positions in a horizontal plane were obtained by manually moving the laser forwards or backwards or from side to side on the frame. However, these lateral movements were restricted because of focal length limitations for the laser and photomultiplier lenses and also because of the presence of the insulation around the edges of the tank. Therefore, measurements were not obtained at positions very close to either of the walls. The experimental set-up for the laser measurements is shown in Figure 23.

Five four-second records of data sampled at a rate of 1000 Hz were recorded at each point. The frequency 1000 Hz was judged to be sufficiently high because a comparison of spectral density estimates for data sampled at various rates ranging between 200 and 2000 Hz showed that there was negligible energy in frequencies greater than about 500 Hz (note that the Nyquist frequency is one-half the sampling rate). The input signal was low-pass filtered at 500 Hz before being recorded by the computer to reduce aliasing. In general, the grid was oscillated for at least 10-15 minutes before any data was recorded, and the data samples were checked for stationarity using a run test (Bendat and Piersol, 1971, p. 235-236). The assumption of stationarity was found to be good at the 95% confidence level for all but four of the test measurements. These

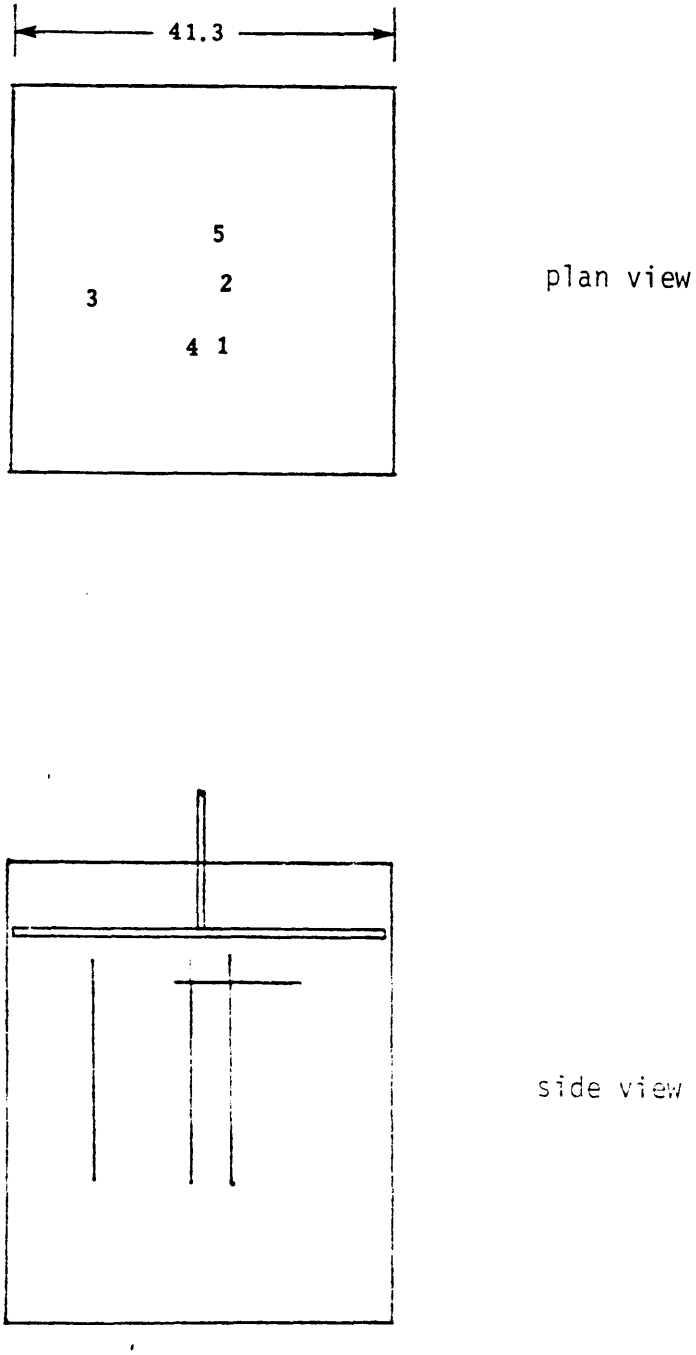

FIGURE 22 Locations For Measurement of Vertical Velocity Profiles in Grid-Mixing Tank

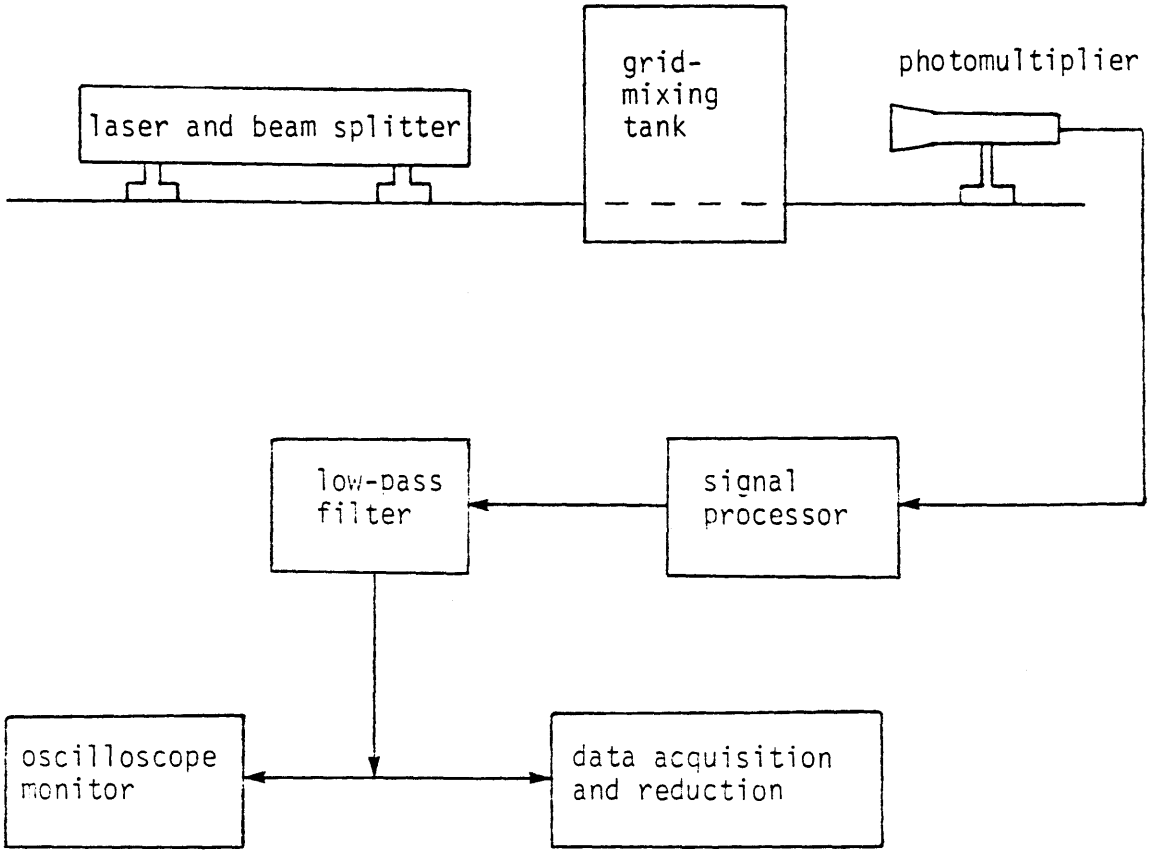

FIGURE 23 Experimental Set-Up For Laser Velocity Measurements

four signals were recorded at the larger depths ($\geq$ 20 cm) from the grid, where signal strength was relatively poor.

Background noise levels were measured by taking data while there was no forcing in the water (i.e., the grid was oscillated, but at a distance well above the water surface). Measurements were also taken while the grid was not in motion so that electrical noise induced by the motor and possible vibrations due to the grid movement might be identified, as well as effects of building and support frame vibration. The background signal consisted of both electrical and mechanical noise and it was desired to remove this noise from the signal when analyzing the velocity measurements.

Background noise proved to be a problem during these tests, primarily because the velocity levels were quite small. Though some electrical noise due to the motor was observed in the photomultiplier signal, it appeared to be filtered out by the signal processing unit of the anemometer, as no significant differences could be seen in the raw data or in the calculated power spectra for background noise in the cases when the motor was off and when it was on (but not connected to the driving rod so that there was no physical connection between the motor and the tank). However, there appeared to be some noise in the signal due to mechanical vibration, either in the laser support frame or the tank structure. A portion of this motion could be traced to low-level vibrations of the building. This was verified by using an accelerometer to measure vibrational motion without the grid moving. Calculations of the power spectra (see Section 4.2) for the accelerometer data revealed that there was significant energy in the background noise at about 19 -20 Hz (Figure 24). As shown in Section 4.3, these peaks also appeared in

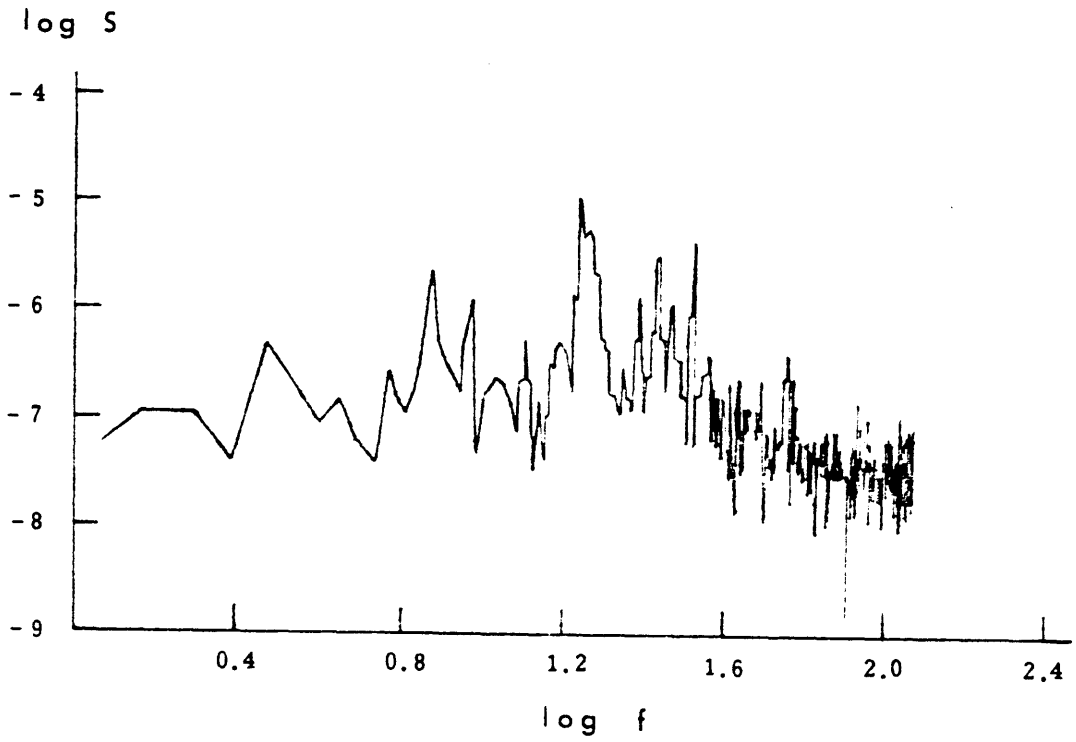

FIGURE 24 Power Spectrum For Accelerometer, Showing Peak Near 20 Hz

the spectra for the laser data. It appears that building vibration was a cause of background noise in these experiments.

Several steps were taken to minimize the background noise level and, therefore, to increase the signal-to-noise ratio. A wire cage was built around the motor, which was connected to a different power supply circuit than the laser so that electrical noise generated by the motor might be minimized. Experiments were run in a darkened room and the flow was seeded with a dilute suspension of very small (mean diameter 1.5 μm) silicon carbide particles to increase the signal strength and reduce noise from background lighting. Seeding was especially helpful in this experiment as the velocities were low and there was minimal mean flow. The measurements were taken at night, when building vibrations were reduced (the lab is situated next to a well-traveled roadway and is also near a subway line). This could be seen by comparing accelerometer data taken at different times during the day. At night it was also possible to turn off many of the large ventilation fans used to circulate air through the building. Along with each of these measures, careful tuning of the signal processor of the anemometer increased the signal strength relative to the noise so that reasonably good data was obtained. In terms of sample variances, the signal was always at least one order of magnitude greater than the background noise. However, background noise was not completely eliminated. In particular, we were unable to identify the source for noise at about 20 Hz, except as being somehow inherent in the building.

4.2 Data Collection and Analysis

As previously mentioned data was primarily collected by the computer data acquisition system, which was also used for much of the data reduction. For the entrainment tests profiles were taken through the interfacial region at various times during the course of an experiment. For each profile the raw voltage outputs for the three measurements were sampled for 10 sec. at 10 Hz as the probes were moved manually through the interface using the point gauge. Afterwards, the calibrations were applied to the raw data and temperature and salinity profiles could be plotted to show the position of the interface. An example of one of these profiles has already been referred to in Figure 18. There was not any noticeable difference in the position or thickness of the thermal and salinity interfaces. When the X-Y plotter was used similar profileswere obtained directly, though the plotter could only be used in this way for singly-stratified conditions (i.e., only temperature or salinity could be plotted vs. position). Another disadvantage of the plotter is that the output must be interpreted graphically and this is more time-consuming and less accurate. Additional entrainment results (i.e.,values of u_e) were obtained from the flow visualization tests, asdescribed in the previous section.

The main result desired from the laser measurements was the determination of the r.m.s. horizontal velocity component and integral length scale at positions in the tank which corresponded with interface locations in the entrainment tests (i.e., at the same distances from the mean grid position). There was also some interest in comparing the present measurements obtained with the LDA with results reported in

previous studies which used rotating hot film probes. Therefore, more detailed vertical profiles were measured. In addition to mean value and variance calculations, power spectra were computed for each measurement point to examine the frequency distribution of the signal. Fast Fourier transforms were used to calculate the spectra and a segment averaging procedure was used to improve the estimates. That is, each full 20 second record was divided into 20 segments of one second each, the statistics were computed for each segment and final estimates were obtained by averaging the values over the segments. Before calculating statistics, however, the set of data points for each segment was augmented by adding a number of zeroes at the end of the sequence so that the total number of points in the segment was a multiple of two. This was necessry for application of the FFT algorithm and also increased the accuracy of the spectral estimates. An estimate for the accuracy of the spectral estimates is the normalized standard error, which Bendat and Piersol (1971) show can be written as $\varepsilon_r = (L/N)^{1/2}$, where L = number of points per segment and N = total number of points in the sample. The normalized standard error for the velocity spectra calculated here is then about 20%, and indicated by the error bars drawn on Figure 25. Estimates for the mean and variance of each signal are considerably better, within 1% of their "true" values.

The procedure for removing noise from the signal to be analyzed consisted of subtracting the variance of the noise from the variance of the recorded turbulence signal, i.e., $\overline{u^2}$ corrected $= \overline{u^2} - \overline{u_n^2}$, where $\overline{u_n^2}$ = variance for noise signal. This assumes that the cross-correlation $\overline{u^2 u_n^2}$ was negligible. Direct estimates of the cross-

correlation were not possible since the turbulence and noise signals could not be recorded simultaneously. However, assuming that the data is stationary, the statistics should not change with time and the calculation was actually made for data samples taken a short time apart. Several tests showed that the cross-correlation was at least one to two orders of magnitude less than the variance of the noise so that its neglect was justified. A similar procedure has been used in previous experiments (Hopfinger and Toly, 1976; Asaeda and Tamai, 1980). This is equivalent to subtracting the areas under the respective power spectral density curves to define the energy added to the water by the grid motion. The r.m.s. velocity is then the square root of the corrected variance multiplied by a scaling factor which depends on the laser characteristics.

In order to define the length scale the integral time scale was first calculated from autocorrelation estimates,

$$\hat{t} = \frac{1}{f_s R_o} \Sigma R_t \quad , \tag{4.6}$$

where R_t = autocorrelation for a time lag t (R_o = variance):

$$R_t = \frac{1}{N-m} \sum_{n=1}^{N-m} (u_n)(u_{n+m}) \quad , \tag{4.7}$$

and N = number of points in sample, m = lag, $t = m/f_s$ and f_s = sampling frequency. A length scale $\hat{l}$ was then defined as the product of $\hat{t}$ and $\hat{u}$ (r.m.s. value). However, as shown by the results in the

following section, the laser signal was dominated by the grid motion for distances from the grid up to at least 10-12 cm. Since the interface in the entrainment experiments was usually ~7-12 cm from the grid it was decided that a more appropriate time scale was simply the period of the grid motion, or $\hat{t} = 1/f$. Since this was constant the numerical value of $\hat{I}$ becomes proportional to the value of $\hat{u}$.

4.3 Results and Discussion

4.3.1 Velocity measurements

Following the procedure outlined above power density spectra were calculated for each velocity measurement point. A strong peak was found to occur at the forcing frequency of 5 Hz for data taken less than about 10 cm (2 mesh spacings) from the grid. At greater distances the 5 Hz peak is not as distinct and energy is spread out over a larger frequency range. Figure 25 shows examples of spectra calculated for several values of h_g = distance between mean grid position and measurement point, for profile position 1 (Figure 22). A spectrum calculated for the noise signal is shown in Figure 26. This signal was recorded just before the velocity measurements were taken by running the motor and moving the grid, but with the tank only about 1/3 full. In this way it was hoped to identify spectral peaks which were associated with background noise arising either from mechanical vibrations due to from the grid motion or inherent in the building and also with electrical noise. For instance, a peak can be seen at about 19-20 Hz in both the background noise spectrum and in several of the velocity spectra, especially at greater h_g (Figure 25). The source for energy at this frequency was apparently associated with a very low level vibration in the building, since the

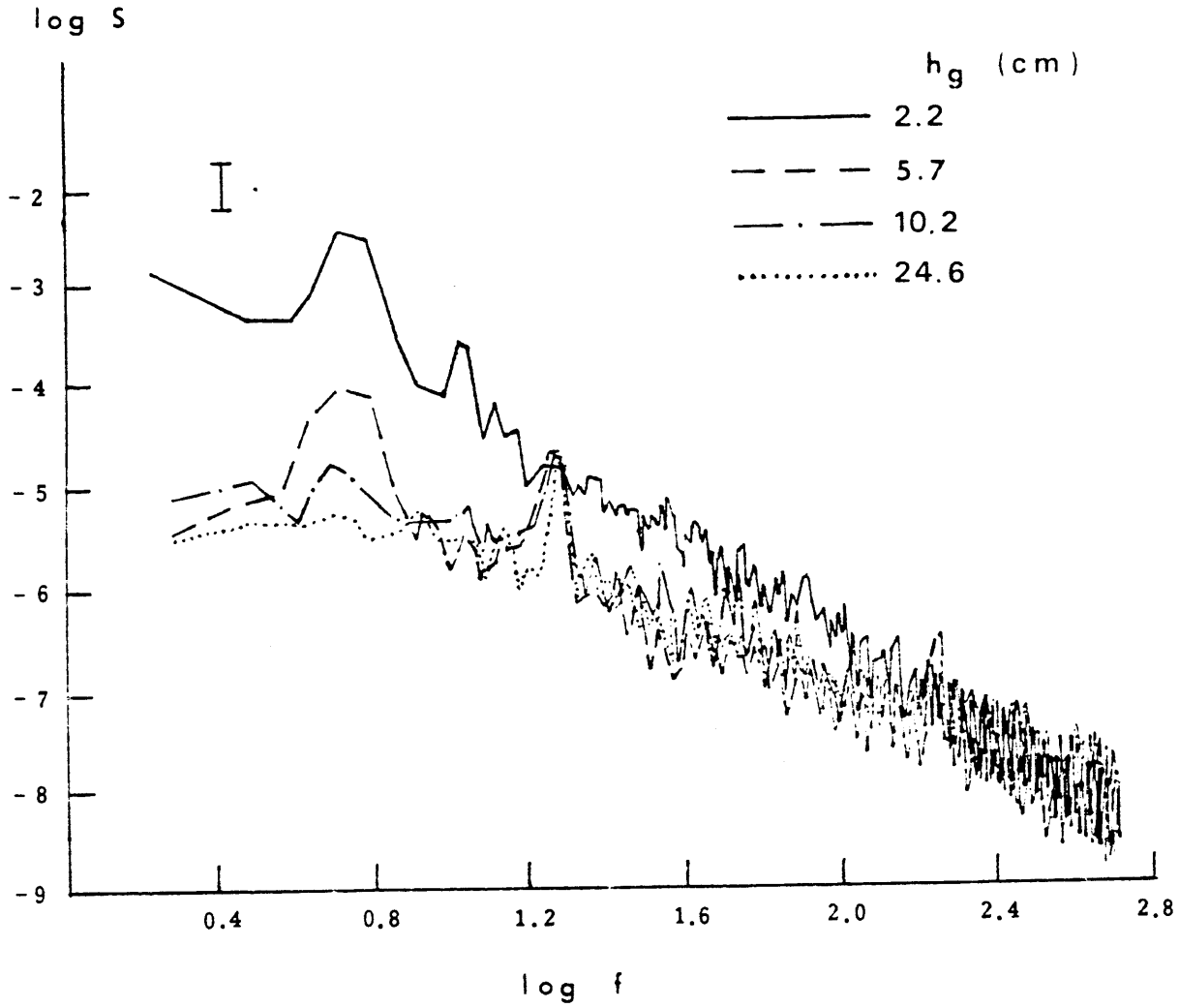

FIGURE 25 Power Spectral Density Calculated For Velocity Signal As a Function of Distance From the Grid

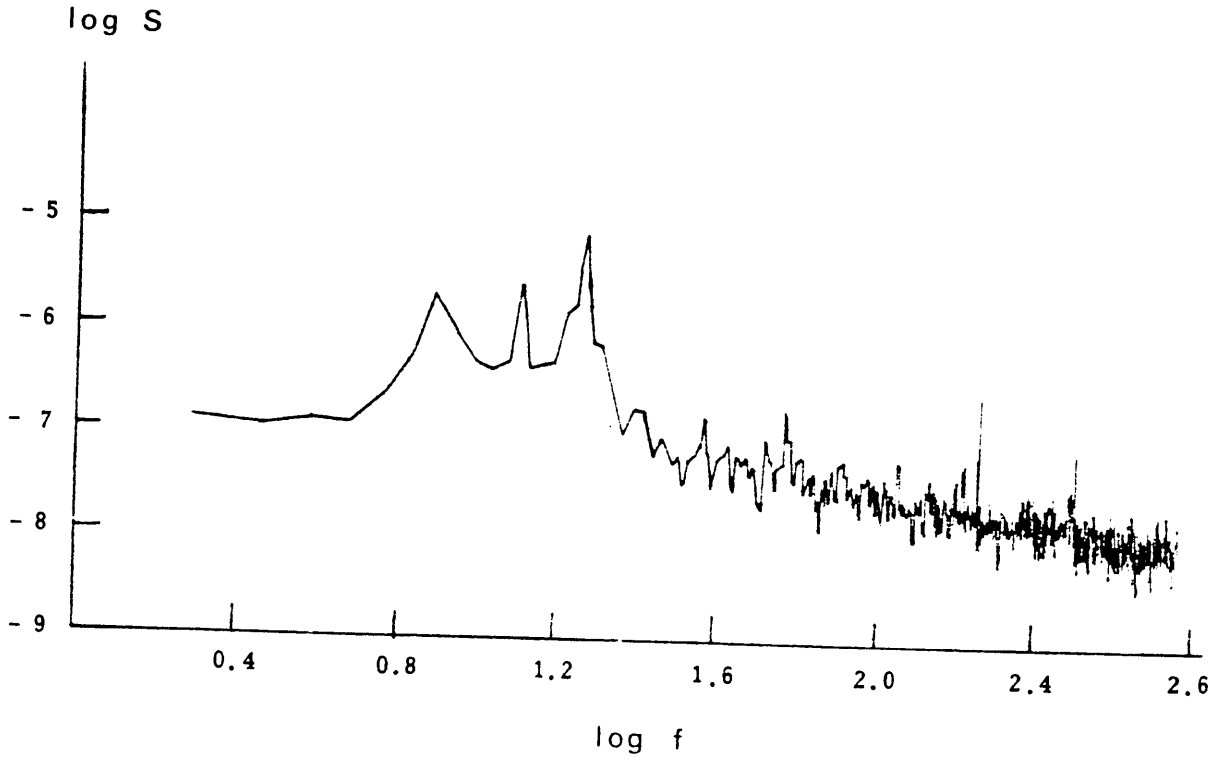

FIGURE 26 Power Spectrum for Noise Signal

same peak was found in the accelerometer data (Figure 24). Background noise data was measured for each profile and the velocity measurements were all corrected by subtracting the noise as explained previously.

Data for profile positions 1, 3, 4 and 5 (Figure 22) were reasonably similar except perhaps for smaller h_g. At positions closer to the grid the effects of being directly under a grid bar or under a space would be more apparent. Profile 2 was taken directly underneath the reinforced center of the grid and the extra solidity there resulted in somewhat stronger forcing (this effect was also observed to some extent during the flow visualization runs, especially for small h_g). Velocity profiles are shown in Figure 27 where $\hat{u}$ is defined as the corrected r.m.s. horizontal velocity component and (fs) gives an estimate of the velocity near the grid (see Eq. 2.10). h_g is scaled by s which is an estimate for the position of the virtual origin of the velocity profile (Hopfinger and Toly, 1976). Results from several earlier grid experiments are also shown on Figure 27 for comparison. It should be noted that Thompson and Turner's curve describes their data only to within about + 50% and Hopfinger and Toly's curve underpredicts much of their data by ~20% and overpredicts Thompson and Turner's data by about the same amount. The range for McDougall's data corresponds with measurements made at different horizontal positions for a constant h_g = 10 cm.

The solid line in Figure 27 is a best fit to the data points after averaging, where the values for profile 2 were weighted by a factor equal to the ratio of the area of the reinforced center to the total area. In other words, it was assumed that the main effect of the increased solidity on the motion was confined to the immediate central area of the

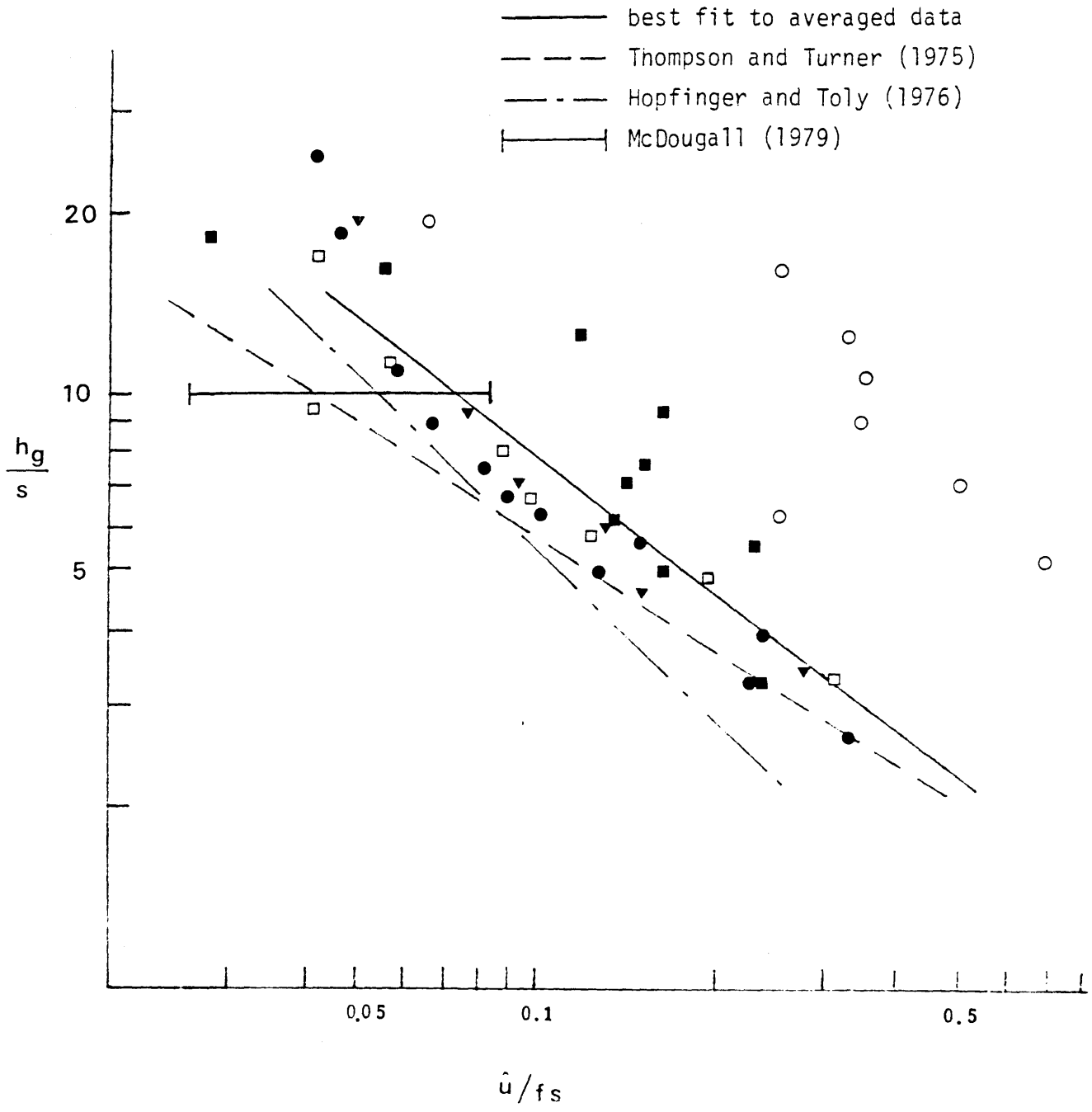

FIGURE 27 Vertical Profiles for r.m.s. Horizontal Velocities Measured In Grid Experiment; ● Profile Position 1, ○ Position 2, ■ Position 3, □ Position 4, ▼ Position 5 (Refer to Figure 22)

tank. Data points for the other profiles were weighted equally. The best-fit curve to the averaged data (obtained by least-squares) is expressed as

$$\frac{\hat{u}}{fs} = 1.5 \left(\frac{h_g}{s}\right)^{-1.3} \quad . \tag{4.8}$$

(Recall that f = 5 Hz and s = 1 cm.) The scaling for this result was chosen to be consistent with (2.10). It can be seen that the r.m.s. velocities here are slightly greater than those predicted by the relations suggested from the previous experiments, but certainly within the same range.

Calculations of the autocorrelation (4.7) showed that there was a strong influence of motion directly induced by the grid, at least for $h_g \tilde{<} 12$ cm. For example, Figure 28 shows the autocorrelation calculated for s h_g = 9.6 cm where it can be seen that the forcing frequency of Hz is still evident. At larger depths this influence diminishes. Time scale calculations according to (4.6) are shown in Figure 29 where some increase in $\hat{t}$ with increasing h_g can be seen for larger h_g. This would be the expected trend if $\hat{\nu}$ were to increase with h_g. It was concluded from these results and also from the power spectrum calculations (Figure 25) that the dominant feature of the motion in the region $h_g < 12$ cm was directly associated with the grid motion. Since the mixing experiments were usually conducted for interfacial positions less that this distance it is supposed that this motion was predominantly responsible for causing entrainment. However, it should be noted that this is not really turbulence, but a more well-ordered motion. In accordance with the discussion of the length

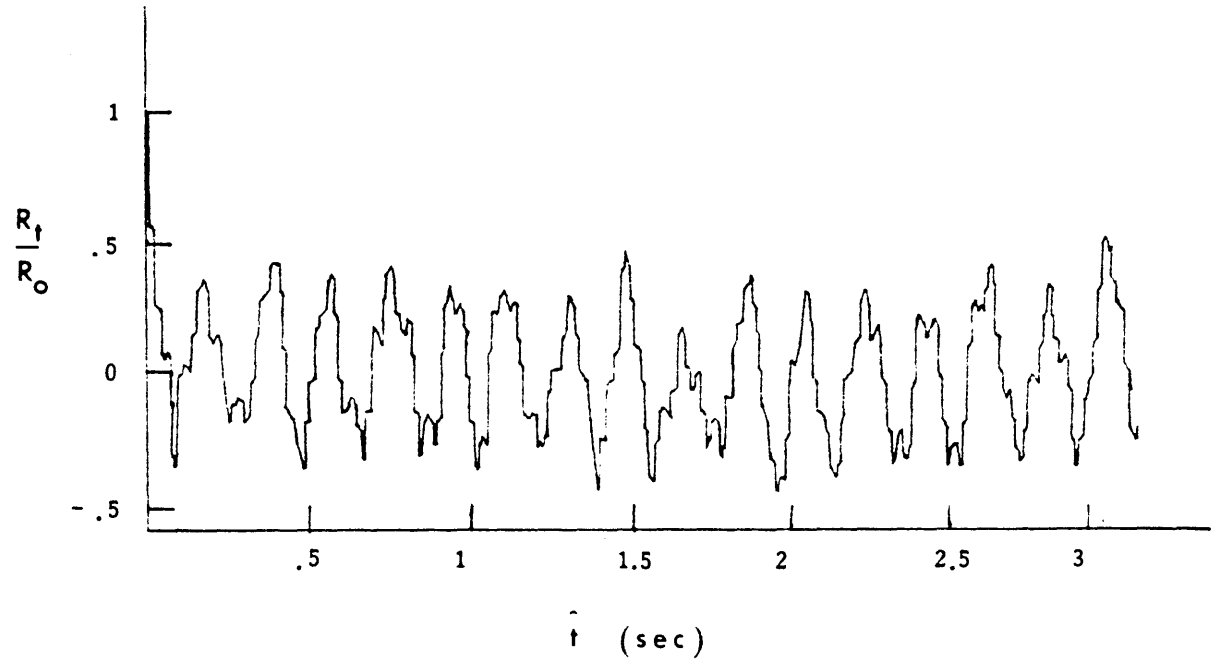

FIGURE 28 Normalized Autocorrelation Function For Signal Recorded at h_g = 9.6 cm

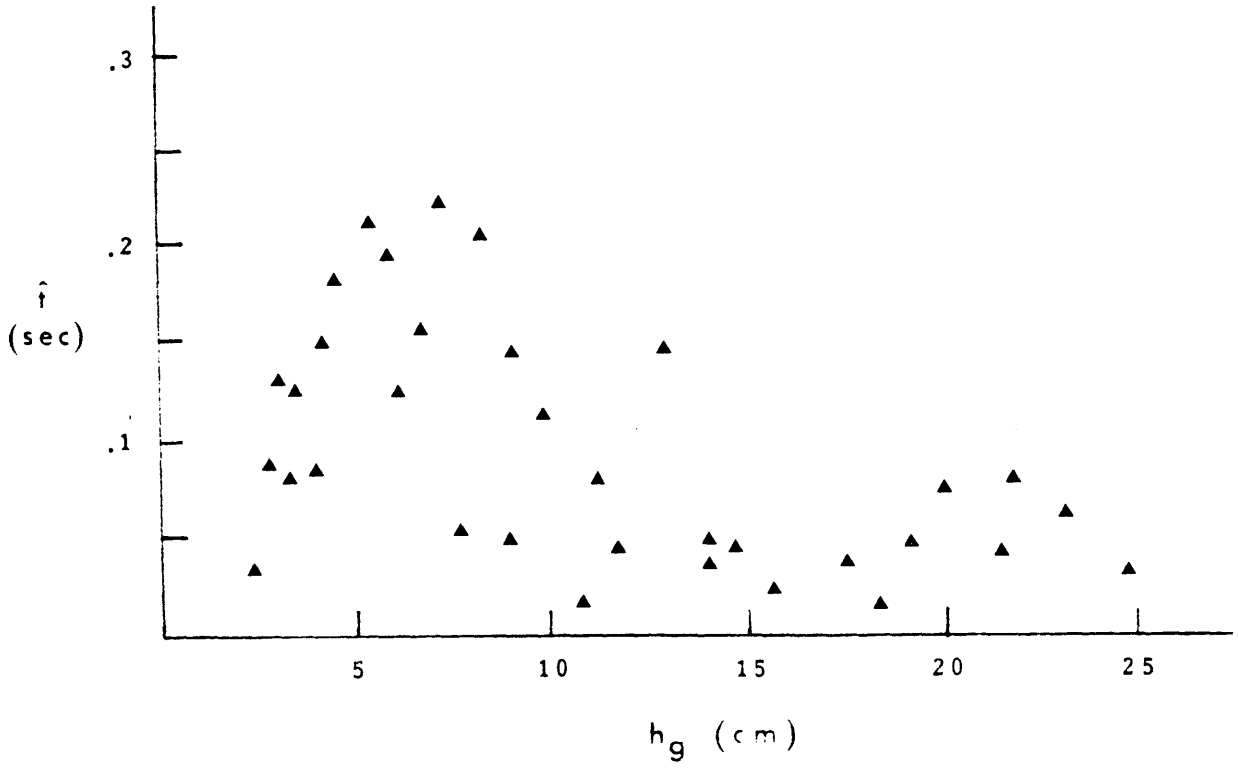

FIGURE 29 Estimates For the Integral Time Scale Calculated From the Autocorrelation

scale at the end of Section 4.2, $\hat{\theta}$ was then estimated as

$$\hat{\theta} = \hat{t}\,\hat{u} = 0.2\,\hat{u} \quad , \tag{4.9}$$

where $\hat{u}$ was calculated from (4.8). It should be noted that (4.9) predicts that $\hat{\theta}$ decreases as h_g^{-1}, a result which contradicts the relationship $\hat{\theta} \propto h_g^{-1.3}$ which arises from the turbulence models (see Section 2.2.1.1). Both Thompson and Turner (1975) and Hopfinger and Toly (1976) reported measurements which seemed to support the direct proportionality between $\hat{\theta}$ and h_g, though a close examination of Thompson and Turner's data reveals that there is no clear relationship between $\hat{\theta}$ and h_g for $h_g \lesssim 10$ cm (Fig.30). Hopfinger and Toly also reported strong peaks in their velocity spectra at the forcing (oscillation) frequency up to about two mesh spacings away from the grid. It may be concluded that turbulence does not constitute a dominant feature of the motions in a grid-mixed layer for distances from the grid less than about 10 cm (at least for the geometry considered here). Therefore, results from a turbulence model would also not necessarily be expected to hold in this region. Scaling of the grid entrainment results using (4.5) to calculate $\hat{\theta}$ leads to a problem in directly comparing present results with those of previous studies, since values for Ri using (4.5) will be approximately an order of magnitude less than values using with those of previous studies, since values for Ri using (4.5) will be $\hat{\theta} = 0.1\ h_g$ (Thompson and Turner result). However, this does not present any problem in comparing the present results for the different kinds of stratification.

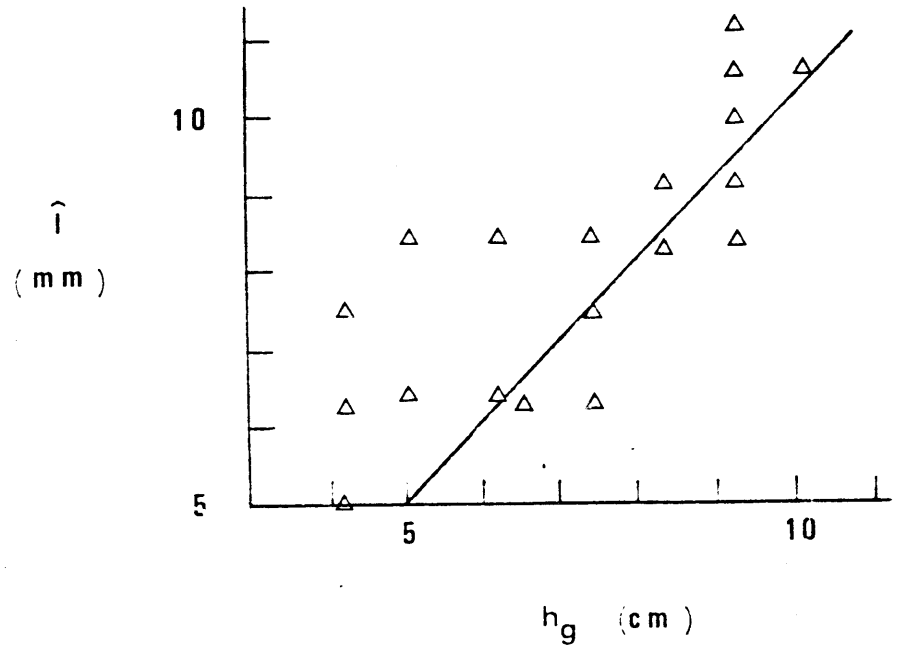

FIGURE 30 Variation of $\hat{\ell}$ with h_g for $h_g < 10$ cm, Reported by Thompson and Turner (1975)

4.3.2 Entrainment results

As described in Section 4.1.1 the position of the interface was observed as a function of time using visual techniques and also by measuring temperature and salinity profiles with the probes. Both methods showed that for a given run the rate at which the interface moved away from the grid decreased slightly with increasing h_g. This is probaby due to the decrease in $\hat{u}$ (or, increase in Ri = $g\Delta\rho'/\rho_o\hat{u}^2$). The flow visualization method produced somewhat smoother results since the measured interface position for each reading was visually-averaged, whereas the position obtained from the probe outputs reflected more of a local value and was subject to perturbations induced by local interface deflections. It was found that a simple power-law curve could usually be fitted quite well to the interfacial position data as shown in Figure 31. As seen by the examples in Figure 31, u_e tended to be more uniform when the stratification was stronger (this is probably because h_g did not vary as much). The entrainment rate at any value of h_g was then evaluated as the slope of the curve at that point.

Temperature and salinity values for each layer were obtained directly from the probe outputs or calculated from (4.4) and (4.5). (4.1) was then used to calculate $\Delta\rho$. Knowing h_g, $\hat{I}$ and $\hat{u}$ could be calculated at each point (eqs. 4.8 and 4.9) and, therefore, $u_e/\hat{u}$ could could be evaluated as a function of Ri. Results of these calculations are shown in Figure 32. Although there is some scatter in the data, the results for only temperature or salinity stratification appear to follow the qualitative relationships reported in previous experiments (Eqs. 2.3

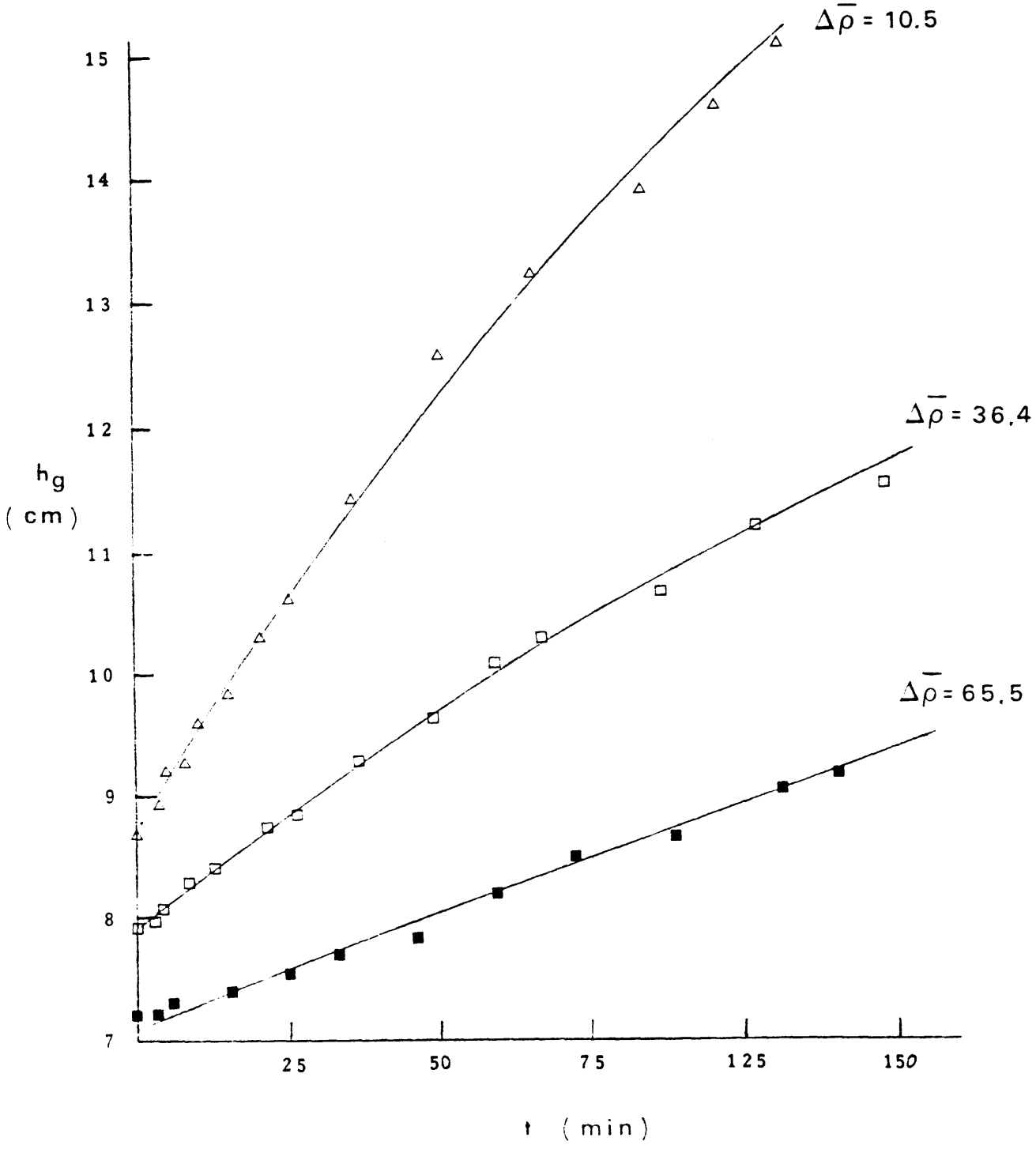

FIGURE 31 Mixed-Layer Deepening in the Grid Experiment As a Function of $\Delta\bar{\rho}$ = Average Density Difference Between The Two Layers (kg/m^3)

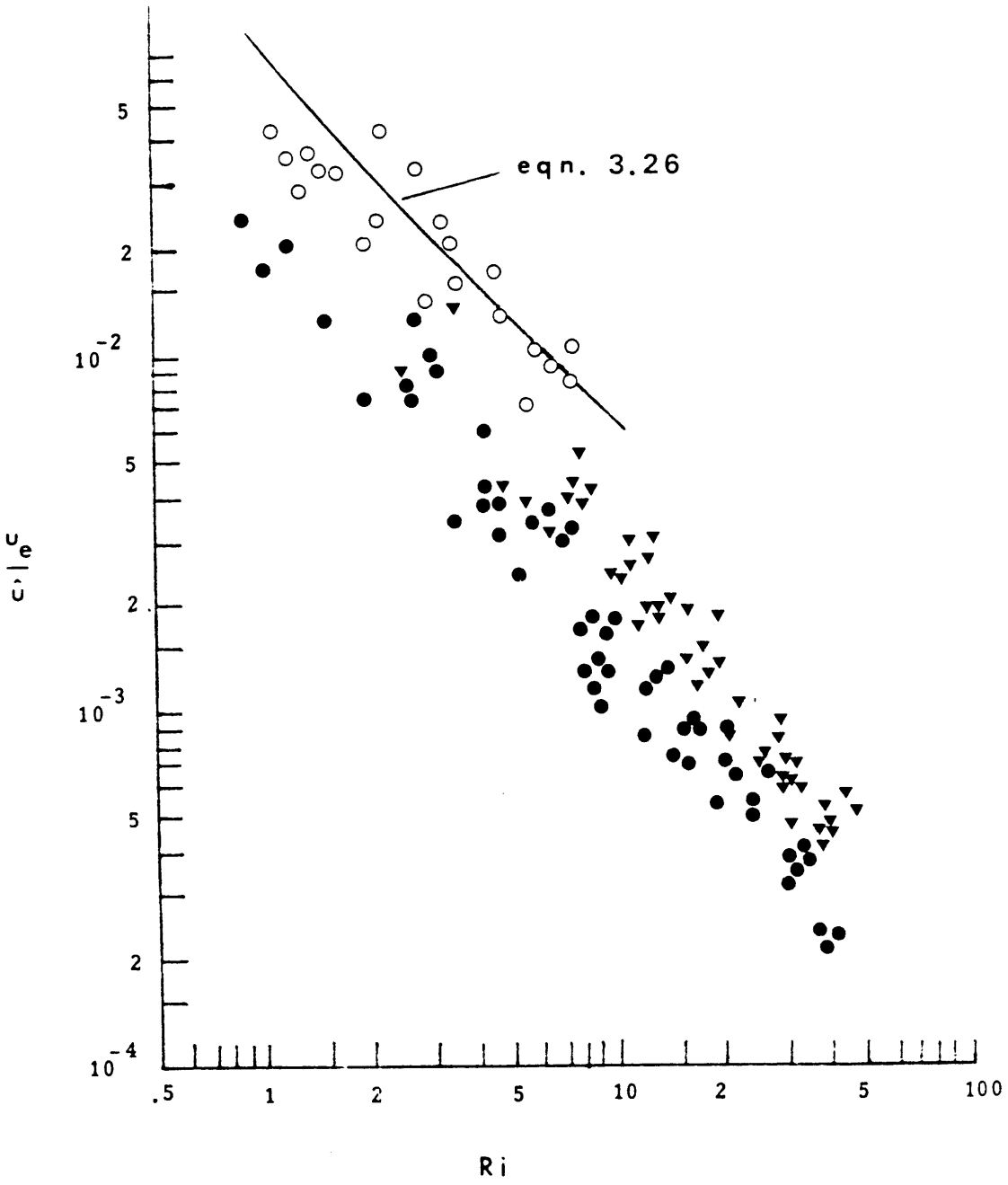

FIGURE 32 Grid Entrainment Results Using $\hat{u}$ = r.m.s. Velocity For Scaling; ● Salt Stratification, ○ Temperature Stratification, ▼ Double-Diffusive Stratification

and 2.4). A comparison of some of the entrainment results was made with Turner's (1973) data by Atkinson and Harleman (1983c), where constant values for the scaling velocity and length were used for each set of data (u_e was evaluated only at h_g = 9 cm). Their results for singly-stratified conditions were consistent with Turner's findings. However, this comparison is not possible directly for the present results because the length scales are defined differently.

The results in Figure 32 indicate that there is some effect of the unstable temperature stratification on the entrainment. Due to the scatter of the data it is not possible to define very precisely the exact influence of ΔT, but there is a clear tendency for u_e to increase with an increase in ΔT (while holding Ri constant). A first possibility to check is whether double-diffusive fluxes might be present. Following the discussion is Section 3.2.3, this will be the case if $t_c < \hat{t}$ = 0.2 sec. For the largest values of ΔT used ($\tilde{}$ 30°C), t_c was calculated by (3.25) as $t_c \tilde{=}$ 10.8 sec., which is easily greater than $\hat{t}$. Therefore, another approach must be followed to explain these results.

Recall that the scaling velocity $\hat{u}$ was obtained under non-stratified conditions. It has also been pointed out that an appreciable heat flux from the lower to the upper layer was observed which could not be accounted for by entrainment alone. This conductive heat flux is calculated by $H_f = \hat{\kappa}\Delta T$ and creates an unstable buoyancy flux across the interface. The buoyancy velocity w_* associated with this flux may then be calculated according to (3.13), where $B_f = \alpha_T g H_f / \rho_o c_p$.

The buoyancy flux leads to large (relatively) scale motions which tend to bring more of the grid energy down to the interface. These motions will occur in both layers and the main effect in the bottom layer is to maintain a mixed condition and a sharp interface (see Figure 18). This is the probable mechanism for the influence of the unstable temperature gradient on u_e. That is, the effect of having an unstable temperature gradient is to cause buoyant convection across the interface, resulting in increased mixing energy being transported to the interface and, therefore, u_e is increased. This effect may be incorporated by scaling the results with an appropriate scaling velocity σ, defined by a modified form of (3.14), where, $\hat{u}$ is used instead of u_* and the proportionality coefficient is placed in front of w_* since there is some uncertainty in the estimate of w_*, while $\hat{u}$ is a measured quantity. Scaling in this way also does not affect the salinity results in Fig. 32. Figure 33 shows the entrainment results scaled with $\sigma=(.125w_*^3+\hat{u}^3)^{1/3}$. It can be seen that this scaling collapses the double-diffusive data (note that $w_*=0$ for the singly-stratified tests).

It appears then that this buoyant convection is the main effect of the imposed temperature gradient, as the increased entrainment rates can be explained by including w_* in defining a scaling velocity. Unfortunately, it was not possible to check this hypothesis directly by taking velocity measurements with the laser near the interface. It is hoped that future experiments will look into this effect, either by using different measuring techniques or by creating density interfaces without refractive index changes (e.g., McDougall, 1979). It is also seen that

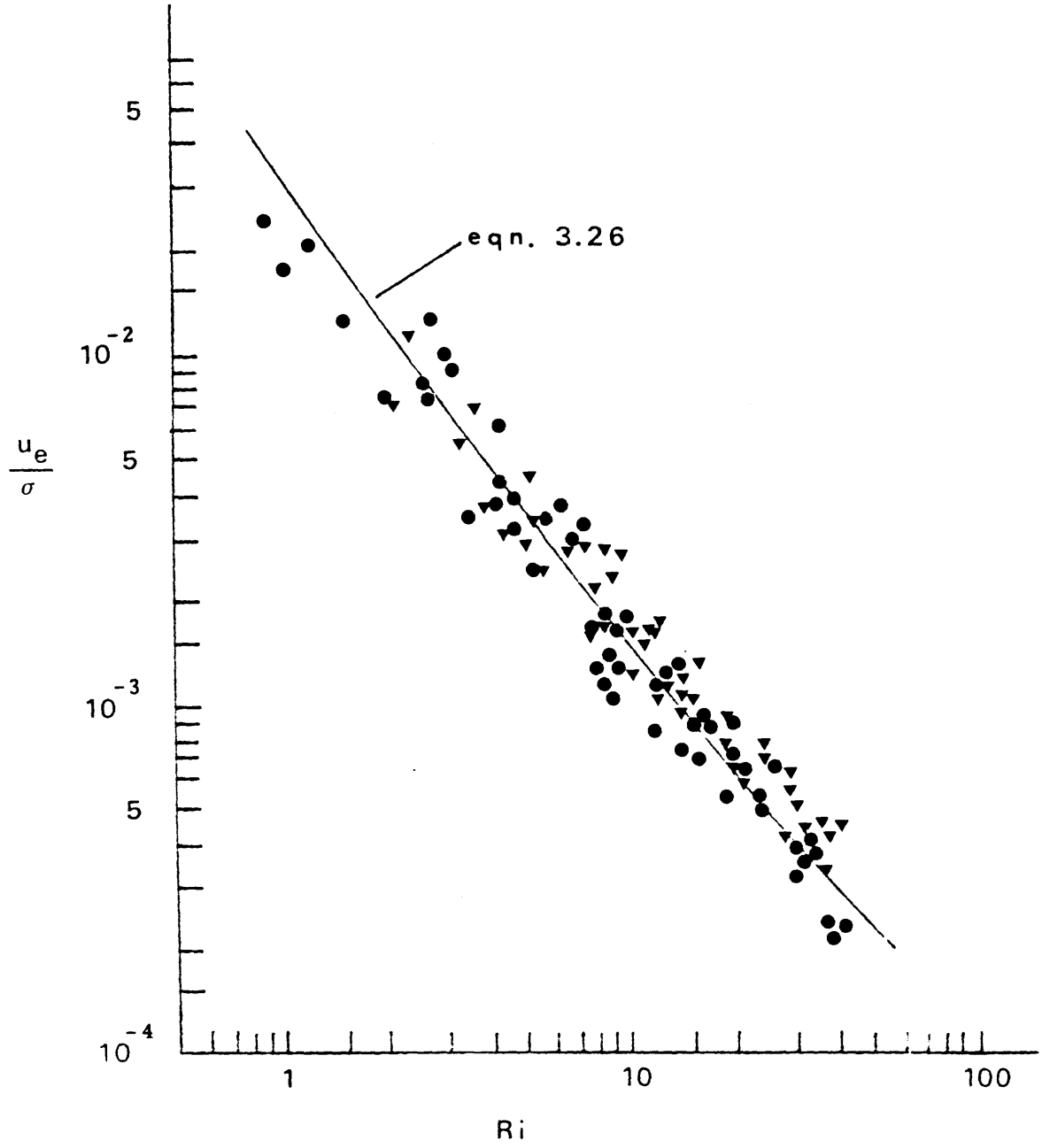

FIGURE 33 Grid Entrainment Results Using σ as the Scaling Velocity for Salt (●) and Double-Diffusive (▼) Stratification

the model developed in Chapter 3 may be used to describe these results. Eq. (3.26) is plotted in Figure 33, with $C_1 = 0.32$ and $C_2 = 0.025$ and $Pe_S = \sigma\hat{\ell}/\kappa_S = 2{,}700$. It can be seen that the data is reasonably well represented by the model. Eq. (3.26) is also plotted in Figure 32 for the temperature stratified reslults, where $Pe_T = 30$. This supports the conclusions at the end of Section 3.2.3.

CHAPTER 5

Wind-Mixing Experiment

The grid-mixing experiment described in Chapter 4 showed that double-diffusive stratification could have an effect on u_e, at least under the conditions of zero mean shear inherent in these tests. Under normal field conditions there will be a mean drift current in the upper layer due to wind shear stress or horizontal inflows and outflows, and shear-induced mixing must be considered. The discussion in section 3.3.1 suggests a possible means by which shear effects may affect u_e and it is shown that an inverse Richardson number entrainment law results when the mixing is primarily caused by turbulence shear production. This relationship (i.e., eq. 3.16) has been supported by a number of experimental results and field observations (see Sections 2.2.2 and 2.2.3). However, it has been pointed out that the range of values of Ri considered in these previous studies is significantly less than the values that might be expected in a SGSP, primarily due to the strong density stratification.

The main purpose of the wind-mixing experiments described in this chapter was two-fold--first, it was desired to check the possible influence of double-diffusive stratification on u_e under conditions with a mean shear present and second, entrainment tests were conducted under conditions where Ri was considerably higher than in previous experiments in order to see if the inverse - Ri law might

hold for solar pond conditions. A secondary part of the wind-mixing experiments, described in Section 5.3, looked at the influence that a grid of floating nets or pipes on the surface of a solar pond might have on the transfer of energy from wind to water and, therefore, on wind-induced mixed-layer deepening. The apparatus and procedure for the wind-mixing tests are described in section 5.1 and results are shown in Section 5.2.

5.1 Apparatus and Procedure

The wind-mixing experiments were conducted in a laboratory wind/wave flume, sketched in Figure 34. The total length of the flume is 31 m, though the wind tunnel covered only 25 m. The tank is 76 cm wide and 87 cm deep. The total water depth was usually 60 cm, leaving a 27 cm high air space. The wind inlet and outlet sections were made of heavy gauge aluminum and the cover consisted of 8' (2.4 m) long 3/4" (1.9 cm) plyron boards clamped along the top. Tape was used to cover all junctions of these pieces to keep the tunnel as air-tight as possible. The inlet section ended in a three-foot (91 cm) long horizontal section which had flow vanes and straighteners to smooth out the air flow. The flow straightener consisted of a close-packed array of 8" (20 cm) long, .25" (.64 cm) drinking straws glued together and wrapped with a wire mesh. The fan was located at the outlet end and sucked air through the tunnel. The wind speed was controlled by the opening of an exhaust damper on the fan and was varied from about 3.4 - 10.2 m/s at five discrete speeds.

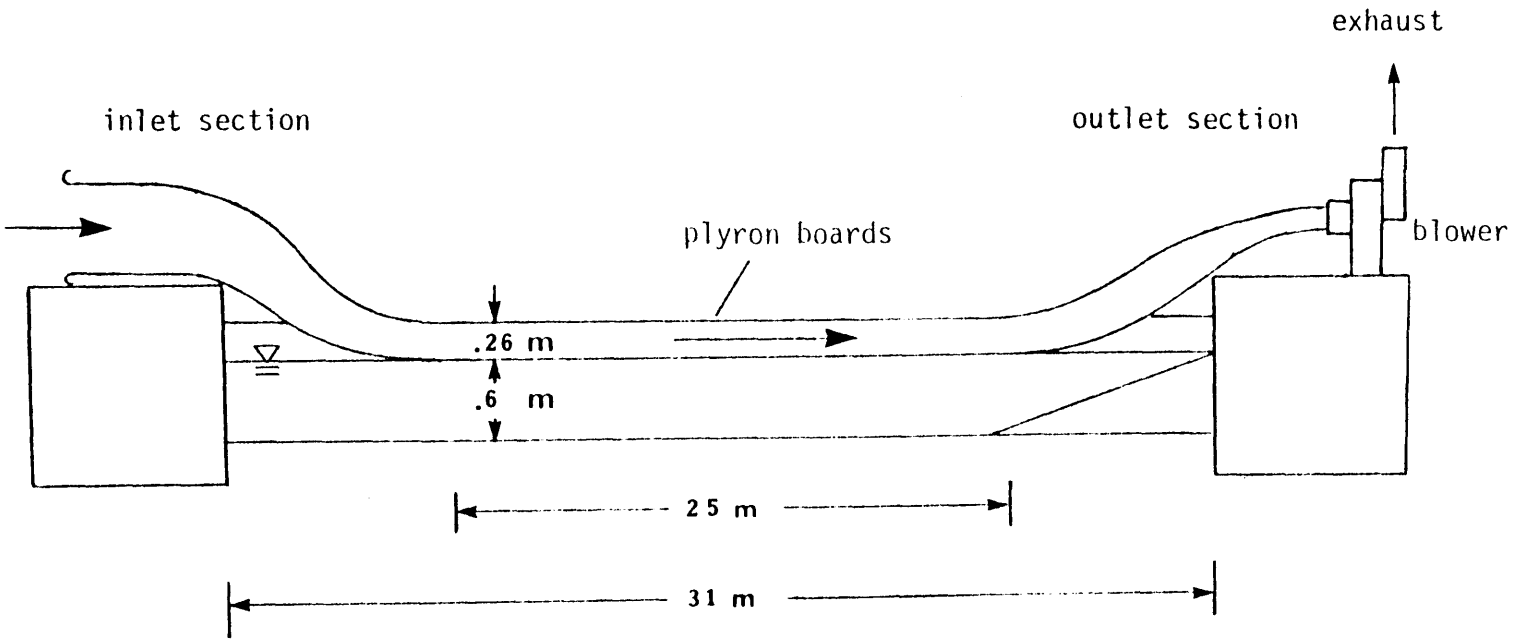

FIGURE 34 Wind-Wave Facility

Several different types of tests were conducted with this facility. The full length of the wind-wave flume was used only for non-stratified conditions and consisted of measurements of wind speed and water velocity profiles at different fetches (distances downwind from the inlet). Water velocity measurements were also taken with wave dampers in place for comparison (see Section 5.3). Density-stratified tests were conducted in shortened test sections of the flume. These consisted of entrainment tests and water velocity measurements for two section lengths, 3.5 m and 7 m. These shortened test sections were created by installing bulkheads in the flume, equal in height to the water depth, with the upwind bulkhead located at the end of the air inlet section. Wave breaking material (4" thick "horsehair" material) was also added at the downwind bulkhead. Velocity measurements were taken both with and without a density interface present so that a comparison could be made between the two sets of measurements. In particular, it was desired to measure the return current near the interface.

Water velocity data was obtained in a similar manner as in the grid experiments, but a different LDA system was used here. Again, the horizontal component only was measured. The anemometer consisted of a Lexcel Ar laser with TSI optics and electronics. This laser system operates in a counting mode and there were some problems in obtaining good data below a density interface since the rate at which particles would pass through the measuring point was very low because of the absence of strong motion below the interface. It should also be noted that data was not obtained at positions very close to the

interface (within about 1-2 cm), since the index of refraction changes caused the laser beams to deflect severely. Backscatter optics were used and the laser was mounted on a carriage which allowed movement of the measurement point in all three coordinate directions. The analog output was filtered at the Nyquist frequency as described for the grid experiments and vertical profiles of mean and r.m.s. velocities were calculated for various fetches and lateral positions.

The usual procedure for measuring vertical velocity profiles consisted of recording data records of length 10 seconds and sampled at 200 Hz for each measurement point. The laser was then lowered to the next measurement location and data was sampled. Mean and r.m.s. velocities were then calculated for each record. This procedure was then repeated a short time after the first profile was recorded to check the accuracy of the measurements. Since a 10-second record length is probably too short to calculate a representative mean value, especially when there is some density stratification, several measurements were also made in which data was sampled at 1 Hz over 5 minutes. These last measurements were of particular interest in determining mean drift currents near the interface (note that the interface position changes very little -- O(1 mm) in 5 minutes). Power spectra were not calculated for these velocity measurements since the sampling frequency would have to have been considerably higher in order to obtain reasonable spectral estimates. This was not practical in the present experiments due to the large number of measurement points used.

Surface drift velocities were estimated by timing the passage of small floats past two points a known distance apart. However, there is some uncertainty in these measurements because the floats were hard to see and sometimes they were not right at the surface. The timing process also has some uncertainty due to the width of the channel. Water velocity measurements were taken with the LDA, but data could not be obtained very close to the surface because of waves and it is difficult to extrapolate to the surface. With these uncertainties in mind the estimates for drift current are plotted in Figure 35.

Air speed measurements were made using a small Pitot-static tube connected to an M.K.S. Baratron pressure transducer with a metered output. The vertical position of the probe was controlled and measured by connecting it to a point gauge. Small sampling holes were drilled in the wind tunnel cover at different fetches along the center line to check the longitudinal development of the mean wind speed profile. Lateral profiles were also measured by moving the probe along the small space at the junction of two cover pieces. The wind speed near the cross-sectional center was found to increase with fetch as boundary layers developed along all four boundaries. Five different wind speed settings were used, each characterized by the areally averaged speed measured near the inlet (where the profiles were closest to being uniform). These five speeds were W = areally averaged wind speed = 3.4, 4.4, 6.1, 7.8, and 10.2 m/s, obtained by averaging vertical profiles for five lateral positions (Figure 36).

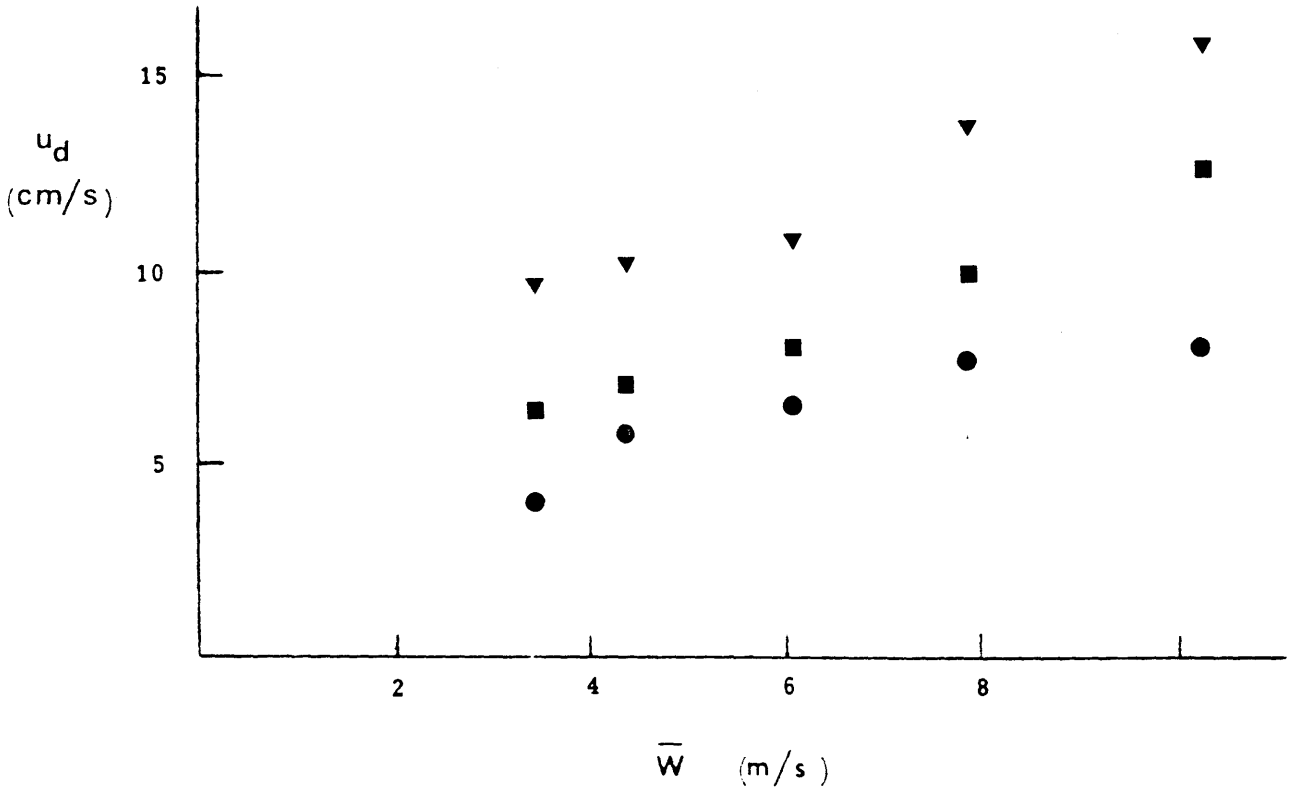

FIGURE 35 Average Surface Drift Currents As a Function of Wind Speed; ● 3.5 m Section, ■ 7 m Section, ▼ Measurements Taken at a Fetch of 5 m Without Bulkheads In Place

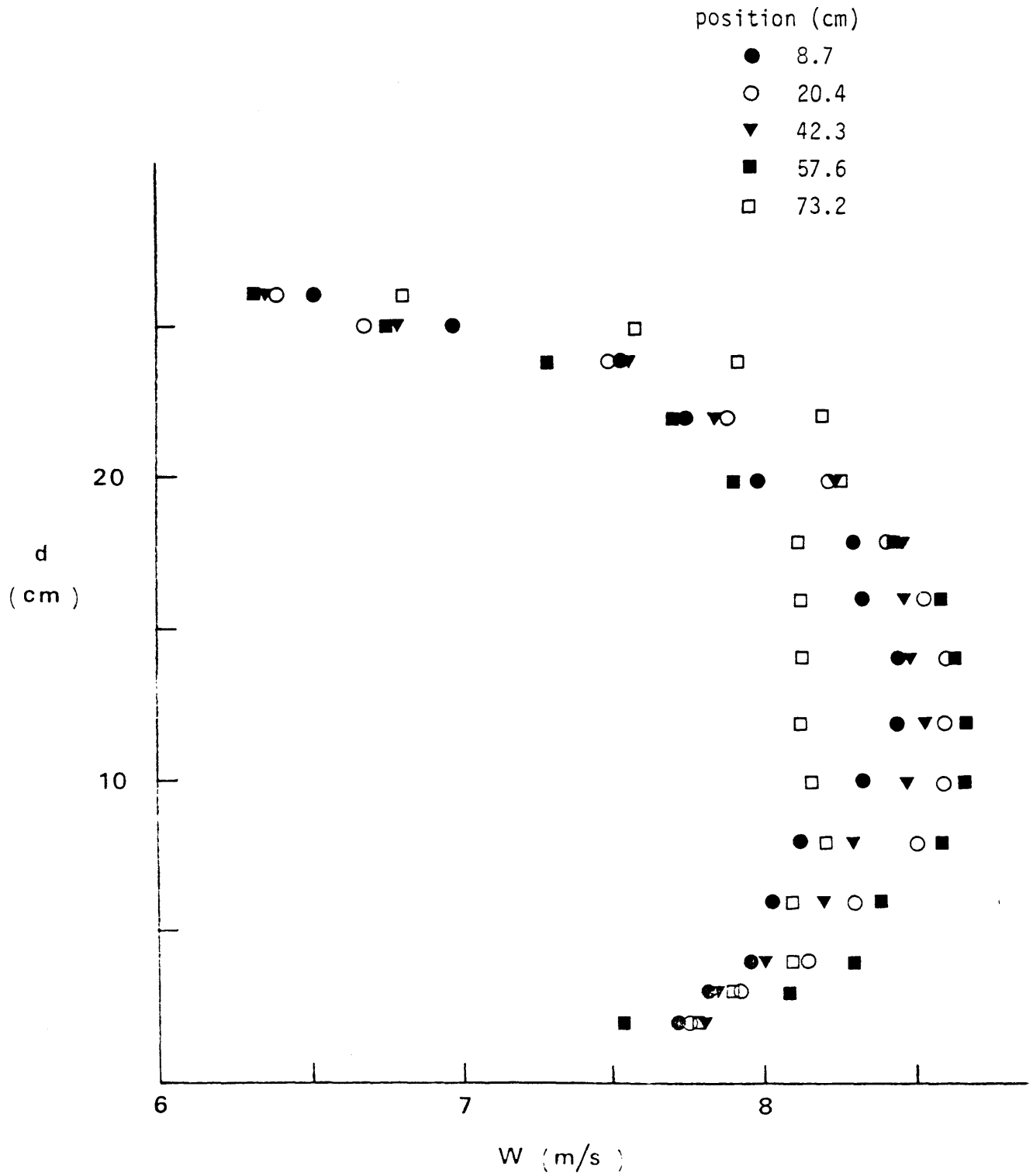

FIGURE 36 Example of Vertical Wind Speed Profiels Measured at 5 Different Lateral Locations at a Fetch of 3.3 m; Position is Noted as Distance From Side Wall of the Flume, With the Total Width Being 76 cm

Lateral profiles at a set vertical position were also measured at different fetches. For example, lateral profiles for W = 7.8 m/s are shown in Figure 37. The depression in the center of the profiles for low fetch is due to a pin in the inlet section which controlled the opening of the tunnel. This depression was not noticeable at greater fetches.

The air friction velocity was obtained as a function of fetch by fitting a logarithmic curve to the vertical air speed profile data taken along the centerline at various fetches. That is, a logarithmic velocity profile is assumed,

$$\frac{W}{u_{*_a}} = \frac{1}{\kappa} \ln\left(\frac{z}{z_o}\right) \tag{5.1}$$

$$\Rightarrow W = \frac{u_{*_a}}{\kappa} [\ln(z) - \ln(z_o)] \tag{5.2}$$

where u_{*a} = air friction velocity, W = wind speed, κ = von-Karman constant and z_o = virtual origin (related to roughness). Plotting W versus log z should then give a straight line with a slope of u_{*a}/κ and intercept at $-u_{*a}$ log zo/κ. Figure 38 shows results of these calculations for measurements at a fetch of 5.8 m. Unfortunately, it was impossible to obtain wind speed measurements very close to the water surface, particularly at larger fetches. This was due primarily to the waviness of the surface and, at higher wind speeds, to spray blown off of the waves which tended to clog the Pitot tube. There is some uncertainty in the calculations for

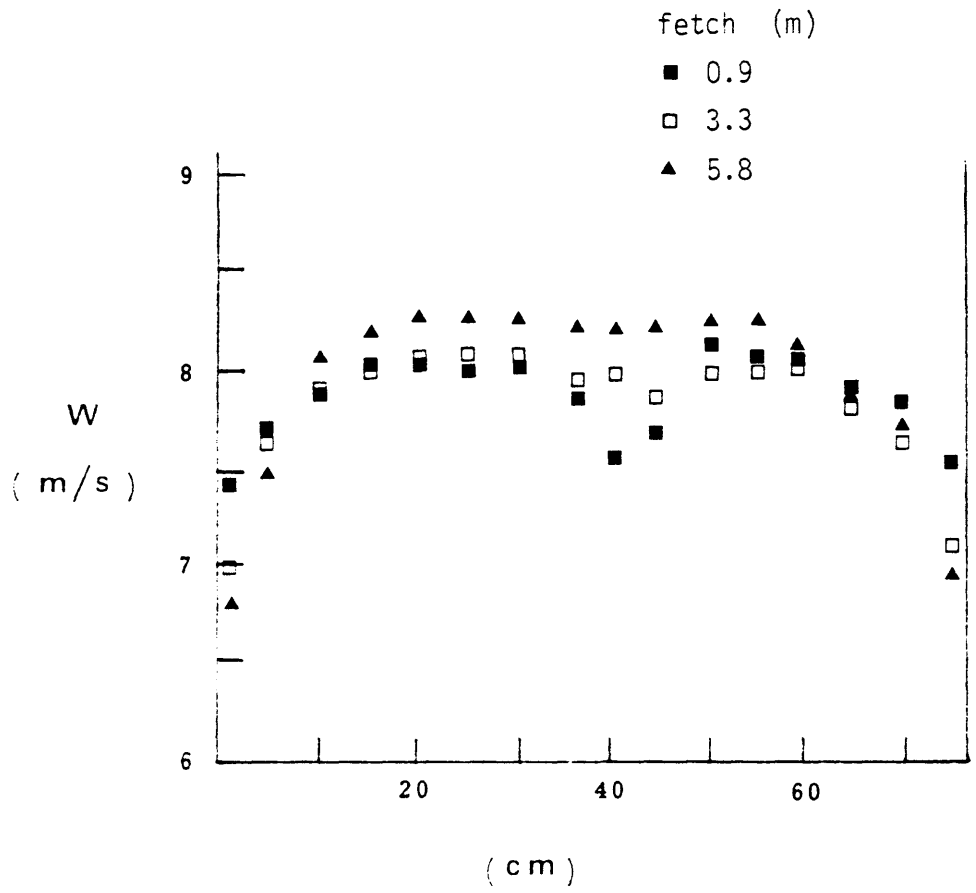

FIGURE 37 Example of Lateral Wind Speed Profiles Measured at 5 cm Above The Water Surface

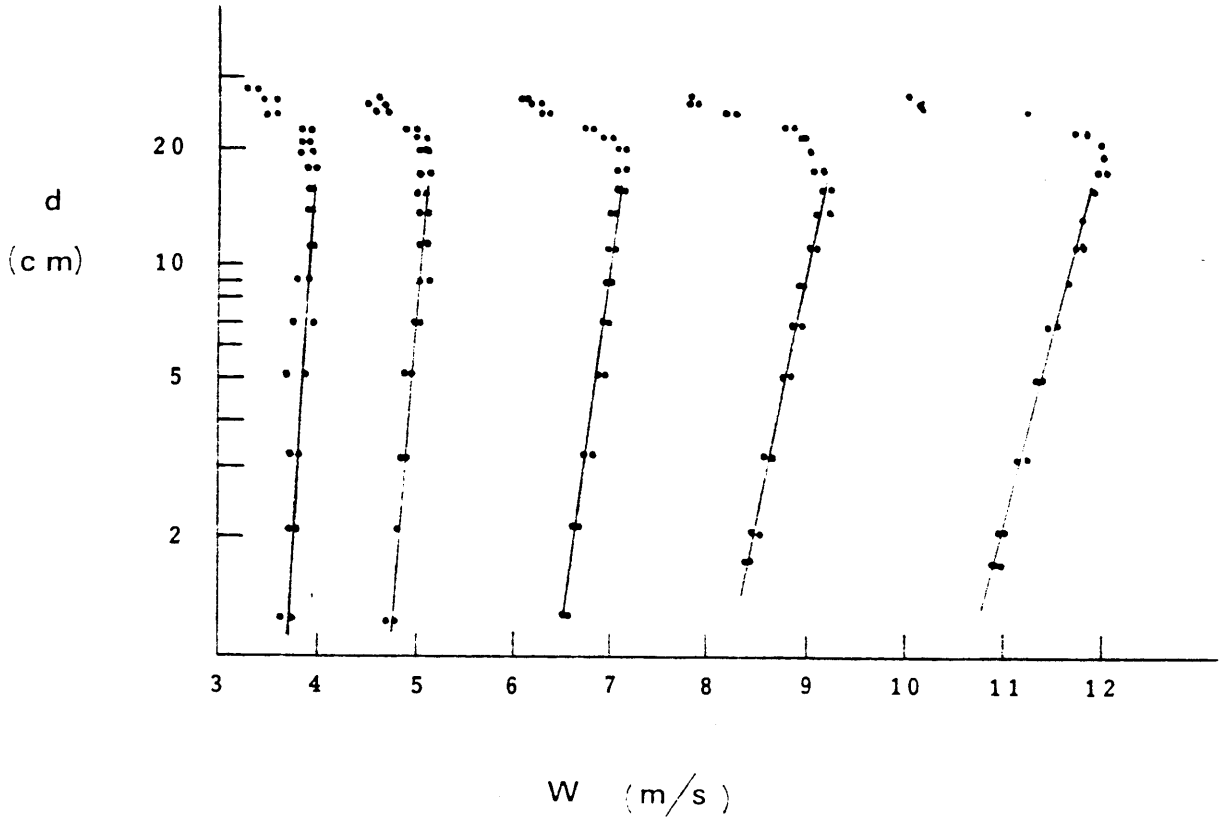

FIGURE 38 Determination of u_{*a} For Each of the 5 Wind Speeds, Measured at a Fetch of 5.8 m

u_{*a} because of this, but the log fit to the rest of the data is very good, as seen in Figure 38. u_{*a} is plotted as a function of X (fetch) in Figure 39 for the five wind speeds. The increase in u_{*a} with increasing X can be attributed to the increasing roughness resulting from the growing waviness of the surface. Power-law fits were made for each wind speed and u_{*a} could be evaluated at any fetch. Average values of u_{*a} were then calculated for the shortened test sections by taking the area under the appropriate curve in Figure 39 between zero and the section length and dividing by the section length.

The variation of u_{*a} with lateral position was also checked at several fetches. For example, Figure 36 shows vertical wind velocity profiles measured for five lateral positions at a fetch of 3.3 m. There is some decrease in velocity very near the walls, but the flow appears to be fairly uniform over much of the tunnel width. A laterally averaged value for u_{*a} was calculated by first finding u_{*a} for each of the individual profiles using the same procedure as described above (eqs. 5.1 and 5.2). The shear stress $\tau = \rho_a u_{*a}^2$ was then calculated for each lateral position and averaged over the width. The average value for u_{*a} was then calculated as $\bar{u}_{*a} = (\bar{\tau}/\rho_a)^{1/2}$, where $\bar{\tau}$ is the averaged value of τ. For small values of fetch ($X \lesssim 5$ m), the value for $\bar{u}_{*a}$ was very close to the value of u_{*a} determined along the centerline. For larger fetches $\bar{u}_{*a}$ appeared to be somewhat smaller than the certerline value, but this relation was not checked in detail (lateral profiles were not measured for large fetch). Therefore, values of u_{*a} for the

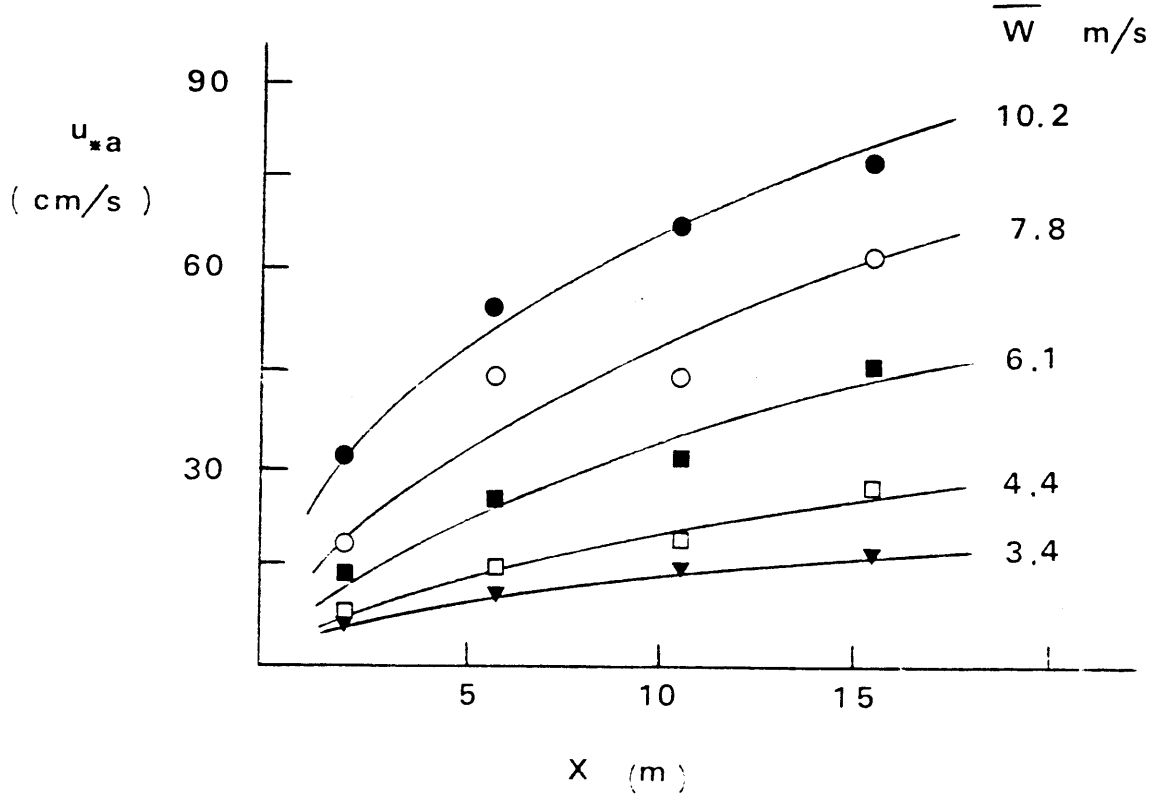

FIGURE 39 Variation of u_{*a} With Fetch

shortened test sections are assumed to be representative of average values (at a given fetch), but there is some uncertainty in the values for larger fetches.

The friction velocity for water u_* was calculated from the longitudinally averaged value for u_{*a} by assuming that the shear stress was constant across the surface, i.e., $\tau=\rho_a u_{*a}^2=\rho_o u_*^2$. This assumption neglects the portion of the shear stress that is used to generate waves (form drag). In the short test section there was not sufficient fetch for waves to develop to any significant degree and even in the longer test section waves developed primarily only for the higher wind speeds. The above assumption is then a fair approximation for the present tests. Average values of u_{*a} and u_* are shown in Figure 40 for the two test sections for each of the wind speeds considered.

5.1.1 Entrainment Tests

Entrainment tests were conducted for two-layer stratification for both test sections and three different wind speeds, 4.4, 7.8 and 10.2 m/s. Two kinds of stratification were considered: (i) Salt stratification only and (ii) "diffusive" stratification (lower layer is warmer and saltier). The stratification was achieved by first filling the lower layer with a solution of desired salinity and temperature. Heating was done by adding hot water initially or by injecting steam into the lower layer. The upper layer, usually about 10 cm deep before mixing was initiated, was then carefully poured on top. Filling of the upper layer was also accomplished by allowing water to overflow the downwind bulkhead; the wave-breaking material

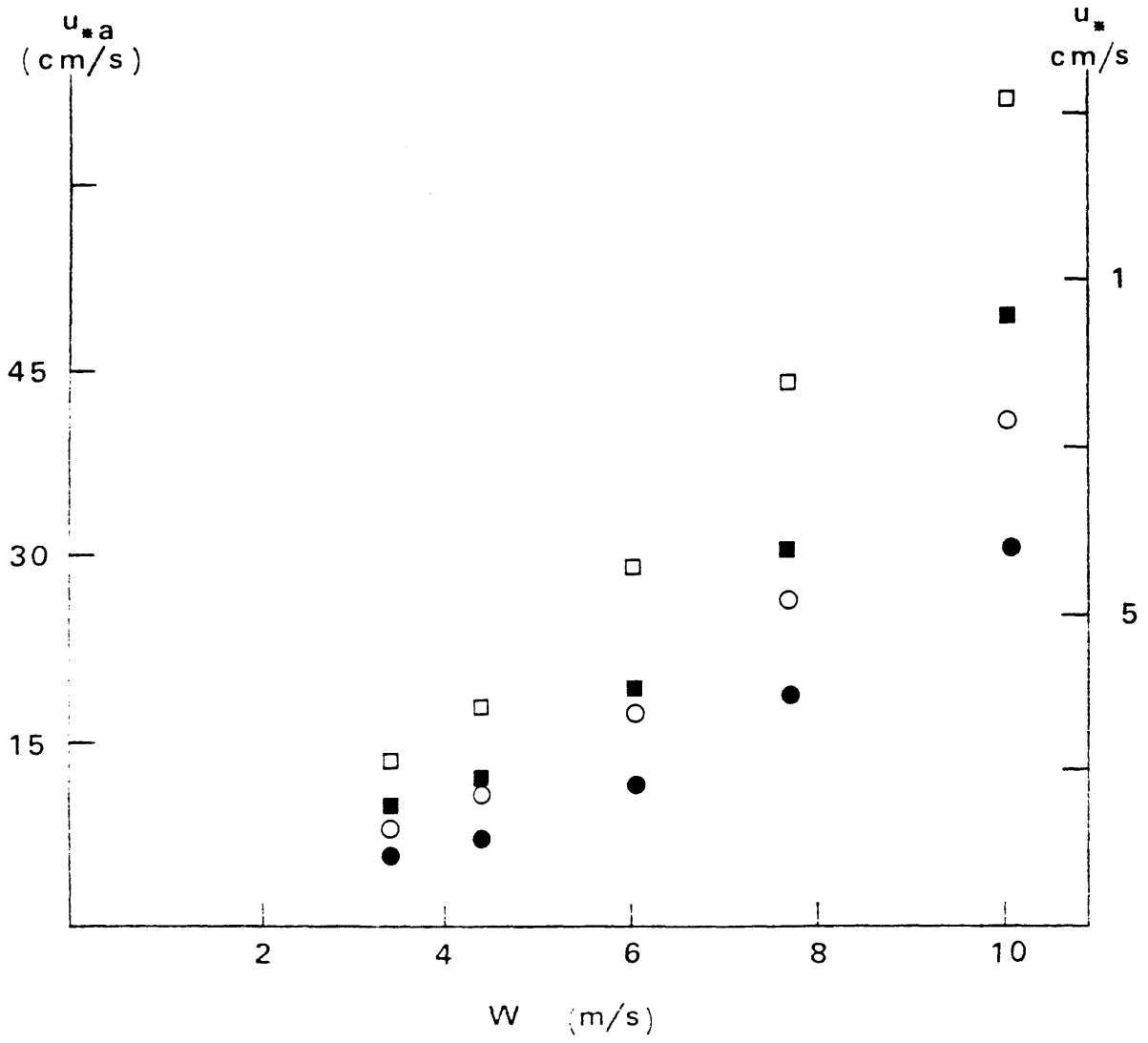

FIGURE 40 Average Friction Velocities For the 2 Test Sections; Circles Represent u_{*a} and Squares Represent u_*; Solid Points Are For the 3.5 m Section and Open Points Are For the 7 m Section

there allowed water to be added without very much mixing. In practice an interfacial thickness of about 0.5 - 1 cm was evident after filling.

Wind was applied by turning the blower on and slowly (over several minutes) opening the exhaust damper from an initially closed position to the desired position. This procedure reduced the effects of an impulsive start, manifested primarily in strong wave motion and mixing along the interface. Depending on the light in the lab, the interface was usually visable by eye simply because of the strong index of refraction change due to salt in the lower layer. However, experiments were also done in which either the upper or lower layer was dyed in order to see the interface more clearly. Vertical salinity and temperature profiles were also monitored using the same probes described for the grid experiments (see Appendix D). It was found that the rate at which the interface moved downward could be determined equally well by either method (i.e., visually, or by profile measurements).

As expected, the interface was observed to tilt when wind stress was applied to the surface, with the degree of tilt depending on the density difference across the interface and on wind speed. In addition an intermediate layer developed just underneath the main interface in the upwind portion of the test section, as sketched in Figure 41. A similar intermediate layer was described by Kit et al. (1980). When one of the layers was dyed it was easily visualized as a region of lighter color, normally in a wedge-like shape as shown in Figure 41. It was also evident by comparing salinity profiles taken

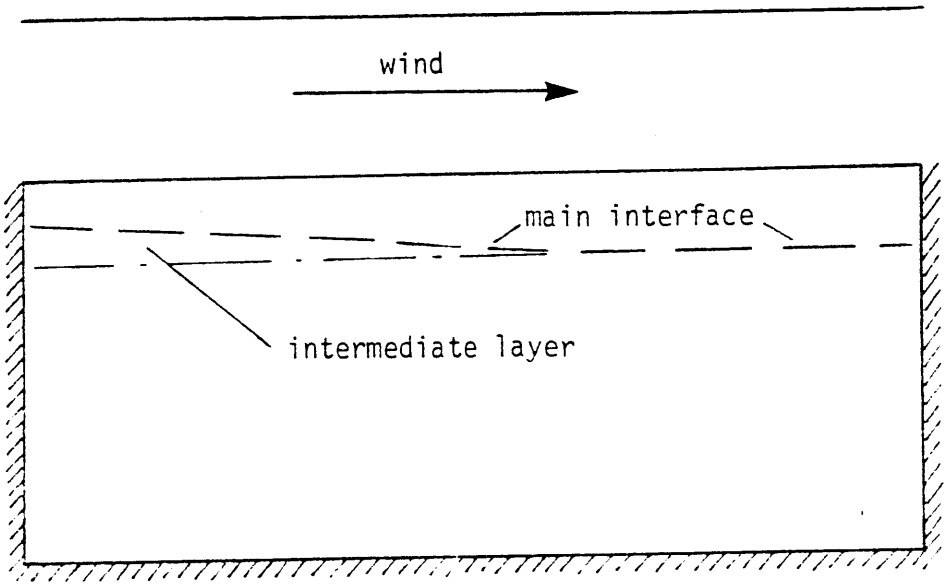

FIGURE 41 Stratification Set-Up During Wind-Mixing Tests

at different positions in the test section (Figure 42). Normally the intermediate region was confined to the upwind half of the test section, but for experiment runs longer than about 1 1/2 - 2 hours it was observed to start creeping towards the downwind end.

Interfacial positions were obtained both from probe outputs and also visually as noted above. Tape measures were placed at three (3.5 m section) or five (7 m section) positions along the test section and interfacial positions were noted at each station for each time reading. An average reading was then obtained and plotted with time in order to estimate the rate of deepening. Unlike the grid-mixing results where u_e was found to decrease with increasing h, the wind-induced entrainment rate was nearly constant (see Figure 43), at least over the time period of the experiments. Entrainment results were also obtained from density profile measurements taken in the center of the test section, by marking the position of the maximum density gradient as a function of time. An example of the temporal development of the salinity profile is shown in Figure 44. Note that the lower side of the interface becomes more diffuse with increasing time. Interfacial position was marked at the top of the interfacial region except in the region of the intermediate wedge layer, where the interface position was recorded as the position of the bottom of the intermediate layer.

5.2 Results and Discussion

Before discussing the quantitative results of the entrainment experiments, several qualitative observations are noted. First, as

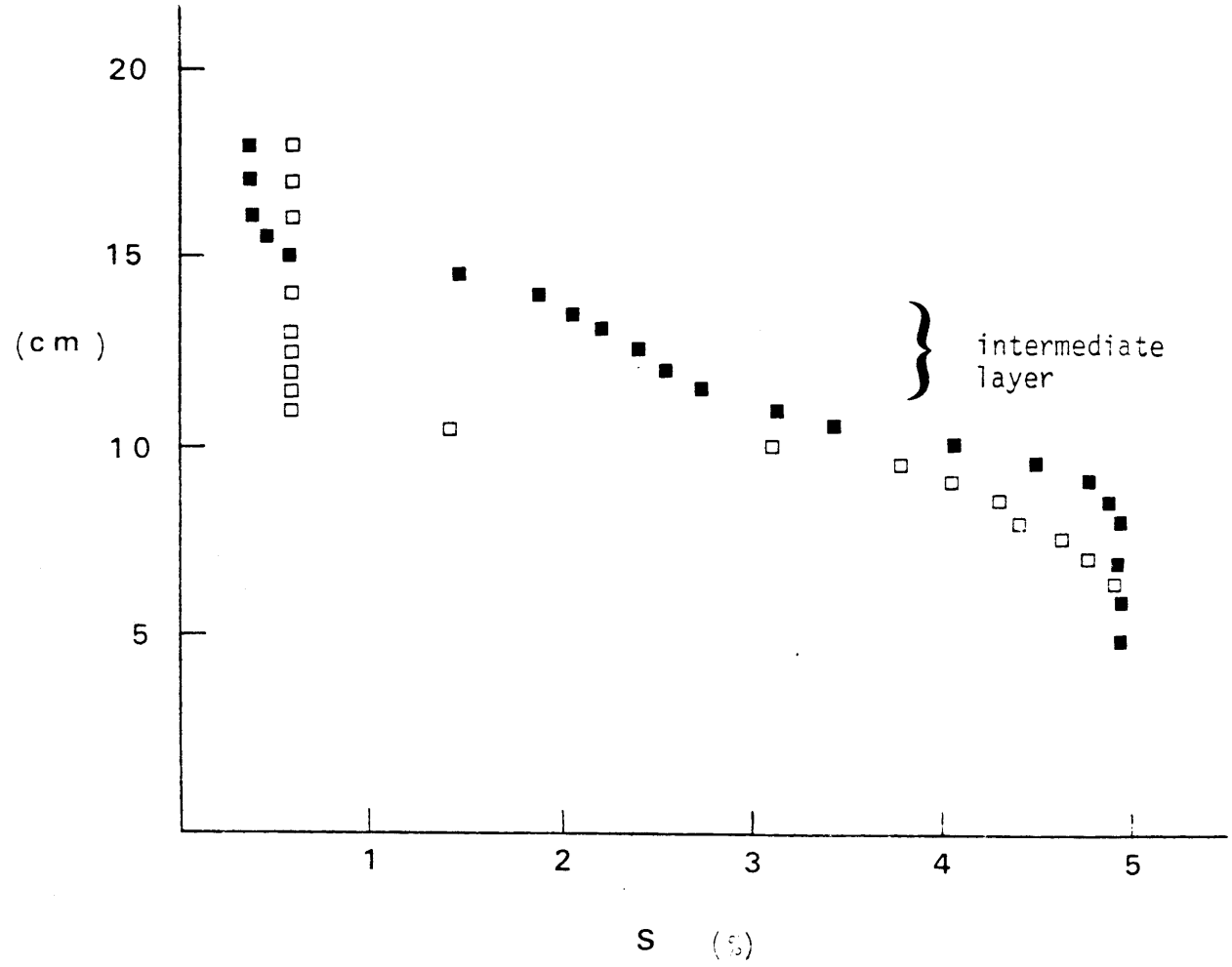

FIGURE 42 Comparison of Salinity Profiles Measured At Fetches of 2 m (■) and 4.4 m (□) in the 7 m Section

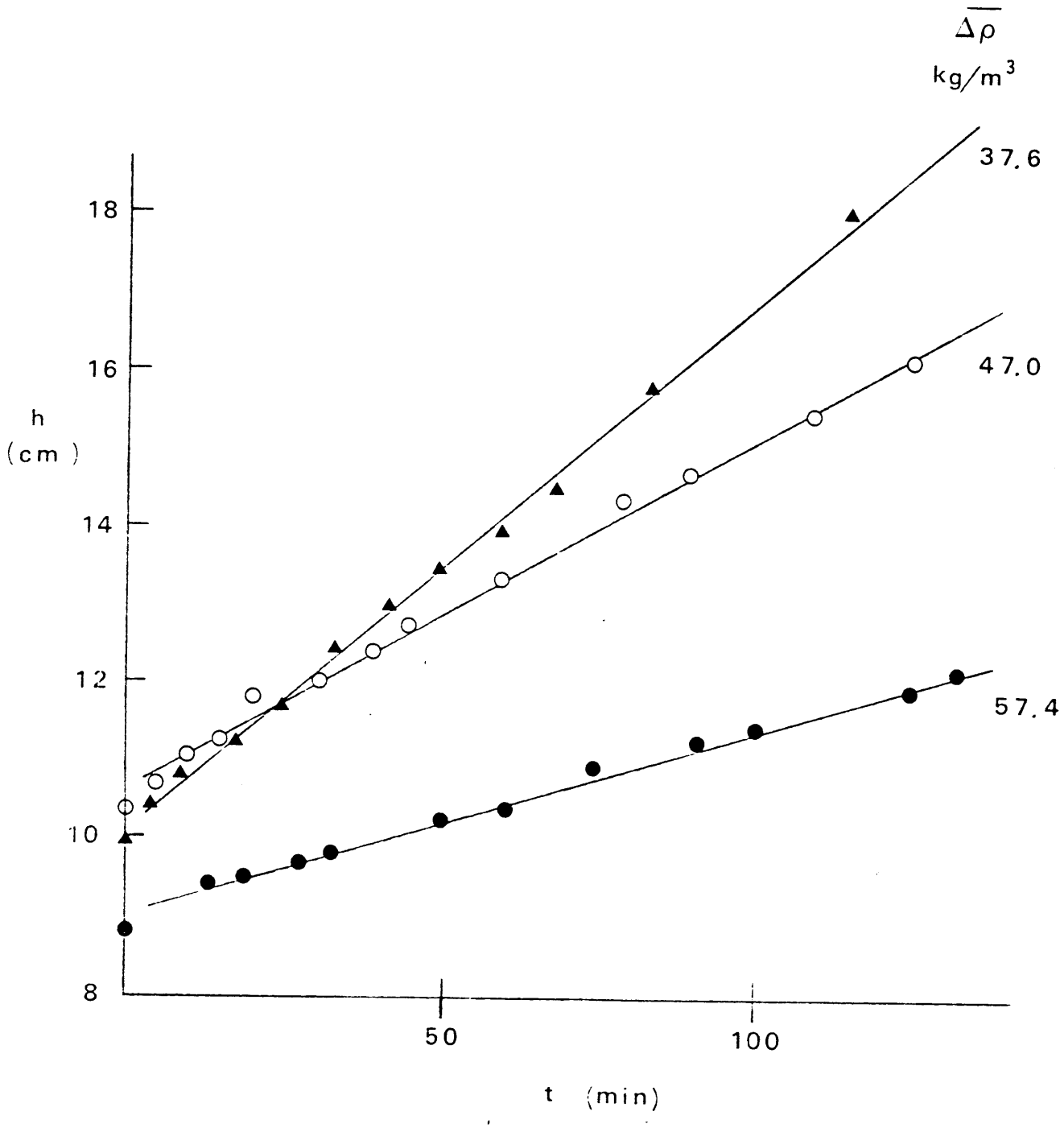

FIGURE 43 Examples of Growth of Mixed Layer for the Wind-Mixing Tests

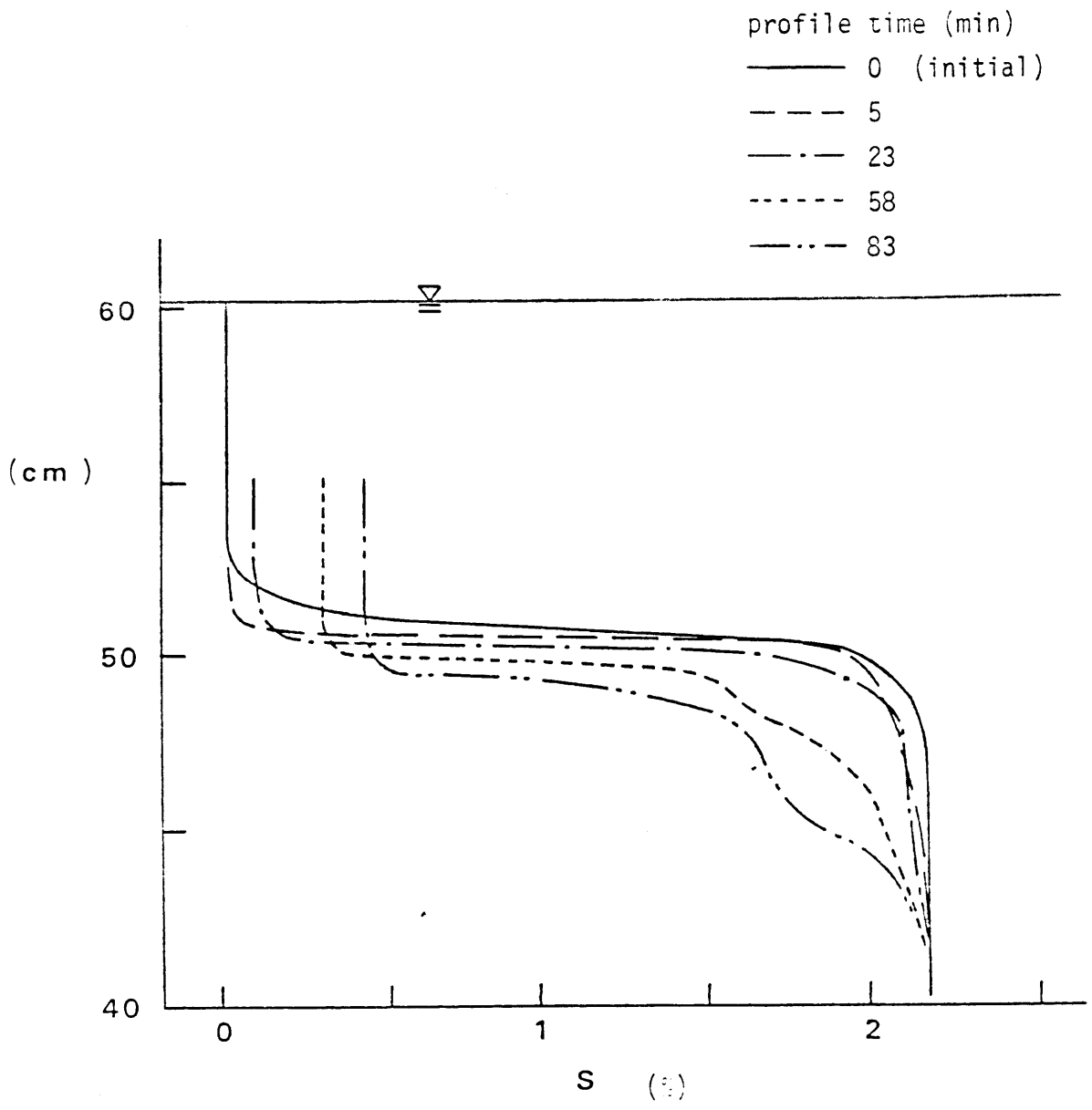

FIGURE 44 Temporal Development of Salinity Profile Measured At The Center of The Test Section

described above, a wedge-shaped layer with density intermediate between the densities of the upper and lower layers was observed for the wind-mixing tests (Figure 41).

Much of the development of the wedge appeared to occur during the initial tilting of the interface when wind was first started. This initial tiling occurred as a wave-like motion traveling from the downwind end towards the upwind end. Upon contact with the upwind bulkhead the wave would break and cause some local mixing (a portion of the wave was also observed to be reflected back along the interface). This resulted in a region of intermediate density occupying a space just under the main tilted interface near the upwind bulkhead which then assumed the wedge-like shape. The initial mixing was reduced with very gradual application of wind stress (damper opened very slowly), but an intermediate layer was always present in these experiments and grew slowly in time. This appeared to be an effect of the presence of the vertical bulkhead, as return flow along the interface would hit the wall and some of it would be directed downward, adding to the intermediate layer.

Flow along the interface was easily visible by eye, again because of the strong refractive index change. In addition, velocity measurements were made with the LDA, though it was not possible to obtain data closer than about 1 - 2 cm from the interface because of index of refraction fluctuations. The laser measurements are discussed below. Qualitatively, a surface drift current developed under the action of the wind stress and appeared to turn under at the downwind bulkhead and start flowing back along the interface. What

appeared to be a predominantly two-dimensional flow started to be established, but very quickly (within several minutes) broke down into a complicated three-dimensional pattern. Figure 45 shows the modes of circulation that were observed. The pattern in Figure 45(b) was quite stable for the 3.5 m test section, though the pattern in Figure 45(c) was prevalent in the 7 m section and was also observed in the shorter section. In addition, there were sometimes changes in the flow pattern longitudinally, where the flow would turn in a lateral sense. This depended somewhat on wind speed.

Specification of the induced flow constitutes a complicated problem in itself and this is not attempted here. The presence of the end walls creates a situation which is probably not very realistic for applying results to field conditions. In particular, the same return flow patterns would usually not be expected to be established in the field, not only because of the much reduced fetch of the laboratory model, but because it would be very rare to have a steady wind blowing over the entire surface of a large pond for any appreciable length of time. Previous investigators have used the friction velocity associated with wind shear stress to scale their results and found that their entrainment rates were lower than the rates for experiments without end walls; this was attributed to the increased complexity of the flows with end walls which resulted in increased dissipation of energy which might otherwise be used for entrainment (see Section 2.2.2). A comparison of the present results with some previous experiments shows a similar behavior (see Figure 46b). Note that the present results show some increase in u_e with

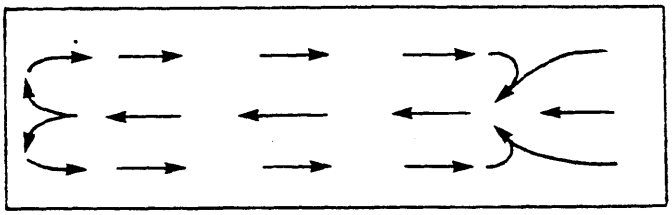

a

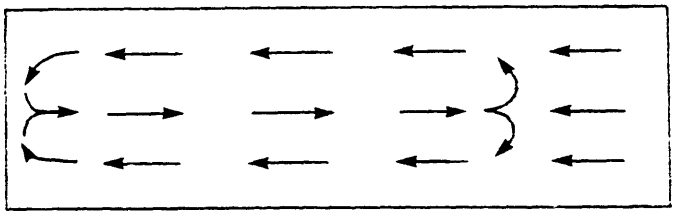

b

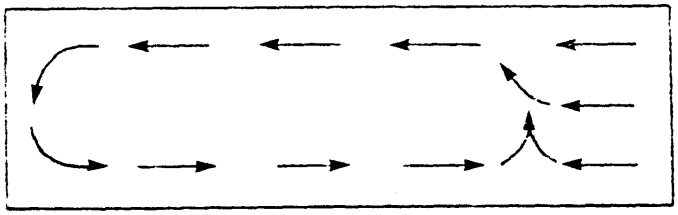

c

FIGURE 45 Plan View Showing 3 Different Return Flow Patterns Observed Along the Interface, For Wind Moving Left To Right

increasing fetch, (conditions for the previous experiments shown in Figure 46b are listed in Table 2).

5.2.1 Velocity Measurements and Scaling of Results

Unlike the grid experiment where energy is transported away from the grid by a diffusive process, there are larger eddies in the wind-mixing tests which will scale on the entire upper mixed layer depth. h then provides the proper length scale for this set of experiments.

Velocity measurements made with the LDA for the entrainment tests include both stratified and unstratified conditions for the 3.5 m and 7 m sections. Mean and r.m.s. horizontal velocities were calculated for each measurement point and vertical profiles were taken at various longitudinal and lateral positions within both test sections. Section 5.1 describes the procedure used for these measurements.

A preliminary scaling of the data is shown in Figure 46, where u_* was used as the scaling velocity. This allows a comparison with some earlier experiments (Figure 46b). It is interesting to note that the results for salt stratification and double-diffusive stratification show no difference--this point is discussed further below. Due to uncertainties regarding the surface stress continuity assumption and also because the energy available at the interface may not be the same as the energy at the surface, it was decided, following the grid experiments, to use the r.m.s. velocity measured under non-stratified conditions and corresponding to the mixed layer depth. The results using this scaling are shown in Figure 47.

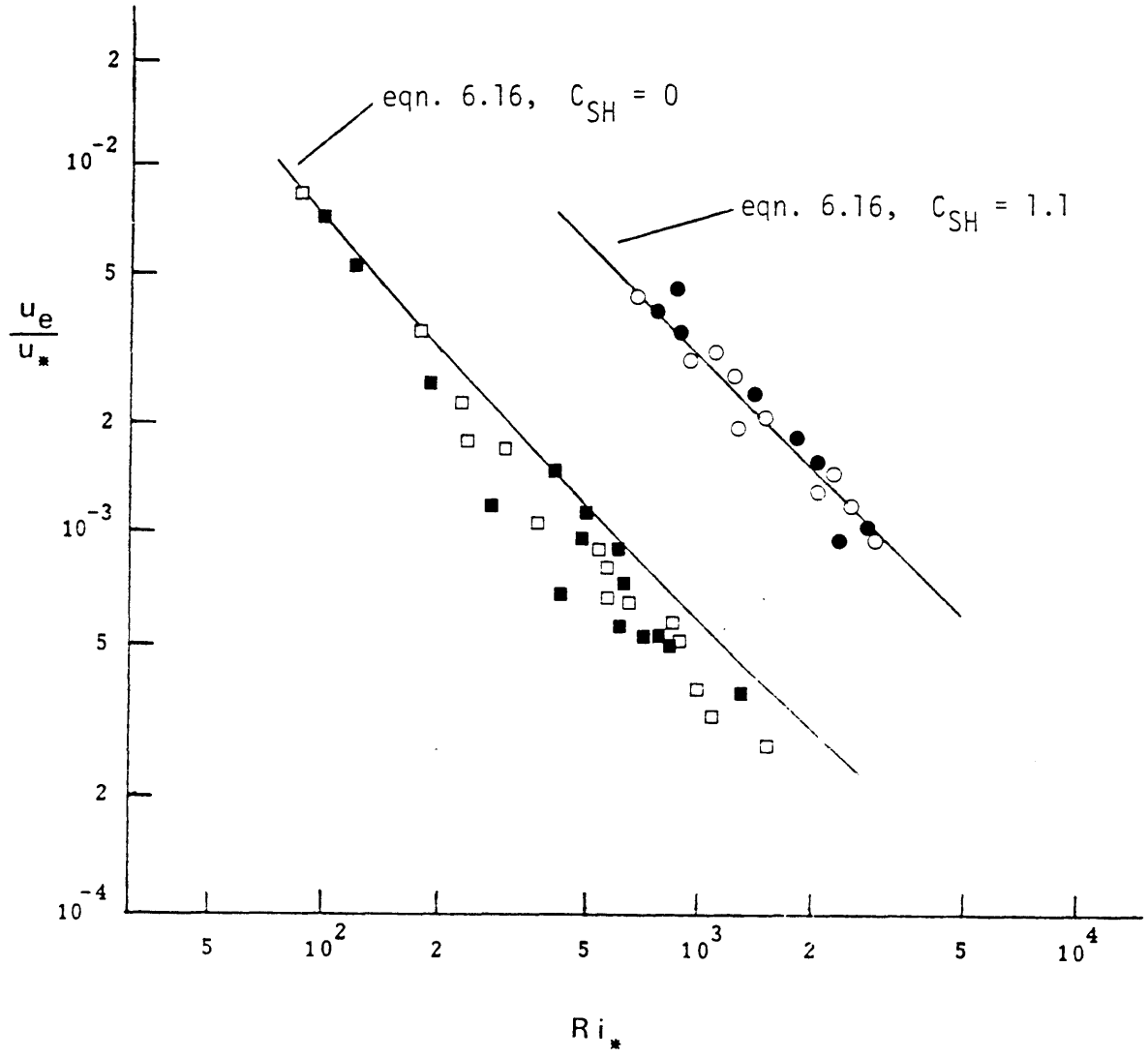

FIGURE 46 u_e/u_* vs. Ri_* For the Wind-Mixing Tests; Solid Points Represent Salt Stratification and Open Points Represent Double-Diffusive Stratification; Squares Represent Data From the 3.5 m Section and Circles Are From the 7 m Section

a) Comparison of Data With Eqn. (6.16)

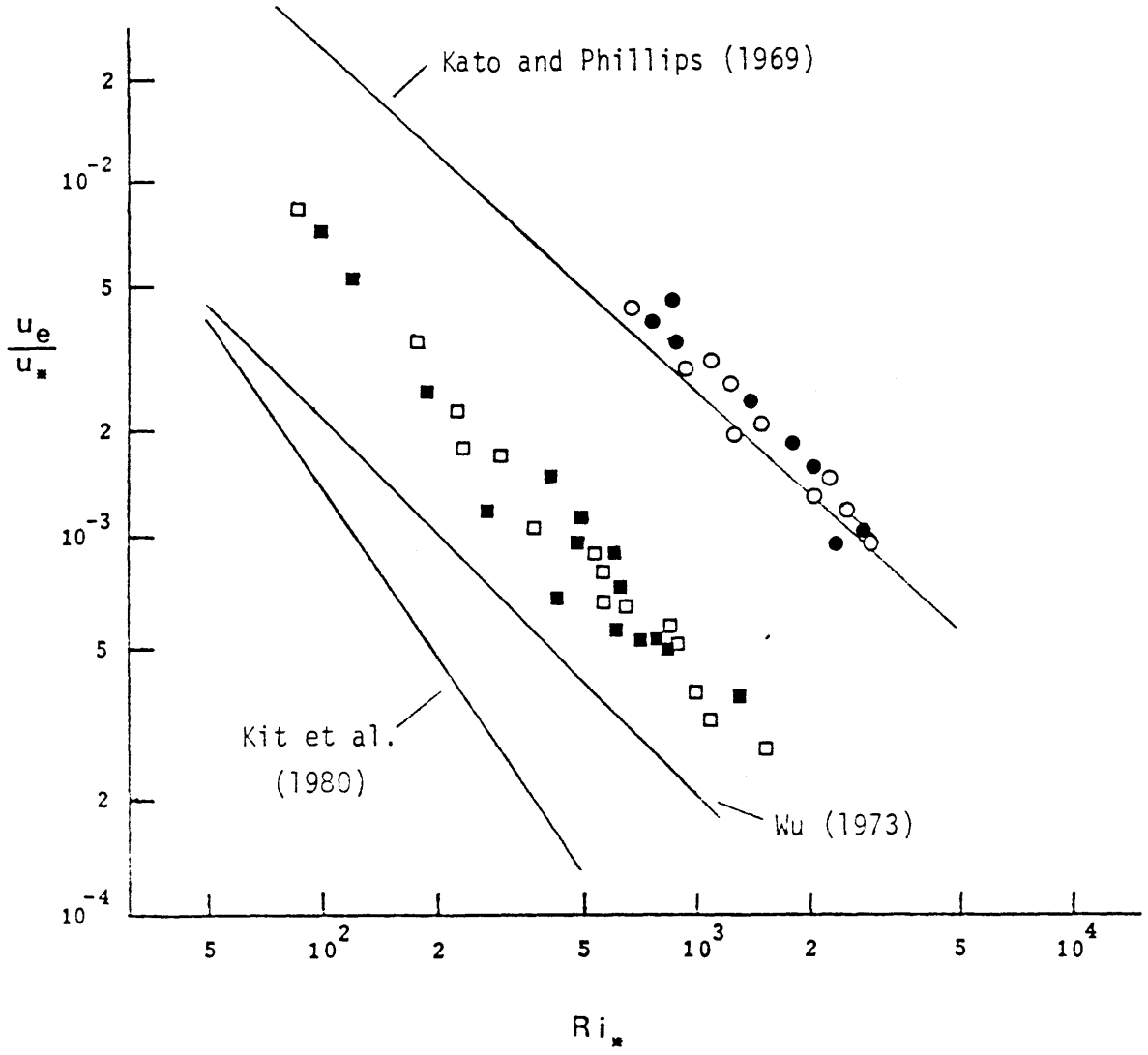

FIGURE 46 (continued)
b) Comparison of Data With Some Previously Reported Relationships (See Table 2)

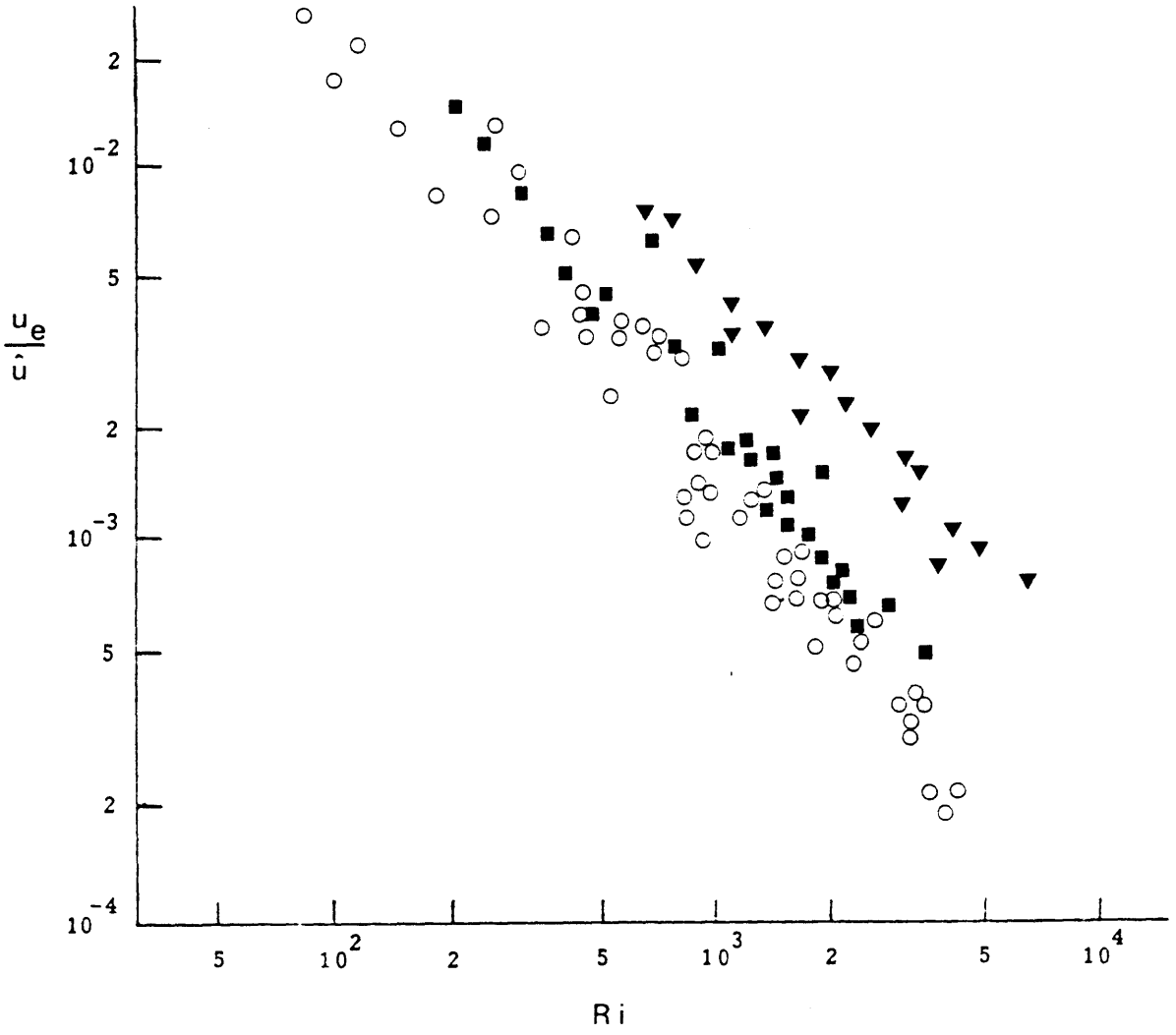

FIGURE 47 $u_e/\hat{u}$ vs. Ri; O Grid Results, ■ 3.5 m Section, ▼ 7 m Section

However, as seen in Figure 48, the r.m.s. velocity remains approximately constant after an initial sharp decrease near the surface. This initial decrease may be attributed to the decay of the wave orbital velocities,observed by monitoring the laser signal with an oscilloscope. The relative constancy of the r.m.s. velocities below the surface region is probably due to larger scale motion associated with the mean flow which tends to mix the layer and transports more energy downward. It is not surprising that the results in Figure 47 are qualitatively similar to those of Figure 46 for the two test sections.

Figure 47 also includes results from the grid experiment for comparison. There is a definite progression in the results, with the lowest entrainment rates associated with the grid and the highest rates associated with the longer test section. This appears to be a function of the presence of mean shear at the interface or, more generally, a function of fetch. That is, stronger mean motion would be expected for larger fetches. Then, if shear production is responsible for entrainment, faster entrainment rates would be expected for larger fetch. Measurements of mean velocity in the two test sections with an interface present did show stronger motion for the longer test section, as shown in Figure 49. An alternative scaling of the wind results is then with the mean return velocity near the interface. Values for u_r (near the interface) were averaged over all measurements taken for a given wind speed for each test section and are shown in Figure 50. Entrainment results, normalized with these values for u_r, are shown in Figure 51, where it can be seen that there is greater similarity in the results for

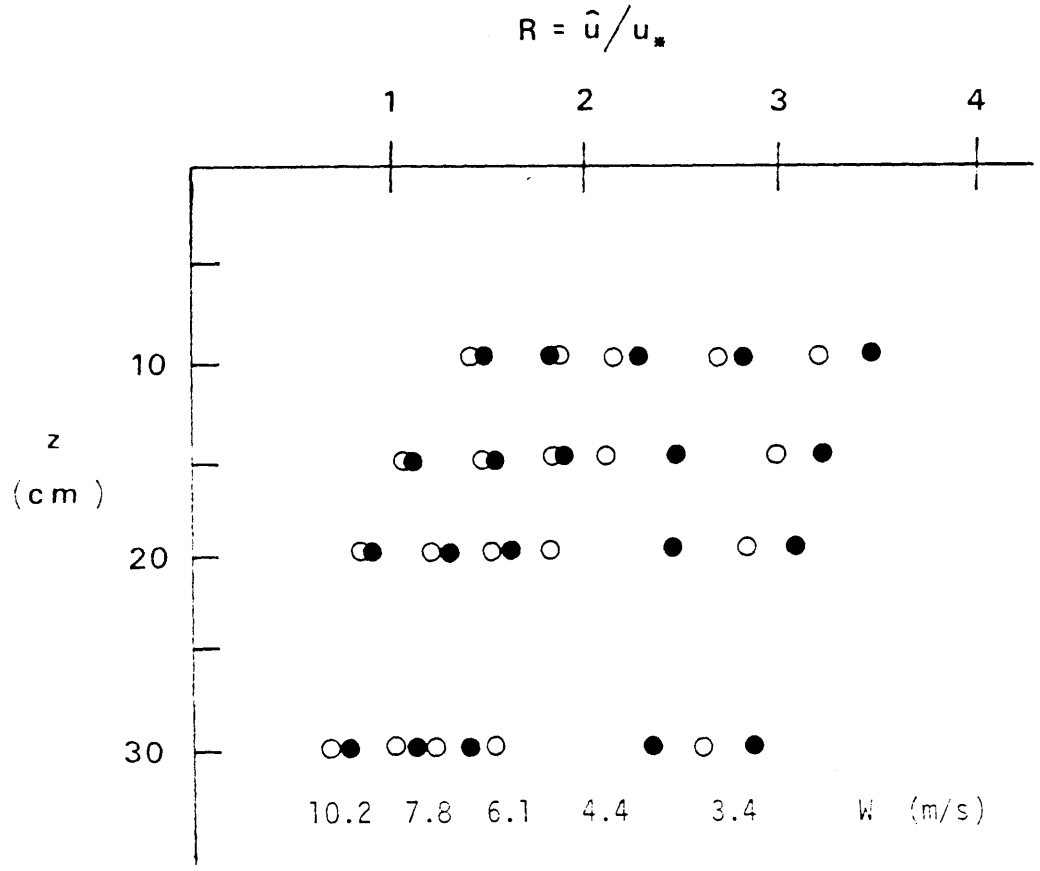

FIGURE 48 Relationship Between $\hat{u}$ and u_* For ● 3.5 m Section and ○ 7 m Section

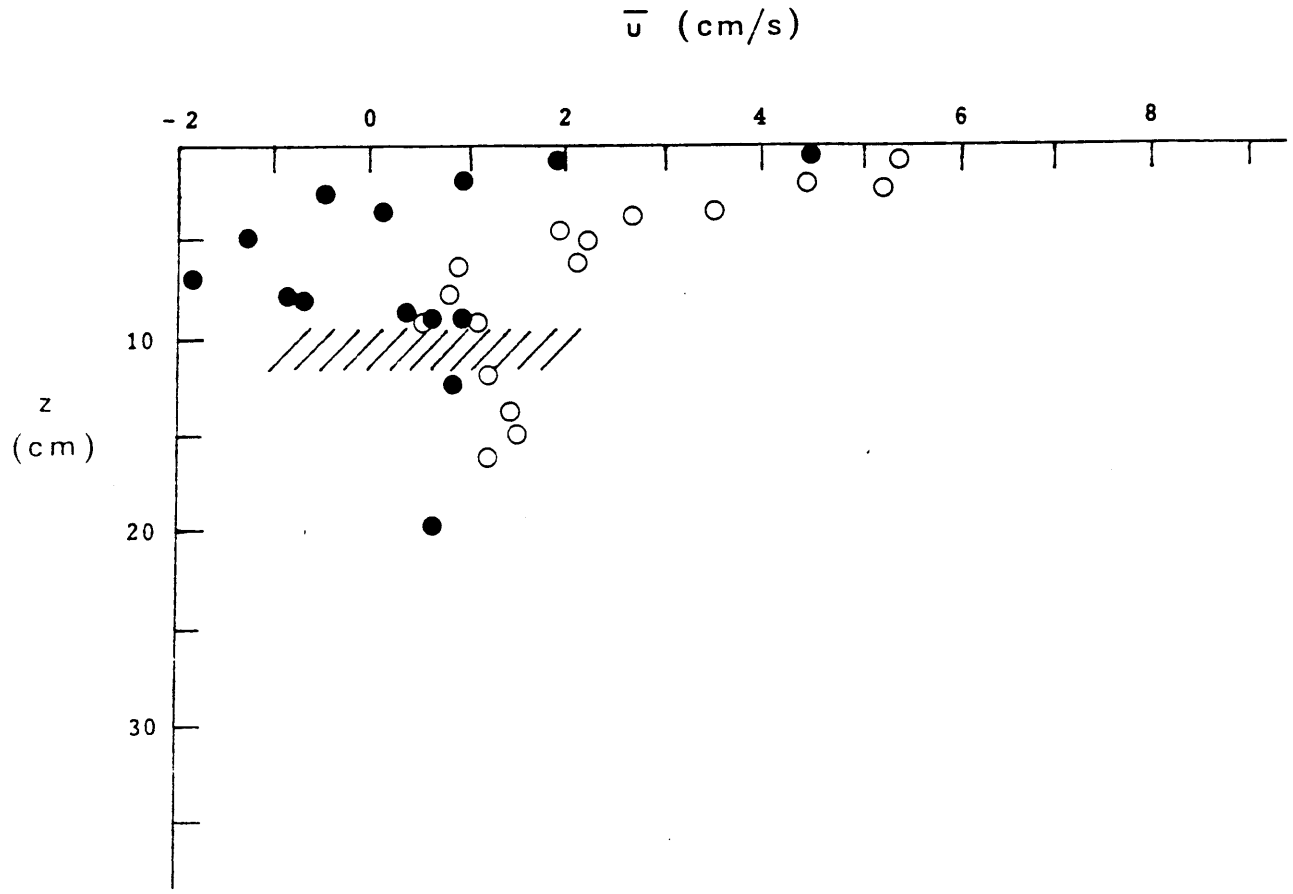

FIGURE 49 Mean Velocity Measured With Density Stratification Present; Solid Points Were Measured Along the Centerline and Open Points Were Measured One-Quarter of the Way Into the Tank; Cross-Hatched Area Indicates Interfacial Region

a) 3.5 m section, $\overline{W}$ = 10.2 m/s

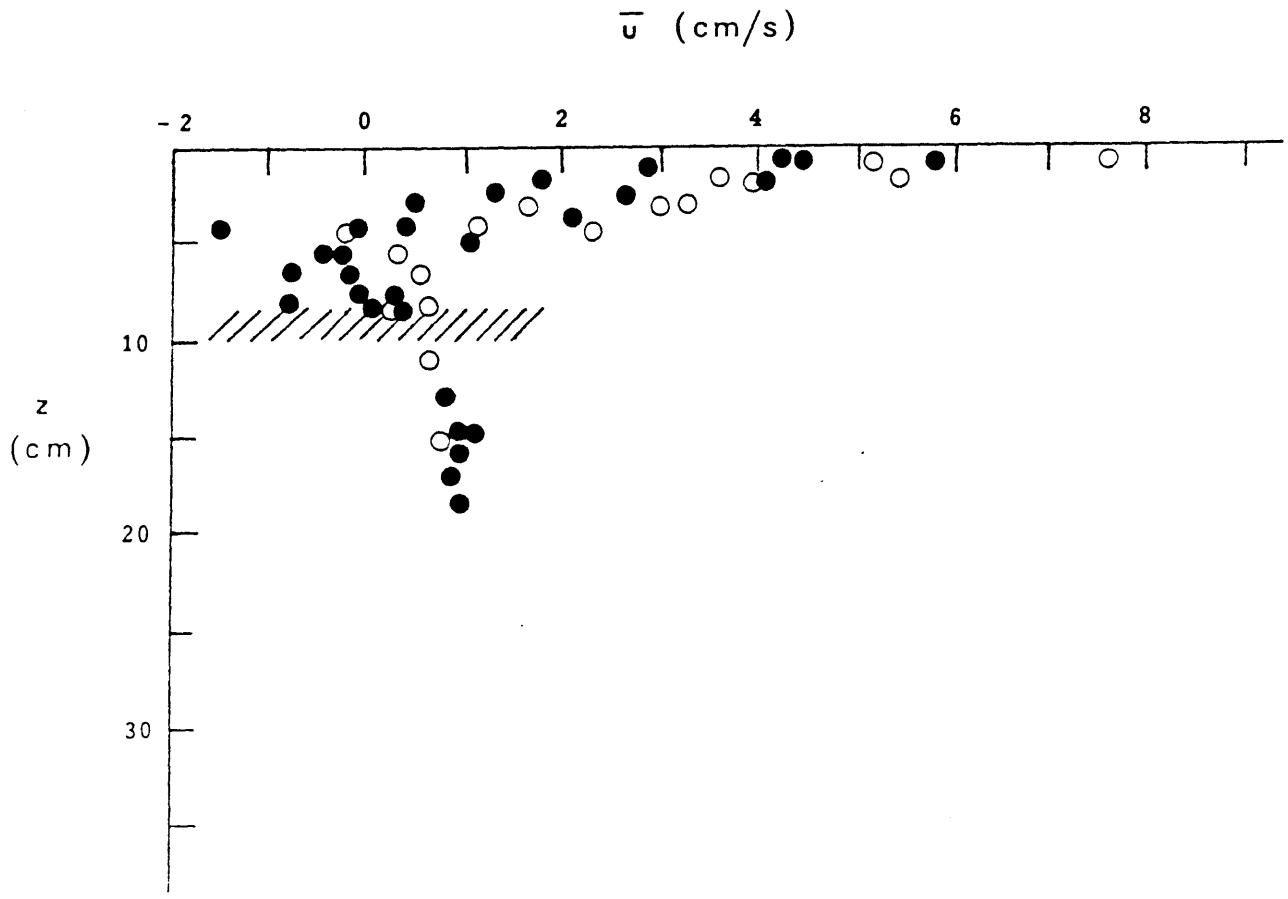

FIGURE 49 (continued)
b) 3.5 m section, $\bar{W}$ = 7.8 m/s

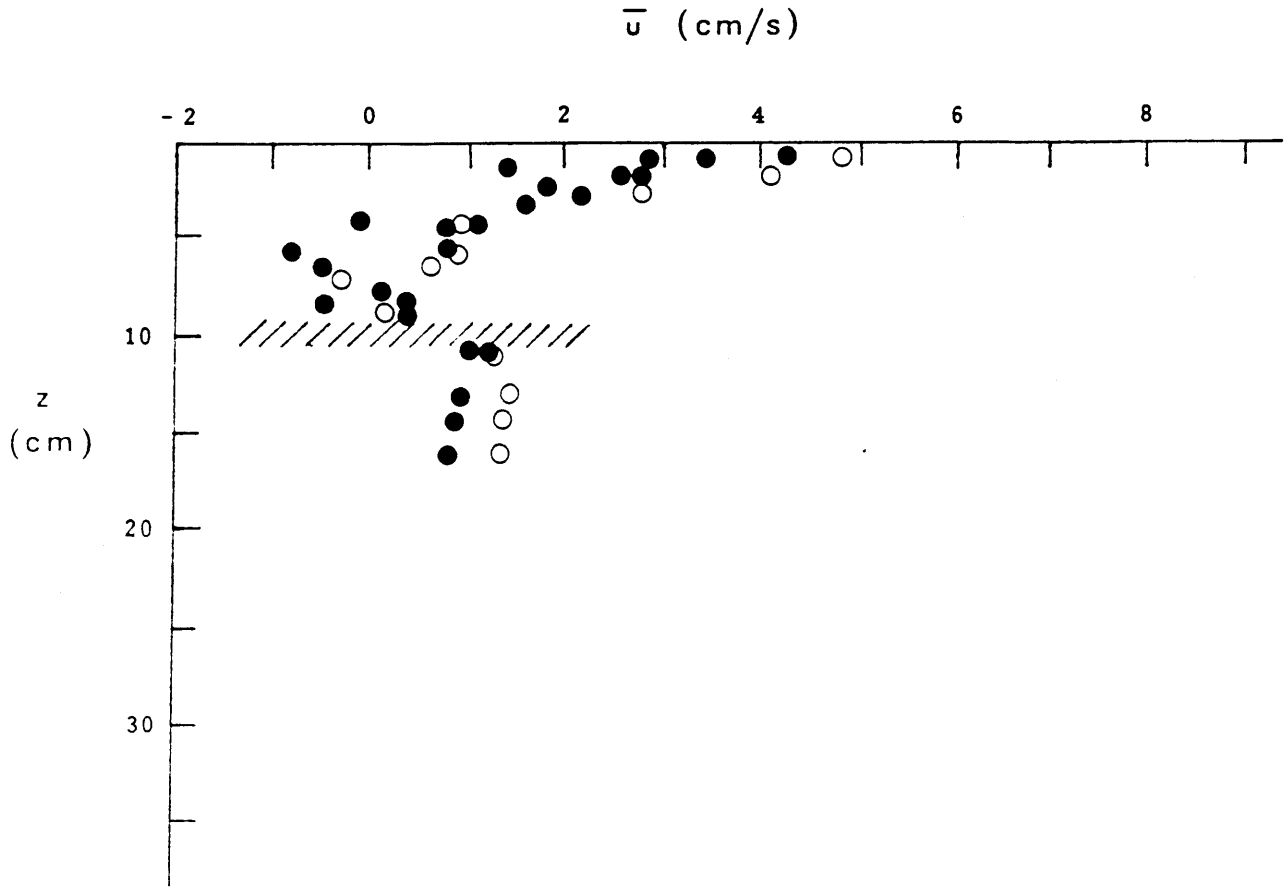

FIGURE 49 (continued)

c) 3.5 m section, $\bar{W}$ = 4.4 m/s

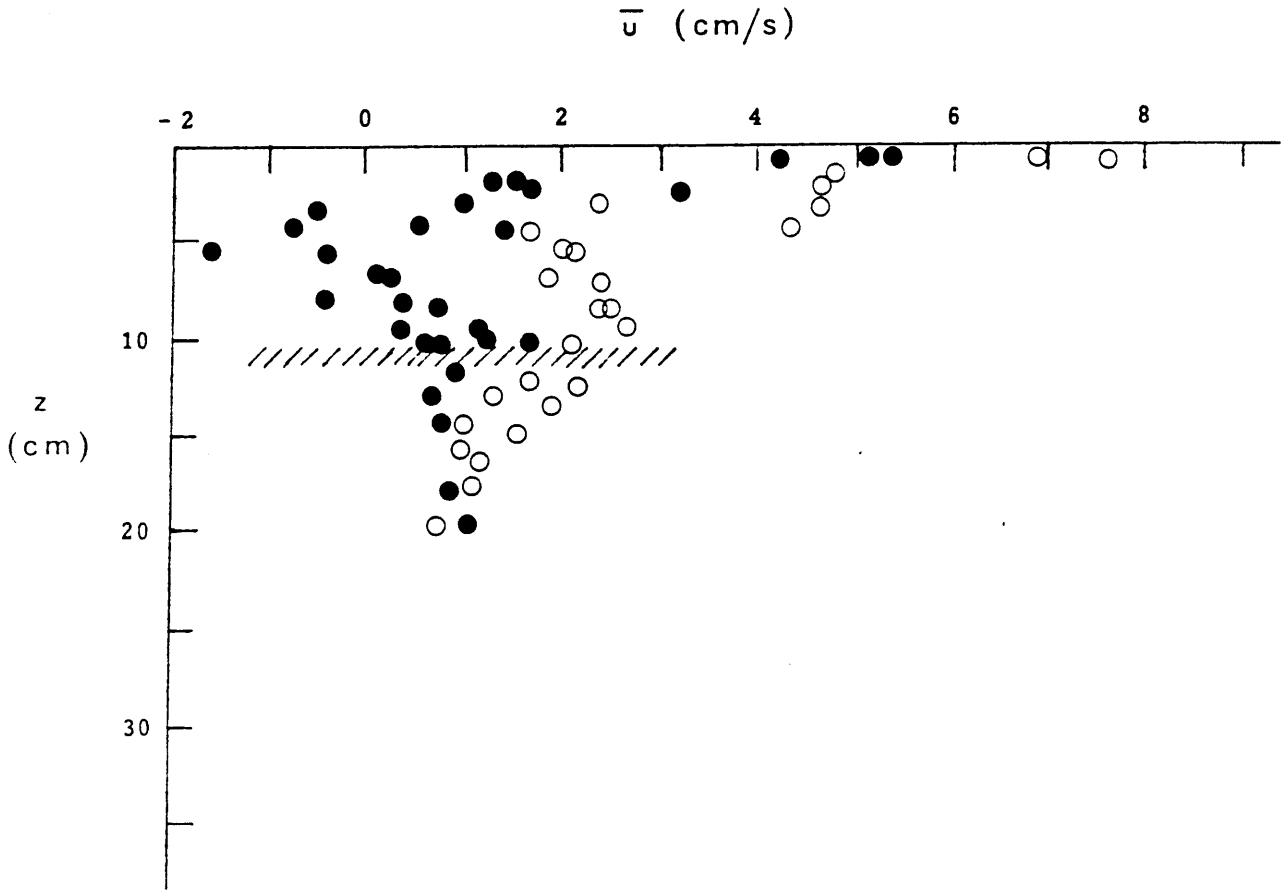

FIGURE 49 (continued)
d) 7 m section. $\bar{W}$ = 7.8 m/s

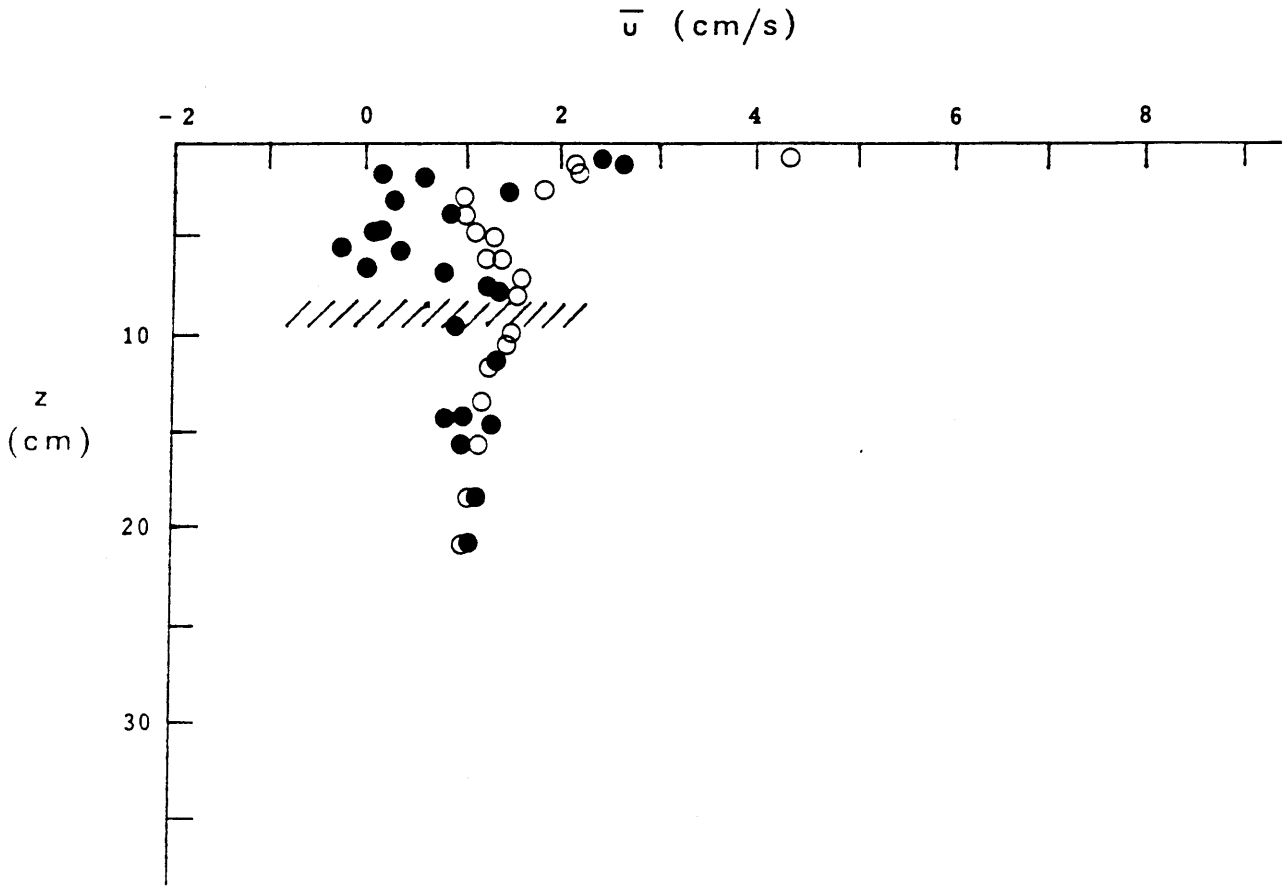

FIGURE 49 (continued)
e) 7 m section, $\bar{W}$ = 4.4 m/s

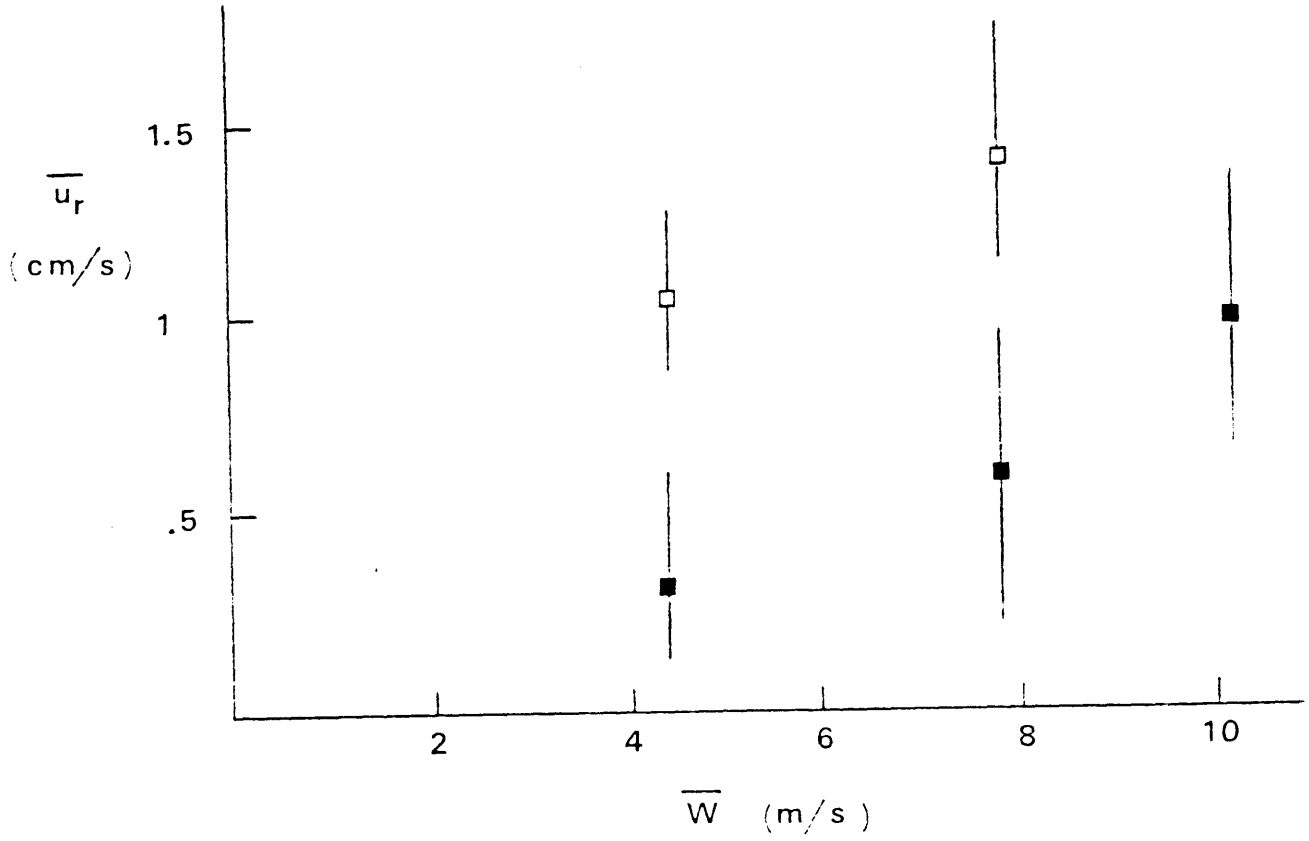

FIGURE 50 Average Velocities Near Interface For ■ 3.5 m Section and □ 7 m Section; Bars Show Range of Values Observed

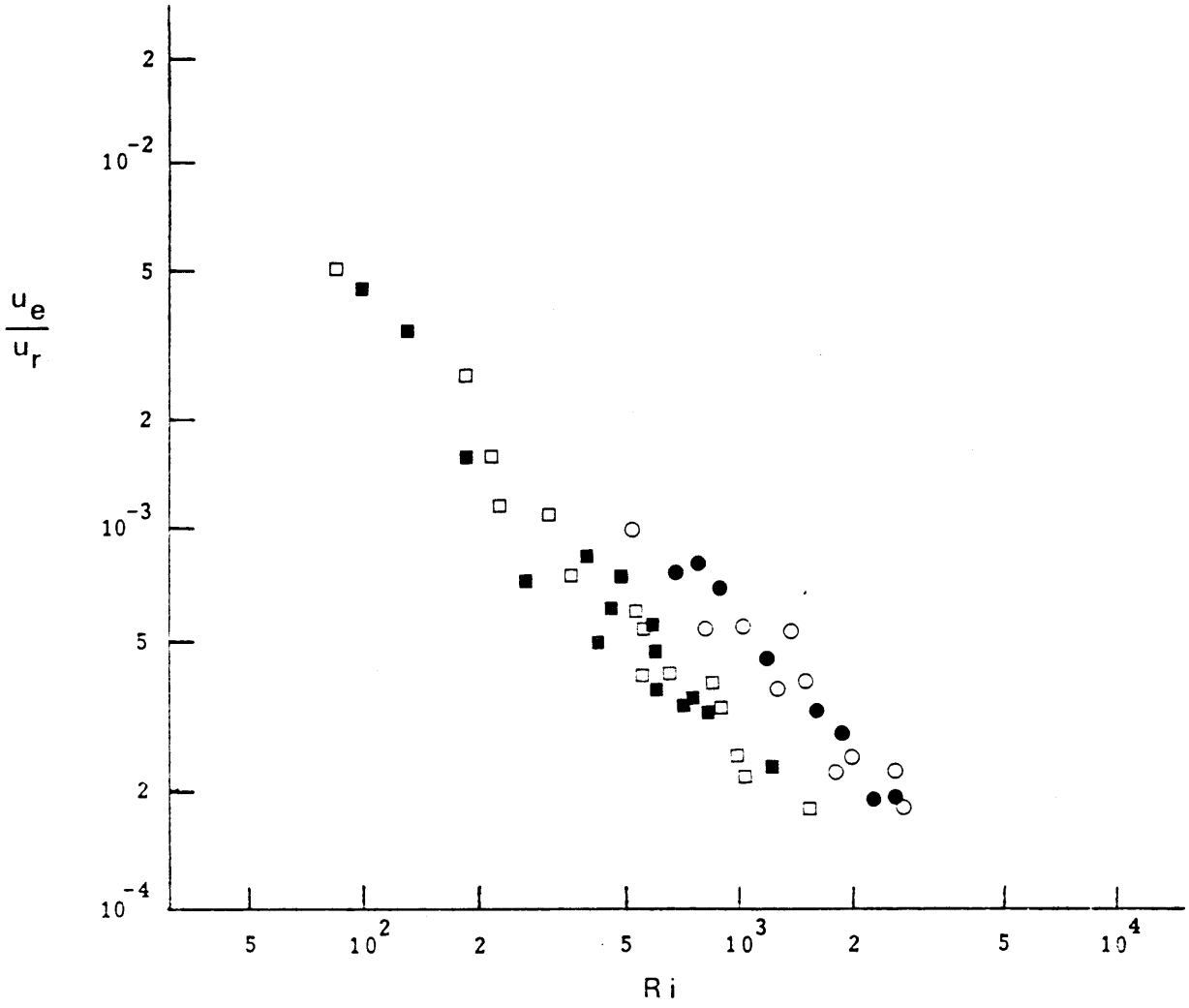

FIGURE 51 u_e/u_r vs. Ri (Symbols Have the Same Meaning As In Figure 46)

the two test sections than in Figure 47, though there is not a perfect collapsing of the data.

From the above results it appears that double-diffusive stratification has no effect on the entrainment. Shear effects are apparently much stronger than double-diffusive effects. The main effect of double-diffusive stratification in the grid experiments was to cause more energy to be available for entrainment due to motion associated with buoyant convection (see discussion in section 4.3.2). In the wind experiments there are already larger scale motions set up by the surface shear stress which are stronger than the motions associated with an unstable buoyancy flux across the interface. In addition, the return flow along the interface serves to scour any developing boundary layers so that double-diffusive instability will not occur. Double-diffusive effects would probably only be seen for very weak winds and very strong (unstable) temperature gradients. In other words, based on the present results double-diffusive effects would not be expected to be important for wind speeds greater than about 3.5 m/s and temperature steps less than about 12°C. The limit for wind speed may be even less, but very low wind speeds were difficult to control in the present facility and quantitative results were not obtained.

The possible effect of an unstable buoyancy flux on entrainment in the wind-mixing tests was considered. However, application of equations (4.4) and (4.5) is difficult here. First of all, only the bottom of the test sections was insulated so that heat loss to the surroundings may not be completely negligible. Secondly, there was

heat transfer at the free surface so that it was not reasonable to compare total heat contents at the beginning and end of each test without knowing the surface heat transfer. An estimate for this might have been possible by measuring air temperature at the wind tunnel inlet and outlet, but then the entire wind tunnel would have to have been insulated. In addition to these experimental uncertainties, the temperature differences used in the wind-mixing tests were relatively low (a maximum of ~12°C) compared with the grid tests. Therefore, since $\hat{\kappa}$ was found to increase with ΔT in the grid tests (Figure 21) and interfacial heat transfer was estimated as $\hat{\kappa}\Delta T$, it was assumed that the buoyancy flux would produce a negligible effect on defining the velocity for scaling the entrainment results for the wind tests.

5.3 Wind-wave Dampers

A set of experiments was performed to test two different devices proposed to reduce wind-induced mixing in solar ponds. The idea is to have a grid of floating wave breaks which reduce the effective fetch for the development of surface waves. Two different materials were examined here. The first consists simply of 1 1/2" PVC pipe. Nielsen (1979) has described the use of a floating grid of similar pipes on a solar pond and concluded that surface waves were reduced. These pipes were laid out in an array with a 10' (3 m) spacing. The second material consists of plastic netting as shown in Figure 52. This netting has been used on several of the Israeli solar ponds and is laid out in a grid of 1 m wide sections with a 5 m spacing (Assaf,

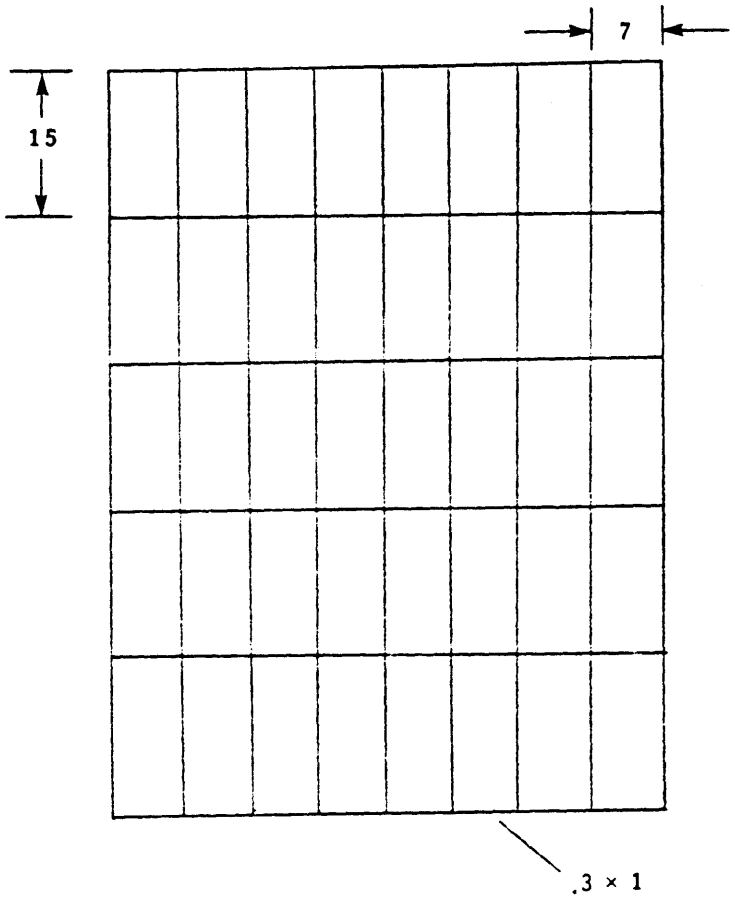

FIGURE 52 Net Material Used For Wind-Wave Suppression Tests, With Dimensions in cm

1983, personal communication). These nets are apparently effective in reducing mixing (Assaf, undated), though there have not been any controlled experiments to test their effectiveness. Both the nets and pipes are anchored at the sides of the pond. For the present experiments a small sample of the Israeli netting was obtained for testing. It should be noted that a third type of wave damping system has been reported (Akbarzadeh et al., 1983) which uses floating plastic rings. Due to time considerations and the geometry of the apparatus it was decided not to test this method.

The pipes and nets were placed in the wind/wave tank and attached by string taped to the sides of the tank. This allowed freedom of movement vertically but prevented drift. Measurements of centerline mean and r.m.s. horizontal velocities in the water were taken with the LDA at variouslongitudinal positions including directly beneath the nets (or pipes). The same velocity measurements were also taken without the nets or pipes so that a comparison could be made and the effect of the nets or pipe could be determined. Note that these tests were done without density stratification. The pupose was to determine the effect of the wave damper on the energy levels in the water and any reduction should relate to a corresponding reduction in entrainment.

An example of velocity measurements taken directly beneath a net or pipe are shown in Figure 53. It was found that neither the pipe nor net had much of an effect on the flow at the lowest wind speed. For intermediate wind speeds there is some reduction in the r.m.s. velocities, with the nets performing slightly better than the pipes.

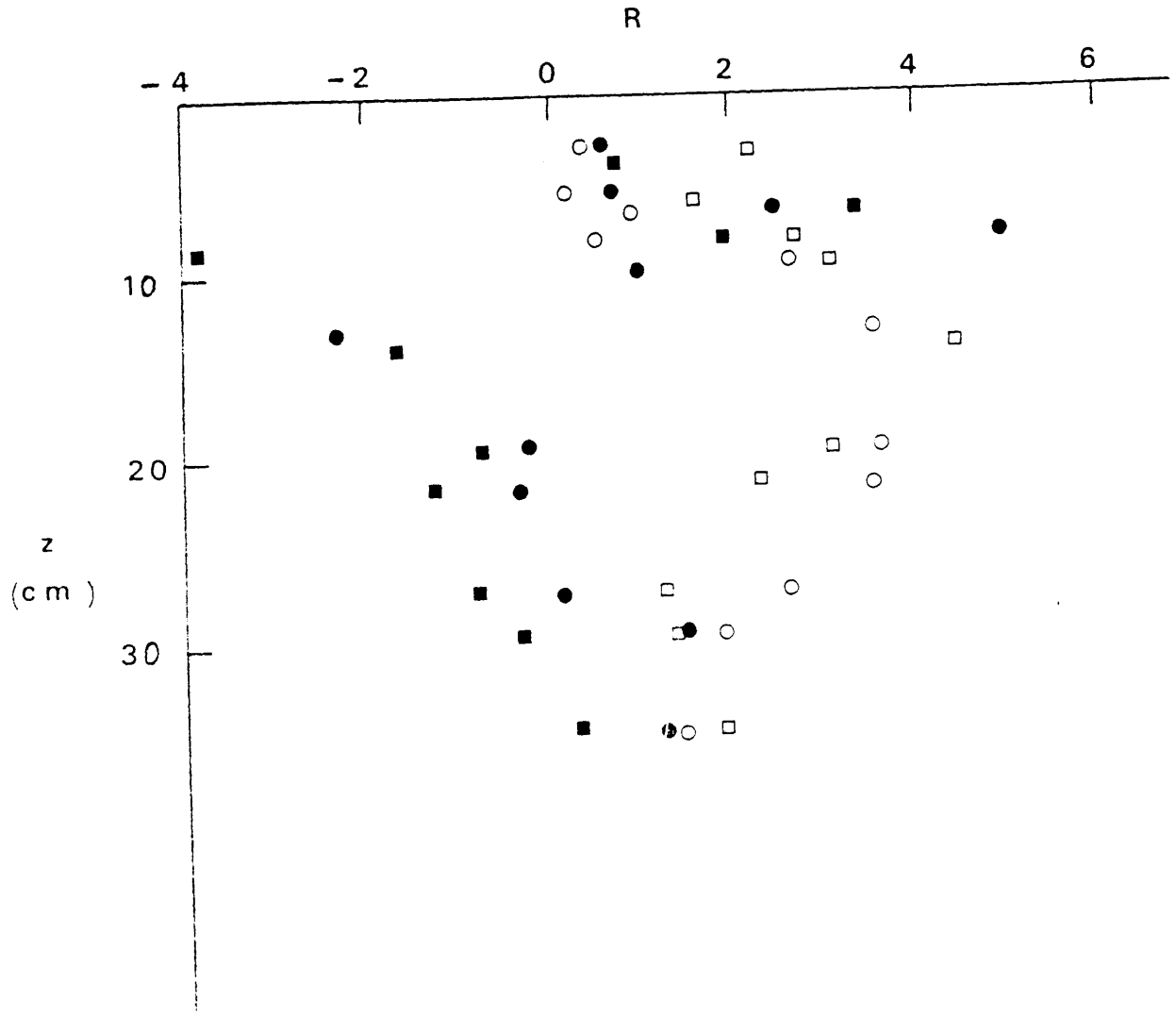

FIGURE 53 Ratio of Velocity Measurements Taken Directly Beneath a Pipe or Net to Measurements Taken At the Same Position, But Without the Pipe or Net, for $\bar{W}$ = 7.8 m/s. Squares Indicate Data For Pipes, Circles Are Data For Nets; Solid Points Give Ratio of Mean Velocities, Open Points Give Ratio of r.m.s. Velocities

However, at larger wind speeds there is actually an increase in the velocities (r.m.s.) when the nets or pipes are present, especially with the pipes. Mean velocities are also affected considerably. The data shown in Figure 53 show this effect. It appears as though the pipes may act in a similar manner as an oscillating grid and add energy to the water column. This is also true with the nets, but to a lesser extent. Some further insight into the effect of the nets or pipes is obtained by some simple flow visualization results, shown in Figures 54 and 55. For these figures dye was sprinkled on the water surface just upwind of the net or pipe. The photographs show the strong turning under of the flow. This effect was not observed at the lowest wind speed, but became more apparent as wind speed was increased.

The above results indicate that some stronger mixing might be expected directly beneath the nets or pipes, depending on wind speed. However, the overall effect of placing these devices on a solar pond is to reduce mixed-layer deepening (Assaf, 1983, personal communication). A series of tests was then performed to measure centerline velocities at various points between two nets and at corresponding positions without the nets present. The results of these tests showed that the energy (measured in terms of r.m.s. velocity) between the nets was reduced from the corresponding values measured without the nets in place (Figure 56). This is consistent with the observation that the waves were attenuated by the presence of nets or pipes (see Figures 54 and 55). Averaged over the entire area of a pond, the effect of having nets in place is then to

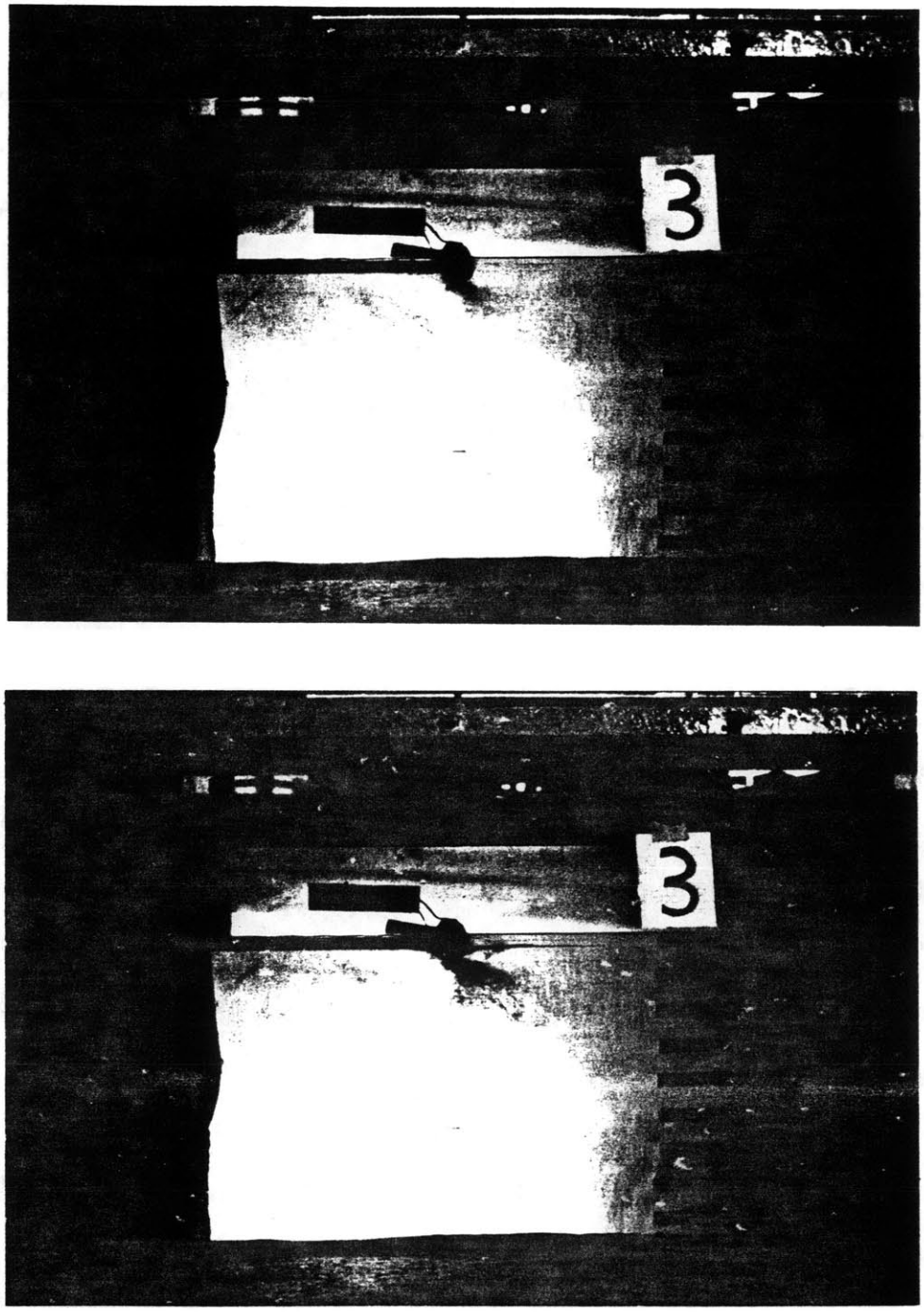

FIGURE 54 Visualization of Effect of a Floating Pipe on Flow Beneath The Pipe; Each Photograph Was Taken at a 10 Second Interval and Wind Moves From Left to Right; the Horizontal Bands are Spaced at 5 cm

a) $\bar{W}$ = 4.4 m/s

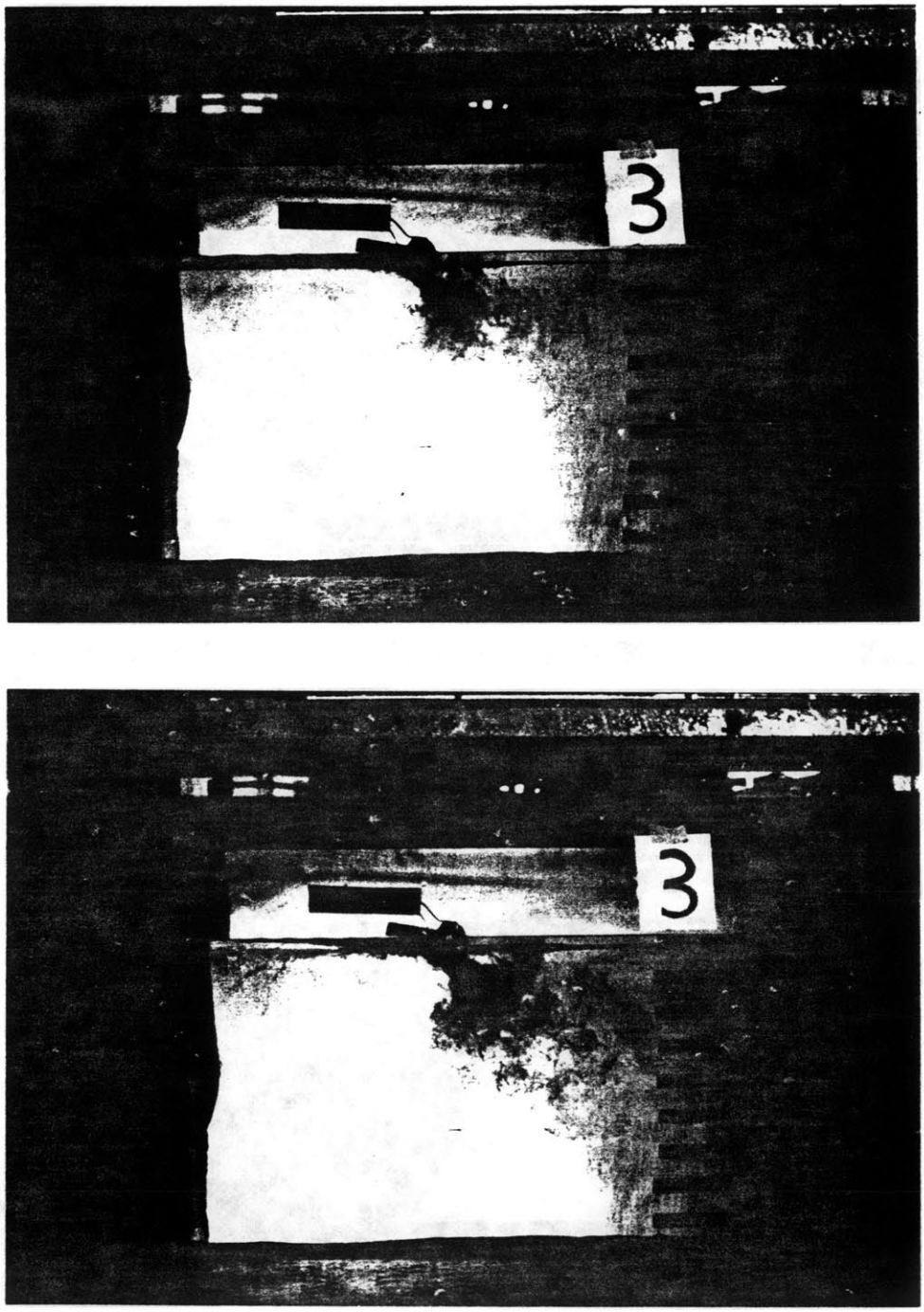

FIGURE 54 (continued) a) $\bar{W}$ = 4.4 m/s

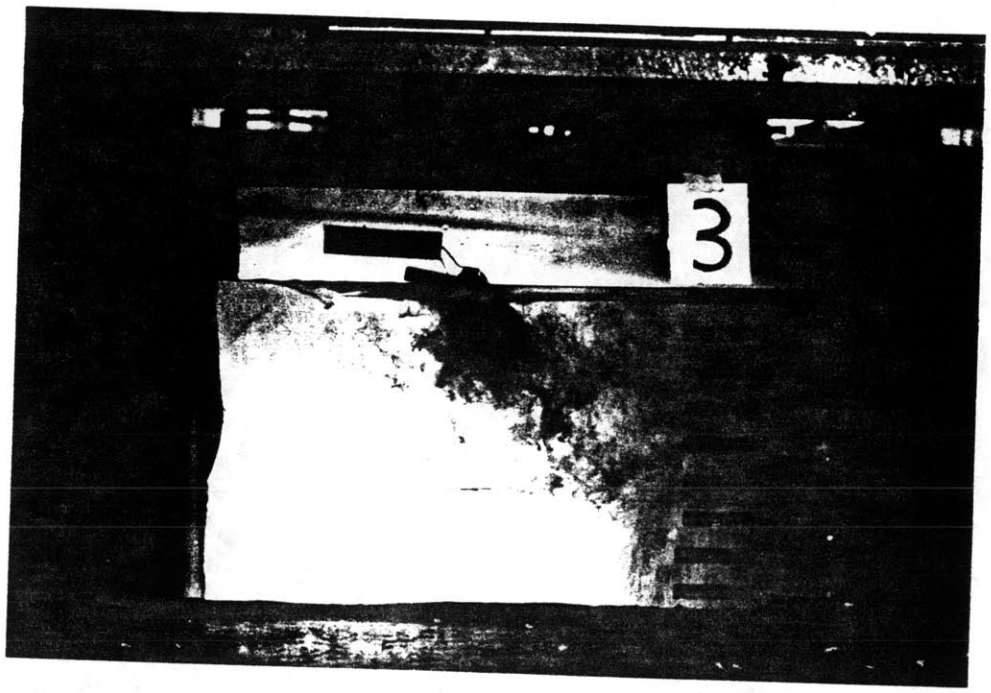

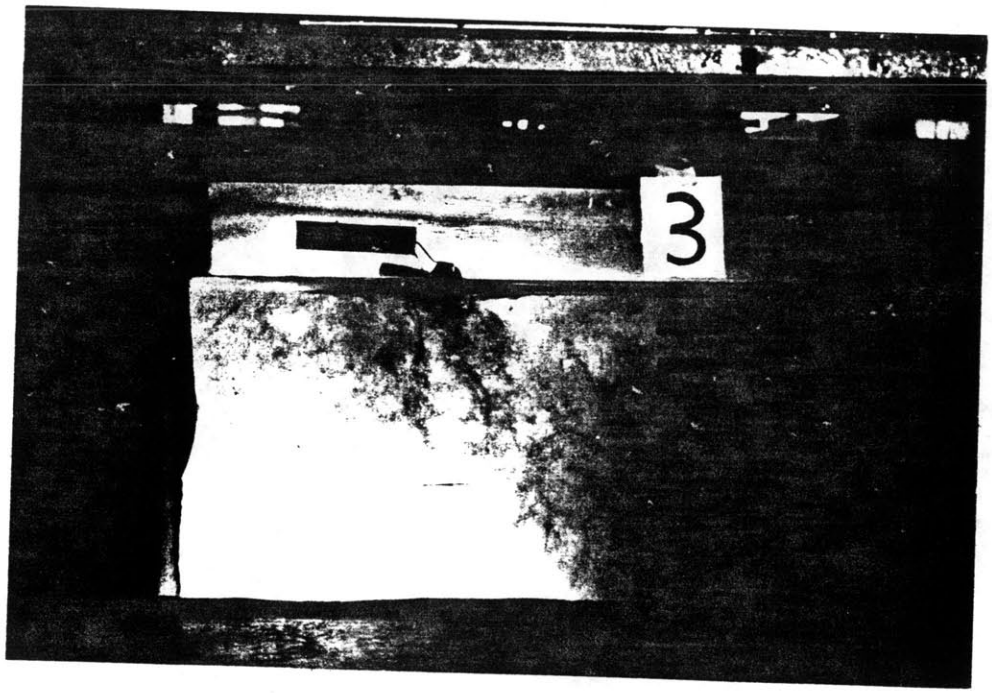

FIGURE 54 (continued a) $\bar{W}$ = 4.4 m/s

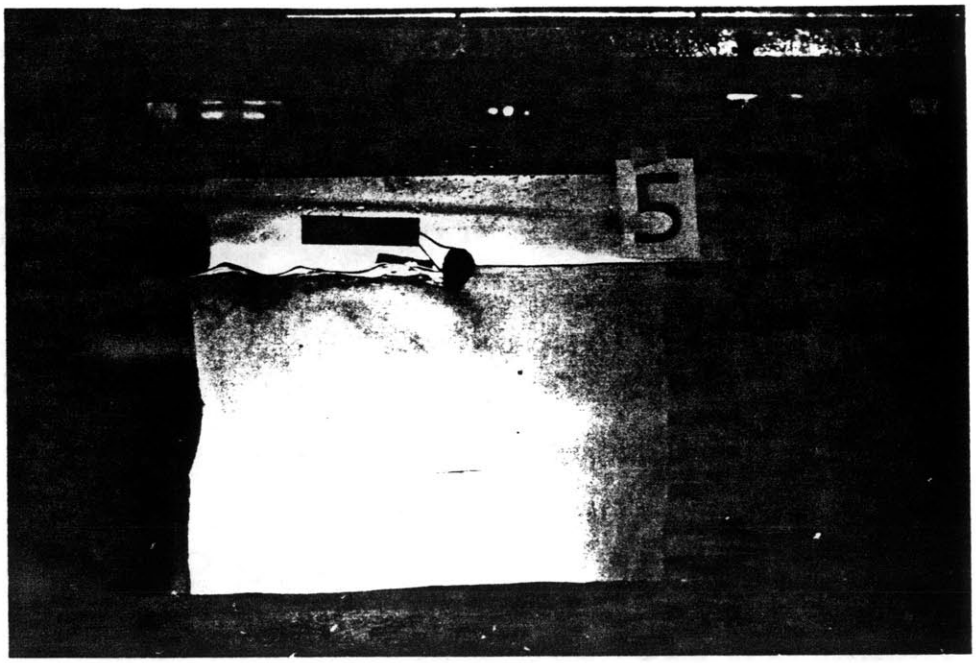

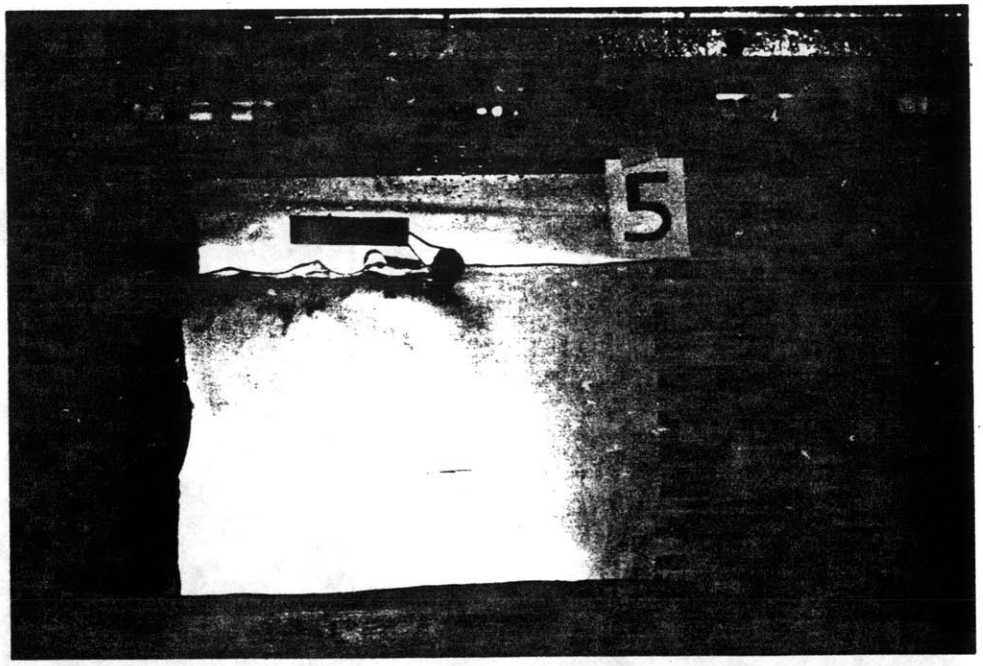

FIGURE 54 (continued) b) $\bar{W}$ = 7.8 m/s

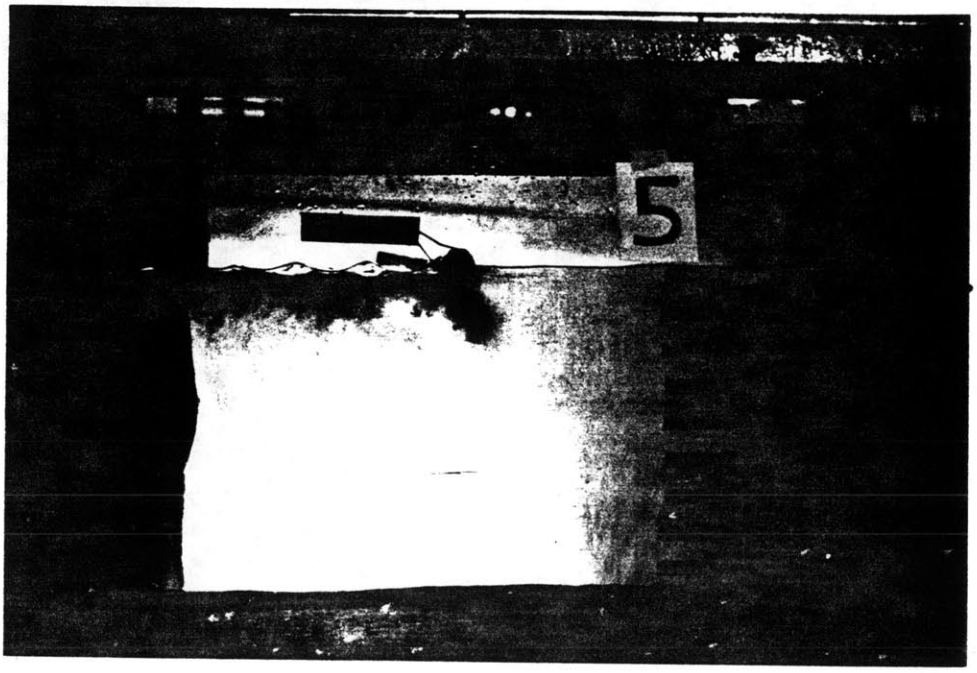

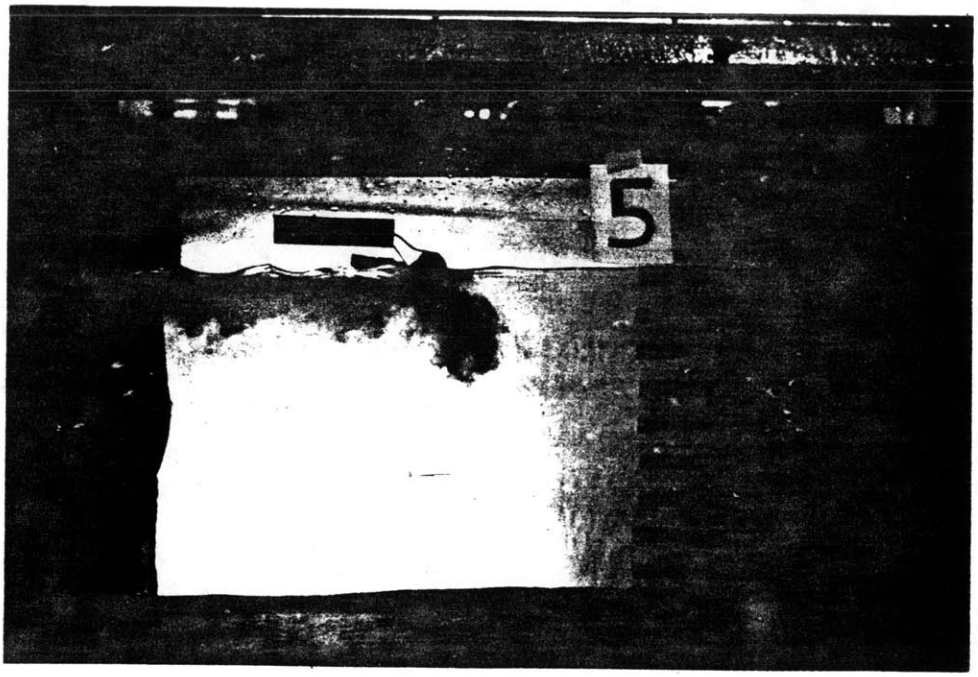

FIGURE 54 (continued) b) $\bar{W}$ = 7.8 m/s

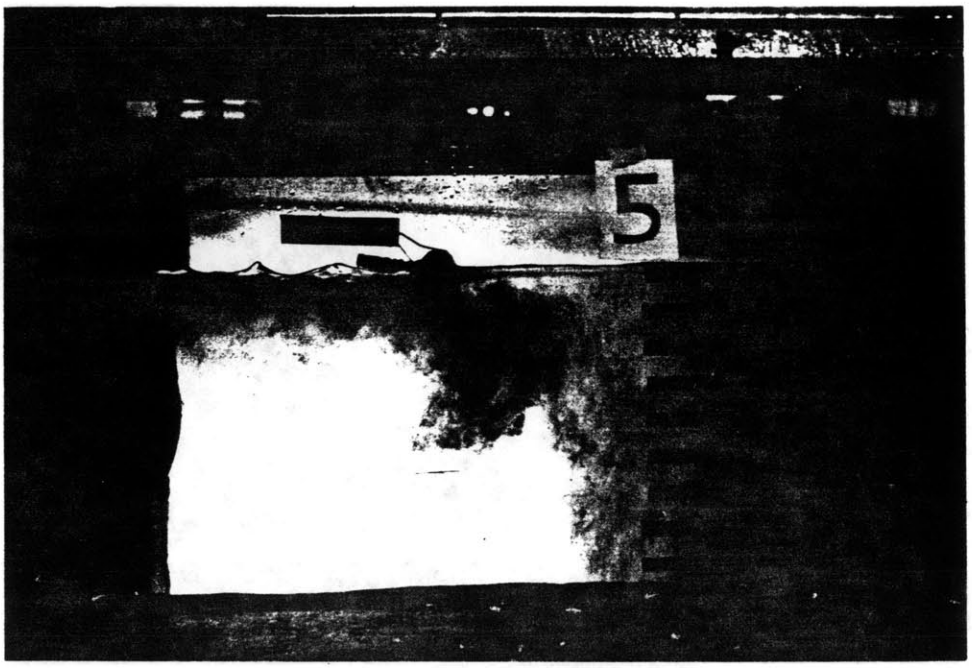

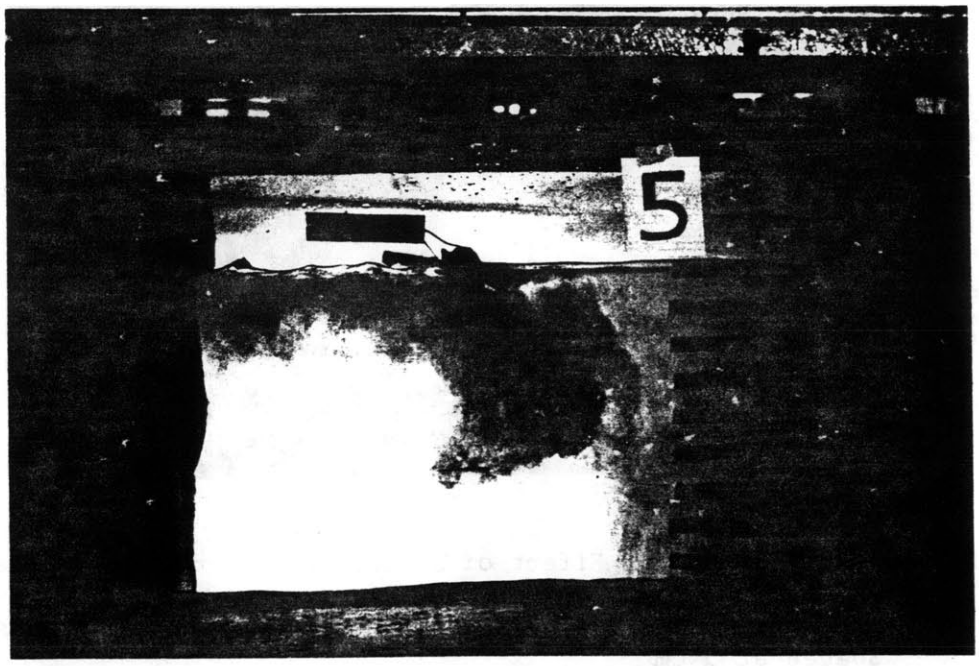

FIGURE 54 (continued) b) $\bar{W}$ = 7.8 m/s

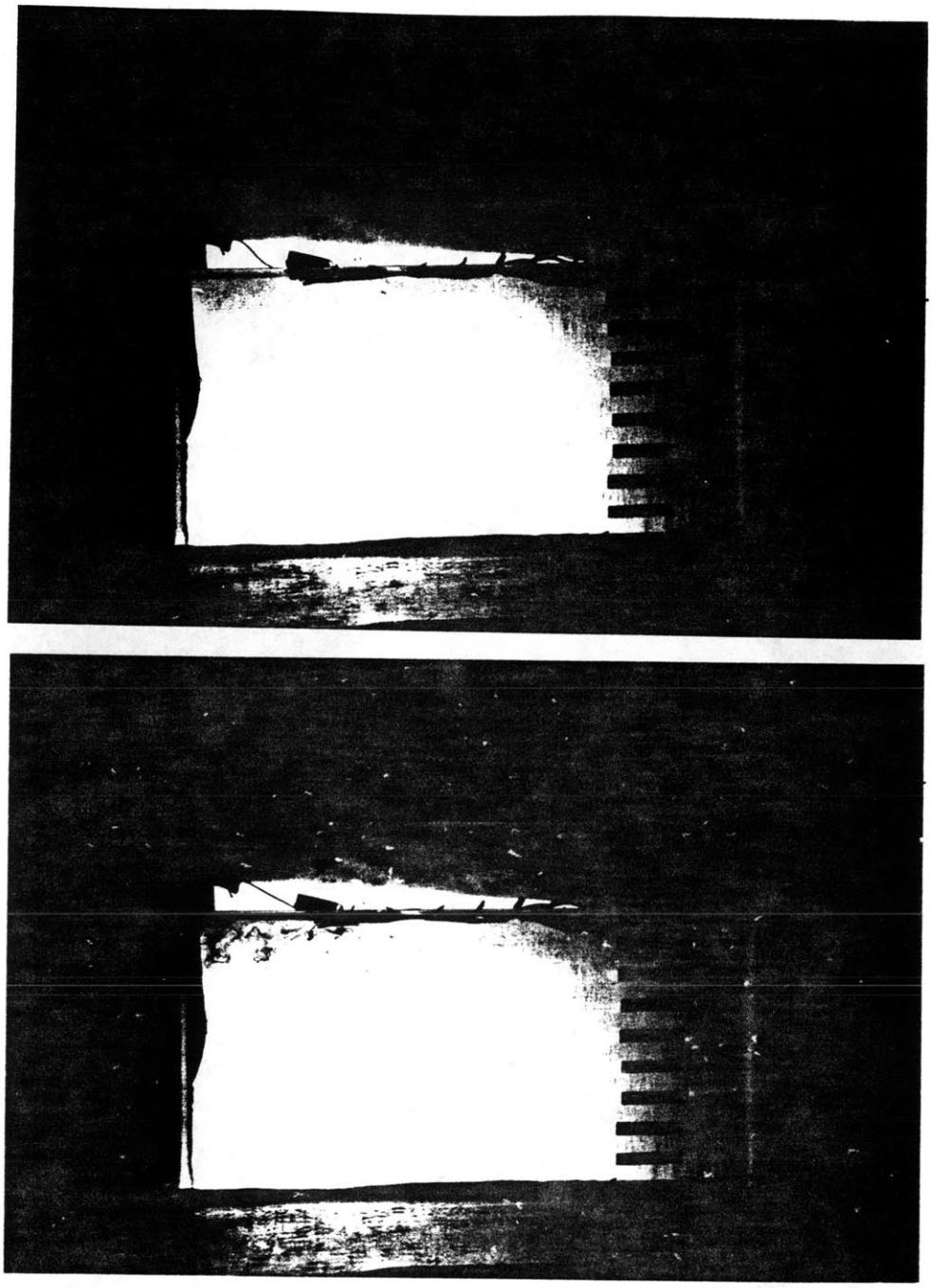

FIGURE 55 Visualization of Effect of a Floating Net on Flow Beneath The Net; Each Photograph was Taken at a 10 Second Interval and Wind Moves From Left to Right; the Horizontal Bands are Spaced at 5 cm

a) $\bar{W}$ = 4.4 m/s

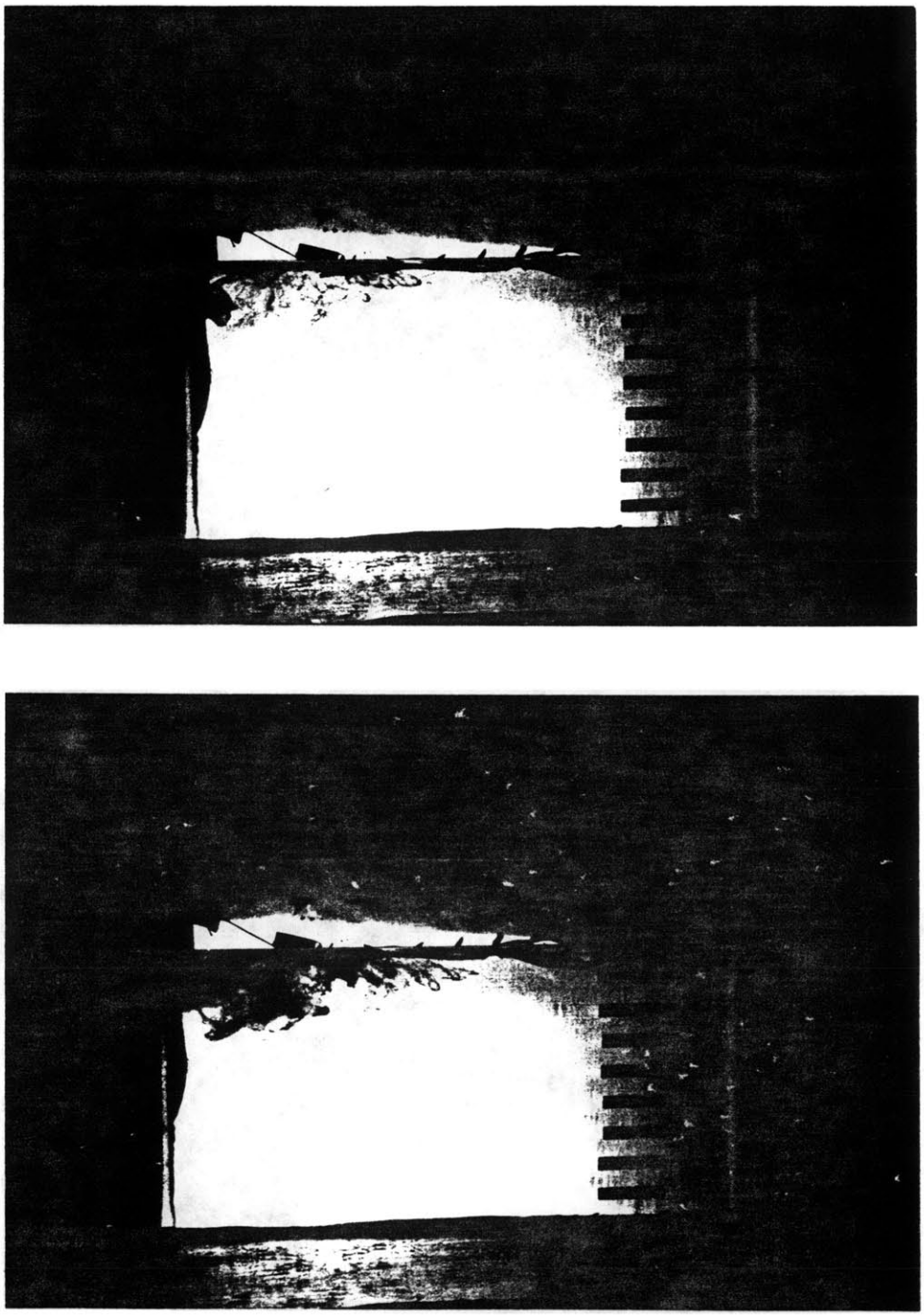

FIGURE 55 (continued) a) $\bar{W}$ = 4.4 m/s

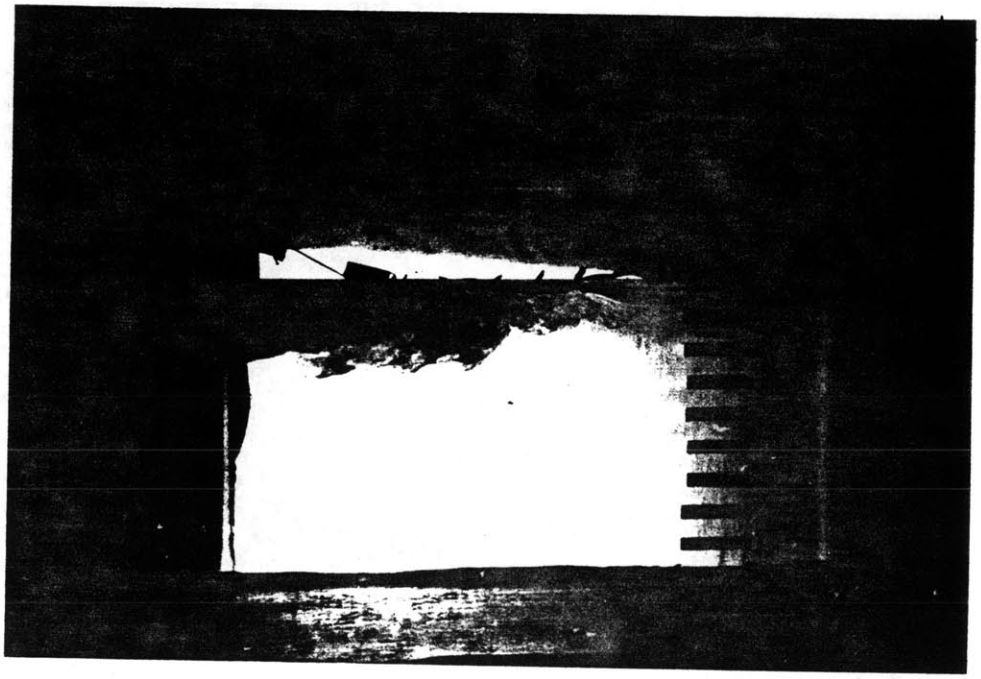

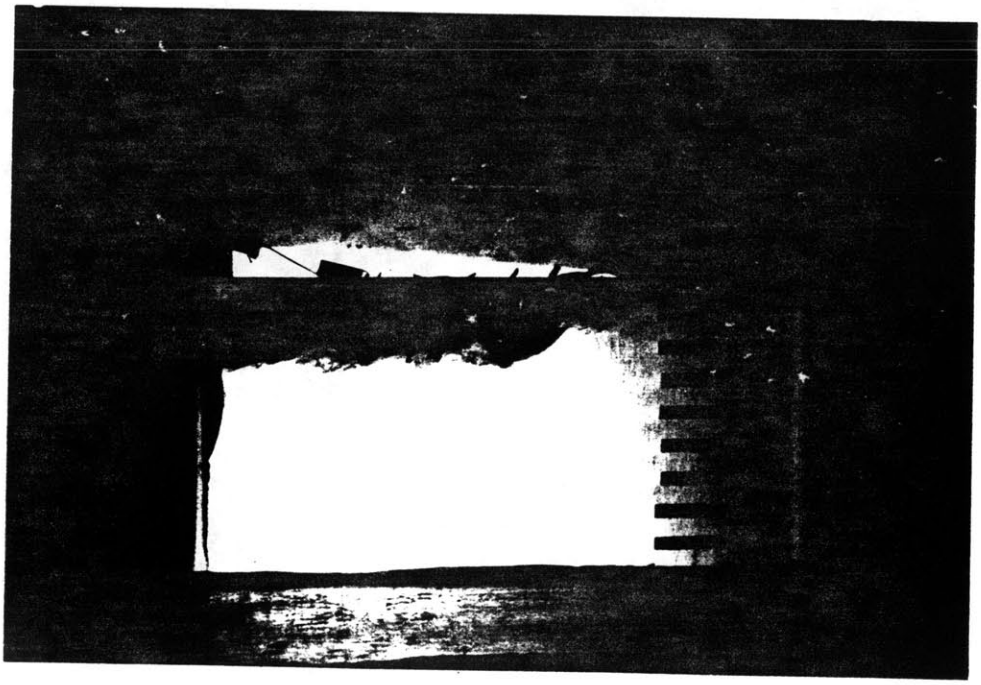

FIGURE 55 (continued) a) $\bar{W}$ = 4.4 m/s

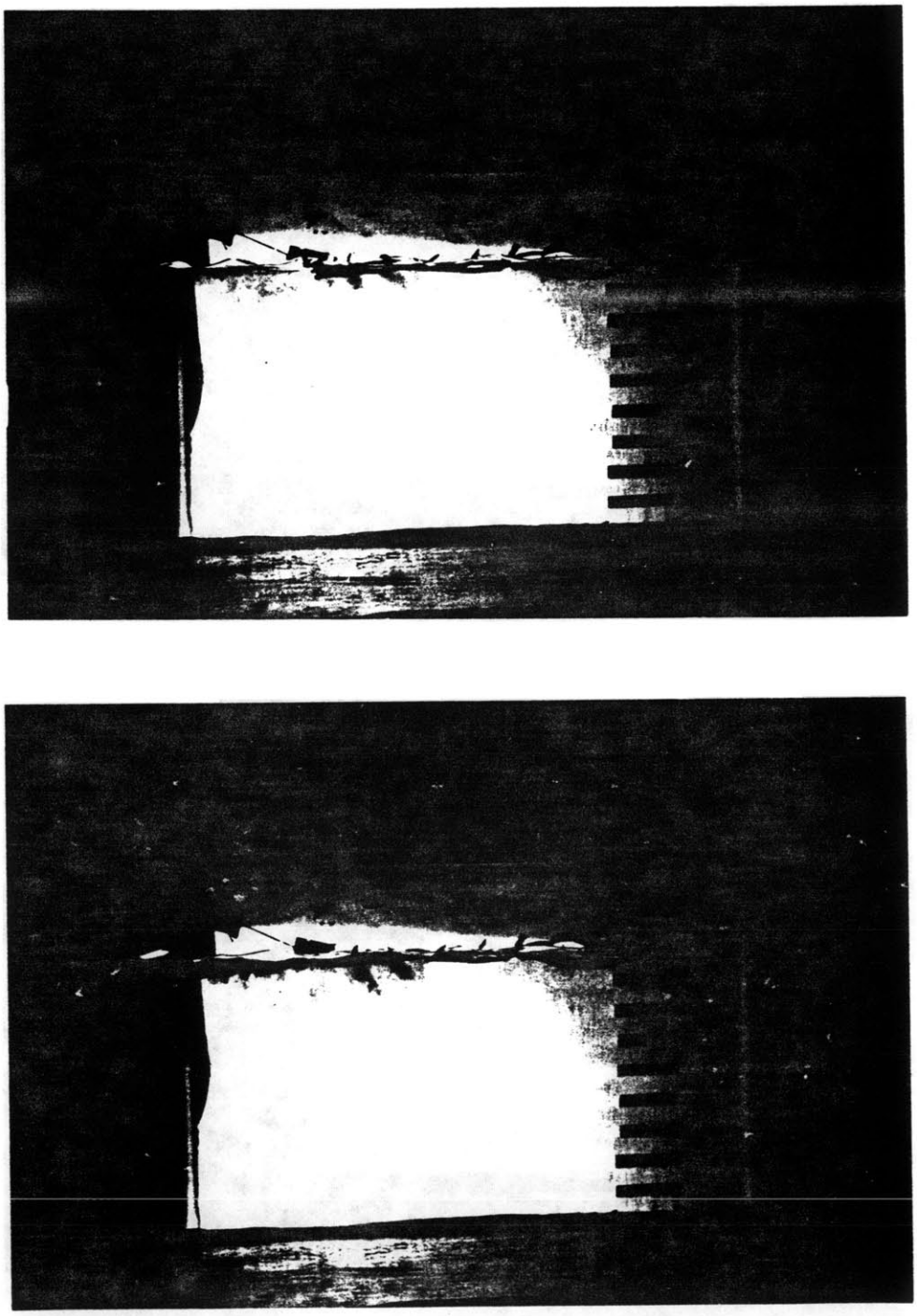

FIGURE 55 (continued) b) $\bar{W}$ = 7.8 m/s

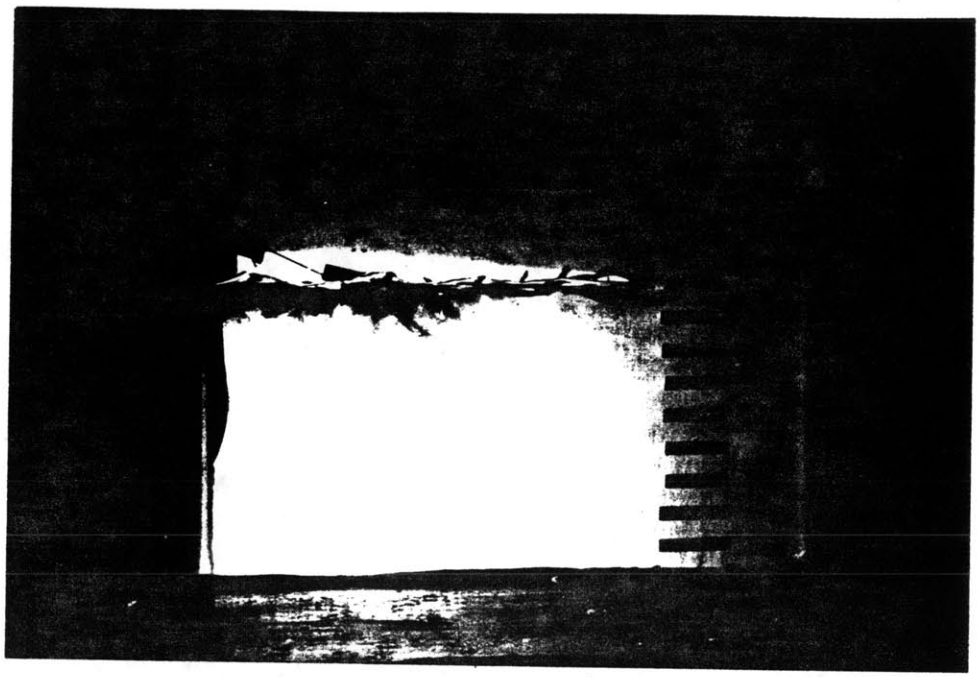

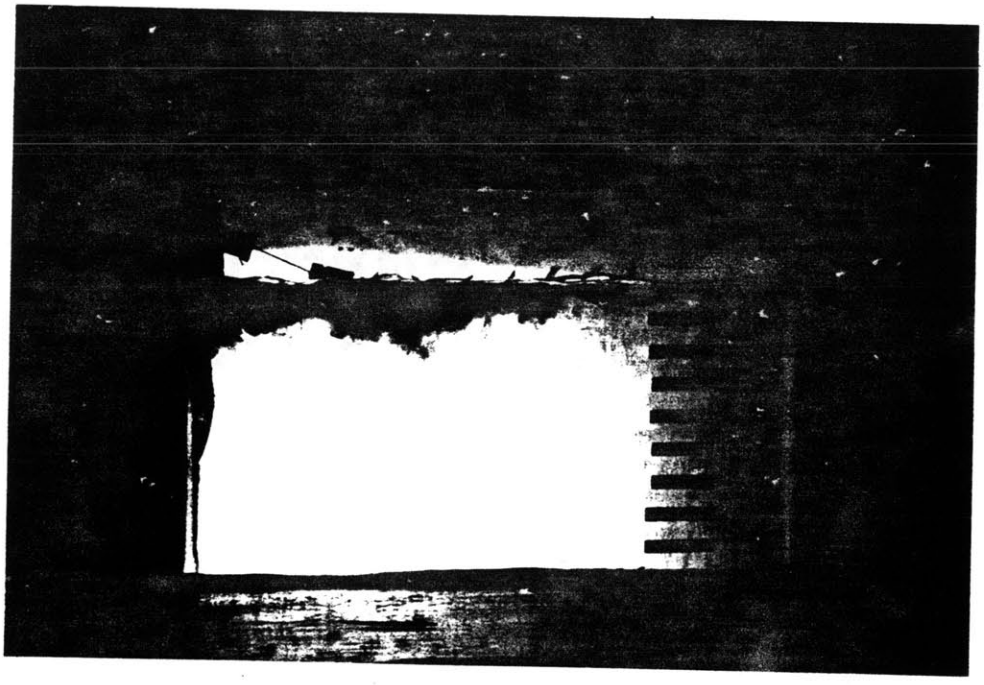

FIGURE 55 (continued) b) $\bar{W}$ = 7.8 m/s

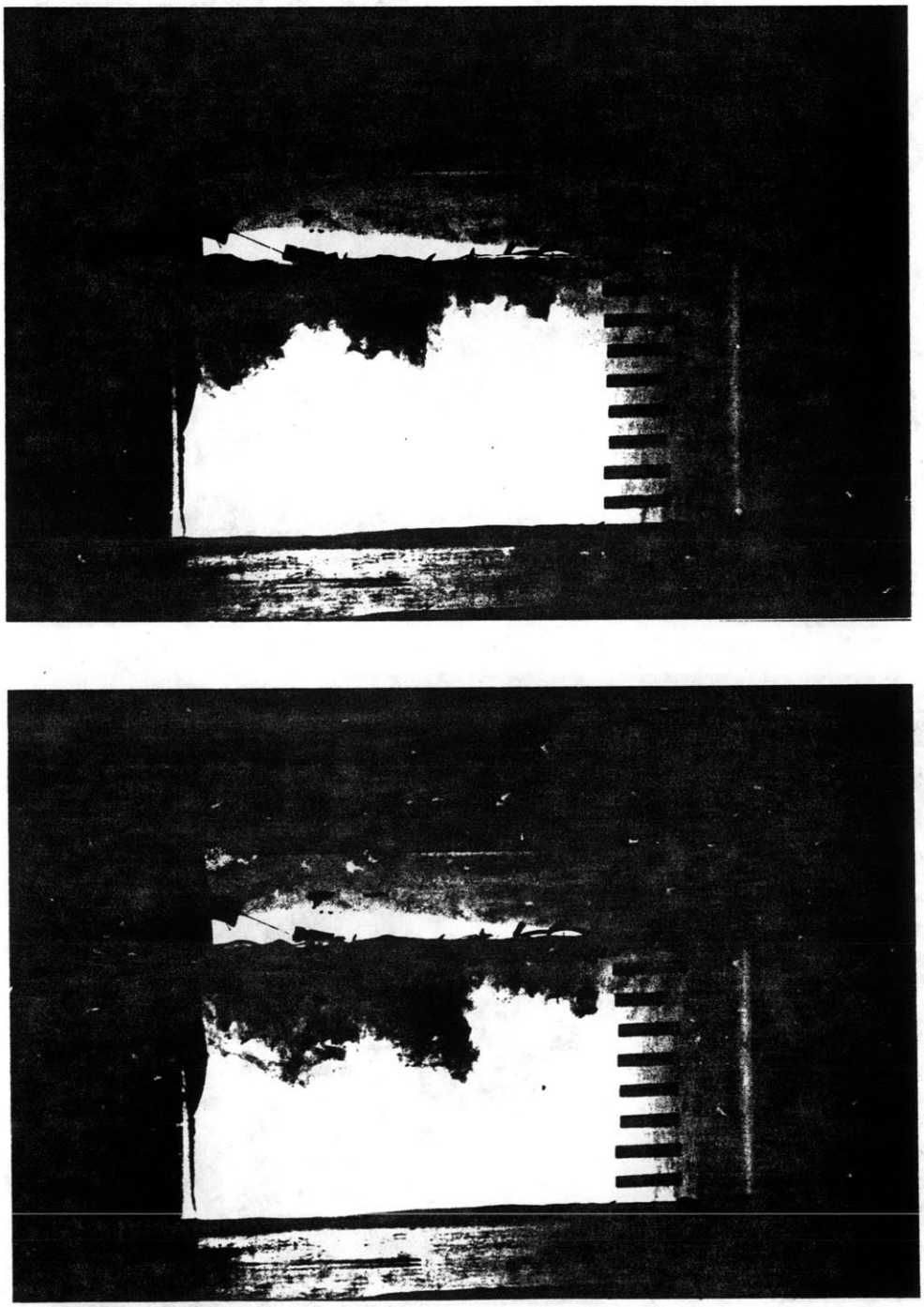

FIGURE 55 (continued) b) $\bar{W}$ = 7.8 m/s

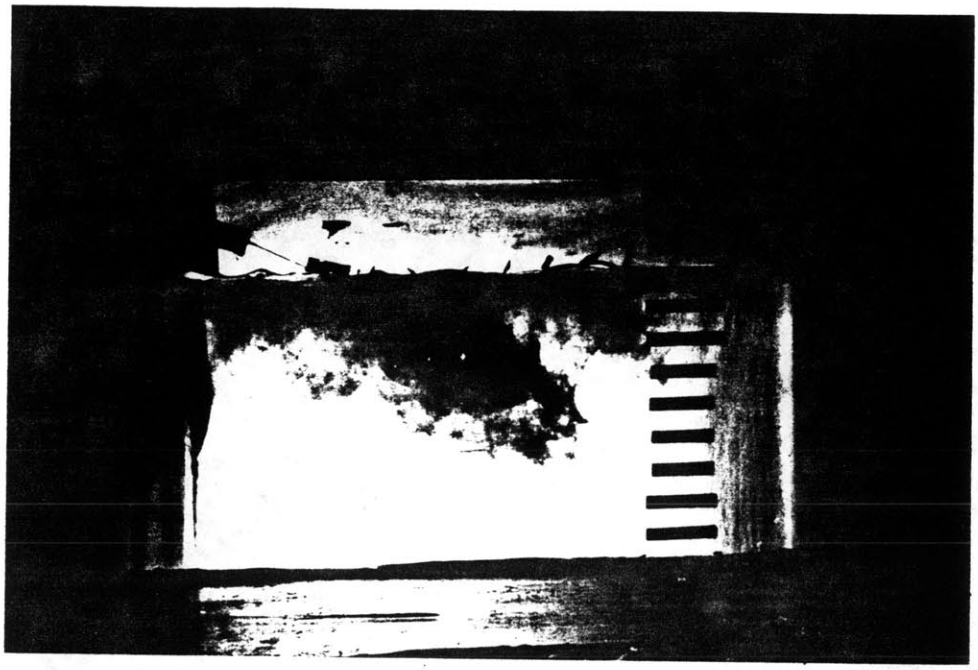

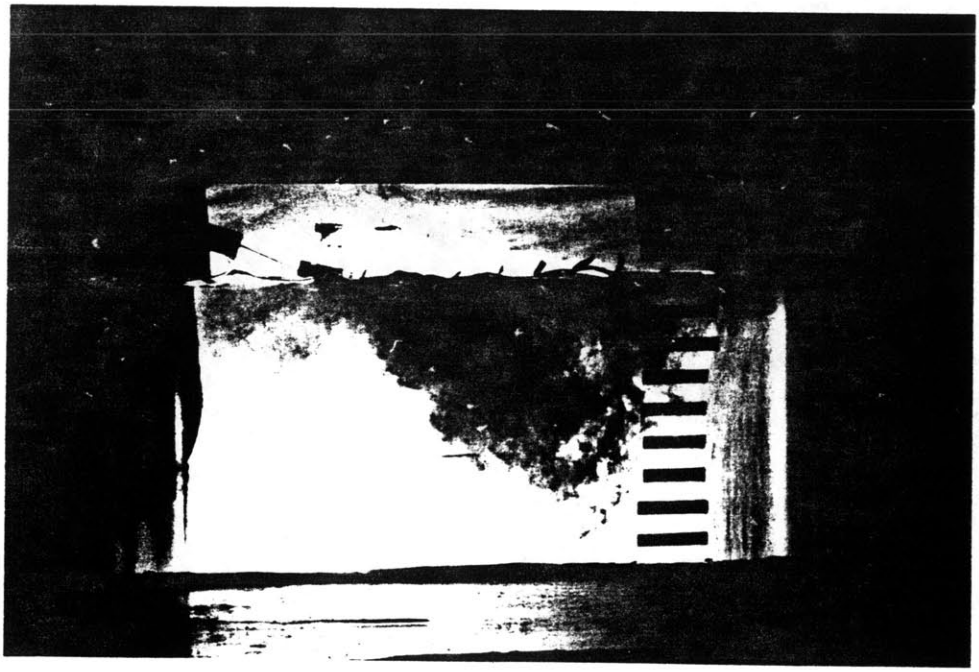

FIGURE 55 (continued) b) $\bar{W}$ = 7.8 m/s

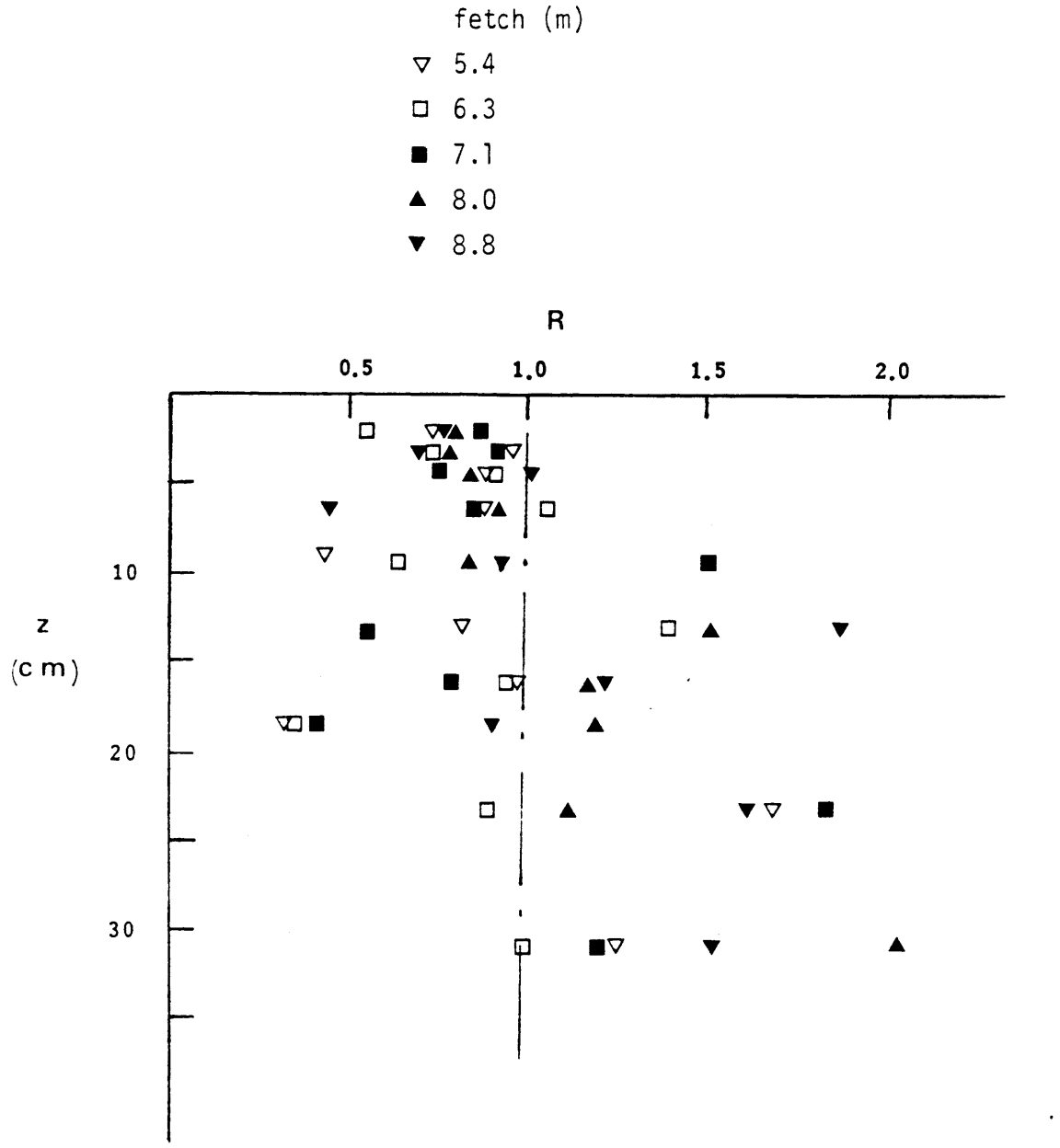

FIGURE 56 Ratio of r.m.s. Velocities Measured With Nets to Measurements Without Nets; Data For Fetches 5.4 m and 8.8 m are Directly Beneath 2 adjacent nets

a) $\bar{W}$ = 10.2 m/s

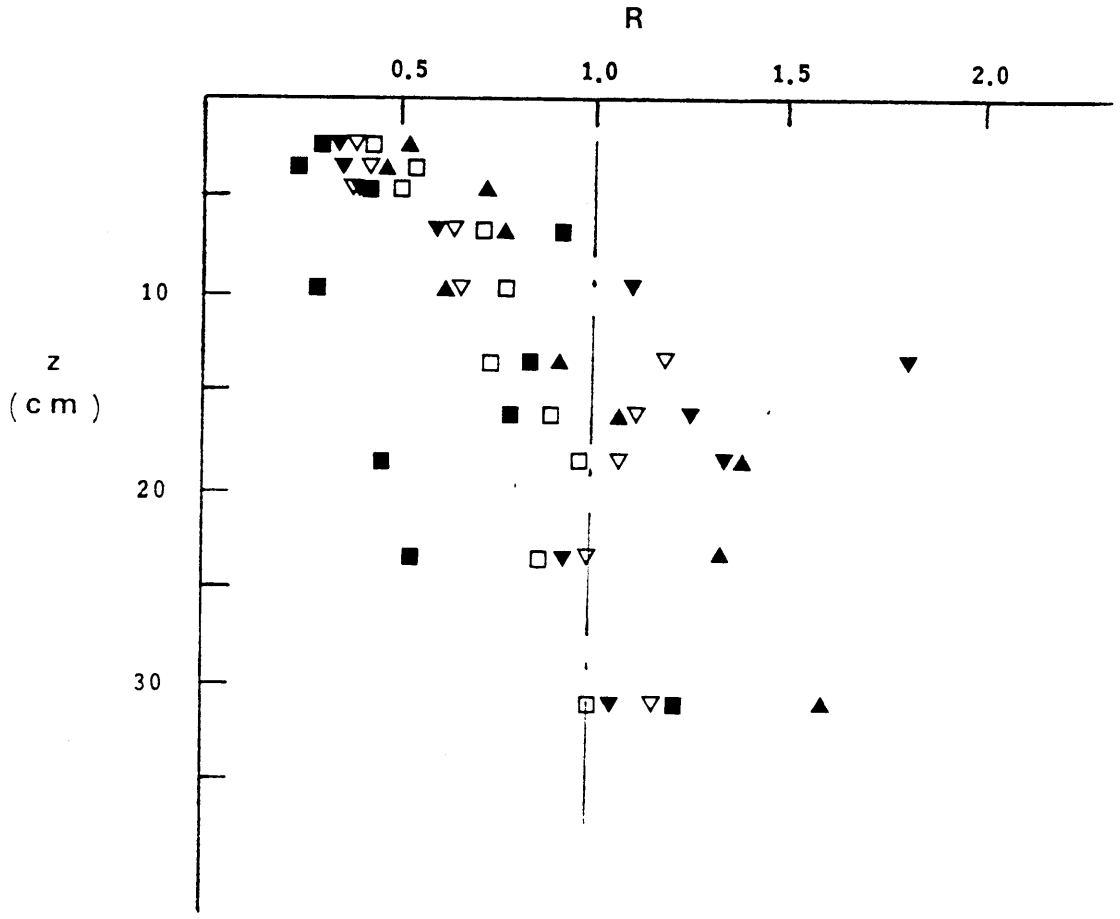

FIGURE 56 (continued) b) $\bar{W}$ = 7.8 m/s

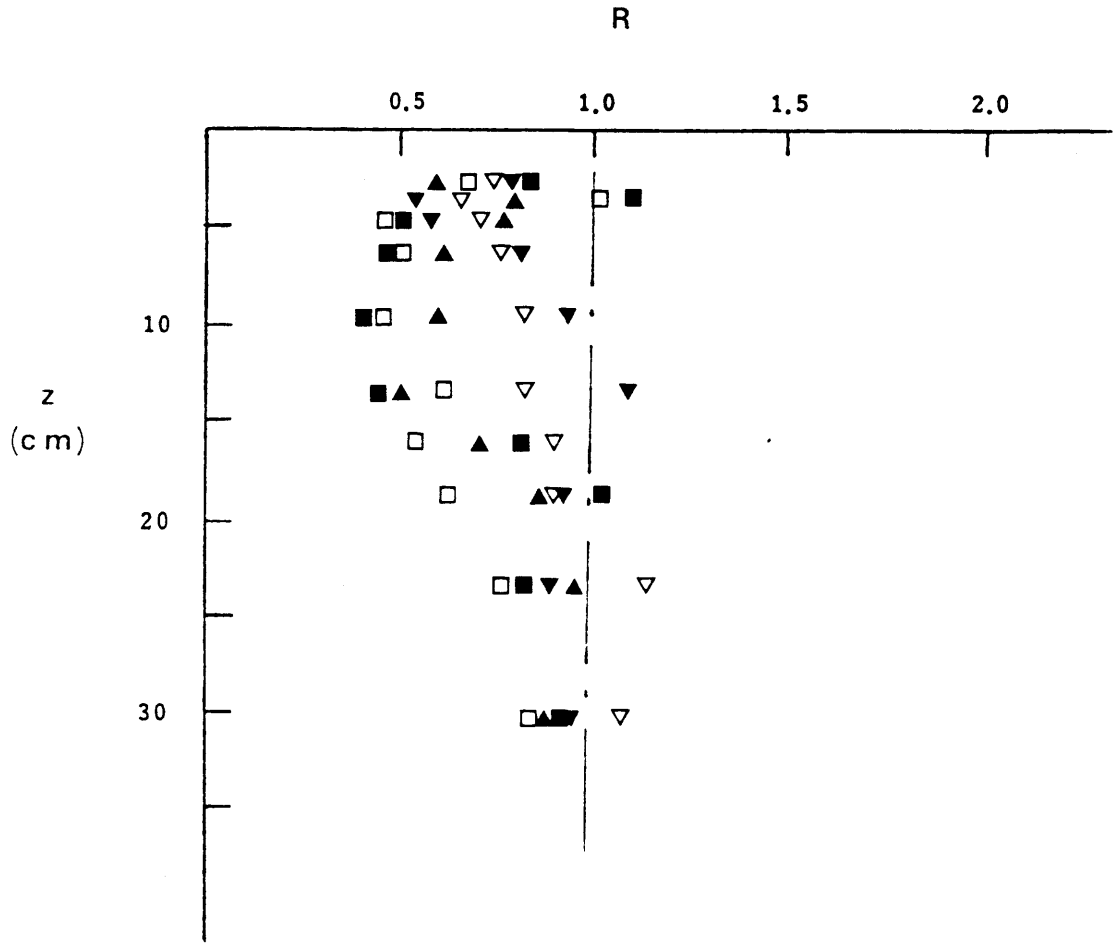

FIGURE 56 (continued) c) $\bar{W}$ = 4.4 m/s

reduce the mixing energy transported downward to the interface, although there may be some increased local mixing directly beneaththe nets themselves. This is due to the fetch control of the nets. With a reduction in wave build-up the friction velocity is also reduced. Also, the limited fetch prevents the build-up of surface drift current so that there is a reduction in the energy transferred to the water column. Entrainment would then be expected to be reduced accordingly. This was not tested directly in the present experiments and future tests might look directly at the effect of the nets on mixed-layer deepening.

It should also be pointed out that in the field the nets (or pipes) will probably be most effective in attenuating waves with a wavelength related to the spacing of the nets on the pond surface. In turn, the wavelength depends on fetch, which could not be duplicated in the laboratory. Further analysis of the affect of the nets should be done using field data.

CHAPTER 6

Application of Results to Wind-Mixing Model for Solar Ponds

6.1 Model Formulation

A numerical one-dimensional mixed layer model has been formulated to simulate the development of the temperature and salinity profiles in a salt gradient solar pond. The model is an extension of the wind-mixing model developed over a number of years at the R.M. Parsons Laboratory for predicting vertical temperature profiles in lakes and reservoirs (see Hurley-Octavio et al., 1975; Bloss and Harleman, 1979). An early version of the model which used the entrainment algorithm described by Bloss and Harleman was described by Atkinson and Harleman (1983a) and much of the following description comes from their paper. The current model includes several improvements in the code and, most significantly, an expanded wind-mixing algorithm which incorporates the entrainment model discussed in Chapter 3 and calibrated with data determined from Chapter 5. A full description of the numerical model is given by Atkinson et al. (1984).

The model performs calculations in two basic steps. First, changes in the profiles are evaluated using the equations governing the distributions of heat and salt in the absence of any external stirring by wind or penetrative convection. This is accomplished by solving (1.2) and (1.3) using an explicit finite difference scheme along with boundary conditions as discussed below. The second basic step involves application of the wind-mixing algorithm.

The pond is considered to be divided into a number of stacked homogeneous horizontal layers of predetermined thickness Δz. Equations (1.2) and (1.3) are then solved for all layers where values for w, u_i and u_o are calculated in a separate subroutine which evaluates a water balance based on inflows, outflow and net evaporation (see also eq. 1.4). The bottom boundary conditions specify a zero flux condition for the salt equation (i.e., $k_S \partial \rho_S / \partial z = 0$) and heat flux is calculated by solving a simple heat conduction equation for the ground beneath the pond, with appropriate values chosen for the thermal conductivity at the pond bottom and also in the ground. The boundary condition for this soil heat conduction equation consists of a constant temperature layer specified at a desired depth in the ground. This might correspond for instance, to the groundwater table. Although salt does not actually cross the upper boundary, surface salinity is affected by evaporation and precipitation. This process is accounted for by using the flux boundary condition (Delnore, 1980):

$$k_S \frac{\partial \rho_S}{\partial z} = \left(\frac{\Phi_e}{\rho_o L_v} \psi\right)\rho_S \quad \text{at} \quad z = z_s \quad , \qquad (6.1)$$

where Φ_e = evaporative heat flux, L_v = latent heat of vaporization and ψ = precipitation.

The surface boundary condition for the thermal energy equation accounts for the heat fluxes due to convection, evaporation and absorption and emission of long- and short-wave radiation. Surface heat exchange plays an important role in the dynamics of the upper mixed layer. For instance, surface heat loss can cause an instability in the

density profile leading to rapid mixing over the unstable region. An unstable buoyancy flux will contribute kinetic energy to the mixed layer which may cause or enhance entrainment (see discussion leading to eq. 3.19 and also results in section 4.3.2). The fluxes due to evaporation, conduction and radiation are calculated to determine the net surface heat flux:

$$\phi_n = \phi_{sn} + \phi_{an} - \phi_{br} - \phi_e - \phi_c \tag{6.2}$$

where ϕ_n = net heat flux, ϕ_{sn} = net solar radiation, ϕ_{an} = net atmospheric radiation, ϕ_{br} = back radiation, ϕ_e = evaporative heat flux and ϕ_c = conduction. In the following evaluations for each of these terms, the units will be W/m^2. The estimation of ϕ_{an} is based on the empirical relation proposed by Swinbank (1963)(for clear sky radiation) and later modified for the effects of cloud cover;

$$\phi_{an} = 5.18 \times 10^{-13} (T_a + 273)^6 (1 + 0.17CC)^2 \tag{6.3}$$

where CC = cloud cover and T_a = air temperature. This expression is obtained from a black-body type radiation expression with an empirical estimate for emissivity which in general is a complicated function of vapor pressure and absolute temperature. The last term in parentheses is the correction for cloud cover. Note that ϕ_{an} consists of long-wave radiation which is essentially completely absorbed at the surface. Part of the radiation is reflected at the surface and this is accounted for in the coefficient of (6.3). The back radiation is calculated by assuming that the water surface acts like a black-body radiator:

$$\phi_{br} = \varepsilon\sigma_s(T_s + 273)^4 \qquad (6.4)$$

where ε = emissivity, σ_s = Stefan-Boltzmann constant and T_s = surface temperature.

The evaporative flux is written as

$$\phi_e = \eta_s \rho_o L_v f(W_z) (e_s - e_z) , \qquad (6.5)$$

where e_s = saturated vapor pressure at temperature T_s, e_z = actual vapor pressure at height z ($e_z = R_h e_s$, where R_h = relative humidity), η_s is a function of salinity (discussed below) and $f(W_z)$ is a "windspeed function" depending on the windspeed measured at a height z. Note that R_h should be measured over the water surface. Various forms for $f(W_z)$ have been proposed and a function of the form $f(W_z) = a + bW_z$ has been found to give acceptable results (see Helfrich et al., 1982). Since the pond surface temperatures should not be appreciably different from a natural water body exposed to the same meteorological conditions, the Lake Hefner formula (Kohler, 1954) is chosen, in which $\rho_o L_v f(W_z) = 3.75W_2$ (wind speed measured at 2 m). Evaporation is also affected by salinity as the presence of salt molecules reduces the "activity" of water molecules near the surface, thus reducing e_s. The most direct means of accounting for this effect is to multiply e_s in (6.5) by a decreasing function of salinity, but it is more convenient for modeling purposes to simply include a factor η_s which decreases ϕ_e according to the salinity. This approach will be satisfactory for the relatively low surface salinities of the UCZ. Salhotra et al. (1984) discuss the effect of salinity on evaporation for

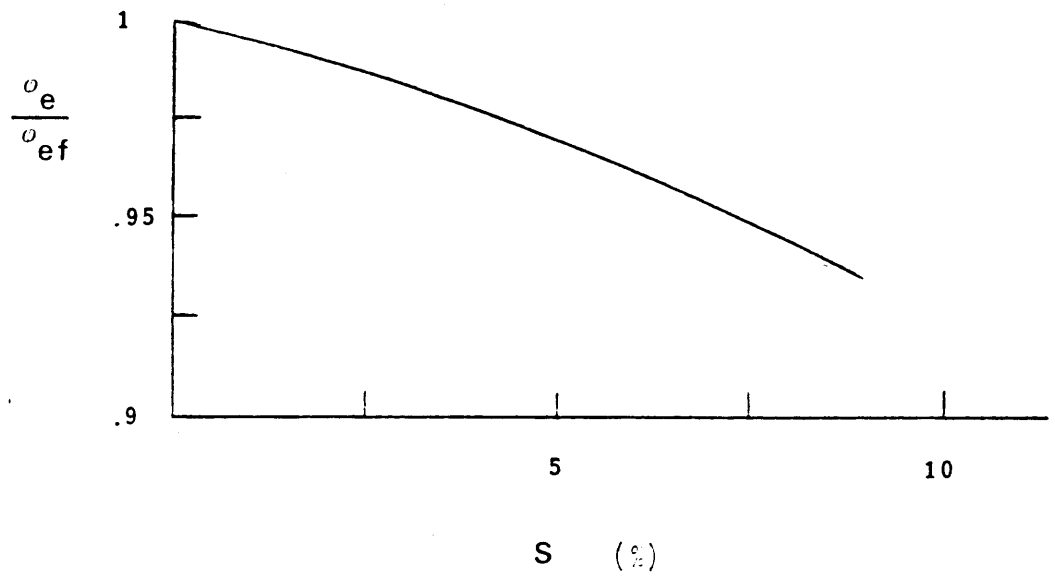

FIGURE 57 Reduction in Evaporation Due to Salinity (Interpolated from Turk, 1970.

higher salinities. η_s may be evaluated by interpolating data of Turk (1970) (Figure 57). For the relatively low salinities of the upper layer, η_s is approximated as $\eta_s = 1.0 - .0054S$. The conductive flux is related to the evaporative flux by means of the Bowen ratio (Bowen, 1926) and is estimated by

$$\phi_c = 0.255\ f(W_z)(T_s - T_a) \tag{6.6}$$

where $f(W_z)$ is the same windspeed function used for calculating ϕ_e.

Evaluation of ϕ_{sn} depends on how solar radiation absorption is modeled and we will first discuss the calculation of ϕ_s=solar radiation flux at depth z. This is an important calculation since ϕ_s provides the energy for warming the pond. Incoming radiation of a given wavelength λ is attenuated as it passes through the water column by the effects of absorption and scattering. Detailed formulations for the energy flux based on radiative transfer theory have been given (e.g., Viskanta and Toor, 1972, 1978) but for the present purpose it is assumed that the reduction in radiant intensity at a given wavelength is proportional to the intensity and to the distance travelled through the water (Lambert's law), i.e.

$$-d\phi_s(\lambda) = \eta(\lambda)\phi_s(\lambda)\left|dz\right|, \tag{6.7}$$

where η is an extinction coefficient. Note that z here is used as the path length of radiation in the water. In general, the path length from the surface to any given depth will depend on the solar angle. For simplicity, it is assumed here that z is measured vertically. With z measured positive downward and assuming η is constant with depth, (6.7)

can be integrated to give

$$\phi_s(\lambda,z) = \phi_{s0}(\lambda)\exp[-\eta(\lambda)(z - z_s)] \quad , \qquad (6.8)$$

where $\phi_{s0}(\lambda)$ is the net solar radiation incident at the water surface at the wavelength λ. In order to obtain the total radiation reaching a given depth, (6.8) must be integrated over the entire spectrum:

$$\phi_s(z) = \int_0^\infty \phi_s(\lambda,z)d\lambda = \int_0^\infty \phi_{s0}(\lambda)\exp[-\eta(\lambda)(z-z_s)]d\lambda \qquad (6.9)$$

Because of variations of both ϕ_{s0} and η with wavelength, different bandwidths contribute in varying degrees to the total radiation reaching a given depth, as illustrated in Table 5.

Several approaches have been proposed to predict total radiation as a function of depth. Perhaps the most straightforward of these is to use a summation approximation to the integral in (6.9). Experimental results have shown that after a sufficient depth the total radiation decreases in an approximately exponential manner (Dake and Harleman, 1969). A factor must then be included to account for the longer wave portion of the solar radiation absorbed near the surface. The resulting equation is then written as

$$\phi_s(z) = \phi_{s0} \sum_{i=1}^{M} (1-\beta_i) \exp[-\eta_i(z - z_s)] \quad , \qquad (6.10)$$

where M is chosen depending on the accuracy desired. β_i is the fraction of energy absorbed near the water surface for the bandwidth

Table 5

Spectral Energy Distribution of Sunlight Passing Through Different Water Thicknesses, Expressed in Thousandths of The Total Radiative Flux

Wavelength (μ)	Thickness of the Water Layer								
	0	0.01 mm	0.1 mm	1 mm	1 cm	10 cm	1 m	10 m	100 m
0.2-0.6	237	237	237	237	237	236	229	172	14
0.6-0.9	360	360	360	359	353	305	129	9	--
0.9-1.2	179	179	178	172	123	8	---	---	--
1.2-1.5	87	86	82	63	17	---	---	---	--
1.5-1.8	80	78	64	27	--	---	---	---	--
1.8-2.1	25	23	11	--	--	---	---	---	--
2.1-2.4	25	24	19	1	--	---	---	---	--
2.4-2.7	7	6	2	--	--	---	---	---	--
2.7-3.0	0.4	0.2	--	--	--	---	---	---	--
Total	1000.0	993.7	952.7	859.4	730.2	549.3	358.1	181.5	13.9

indexed by i and η_i is the corresponding extinction coefficient. Rabl and Nielsen (1974) proposed a 4-term expression, with values for β_i and η_i based on the data of Table 5. A model using forty terms has also been proposed, but it has been shown that a 4-term fit to the results generated with this model performs sufficiently well (Hull, 1980).

A simple and convenient model to calculate $\phi_s(z)$ is to assume that water is a "gray absorber," that is, η is independent of wavelength. This is equivalent to setting M=1 in (6.10):

$$\phi_s(z) = (1-\beta)\phi_{so} \exp[-\eta(z-z_s)] \quad , \tag{6.11}$$

where $\phi_{so} = \int_o^\infty \phi_{so}(\lambda)d\lambda$ is the total net solar radiation at the surface.

The closeness with which (6.10) or (6.11) can approximate the actual attenuation of sunlight through water, especially near the surface, depends on the optical quality of the water. The sensitivity of the wind-mixing model to the value of $\phi_s(z)$ calculated by (6.10) or (6.11) is examined in Section 6.2.

Additional models have been proposed to model $\phi_s(z)$, but these are primarily empirical in nature. Table 6 lists several examples and Figure 58 shows a comparison of the various models. It should be noted that when applying either of these models field measurements should be made to determine the clarity of the water so that the coefficients may be adjusted to fit localconditions. For instance, the coefficient values in models (2) - (4) were chosen to reproduce clear sea water data.

TABLE 6

Expressions for $\phi_s(z)/\phi_{so}$

	Reference	$\phi_s(z)/\phi_{so}$
(1)	Rabl and Nielsen (1974), Hall (1980), Atkinson and Harleman (1983a)	$\sum_{i=1}^{M} (1-\beta_i) \exp[-\eta_i(z-z_s)]$
(2)	Ivanoff (1977)	$\exp[-\eta(z-z_s)]$, $\eta=.05z^{1.22}$
(3)	Bryant and Colbeck (1977)	$0.76 - 0.08 \ln(z-z_s)$
(4)	Zaneveld and Spinrad (1980)	$\exp(-c_1 z)[1-0.42 \tan^{-1}(c_2 z)]$

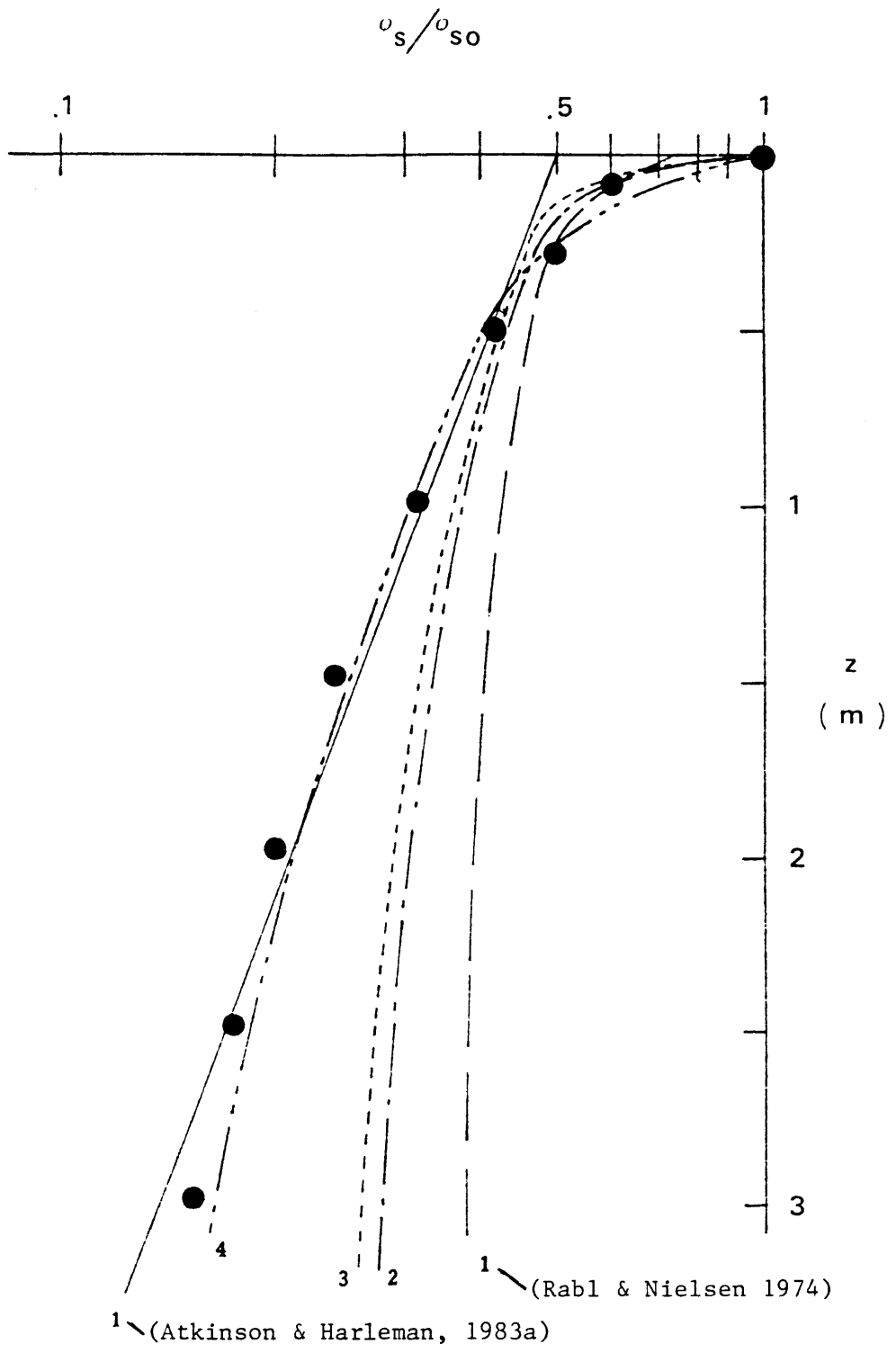

FIGURE 58 Comparison of Radiation Models Listed in Table 6 With Data For Weinberger Type 3 Water (Weinberger, 1964)

As shown in Section 6.2 the use of (6.11) to calculate $\phi_s(z)$ is adequate as long as appropriate values for η and β are used. Then, assuming an average value for reflection as 6% of the incident radiation, we have

$$\phi_{sn} = 0.94\ \beta\ \phi_{si} \quad . \tag{6.12}$$

where ϕ_{si} is the incident solar radiation.

The surface boundary condition for the heat equation is then

$$-\kappa_T \frac{\partial T}{\partial z} = \phi_n \quad \text{at} \quad z = z_s \quad , \tag{6.13}$$

where ϕ_n is evaluated from (6.3) - (6.12).

6.1.1 Incorporation of Entrainment Algorithm

After (1.2) and (1.3) are evaluated, the wind-mixing algorithm is applied. From the discussion in Section 1.1.2, Rf must be calculated by substituting an entrainment relation into (1.9). If all the kinetic energy is used to increase the potential energy (Rf = 1), then

$$u_e/u_* = 2C_1 R_i^{-1} \tag{6.14}$$

which is very close to the relationship proposed by Kato and Phillips (1969). However, as previously discussed, there is evidence to suggest that this inverse Richardson number law is not valid over a large range of Ri values, particularly in the higher range ($\gtrsim$200). This observation, coupled with the fact that an earlier version of the M.I.T. wind-mixing model tended to overpredict the upper mixed layer depth when operating under this assumption (Hurley-Octavio et al., 1975), resulted in the

modification introduced by Bloss and Harleman (1979). They used the entrainment relation developed by Zeman and Tennekes (1977) and discussed in Chapter 3. The current model uses (3.31) to define u_e/σ and the change in mixed layer depth is then calculated from the change in potential energy.

The results of the entrainment tests may be used to estimate some of the coefficients in the entrainment model developed in Chapter 3 (eq. 3.31). First, however, it should be noted that the best scaling of data for the wind entrainment experiments was obtained using the return flow velocity along the interface, which seemed to account for differences in fetch. It is not expected that these kinds of measurements would be routinely available for modeling field conditions and the modeler will probably be forced to use wind speed measurements to estimate entrainment. If water velocity measurements were available, the results in Figure 51 might be used directly, which suggests that

$$\frac{u_e}{u_r} \propto Ri_r^{-1} \tag{6.15}$$

where $Ri_r = g'h/u_r^2$. In the absence of water velocity measurements u_* must be determined from u_{*a} obtained by wind speed measurements. A momentum equation might then be used to obtain $\bar{u}$, the average velocity in the layer, a possible estimate for u_r (this approach was first suggested by Pollard, Rhines and Thompson (1973) in their mixed-layer model). However, the relationship between u_* and u_r becomes more complicated under unsteady

conditions and when effects of finite fetch are considered, as will normally be the case for solar ponds. There is some uncertainty in extrapolating the present results to field conditions, considering the difference in length scale between the laboratory facility and a working solar pond.

From the above considerations it seems best to calibrate the model in terms of u_*. We note once again that the model based on the present results may underpredict field entrainment slightly due to the effect of the end walls in the experiments. The coefficients to be determined are C_F, C_{SH}, C_D, C_T, C_S, and C_V. With finite fetch, u_r is substituted for $\bar{u}$ in (3.31) as a more appropriate scaling for shear production near the interface. The present experiments do not provide any new information for the values of C_D (no stratification in entrained layer, i.e., $\Gamma = 0$), C_t, C_T or C_S (experiments not performed with Ri_* sufficiently low or high). Therefore, previously determined values for C_D and C_t are used from Table 4: $C_D = 0.01$ and $C_t = 2.25$, and estimates for C_T and C_S follow from the discussion in Section 3.1: $C_T = C_S \tilde{=} 3 \times 10^{-4}$. The only information available for determining C_V comes from previous experiments (Table 4) and the present grid experiment. However, recall that for the grid experiment the coefficient multiplied w_*, due to the greater uncertainty for that parameter, but (3.14) uses C_V multiplying u_* and in the field there is some uncertainty in evaluating both w_* and u_* as appropriate scaling velocities. The relative

importance of w_* and u_* is determined either by multiplying u_* by C_V or w_* by $1/C_V$, but the magnitude of σ will depend on which multiplication is used. In order to be consistent with (3.14), C_V will be chosen to multiply u_*. Previous results listed in Table 4 indicate $C_V \simeq 2$ and this is consistent with the value $1/D_V = .5$ used to correlate the grid results. Now, as noted by Zeman and Tennekes (1977), a turbulent front entraining into neutrally stratified fluid moves at a rate given by $u_e/\sigma = 0.3$ (this was also mentioned in Chapter 3). For neutrally stratified fluid Ri = 0 and (3.31) reduces to $u_e/\sigma = C_F/C_t$, which then gives $C_F = 0.3\ C_t/C_V$, where $w_* = 0$ is assumed. Then, with the above values we have $C_F = 0.34$. The last parameter to be determined is C_{SH}, which is obtained by comparison with the wind-experiment results. A good fit to the data for the 7 m section was obtained with $C_{SH} = 1.1$ (see Figure 46). The entrainment model is then

$$\frac{u_e}{\sigma} = \frac{0.34 + 1.1\left(\frac{\bar{u}}{\sigma}\right)^3 - \varepsilon_2' + 3 \times 10^{-4}\left(Ri_T\, Pe_T^{-1/2} - Ri_s\, Pe_s^{-1/2}\right)}{2.25 + Ri} \qquad (6.16)$$

For the conditions considered in the present experiments $w_* = 0$ and (6.16) may easily be evaluated for u_e/u_* by noting that $\sigma = C_V u_*$ and this was done for plotting the equation in Figure 46. Note that (6.16) overpredicts the entrainment for the 3.5 m section, and a reasonable fit was obtained only by setting $C_{SH} = 0$.

This indicates that shear production was much less important in the shorter section than in the longer section and supports the discussion in section 5.2.1.

The entrainment rate calculated by (6.16) depends not only on the various proportionality coefficients but also on the specific values of parameters describing the stratification. This is seen in the expression for the leakage term ε_2' (equ. 3.10). That is, u_e/σ is not a simple function of Ri, but also depends on the individual values of N, $\Delta\rho$, h and σ. In addition, the value of the mean velocity $\bar{u}$ is important in evaluating the shear production term. In order to see the effects of different stratification conditions and also to look at the sensitivity of the model to some of the coefficients, three representative physical systems were chosen and (6.16) was calculated for each of these systems while varying the coefficients. The three systems include a solar pond, an inland fresh water lake or reservoir and an ocean. For the solar pond values of h = 50 cm, $g' = 20$ cm/s^2 and $N = 8$ s^{-1} were chosen. This corresponds to a salinity step of about 3% and a salinity gradient of approximately 12%/m. Note that by setting h and g', σ is obtained by choosing Ri. The lake values assumed h = 5 m, $g' = 2$ cm/s^2 and $N = 0.6$ s^{-1} and for the ocean h = 30 m, $g' = 0.7$ cm/s^2 and $N = 0.2$ s^{-1}. These values correspond roughly to temperature steps of 15°C and 5°C across the thermocline and temperature gradients of 2°C/m and 0.2°C/m for the lake and ocean systems, respectively. A value of $\bar{u} = 1$ cm/s was arbitrarily set for all three systems.

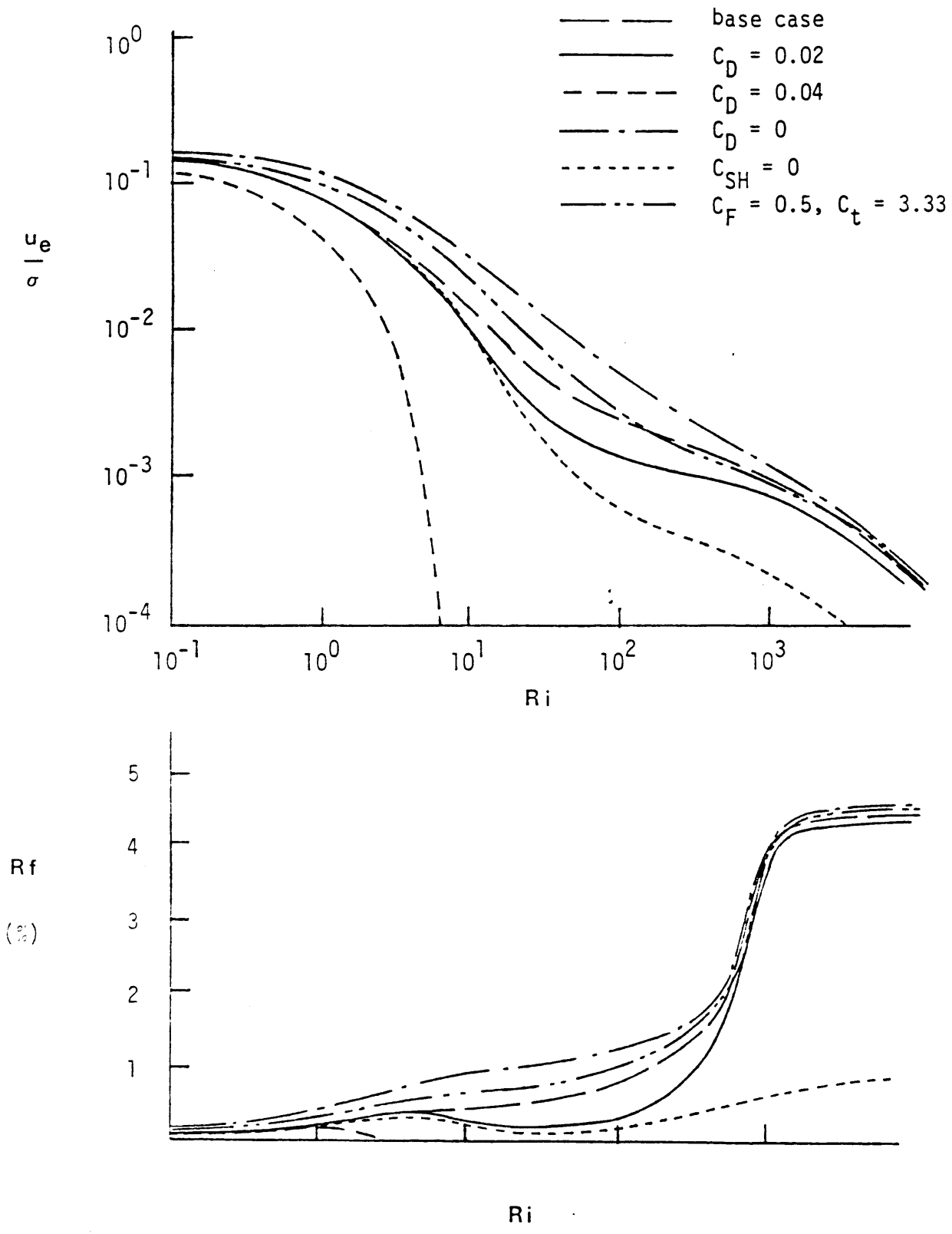

FIGURE 59 u_e/σ vs. Ri and Rf vs. Ri for 3 Different Physical Systems (See Notes)

a) solar pond

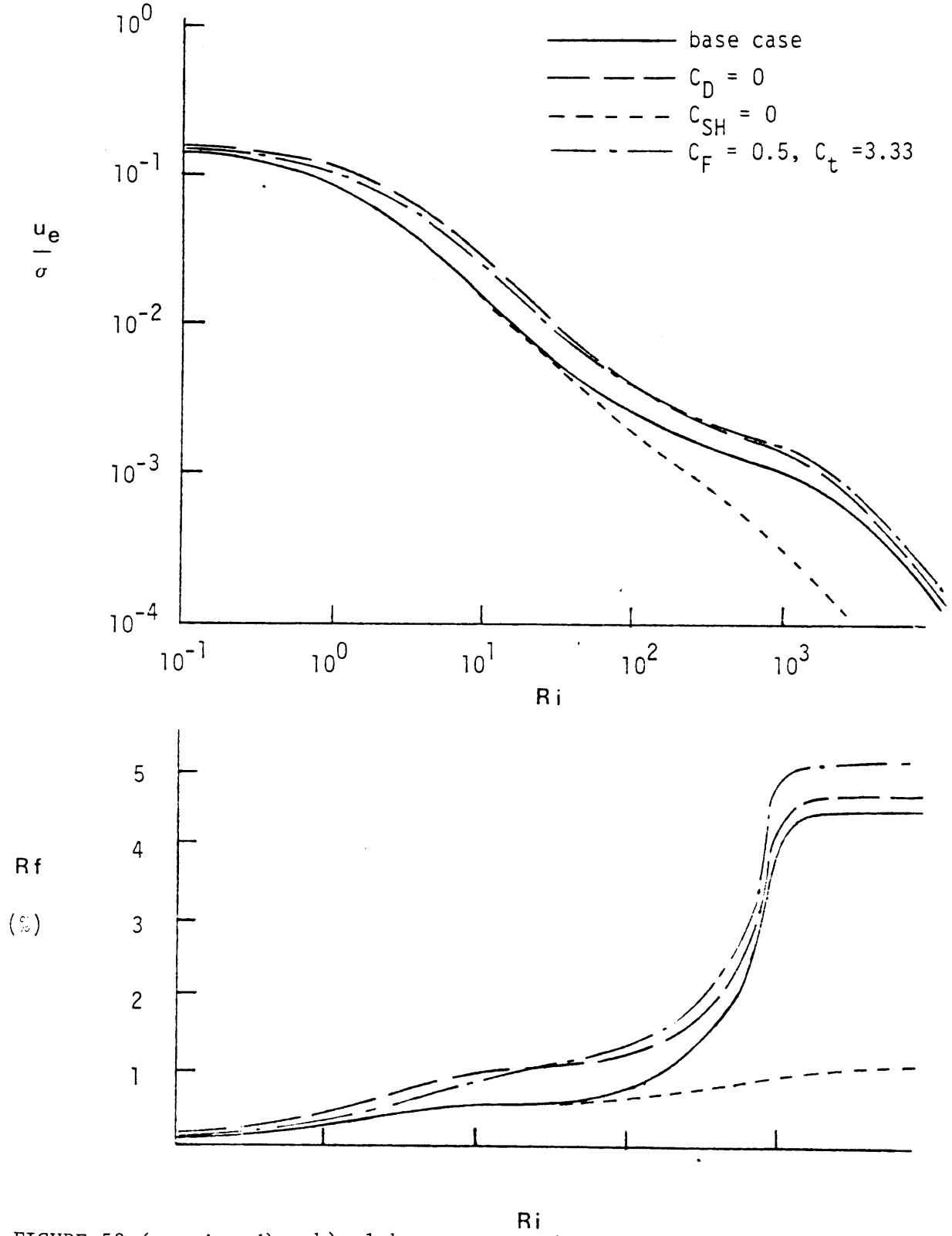

FIGURE 59 (continued) b) lake or reservoir

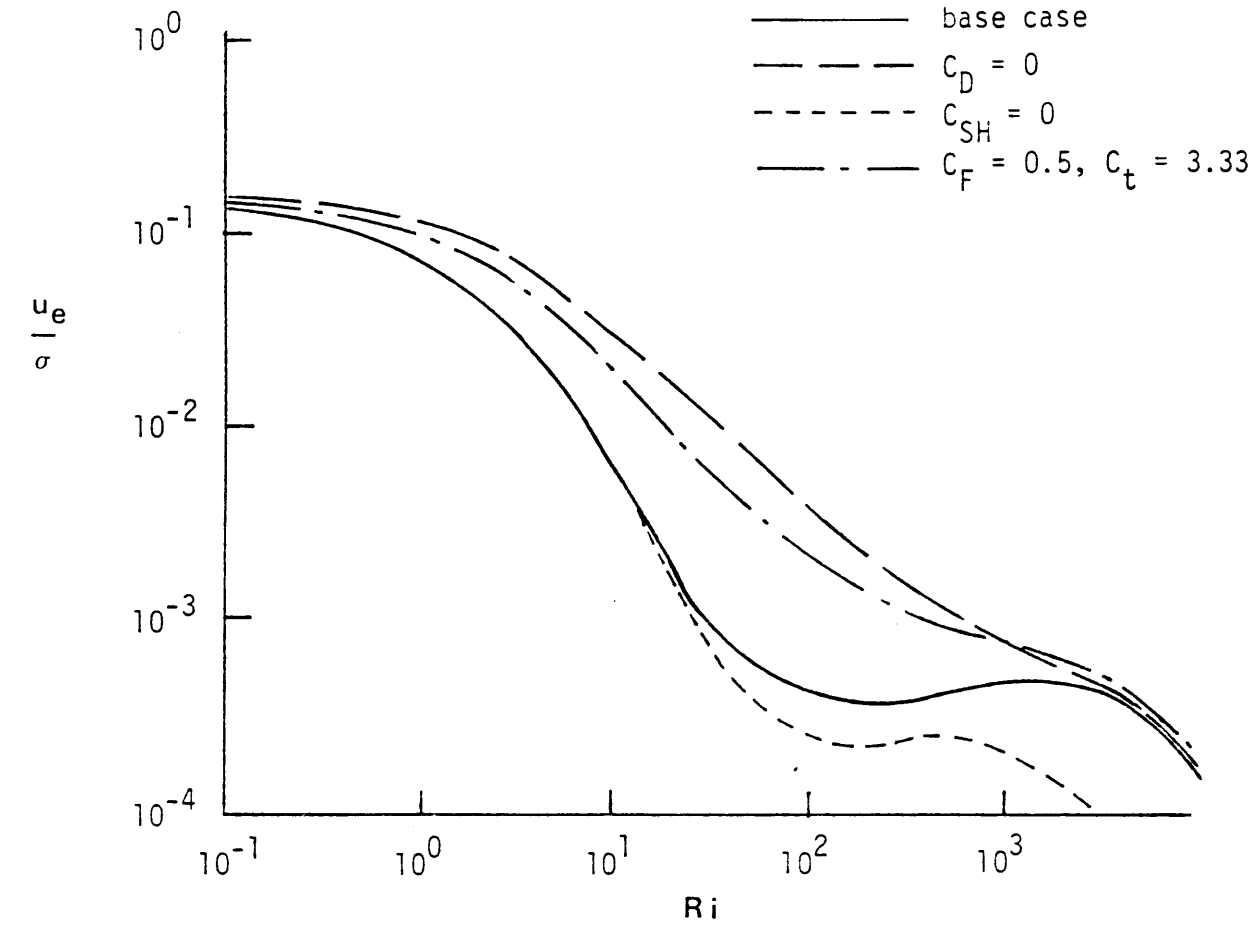

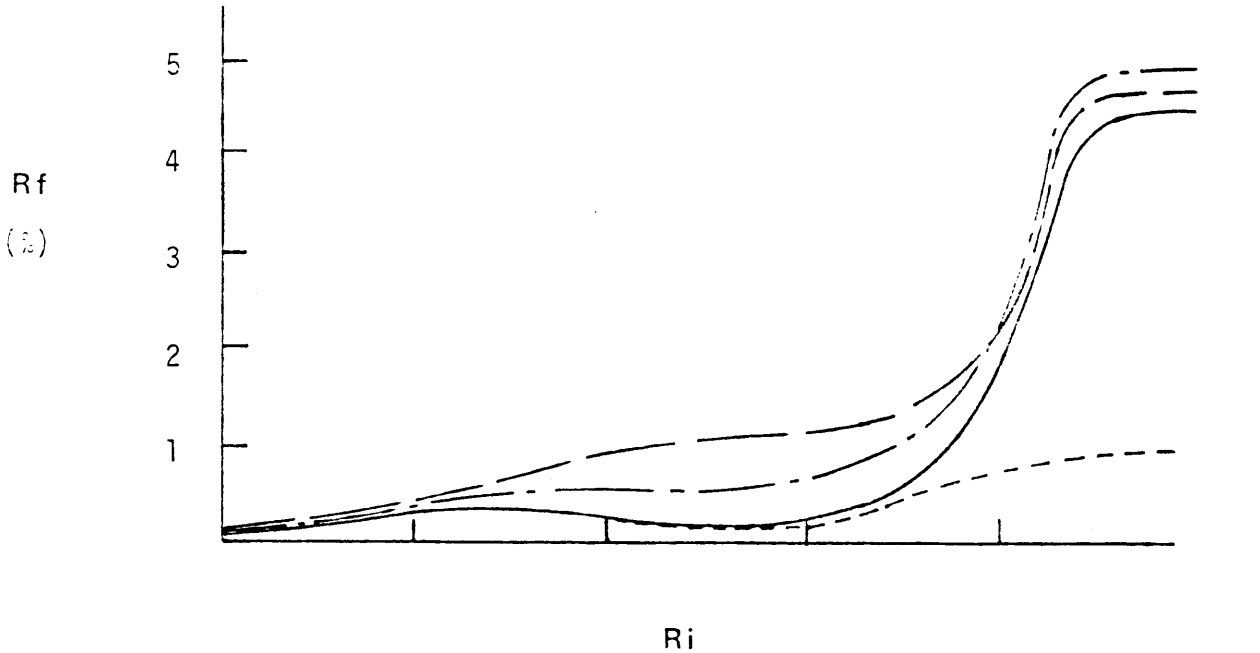

FIGURE 59 (continued) c) ocean

Notes for Figure 59

Each curve is calculated from (6.16) and (1.9), using parameter values for the base case:

$$C_D = 0.001,\ C_F = 0.34,\ C_V = 2,\ C_l = 16,$$
$$C_t = 2.25,\ C_{SH} = 1.1,\ \text{and}\ C_r = C_S = 3 \times 10^{-4}$$

Conditions assumed for each system:

		h(cm)	g' (cm/s^2)	N(s^{-1})	$\bar{u}$ (cm/s)
a)	solar pond	50	20	8	1
b)	lake	500	2	0.6	1
c)	ocean	3000	0.7	0.2	1

Results of the calculations are shown in Figure 59a - 59c which also include corresponding values for Rf. As might be expected, there is considerable sensitivity to the value of C_D, which parameterizes the leakage term. This is particularly true for the solar pond, where $\Delta\rho$ (g') and N are both relatively large, and for the ocean, where h is large. Further experiments will be needed to refine the value of C_D, since the present experiments do not address this problem. At high Ri the value of C_D becomes less important since ε_2' is a decreasing funciton of Ri. At large Ri (6.16) approaches the same inverse Ri form for each system, as shown by the horizontal asymptotes in the curves for Rf. It should be noted that u_e (and Rf) for each of the curves in Figure 59 will eventually go to zero when Ri is sufficiently large, due to the diffusive terms (see discussion in Section 3.1).

Sensitivity of the model to the value of C_F is seen to be relatively minor, but there is a noticeable effect. The value of C_{SH} is seen to have a significant effect, though the calculations here really check sensitivity to the term ($C_{SH}\ \bar{u}^3\ /\sigma^3$) and not to C_{SH} alone, since $\bar{u}$ is fixed. The calculations here are actually somewhat artificial in this respect, since a value of $\bar{u}$ = 1 cm/s may be inconsistent with the applied shear stress at high Ri (i.e., low σ). In order to keep ($\bar{u}/\sigma$) from becoming arbitrarily large an upper bound of unity was set. The curves in Figure 59 are plotted to give an idea of the shape of the function represented in (6.16), butthe above limitation should be kept in mind. In order to apply

(6.16) in a numerical model, values of g', N, h and $\bar{u}$ must be known.

When calculating Rf a value for $C_1 = u_s/u_*$ must be determined. Upon comparing u_s with the averaged value of u_* for each test section, the results shown in Figure 60 were obtained. An averaged value of $C_1 = 16$ was found, but it should be noted that this value is obtained for very steady conditions and field values will probably be much less due to the unsteadiness of the wind field. Estimates for Rf shown in Figure 59 may therefore be somewhat low, although maximum values of around 5% are consistent with the field observations of Kullenberg (1977).

Some further explanation is required for the evaluation of C_F. Above, it has been assumed that C_F is a constant, whereas in the grid-mixing model it was derived as a function of Ri and Pe, $C_F = C_1\ Pe^{-1/2} + C_2\ Ri^{-1/2}$ (see eq. 3.24). (Note that this C_1 is not the same parameter as the value found above when evaluating Rf.) Due to differences in scaling (length scale, primarily), values for C_1 and C_2 determined in the grid experiments are not expected to hold for the wind tests directly. Also, there was no attempt made to look at different diffusivities in the wind tests (i.e., temperature stratification only), so values of $Pe = u_*h/k_S$ did not vary significantly and it is not possible to check on possible effects of diffusivity from the present results. Note that values of Pe defined in this way are in the range $Pe \sim O(10^7)$, which implies that $C_1 \sim O(10^3)$ in order for the term $C_1 Pe^{-1/2}$ to make a noticeable contribution to the calculated

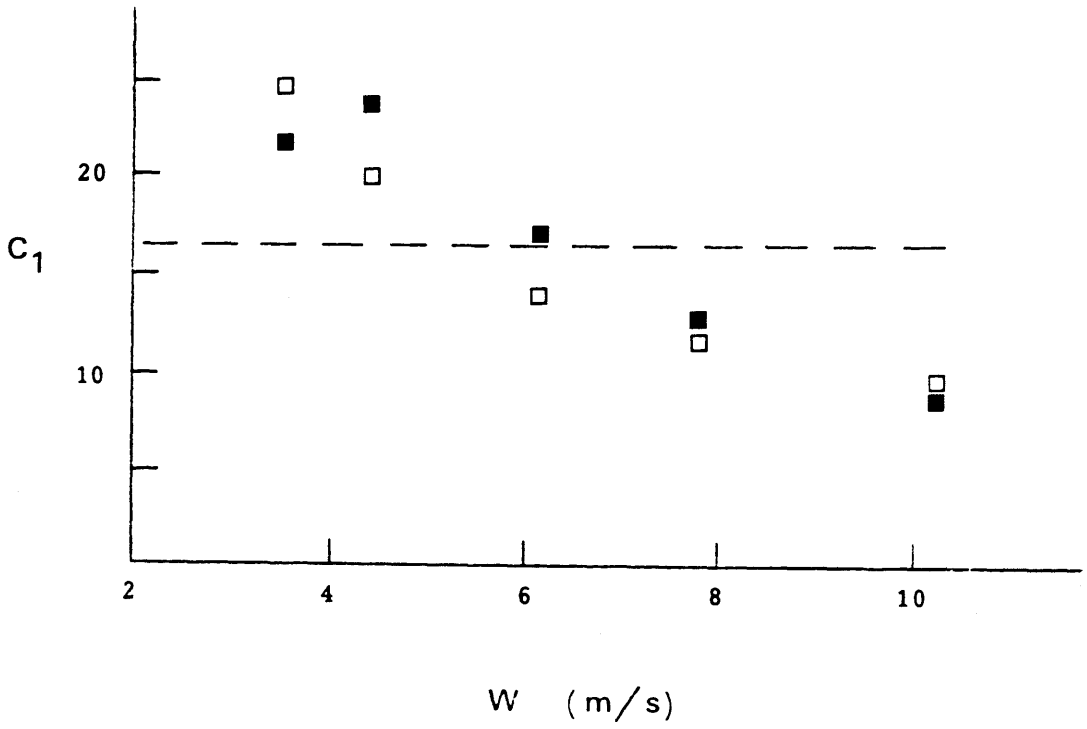

FIGURE 60 Calculated Values of $C_1 = u_s/u_*$ for ■ 3.5 m Section and □ 7 m Section; Dashed Line Gives Mean Value for C_1

entrainment. Similarly, with Ri ~ $0(10^2 - 10^4)$ in these tests, C_2 would be of 0 $(10\text{-}10^2)$. Since (6.16) appears to reproduce the data reasonably well with a constant C_F, it is assumed that the $Ri^{-1/2}$ term is negligible in calculating C_F (i.e., $C_2 \ll 0(1)$) and $C_1 Pe^{-1/2} \sim 0.34$, as above. More detailed calculations of C_1 and C_2 were not deemed necessary here, since the data did not warrant it. Future experiments might consider looking in more detail at the possible dependnce of C_F on Ri and Pe, as suggested above.

In order to evaluate the wind-induced change in potential energy of the mixed layer, the flux of kinetic energy across the air-water interface due to wind shear must be determined. Equation (1.5) may be used for this purpose as long as τ_s and u_s can be found. As previously mentioned, it is assumed that:
$u_s \propto u_*$ and $u_* = (\tau_s/\rho_0)^{1/2}$. Following Bloss and Harleman (1979) we asssume that the total momentum flux across the surface is used for TKE production via breaking of small waves or direct viscous shear (i.e. the part of the wind stress that might be used for the drag of longer waves is neglected - this will be true for fully developed wave fields). Then the shear stress across the surface is continuous: $\tau_s = \rho_0 u_*^2 = \rho_a u_a^2$, where the subscript a refers to the ambient air.

The total wind shear is related to the wind velocity measured at a given height by means of a drag coefficient:

$$\tau_s = C_z \rho_a W_z^2 \quad . \tag{6.17}$$

In general, C_z will depend on W_z. The wind speed profile over the water surface is assumed to follow the usual logarithmic profile (5.1), so we have

$$C_z^{-1/2} = \frac{\kappa}{\ln(gz/\alpha_c C_z W_z^2)} \tag{6.18}$$

where $\alpha_c = gz_o/u_{*a}^2$ = Charnock's (1955) constant. Charnock suggested that $\alpha_c = 0.011$, though other investigators have suggested values ranging from 0.008 - 0.035 (Amorocho and Devries, 1980; Wu, 1980).

It should be noted that in writing (5.1), we are implicitly assuming that the pond has large enough area so that a logarithmic profile would be established over much of the surface. The validity of this assumption depends on fetch. The result (6.18) will be valid as long as z (anemometer height) is chosen to take wind speed measurements where the log profile is valid. Wu (1980) suggests

$$z = \begin{cases} 10 \text{ cm}, & \text{Re} < 5 \times 10^7 \\ 7.35 \times 10^{-5} \text{Re}^{2/3} (\text{cm}), & 5 \times 10^7 < \text{Re} < 5 \times 10^{10} \\ 10 \text{ m}, & \text{Re} > 5 \times 10^{10} \end{cases} \tag{6.19}$$

where $\text{Re} = W_z X/\nu$ = fetch Reynolds number. The wind over small ponds is probably better characterized as a random mixture of eddies with some dependence on the geometry of the pond and its surroundings, and it is not clear how best to parameterize the transfer of energy from wind to water in this case. An empirical adjustment of the drag coefficient in (6.17) may provide a reasonable estimate of the shear transfer, but more

detailed studies are required.

In addition to the solution of the convection/diffusion equations and wind-induced entrainment, the water column is checked for stability according to the criterion (1.23), with density calculated by (4.1). When this criterion is violated thermohaline convection may occur. The effect of this instability has previously been modeled by using eddy values in convecting regions rather than the molecular values κ_T and k_S (Meyer, 1982). A further stability requirement is that density must increase with depth, but this will always be true as long as (1.23) is satisfied. These conditions are checked at each iteration (time step) of the model and adjacent layers are mixed together to eliminate any density instabilities. This procedure also effectively accounts for mixing induced by an unstable profile resulting from surface cooling. The effect of entrainment by penetrative convection is accounted for by including an estimate for w_* in defining σ in the entrainment relation, as previously discussed.

Hydrodynamic stability with respect to selective withdrawal for heat extraction may also be considered. This problem has been studied previously and criteria have been developed for estimating the depth of the withdrawal layer in solar ponds (Daniels and Merriam, 1975; Elata and Levin, 1965). This effect is not included in the present version of the wind-mixing solar pond model, since it is assumed that a pond would be operated (i.e., flow rates would be chosen) so that the withdrawal layer would be confined within the storage zone.

Since the effects of heating and wind-mixing have been decoupled, the surface temperature calculated from (1.2) will be slightly changed

after the wind-mixing algorithm has been applied. Therefore, following the first heating and mixing steps, the surface heat flux is recomputed using the slightly changed temperature of the wind-mixed layer. An iterative procedure is then used in each time step in which the heating and mixing steps are successively applied until there is no significant change in the surface heat flux. The basic structure of the model is summarized in Figure 61.

6.2 Simulation results and sensitivity

In order to test the sensitivity of the model to some of the factors discussed above, results have been obtained for a number of 1-yr simulations using the wind-mixing model. A vertical step size $\Delta z = 0.1$ m and a time step $\Delta t = 3$ hr were used. Meteorological data for the period from April 1974 to April 1975, from an area near Richmond, Virginia, was used for each simulation. In order to keep the following comparisons uncomplicated, the effects of precipitation and evaporation on the overall water budget have been ignored. The hypothetical pond being modeled is assumed to have a surface area of 1 km^2 and (constant) 3 m depth. Edge and ground losses are neglected and the initial temperature distribution, corresponding to 1 April 1974, is assumed to be isothermal at 10°C. In order to examine the effect of changing some of the features of the model a "base case" was defined. This base case pond had an initial storage layer depth of 1.5 m and salinity decreasing linearly from 15 per cent (by weight) - the salinity of the storage layer - to 0 per cent at the surface (Figure 62). Molecular values for κ_T and k_S were used and solar radiation was expressed as in (6.11) with $\beta = 0.5$ and

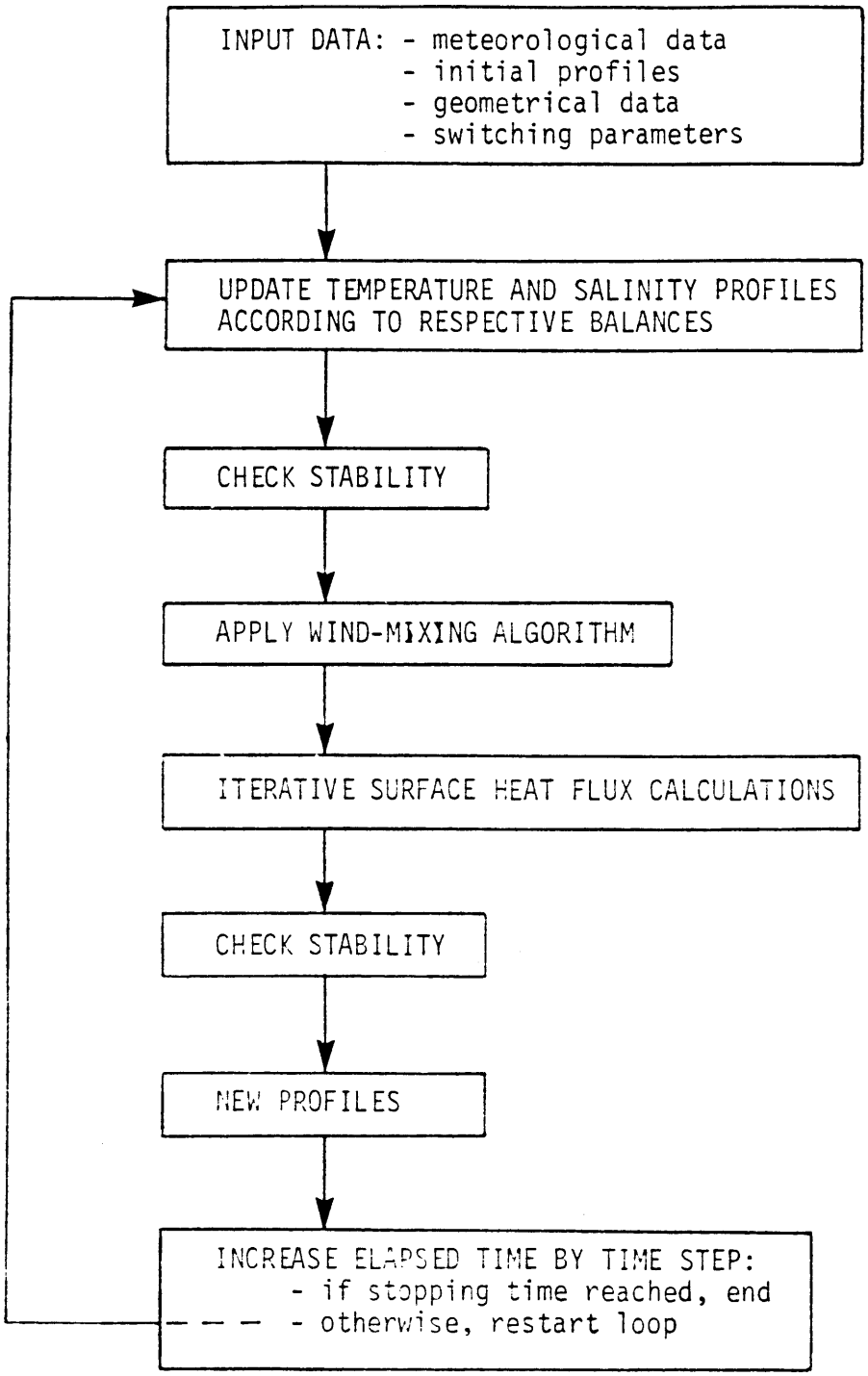

FIGURE 61 Basic Structure of Numerical Simulation Model

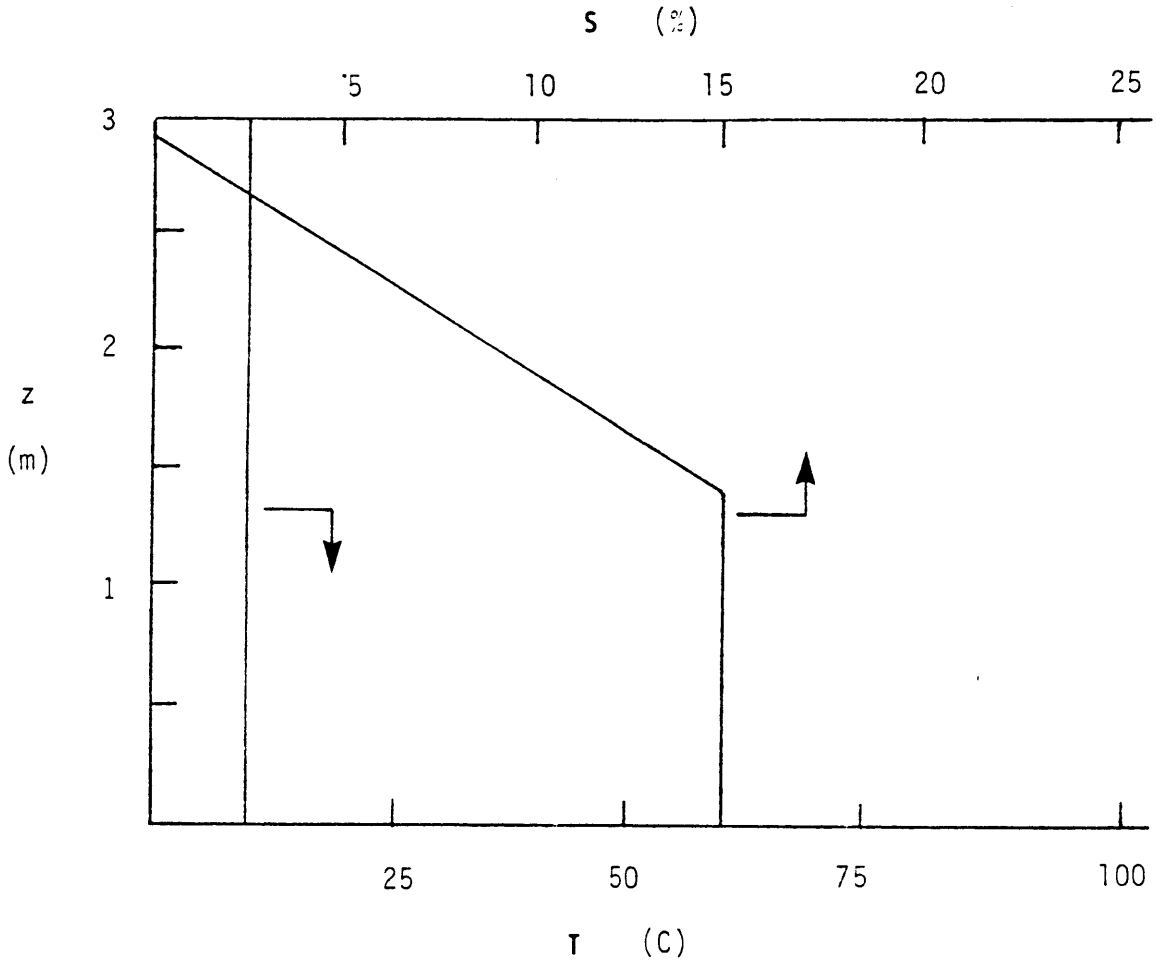

FIGURE 62 Initial Profiles For Simulation

$\eta = 0.5\ m^{-1}$. No energy extraction was assumed and the pond bottom was assumed to be well-insulated.

Parameter values for the base case were chosen to represent a typical pond which is first filled in early spring. Predicted profiles at 6 months and 12 months for two different wind-mixing models may be seen in Figure 63. For this comparison the wind-mixing model developed in the previous section was compared with the model of Bloss and Harleman (1979). However, a value of $C_1 = 1$ was assumed for these simulations, which is consistent with the value assumed by Bloss and Harleman. Then the relationship for Rf will still have the same shape as shown in Fig. 59, but all the values should be multiplied by 16. A comparison between the two models then shows that the Bloss and Harleman model predicts greater mixing for low Ri, but less mixing for large Ri (see Figure 12). Since Ri is large in solar pond conditions, it would be expected that (6.16) should predict slightly greater mixing and this is seen in the results in Figure 63.

The step in the profiles at the top of the storage zone for times greater than three months is due to the mixing of two adjacent layers to eliminate an instability in the density profile. Similar step structures were very evident in the predicted profiles for simulations in which a small extinction coefficient was used, allowing a greater amount of solar radiation to penetrate to greater depths. These internal convecting regions have been observed in man-made solar ponds and also in natural water bodies with downward gradients of both temperature and salinity. For example, Nielsen (1976) reported the presence of convective layers due to instabilities associated with side wall heating which propagated

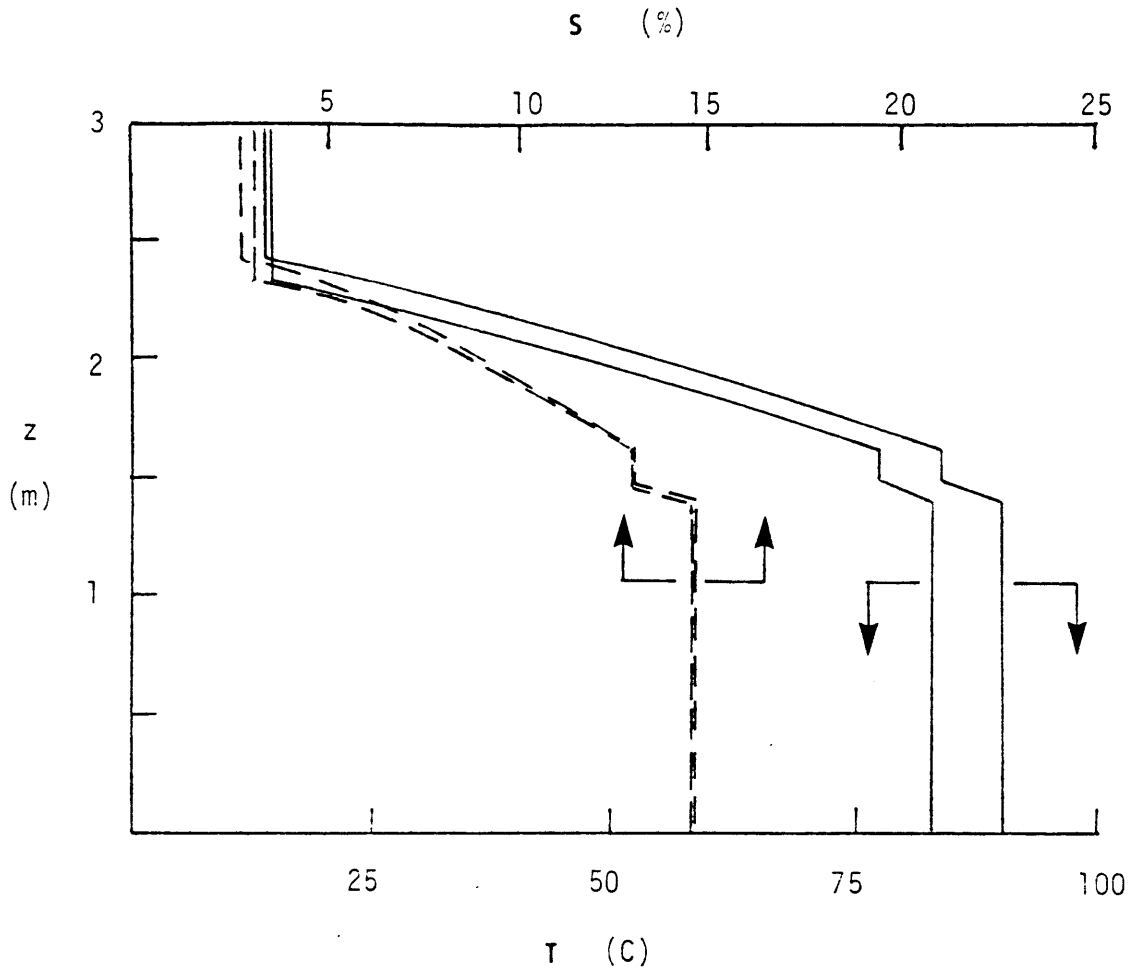

FIGURE 63 Simulation Results, Where the Curves Showing Greater Mixed Layer Depth Resulted From Using (6.16) to Evaluate Entrainment While the Second Set of Curves Resulted From Using The Bloss and Harleman (1979) Model

a) Profiles after 6 months

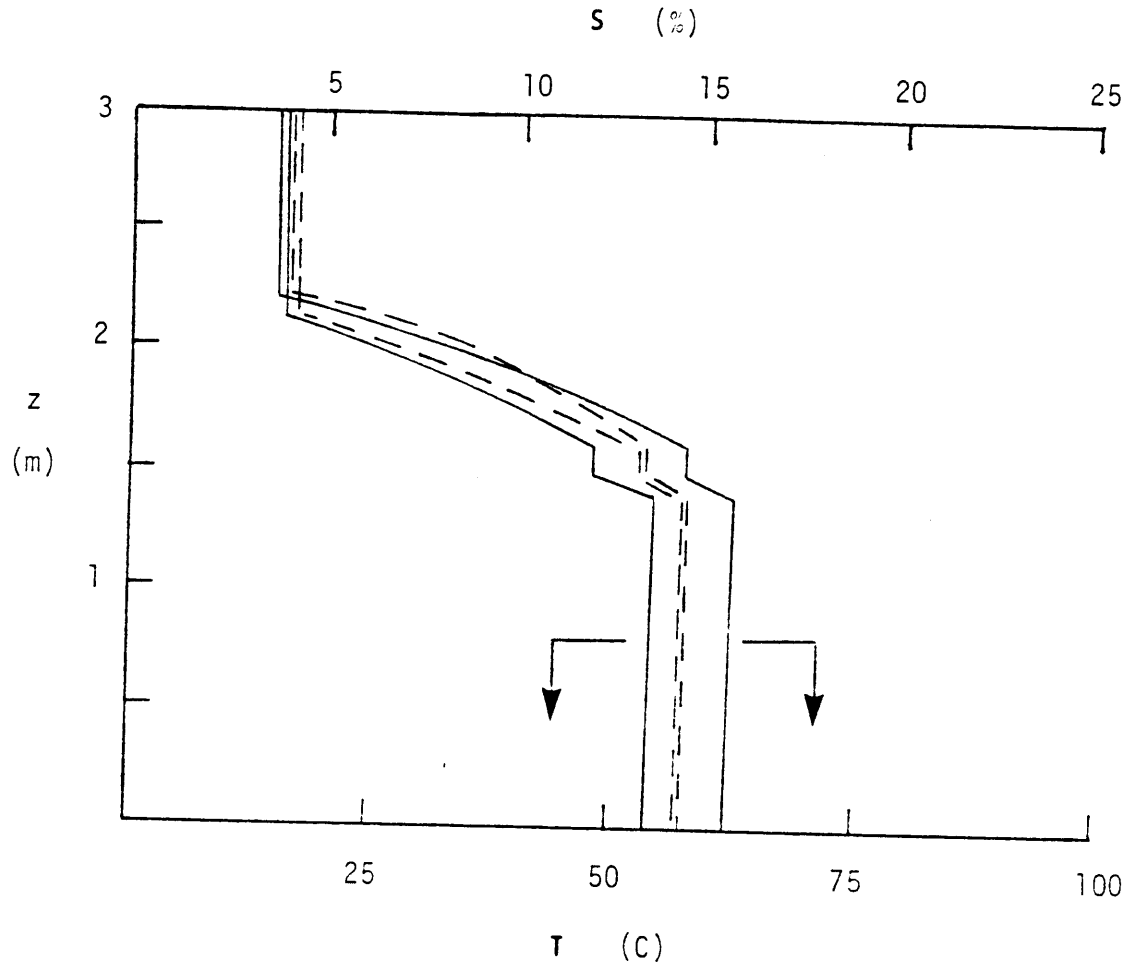

FIGURE 63 (continued) b) Profiles after 12 months

horizontally throughout the pond. It is interesting to note that the upper mixed layer grows to about 0.75 m after 1 yr. This layer grows very quickly from the initial value of zero (Figure 62) to about 0.45 m within the first month (Figure 64). It then remains at a relatively steady value until the last few months of the simulation. The mixing events are well-correlated with periods of relatively strong winds, as may be seen from Figure 65. In particular, the greatest mixing occurs near the beginning and end of the simulation period, which is also the time when winds are the strongest.

It is interesting to note that for simulations where there was no wind-mixing, the stabilizing salinity gradient was apparently strong enough to prevent any appreciable mixed layer growth by penetrative convection since there was no deepening of the UCZ for this case. Actually, the finite difference scheme imposes a minimum upper mixed layer depth equal to the grid thickness and any mixed layer depth that is not appreciably greater than 10 cm would not be evident. A more detailed study would necessitate the use of a finer grid structure.

An upper mixed layer depth of ~0.75 m is much greater than has been assumed in earlier models and indicates that wind-mixing can indeed pose an important problem in large-scale solar pond design. The growth of the mixed layer is dependent upon the density gradient in the non-convecting zone. This can be seen in Figure 64, where the temporal variation of mixed layer depth is plotted for several cases with varying density gradients. These include: (a) the base case, (b) initial salinity distribution decreasing linearly from 0 per cent at the surface to 15 per cent at a depth of 2.0 m (i.e., a 1 m storage zone) and (c) initial

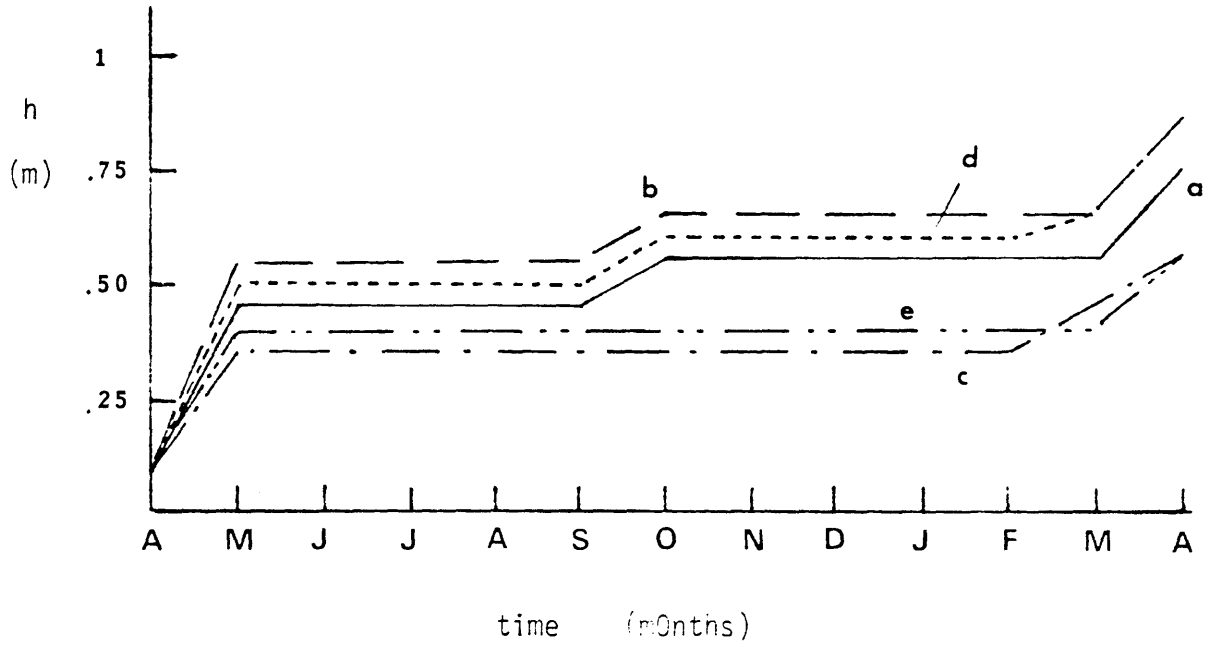

FIGURE 64 Growth of Mixed Layer With Time

a) Bloss and Harleman Model
b) Same as (a), but with a 2 m GZ initially
c) same as (a), but with a 1 m GZ initially
d) eqn. (6.16) used for entrainment
e) surface washing (see text), with Bloss and Harleman wind-mixing

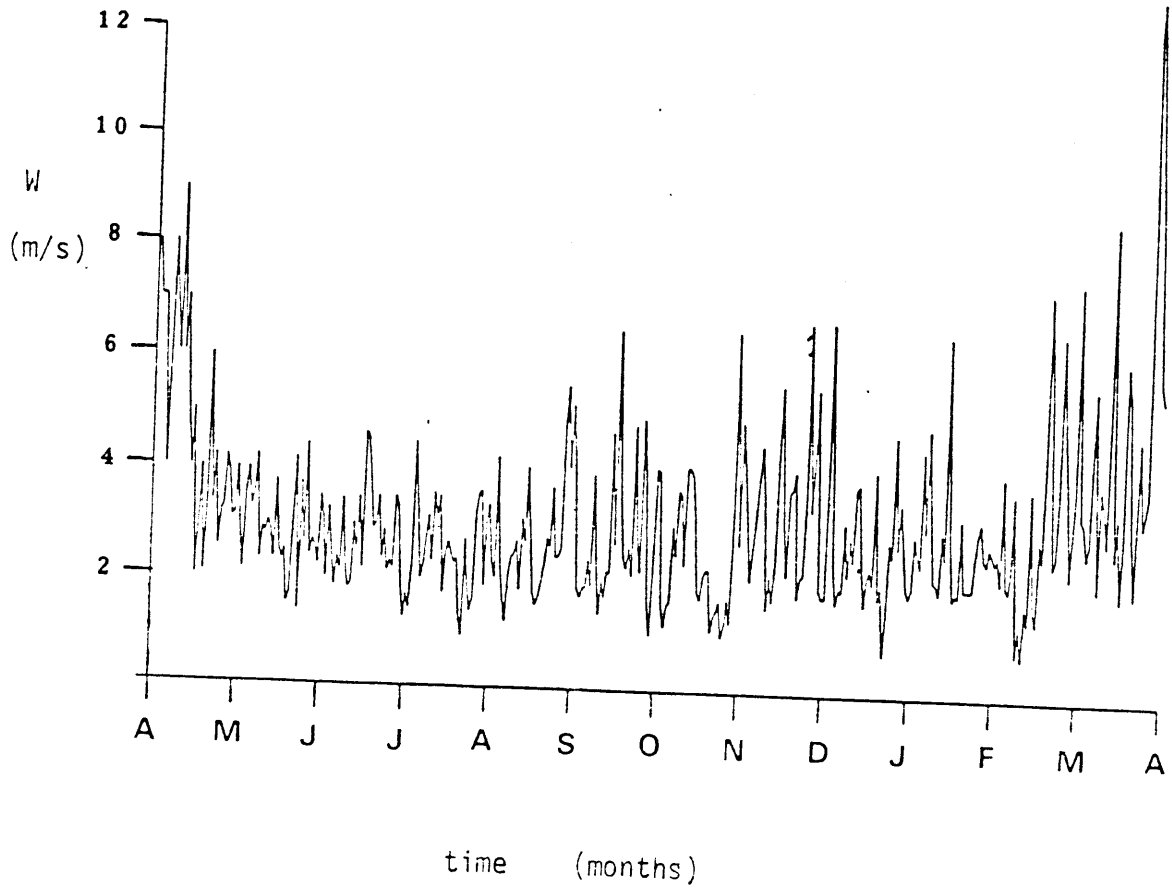

FIGURE 65 Daily Average Wind Speed Data Used in Simulations

salinity distribution decreasing linearly from 0 per cent at the surface to 15 per cent at 1 m depth (2 m storage zone). It can be seen that a stronger stabilizing gradient results in a reduction in mixed layer depth. This effect will also depend on the choice of entrainment function, as shown by curve (d) which used (6.16) to calculate entrainment.

Surface washing with relatively fresh water has been proposed as a means of maintaining the necessary reduced salinity in the upper part of the pond. A simulation run was made in which a constant flow of 1.0 m^3 min^{-1} was input at the surface. That is, fresh water was pumped into one end of the pond at the surface and water was pumped out at the other end at the surface and at the same flowrate (evaporation losses are neglected). Results for this run have also been plotted in Figure 64(e). It appears that surface washing helps somewhat to reduce the upper mixed layer depth. However, it can be seen that further steps will have to be taken in order to maintain a more acceptable mixed layer depth on the order of 20-30 cm. One possible method of accomplishing this is with the use of floating nets which act to dissipate wind energy (see Section 5.3).

A further comparison of the effect of the entrainment algorithm is shown in Figure 66, which plots temperature of the LCZ for several different wind-mixing models. Note that the algorithm of Hurley-Octavio et al. (1975) assumes that all of the input TKE is available for entrainment (see eq. 6.14). This model predicted fully mixed conditions after less than a month and persisting throughout the year. As may be expected, a wind-mixing algorithm which moderates between this extreme

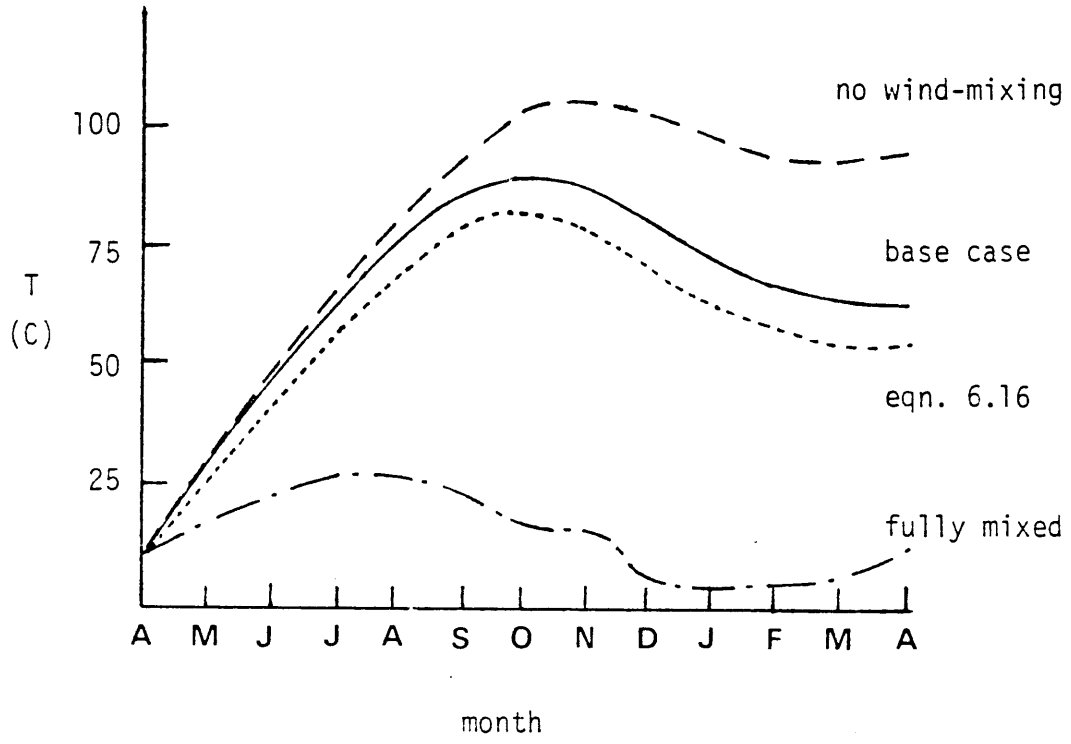

FIGURE 66 Predicted LCZ Temperatures Using 4 Different Assumptions For Wind-Mixing

and the case of zero wind mixing should more closely model field conditions. The base case, using the model of Bloss and Harleman (1979), represents a possible method of doing this, as does the model given by (6.16). Temperatures predicted using (6.16) are seen to be slightly less than those predicted using the Bloss and Harleman model, predominantly because the mixing is somewhat greater. (Figure 64). Note that the temperatures for the fully-mixed case are similar to the temperatures that may be expected in a natural fresh water body of the same depth.

The sensitivity of the wind-mixing model to the assumed form of the solar radiation function was examined and results from the simulations are plotted in Figure 67. As previously noted, the base case assumed that the incoming solar radiation was represented by (6.11), with extinction coefficient $\eta = 0.5\ m^{-1}$. For two of these runs the value of η was varied from $1.0 m^{-1}$ to $0.25\ m^{-1}$. Over the first half of the simulation it can be seen that a lower value of extinction coefficient results in higher temperatures, which is the expected result. However, in the second half of the year temperatures associated with the lowest extinction coefficient dropped below the temperatures for the higher values of η. This may be explained by increased upward diffusion of heat due to the very steep temperature gradients established during summer conditions for the run with $\eta = 0.25\ m^{-1}$. Considering the very large change in extinction coefficient values for these runs, it appears that the model is not overly sensitive to η.

One further run was made in which the radiation model of Rabl and Nielsen (1974) was used. As seen in Figure 67, this run produced the highest storage zone temperature (106°C near the end of September) and

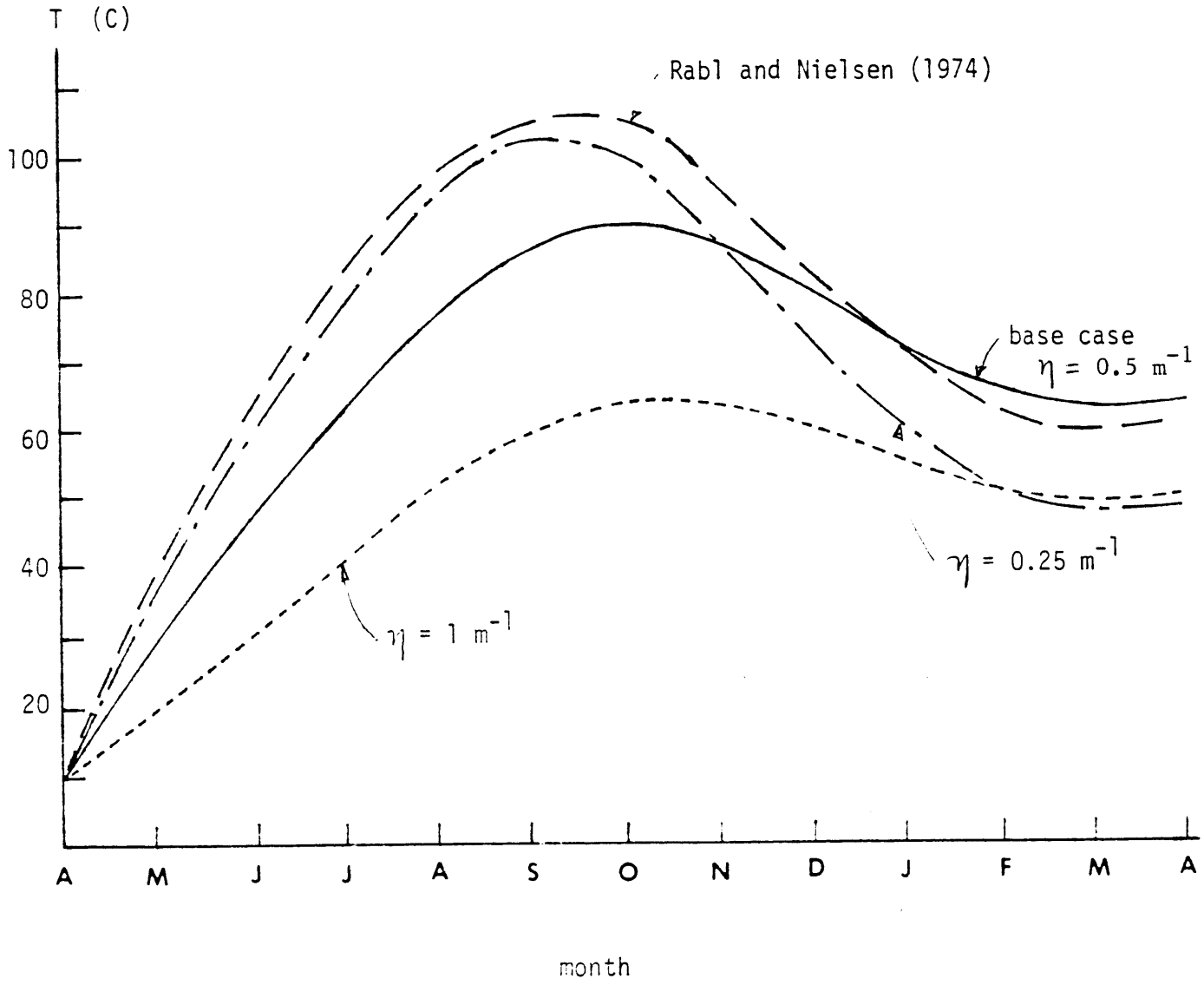

FIGURE 67 Sensitivity of Predicted LCZ Temperatures to the Solar Radiation Model

the shape of the curve is very similar to the curve produced using a low value of η. It should be noted that the Rabl and Nielsen model was formulated for clear water containing no contaminants which might effect the transmission of radiation. In practical situations water clarity will most likely be far from ideal so that radiation expressions based on pure water data will tend to overpredict expected pond temperatures. Transmission data will have to be collected on a site-specific basis for an accurate representation of radiation absorption, and judging by the shape of the curves in Figure 67, the use of a single-term exponential function, with appropriately chosen values for β and η appears to be sufficient.

In order to see how well the model was able to predict temperature and salinity profiles, field data was obtained from the solar pond operated by the Ohio Agricultural Research and Development Center (OARDC) in Wooster, Ohio. This pond has a depth of nearly 3 m and a surface area of 155 m^2. Temperature and salinity measurements at 5 cm intervals were supplied, along with wind speed, solar radiation, precipitation and air temperature. Other meteorological data needed by the model consists of cloud cover and relative humidity and this information was obtained from NOAA data recorded at the Akron, Ohio airport. Values for β and η were taken from Shah et al. (1981). The thermal diffusivity of the ground beneath the pond was set at 0.02 cm^2/sec and, since this pond is insulated, the thermal diffusivity for the pond bottom was assumed to be approximately an order of magnitude less than the ground value.

Average storage zone temperatures for a 6-month simulation period during 1980 are shown in Figure 68, using the Bloss and Harleman (1979)

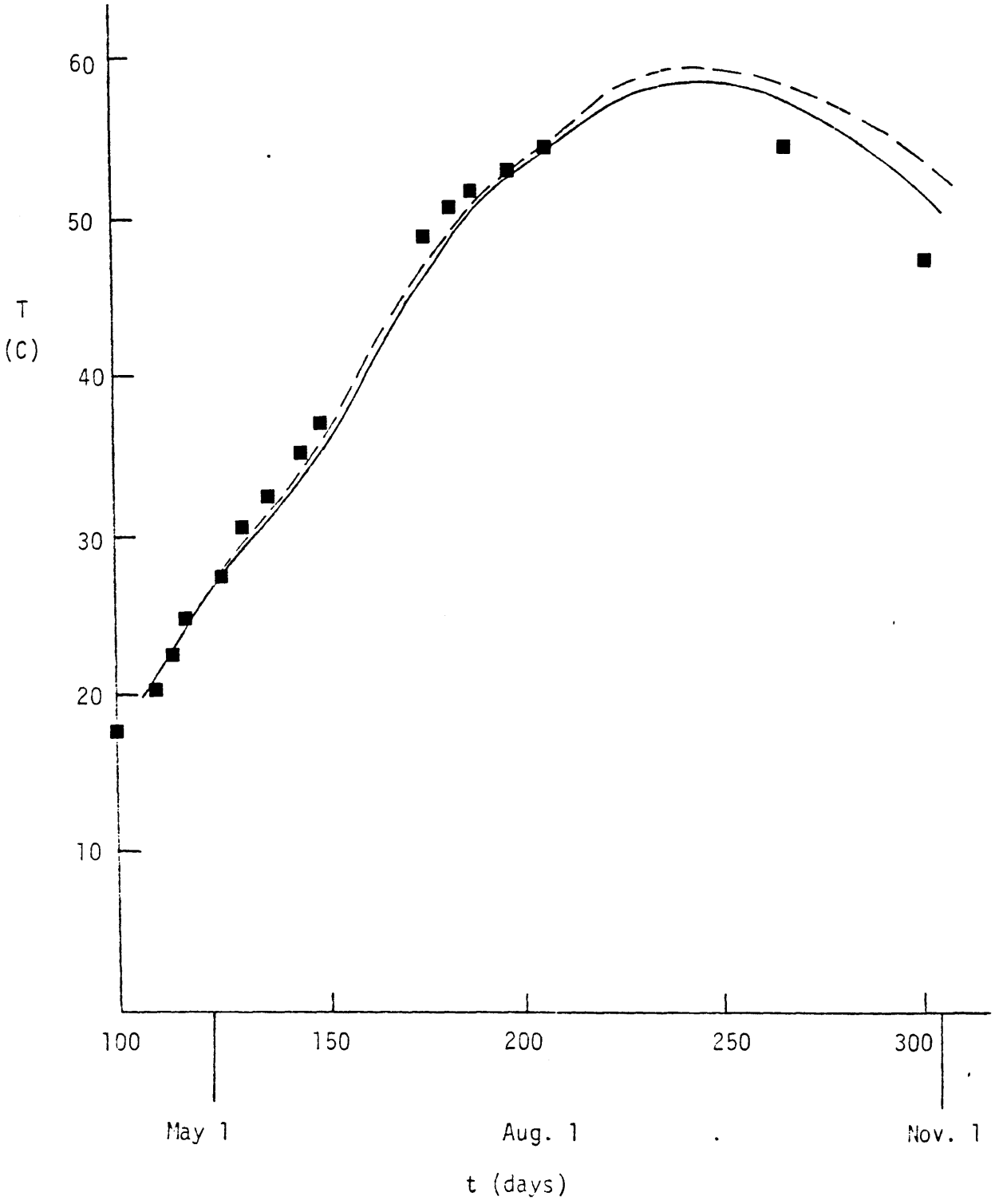

FIGURE 68 LCZ Temperatures in the OARDC Pond, Showing Comparison of Model Results and Reported Data Points. The Dashed Line Gives Model Results Without Wind-Mixing

wind-mixing model. The comparison is good except for the last few months when the model tended to predict temperatures significantly higher than the data points. However, this can be explained by the fact that energy was extracted from the pond starting in October and this heat extraction was not included in the simulations. Figure 69 compares predicted profiles with data at several times during the simulation period, with initial conditions indicated in part (a). The comparison appears to be quite good. Figures 68 and 69 also show results for simulations which did not apply wind-mixing. The predictions are very similar for both cases (with and without wind-mixing), which indicates that wind-mixing is probably not a very strong influence in this pond. However, later in the simulation period the model without wind-mixing tends to underpredict the upper layer depth (Figure 69), resulting in a slight increase in storage layer temperature (Figure 68). Although both models produce reasonable results here, it appears that the inclusion of wind-mixing gives a slightly better comparison with the data. It may also be noted that the model overpredicts the surface temperature, but this is probably related to a problem in the meteorological data. Because of its size, this pond is not ideal for testing the wind-mixing algorithm and it was decided that it would not be worthwhile running additional simulation with different wind-mixing models (e.g. eq. 6.16). However, the closeness with which the upper mixed layer depth is predicted indicates that the model may be useful in small as well as large pond design. More studies are needed to know this for certain.

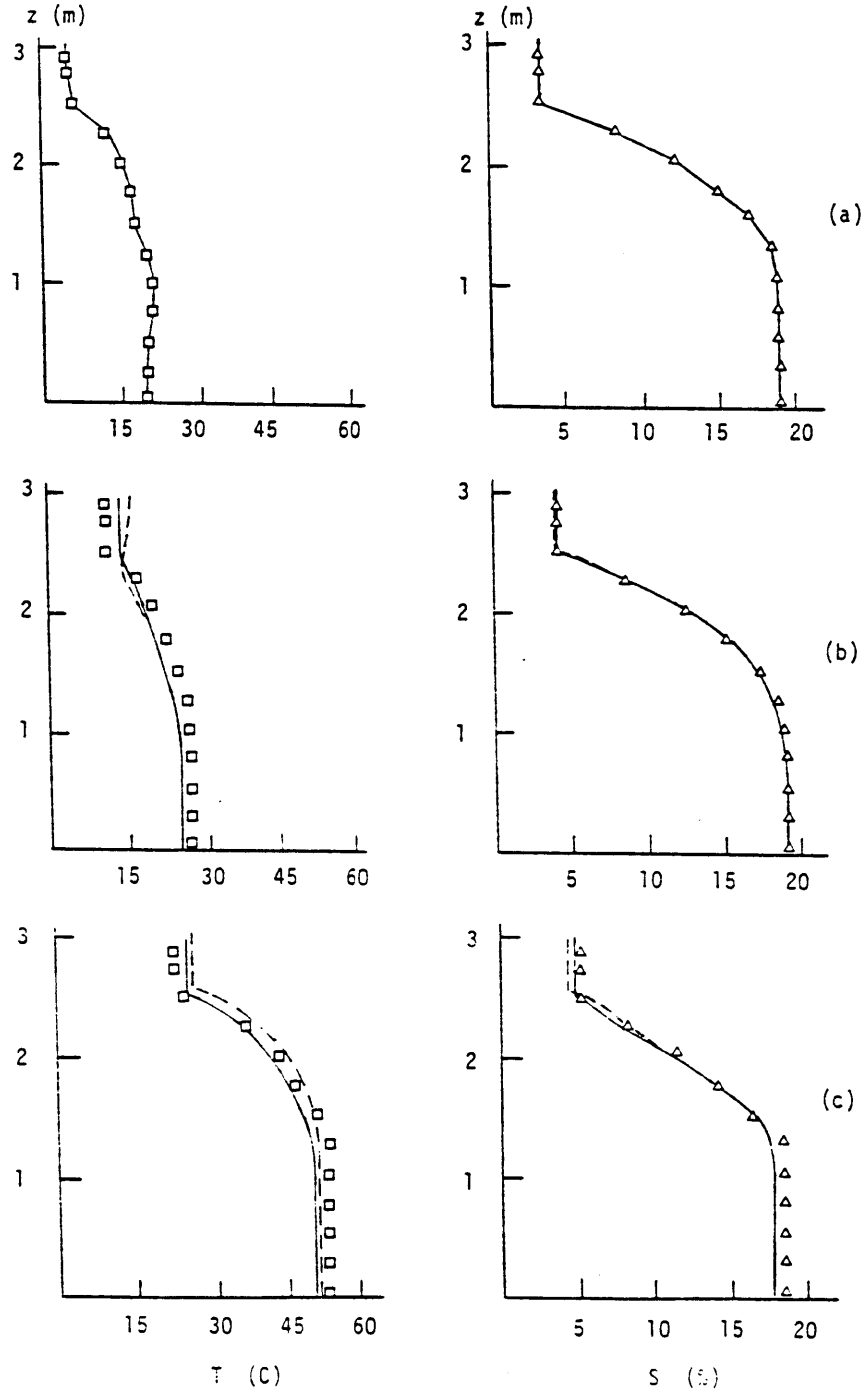

FIGURE 69 Temperature and Salinity Profiles in the OARDC Pond: (a) initial profiles; (b) profiles after 2 weeks and (c) profiles after 11 weeks. The Dashed Line Gives Model Results Without Wind-Mixing

CHAPTER 7

Summary and Conclusions

7.1 Entrainment Model

The main purpose of this study was to develop an entrainment algorithm which could be used in a numerical one-dimensional mixed-layer model for salt gradient solar ponds. A literature review indicated that previous studies had not considered mixed-layer entrainment in strongly stratified double-diffusive systems. A general entrainment model was derived in Chapter 3 and several special cases were looked at, namely, grid-mixing and shear-induced mixing. The grid experiment described in Chapter 4 showed that double-diffusive stratification could affect the entrainment rate, at least under conditions of zero mean shear. It was also shown that this effect could be modeled by modifying the scale velocity and the model developed in Chapter 3 could then be used to describe the results. Results from the wind-mixing experiment described in Chapter 5 indicated that shear effects dominated any double-diffusive effects. The wind-mixing results also provide data with which the entrainment model may be calibrated. Recall that the model is written as

$$\frac{u_e}{\sigma} = \frac{C_F + C_{SH}\,\bar{u}^3/\sigma^3 - \varepsilon_2' + C_T Ri_T Pe_T^{-1/2} - C_S Ri_S Pe_S^{-1/2}}{C_t + Ri} \qquad (3.31)$$

where ε_2' is given by

$$\varepsilon_2' = \frac{C_D}{\sigma N} \quad [2Ri\ g' + N^2 h - 2Ri(g'^2 + N^2\sigma^2)^{1/2}] \qquad (3.10)$$

and $Ri = g'h/\sigma^2$ and $\sigma = (w_*^3 + C_v^3 u_*^3)^{1/3}$. From Section 6.1.1 the coefficient values are summarized as follows:

$$\begin{aligned} C_F &= 0.34 \\ C_{SH} &= 1.1 \\ C_D &= 0.01 \\ C_T &= 3 \times 10^{-4} \\ C_S &= 3 \times 10^{-4} \\ C_t &= 2.25 \\ C_V &= 2.0 \\ C_1 &= 16 \end{aligned} \qquad (7.1)$$

The values of C_F, C_D, and C_t, were chosen from the literature, C_T and C_S were evaluated by looking at some reported experiments in double-diffusive interfacial growth and the remaining parameters were evaluated from current experimental results.
It was shown (Figure 46) that this model could be used to reproduce data from the wind-mixing experiment.

From section 3-2 the grid-mixing model was seen to be a special case of (3.31) and C_F was shown to depend on both Ri and Pe, though the assumption of constant C_F (eq. 7.1) produced good results for the wind tests. The grid-mixing model is written as

$$\frac{u_e}{\sigma} = Ri^{-1} (C_1 Pe^{-1/2} + C_2 Ri^{-1/2}) \qquad (3.26)$$

where Ri and Pe are defined in terms of the local velocity and length

scale for the eddies near the interface and σ incorporates the buoyancy velocity induced by the unstable temperature gradient in double-diffusive stratification. Eq. (3.26) was shown to reproduce the grid results fairly well for the different kinds of stratification considered (Figures 32 and 33), but the coefficient values are not directly applicable to the wind-mixing model because of differences in scaling. Equation (3.26) also shows that grid entrainment results for both salt and heat stratification may be expressed by a single equation, and neither an Ri^{-1} nor an $Ri^{-3/2}$ entrainment "law" will hold absolutely.

The applicability of (3.31) for modeling field conditions has been discussed in Chapter 5 in terms of the effect of finite fetch and the presence of end walls. Although the parameterization allows this effect to be incorporated to some degree through changes in $\bar{u}$ (actually, u_r), there is still some uncertainty in applying the model to field conditions. It is unfortunate that adequate field data has not been available for calibrating the model. It is interesting to note that at high Ri values (3.31) predicts greater mixing than would be predicted by the Bloss and Harleman (1979) model previously used (see Figures 12 and 59). This was shown in the simulation runs discussed in Chapter 6. Of course this depends on the stratification and on values for the coefficients, particularly C_l and C_V.

It should be recalled from the discussion in Section 6.1.1 that there is still some uncertainty in the values for the coefficients in (7.1). Along with coefficient values obtained from the literature,

the present experimental results were used to estimate C_{SH}, C_V and C_1 and values were chosen to reproduce the wind-mixing data. One of the possible drawbacks of the entrainment model is the relatively large number of empirical coefficients used, and the uncertainty for each of the values. The ranges listed in Table 4 provide some idea of the variations found in previous experiments for the values of C_F, C_D, C_{SH}, C_t and C_V. Values for C_T and C_S are only rough estimates obtained from an experiment which was not designed specifically to evaluate these parameters. The values chosen for C_T and C_S, though relatively unimportant over much of the Ri range, do become important in determining a limiting value of Ri beyond which entrainment ceases. The value of C_1 will be site-specific, depending on the relative steadiness of the wind. Relatively high values of C_1 were found in the present experiments (Figure 60), primarily because of the steady wind speeds used. C_1 will be significantly lower under non-steady conditions and this would greatly influence the calculation of Rf. When applying this model to field conditions where current measurements are not available, a possible approach would be to assume that $u_s \sim .03$ W, though this may overestimate u_s.

The influence of fetch is also incorporated in the model through the shear production term in the parameterized TKE budget (3.31). In the present tests it was shown that the return current u_r near the interface depended on the length of the test section., In the field it is expected that u_r will also depend on the pond geometry and wind characteristics and ideally u_r should be measured, or at least

estimated by a momentum balance applied to the UCZ. Future calibration of the model with field data will probably result in further refinement of the estimate for C_{SH}.

7.2 Double-diffusive Effects

One of the purposes of the present research was to see if double-diffusive effects would be important in entrainment. The grid results indicated that double-diffusive stratification could have a significant effect on values for u_e (Figure 32), but that this effect could be modeled by a suitable definition for the scaling velocity. In other words, the main effect of double-diffusive stratification in the grid tests was to cause an unstable interfacial buoyancy flux, adding additional kinetic energy to the layer. Double-diffusive stratification had no appreciable impact on the wind-mixing results, at least for the parameter range considered here. It is believed that shear-induced mixing dominated any double-diffusive effects in these tests, and the same entrainment relation was applicable for both salt and double-diffusive stratification. Double-diffusive effects may become important under conditions of negligible wind-mixing, or possibly when nets are used to dampen wind waves.

When modeling solar ponds, not only is the movement of the interface of interest, but also the fluxes of heat and salt that may cross the interface. For instance, upward heat flux is obviously undesirable, since this decreases the thermal efficiency of the pond. Upward salt flux is equally undesirable though, since this

flux represents salt which must somehow be replaced in the pond. Upward salt flux also increases the density of the UCZ, thus weakening the density step at the bottom of the UCZ and increasing the possibility of entrainment.

In the current solar pond model, described in Chapter 6 (see also Atkinson et al., 1984), fluxes of heat and salt across the interface between the UCZ and GZ are calculated simply as the fluxes that would be expected by molecular diffusion (see 1.2 and 1.3),when solar radiation is neglected. Of course, there is also a flux contribution to the UCZ due to the movement of the interface (i.e., entrainment). The entrainment flux of salt will be

$$F_e = u_e \Delta\rho_S \quad , \tag{7.2}$$

where $\Delta\rho_S$ is the step in the salt concentration profile at the entrainment interface. The diffusive flux of salt is

$$F_d = k_S \frac{\partial \rho_S}{\partial z} \sim k_S \frac{\Delta\rho_S}{l_S} \quad , \tag{7.3}$$

where l_S is a diffusive length scale used as an estimate for the salt interface thickness. This is consistent with Newell's (1984) suggestion that the interfacial thickness would be controlled by the diffusion of salt. Similar to the development in Chapter 3, l_S is estimated as $l_S \sim \sqrt{k_S \hat{t}}$, where $\hat{t} = \hat{l}/\hat{u}$ and $\hat{l}$ and $\hat{u}$ are the length and velocity scales for the motion in the upper layer. In the case of wind-mixing, $\hat{l} \sim h$ and $\hat{u} \sim u_*$, so $\hat{t} = h/u_*$. Taking the ratio of (7.3) to (7.2) will then give the relative strength of the diffusive flux to the entrainment flux:

$$\frac{F_d}{F_e} = \frac{k_S}{u_e} \frac{1}{\sqrt{k_S h/u_*}} = \left(\frac{u_e}{u_*}\right)^{-1} \left(\frac{k_S}{u_* h}\right)^{1/2} = \left(\frac{u_e}{u_*} Pe_S^{1/2}\right)^{-1}, \quad (7.4)$$

where $Pe_S = u_* h/k_S$. A similar analysis for the fluxes of heat will result in an expression equivalent to (7.4), but with $Pe_T = u_* h/k_T$ in place of Pe_S.

Now, $Pe_S \sim O(10^3)$ and $Pe_T \sim O(10)$, while $u_e/u_* \sim O(10^{-1} - 10^{-4})$, depending on Ri. Thus, it can be seen that the diffusive fluxes can be quite important relative to the entrainment fluxes, especially with increasing Ri, as expected. Note that (7.4), as well as the equivalent expression for heat, is written in terms of molecular diffusivity. It has been suggested (Meyer, 1982) that double-diffusive fluxes must be accounted for when calculating the total fluxes of heat and salt across an interface. However, the arguments given in Chapters 3 and 4 suggest that the incorporation of double-diffusive fluxes is valid only when double-diffusive boundary layer instability is allowed to develop. Otherwise, molecular diffusion leads to the interfacial fluxes. It should also be noted that the values for the double-diffusive "effective" diffusivities are generally less than the molecular values (see Appendix C), so that a model relying on these "effective" values will underpredict the fluxes of heat and salt across the interface into the UCZ and the relative effect of diffusion will be lessened (eq. 7.4).

In terms of a solar pond model, it is therefore concluded that in general it is not necessary to include double-diffusive effects explicitly when calculating entrainment or interfacial fluxes into

the UCZ, at least under conditions where wind-mixing is important. However, the stability criterion for thermohaline systems (1.23) will still hold, and double-diffusive fluxes may become important under conditions of no mixing. It is expected that this will not usually be the case.

7.3 Implications for Solar Pond Model

Chapter 6 discussed the incorporation of the entrainment model in the solar pond simulation model and results were obtained which appeared to be reasonable. From the above discussion (Section 7.2) and also from results in Chapter 5 it is concluded that double-diffusive effects should appear explicitly in the model only for the stability criterion. It should be noted, however, that results in Chapter 5 were not obtained for very low wind speeds and it is under such conditions that double-diffusive effects are expected to possibly become important. At this point it is assumed that in most cases there will be sufficient mixing in an operating pond that this will not be the case.

It is unfortunate that field data has not been available for calibrating and verifying the model. Funding for solar pond research in the U.S. has been cut back severely in the past several years and the data required for running the model has been very difficult to find. There is, however, an effort underway to obtain data from the Argonne solar pond. (Table 3). There is some promise that the data will be sufficient to run a reasonable calibration of the model, but this has not yet been done.

7.3.1 Use of Floating Nets to Control Wind-Mixing

The tests in Section 5.3 were meant to provide a first look at the effect of placing a grid of floating nets (or pipes) on the pond surface, in terms of reducing entrainment. Field observations have indicated that these nets are effective in maintaining smaller UCZ depths. The experiments described in Section 5.3 provide qualitative and some quantitative results, though further experiments are needed before definite conclusions may be reached. At this point it appears that the presence of the floating nets does in fact serve to reduce the transfer of energy into the water column, and a corresponding decrease in the entrainment might be expected.

It should be noted that these tests were not conducted with a density interface present, so the present conclusions are primarily qualitative in nature. Future experiments should be conducted with a density interface in order to compare u_e with and without the nets. Based on the present observations the presence of the nets should have a marked effect on the flow structure, which will be especially important in looking at the currents and r.m.s. velocities near the interface. Due to problems that may be encountered in setting up the desired stratification in a large laboratory tank, these experiments might best be conducted on a well-instrumented field installation. From data shown in Figure 56 it might be expected that the nets would reduce entrainment by up to 30-40%, depending on wind speed and UCZ depth.

7.4 Suggestions for Further Research

Suggestions for further research have been pointed out at several places above and in the previous chapters and these suggestions as well as a few others are summarized below.

For the grid experiment, the hypothesis for the effect of double-diffusive stratification on u_e might be checked by taking velocity measurements not only under non-stratified conditions, but also under double-diffusively stratified conditions. It was noted in Chapter 4 that these measurements were not possible with the present apparatus because of fluctuations in the index of refraction of the solution near the interface. Use of an LDA for the proposed measurements would require density stratification to be set up without changing the index of refraction of the liquid. This has been done by McDougall (1979). Experiments might then be done in a manner similar to that of Kantha and Long (1980), where a buoyancy flux is imposed on a grid-mixed layer by adding heavier fluid at the surface.

Further experiments associated with the grid-mixing tests might also be conducted to look at the detailed structure of a double-diffusive interface in terms of the salinity and temperature profiles. Crapper and Linden (1974) measured such profiles but only for singly-stratified conditions, and similar measurements have not, to the author's knowledge, been reported. This might allow additional understanding of the effect of double-diffusive stratification on the entrainment process, as noted in Chapter 4.

The influence of mean motion on grid-induced entrainment, as

suggested in Section 3.3.1, might be checked using a facility which could impose both grid-mixing and mean flow in a stratified tank. In this way the relative importance of shear effects could be tested, and different slopes for the entrainment relation might be expected depending on the relative strengths of grid and shear effects.

For the wind-mixing tests there are two basic experiments which might be conducted to add to the present results. The first of these was described in the previous section and involves running entrainment tests with the floating nets in place. The second set of experiments would look at entrainment for a linearly stratified fluid, rather than the two-layer stratification used here. It may be difficult to achieve linear double-diffusive stratification, but from the present results it might be expected that there would not be any difference between double-diffusive results and salt-stratified results, so tests might be run with linear salt stratification only. Results from this experiment could be used to compare with those of Kit et al., (1980) and, along with the results in Chapter 5, might be used to better estimate the role of energy leakage by internal waves in the stratified layer. This might lead to a more definite estimate for the parameter C_D in the entrainment relation (3.31).

REFERENCES

Akbarzadeh, Aliakbar and Goodarz Ahmahdi (1980), Computer simulation of the performance of a solar pond in the southern part of Iran, Solar Energy, 24, 143-151.

Akbarzadeh, A., R.W.G. MacDonald and Y.F. Wang (1983), Reduction of mixing in solar ponds by floating rings, Solar Energy 31, 377-380.

Amorocho, J. and J.J. Devries (1980), A new evaluation of the wind stress coefficient over water surfaces, J. Geophys. Res. 85 (C1), 433-422.

Asaeda, Takashi and Nobuyaki Tamai (1980), Turbulent entrainment in stratified flows, 3rd Int. Symp. on Stochastic Hydraulics, Tokyo, Japan, C2-1-C2-12.

Assaf, Gad (1976), The Dead Sea: A scheme for a solar lake, Solar Energy 18, 293-299.

Assaf, Gad and E. Dagan (undated), Observations of wind-mixing in solar ponds, unpublished report, Solmat Systems, Jerusalem, Israel.

Atkinson, Joseph F. and D.R.F. Harleman (1983a), A wind-mixed layer model for solar ponds, Solar Energy 31, 243-259.

Atkinson, Joseph F. and D.R.F. Harleman (1983b), Wind-mixing in solar ponds, from Progress in Solar Energy, Vol. 6, proc. A.S.E.S. conf., 393-398.

Atkinson, Joseph F. and D.R.F. Harleman (1983c), Entrainment in a thermohaline double-diffusive system, Frontiers of Hydraulic Engineering, ed. Hung Tao Shen, proc. ASCE Hyd. Div. Conf., 8-14.

Atkinson, J.F., J. Munic and D.R.F. Harleman (1984), A note on gradient maintenance in a salt gradient solar pond, to appear in Solar Energy.

Atkinson, Joseph F., E. Eric Adams, Atul Salhotra and D.R.F. Harleman (1984), User's manual for Massachusetts Institute of Technology Solar Pond Program (MITSOL), Tech. Rep. in preparation, Ralph M. Parsons Laboratory, M.I.T., Cambridge, MA.

Baines, P.G. and A.E. Gill (1969), On thermohaline convection with linear gradients, J. Fluid Mech. 37, 289-306.

Batchelor, G.K. (1953), Homogeneous Turbulence, Cambridge Univ. Press.

Battelle, Pacific Northwest Laboratory (1982), The technical and economi feasibility of salt-gradient solar ponds at the Truscott Brine Lake of the Red River chloride control project, A report to the House-Senate Committee on Appropriations of the Ninety-Seventh Congress, Report PNL-4396/uc-626.

Battelle, Pacific Northwest Laboratory (1983), Optimization and preconceptual design of a 5 MWe salt-gradient solar pond power plant at Great Salt Lake, Report PNL-4667/uc-626.

Bloss, S. and D.R.F. Harleman (1979), Effect of wind-mixing on the thermocline formation in lakes and reservoirs, Tech. Rep. 249, Ralph M. Parsons Lab. for Water Res. and Hydrodynamics, M.I.T., Cambridge, MA.

Bendat, J. and B. Piersol (1971), Random Data: Analysis and Measurement Procedures, Wiley-Interscience, New York

Bo Pedersen, Fleming (1980), A monograph on turbulent entrainment and friction in two-layer stratified flow, Series paper 25, Inst. Hydrodyn. and Hyd. Eng., Tech. Univ. Denmark.

Bowen, I.S. (1926), The ratio of heat losses by conduction and evaporation from any water surface, Phys. Rev. 27, 779-787.

Bronicki, Y.L., J. Lever and Y. Porat (1980), Large solar electric power plants based on solar ponds, Proc. 11th World Energy Conf., Munich, 739-758.

Browand, F.K. and Y.H. Wang (1972), An experiment on the growth of small disturbances at the interface between two streams of different densities and velocities, Int. Symp. on Stratified Flows, Novosibirsk, 491-498.

Bryant, H.C. and Ian Colbeck (1977), A solar pond for London? Solar Energy 19, 321-322.

Buch, Eric (1982), On entrainment observed in laboratory and field experiments, Tellus 34, 307-311.

Caldwell, Douglas R. (1973), Thermal and Fickean diffusion of sodium chloride in a solution of oceanic concentration, Deep Sea Res. 20, 1029-1039.

Cha, Y.S., W.T. Sha, and W.W. Shertz (1981), Modeling of the surface convective layer of salt gradient solar ponds, 15th I.E.C.E.C. Conf., Atlanta, Ga.

Charnock, H. (1955), Wind stress on a water surface, Q.J. Roy. Met. Soc., London 81, 639-640.

Chashechkin, J.D. (1980), Experimental studies of the mixed layer in stratified liquids, Second Int. Symp. on Stratified Flows, Norwegian Inst. Tech., Trondheim, Norway, 783-790.

Chen, C.F. and D.H. Johnson (1984), Double-diffusive convection: A report on an engineering foundation conference, J. Fluid Mech. 138, 405-416.

Chinery, G.T., G.R. Siegel and W.C. Irwin (1983), Gradient zone establishment and maintenance at TVA's 4000 m^2 nonconvecting salt gradient solar pond, from Progress in Solar Energy, proc. A.S.E.S. conf., Vol. 6, 399-404.

Clark, Wilson (1980), Take some sun and salt, add some water - the result is energy, Smithsonian, Oc., p. 143.

Crapper, P.F. and P.F. Linden (1974), The structure of turbulent density interfaces, J. Fluid Mech. 65, 45-63.

Crapper, P.F. (1976), Fluxes of heat and salt across a diffusive interface in the presence of grid generated turbulence, Int. J. Heat Mass Transf. 19, 1371-1378.

Cromwell, Townsend (1960), Pycnoclines created by mixing in an aquarium tank, J. Mar. Res. 18, 73-82.

Dake, J.M.K. and D.R.F. Harleman (1969), Thermal stratification in lakes: Analytical and laboratory studies, Water Res. Res. 5, 484-495.

Defant, A. (1961), Physical Oceanography, Pergamon Press, Oxford, p. 53.

Delnore, Victor E. (1980), Numerical simulation of thermohaline convection in the upper ocean, J. Fluid Mech. 96, 803-826.

Denman, K.L. (1973), A time-dependent model of the upper ocean, J. Phys. Oceanog. 3, 173-184.

Denton, Richard A. (1978), Entrainment by penetrative convection at low Peclet number, Ph.D. thesis, Dept. Civil Eng., Univ. Canterbury, Christchurch, New Zealand.

Eckart, C. (1962), The equations of motion of sea water, from The Sea, ed. M.N. Hill, Interscience, NY, 31-42.

Edesess, Michael (1982), On solar ponds: Salty fare for the world's energy appetite, Tech. Rev. 85, 58-68.

Elata, C. and O. Levin (1965), Hydraulics of the solar pond, Int. Assoc. Hyd. Res. 11th Int. Conf., Leningrad.

Ellison, T.H. and J.S. Turner (1959), Turbulent entrainment in stratified flows, J. Fluid Mech. 6, 423-448.

Elwell, D.L., T.H. Short and P.C. Badger (1977), Stability criteria for solar (thermal-saline) ponds, Proc. 1977 Ann. Meeting of Am. Sec., Int. Solar Energy Soc., Orlando, FL.

Fernando, H.J.S. and R.R. Long (1983), The growth of a grid-generated turbulent mixed layer in a two-fluid system, J. Fluid Mech. 133, 377-395.

Fofonoff, N.P. (1962), Physical properties of sea water, from The Sea, ed. M.N. Hill, Interscience, NY, 3-30.

Fortesque, G.E. and J.R.A. Pearson (1967), On gas absorption into a turbulent liquid, Chem. Eng. Sci. 22, 1163-1176.

Gartrell, Gregory Jr. (1979), Studies on the mixing in a density-stratified shear flow, Rep. KH-R-39, W.M. Keck Lab., Cal. Inst. Tech., Pasadena, CA.

Harleman, D.R.F. (1982), Hydrothermal anlaysis of lakes and reservoirs, J. Hyd. Div., A.S.C.E. 108, 301-325.

Harleman, D.R.F., Atul Salhotra and Eric Adams (1983), Solar pond feasibility study for Egypt, Parsons Lab. Report, M.I.T.

Helfrich, K.R., E.E. Adams, A.L. Godbey and D.R.F. Harleman (1982), Evaluation of models for predicting evaporative water loss in cooling impoundments, E.P.R.I. Tech. Rep. CS-2325, Project 1260-17.

Henderson, J. and C.M. Leboeuf (1980), SOLPOND - A simulation program for salinity gradient solar ponds, Solar Energy Research Institute, SERI/TP-351-559.

Hopfinger, E.J. and J.A. Toly (1976), Spatially decaying turbulence and its relation to mixing across a density interface, J. Fluid Mech. 78, 155-175.

Hopfinger, E.J. and P.F. Linden (1982), Formation of thermoclines in zero-mean-shear turbulence subjected to a stabilizing buoyancy flux, J. Fluid Mech. 114, 157-173.

Hull, John R. (1980a), Wind-induced instability in small salt gradient solar ponds, proc. ASES conf., Phoenix, 371-375

Hull, J.R. (1980), Computer simulation of solar pond thermal behavior, Solar Energy 25, 33-40.

Hull, J.R., K.V. Lin, Y.S. Cha, W.T. Sha, T. Kamal and C. Nielsen (1981), Dependence of ground heat loss upon solar pond size and perimeter insulation: Calculated and experimental results, proc. I.S.E.S. Conf., Brighton, England.

Hull, J.R., J. Kamal and C.E. Nielsen (1983), Time dependence of ground heat loss from solar ponds, from Progress in Solar Energy, vol. 6, proc. A.S.E.S. conf., 381-386.

Huppert, Herbert E. (1971), On the stability of a series of double-diffusive layers, Deep Sea Res. 18, 1005-1021.

Huppert, Herbert E. and P.F. Linden (1979), On heating a stable salinity gradient from below, J. Fluid Mech. 95, 431-464.

Huppert, Herbert E. and J. Stewart Turner (1981), Double-diffusive convection, J. Fluid Mech. 106, 299-329.

Hurle, D.T.J. and E. Jakeman (1969), Significance of the Soret effect in the Rayleigh-Jeffreys problem, Phys. Fluids 12, 2704-2705.

Hurle, D.T.J. and E. Jakeman (1971), Soret-driven thermosolutal convection, J. Fluid Mech. 47, 667-687.

Hurley-Octavio, K.A., G.H. Jirka and D.R.F. Harleman (1977), Vertical heat transport mechanisms in lakes and reservoirs, Tech. Rep. 227, Ralph M. Parsons Lab. for Water Res. and Hydrodynamics, M.I.T., Cambridge, MA.

Imberger, J. and J. Patterson (1981), A dynamic reservoir simulation model - DYRESM:5, from Transport Models for Inland and Coastal Waters; Proceedings of a Symposium on Predictive Ability, ed. H.B. Fischer, Academic Press.

Ivanhoff, Alexandre (1977), Oceanic absorption of solar energy, from Modeling and Prediction of the Upper Layers of the Ocean, ed. E.B. Kraus, Pergamon Press.

Kantha, L.H. (1977), Note on the role of internal waves in thermocline erosion, from Modeling and Prediction of the Upper Layers of the Ocean, ed. E.B. Kraus, Pergamon Press, Oxford.

Kantha, L.H. and R.R. Long (1980), Turbulent mixing with stabilizing surface buoyancy flux, Phys. Fluids 23, 2142-2143.

Kantha, L.H., O.M. Phillips and R.S. Azad (1977), On turbulent entrainment at a stable density interface, J. Fluid Mech. 79, 753-768.

Kato, H. and O.M. Phillips (1969), On the penetration of a turbulent layer into stratified fluid, J. Fluid Mech. 37, 643-655.

Kellogg, M.W. Co. (1965), Saline Water Conversion Engineering Data Book, prepared for the Office of Saline Water, U.S. Dept. of the Interior.

Kirkland, D.W., J.P. Bradbury and W.E. Dean (1980), The heliothermic lake - a direct method of collecting and storing solar energy, U.S.G.S. open file rep. 80-807.

Kit, E., E. Berent and M. Vajda (1980), Vertical mixing induced by wind and a rotating screen in a stratified fluid in a channel, J. Hyd. Res. 18, 35-58.

Kitaigorodskii, S.A. (1960), On the computation of the thickness of the wind-mixing layer in the ocean, Bull. Acad. Sci. U.S.S.R., Geophys. Ser. 3, 284-287.

Kitaigorodskii, S.A. (1979), Review of the theories of wind-mixed layer deepening, from Marine Forecasting, ed. Jacques J. Nihoul, Elsevier, Amsterdam.

Kohler, M.A. (1954), Lake and pond evaporation in water loss investigations - Lake Hefner studies, Tech. Rep., U.S.G.S. Professional Paper 269.

Kooi, C.F. (1979), The steady state salt gradient solar pond, Solar Energy 23, 37-45.

Kraus, E.B. and C. Rooth (1961), Temperature and steady state vertical heat flux in the ocean surface layers, Tellus 13, 231-238.

Kraus, E.B. and J.S. Turner (1967), A one-dimensional model of the seasonal thermocline II: The general theory and its consequences, Tellus 19, 98-105.

Kranenburg, C. (1981), Wind-induced mixing in stratified flow, proc. A.S.C.E. HY5, 632-637.

Kreider, Jan F. and Frank Kreith (1981), Solar Energy Handbook, McGraw-Hill, NY, p. 10-1 - 10-29.

Kullenberg, G. (1977), Entrainment velocity in natural stratified vertical shear flow, J. Estuarine Coast. Mar. Sci. 5, 329-338.

Lin, E.I.H. (1982), Regional applicability and potential of salt gradient solar ponds in the United States, prepared for U.S.D.O.E., DOE/JPL-1060-50.

Linden, P.F. (1971), Salt fingers in the presence of grid-generated turbulence, J. Fluid Mech. 49, 611-624.

Linden, P.F. (1973), The interaction of a vortex ring with a sharp density interface: A model for turbulent entrainment, J. Fluid Mech. 60, 467-480.

Linden, P.F. (1974a), A note on the transport across a diffusive interface, Deep Sea Res. 21, 283-287.

Linden, P.F. (1974b), Salt fingers in a steady shear flow, Geophys. Fluid Dyn. 6, 1-27.

Linden, P.F. (1975), The deepening of a mixed layer in a stratified fluid, J. Fluid Mech. 71, 385-405.

Linden, P.F. (1976), The formation and destruction of fine-structure by double-diffusive processes, Deep Sea Res. 23, 895-908.

Linden, P.F. and T.G.L. Shirtcliffe (1978), The diffusive interface in double-diffusive convection, J. Fluid Mech. 87, 417-432.

Lofquist, K. (1960), Flow and stress near an interface between stratified liquids, Phys. Fluids 3, 159-175.

Long, R.R. (1975), The influence of shear on mixing across density interfaces, J. Fluid Mech. 70, 305-320.

Long, R.R. (1978a), A theory of mixing in stably stratified fluid, J. Fluid Mech. 84, 113-124.

Long, R.R. (1978b), Theory of turbulence in a homogeneous fluid induced by an oscillating grid, Phys. Fluids 21, 1887-1888.

Long, R.R. (1978c), The growth of the mixed layer in a turbulent stably stratified fluid, Geophys. Astrophys. Fluid Dynamics 11, 1-12.

Marmorino, George O. and Douglas R. Caldwell (1976), Heat and salt transport through a diffusive thermohaline interface, Deep Sea Res. 23, 59-67.

Mancini, T.R., R.I. Loehrke and R.D. Haberstroh (1976), Layered thermohaline natural convection, Int. J. Heat Mass Trans. 19, 839-848.

McDougall, Trevor J. (1979), Measurements of turbulence in a zero-mean-shear layer, J. Fluid Mech. 94, 409-431.

Meyer, K.A. (1982), Numerical modeling of layer behavior in a salt gradient solar pond, Rep. LA-UR-82-905, Los Alamos Nat. Lab., Los Alamos, NM.

Miller, James R. (1976), The salinity effect in a mixed layer ocean model, J. Phys. Oceanog. 6, 29-35.

Moore, M.J. and R.R. Long (1971), An experimental investigation of turbulent stratified shearing flow, J. Fluid Mech. 49, 635-655.

Murota, Akira and Kohji Michioku (1983), Stability and vertical mixing process in double-diffusive stratification system composed of heat-salt complex, J. Hydrosci. Hyd. Eng. 1, 53-63.

Newell, T.A. (1984), Characteristics of a double-diffusive interface at high density stability ratios, submitted to J. Fluid Mech.

Nield, D.A. (1967), The thermohaline Rayleigh-Jeffreys problem, J. Fluid Mech. 29, 545-559.

Nielsen, C.E. (1976), Experience with a prototype solar pond for space heating, from Sharing the Sun, proc. joint conf. Am. Can. Solar Energy Soc. 5, 169-182.

Nielsen, C.E. (1979), Control of gradient zone boundaries, from Sun II, proc. I.S.E.S. cong., ed. Karl Boer and Barbara Glenn, 1010-1014.

Nielsen, C.E. (1980), Nonconvective salt gradient solar ponds, from Solar Energy Technology Handbook, Part A, Marcel Dekker, New York.

Nielsen, C.E. (1983), Experience with heat extraction and zone boundary motion, from Progress in Solar Energy, Vol. 6, proc. A.S.E.S. conf., 405-510.

Niiler, P.P. (1975), Deepening of the wind-mixed layer, J. Marine Res. 33, 405-422.

Niiler, P.P. and E.B. Kraus (1977), One-dimensional models of the upper ocean, from Modeling and Prediction of the Upper Layers of the Ocean, ed. E.B. Kraus, Pergamon Press, Oxford.

Panahi, Zahra, J. Clair Batty and J. Paul Riley (1982), A one-dimensional finite element ocmputer model to simulate the performance of salinity gradient solar ponds, Winter Annual Meeting, A.S.M.E., paper 82-WA/SOL-24.

Phillips, O.M. (1977), Entrainment, from Modeling and Predictin of the Upper Layers of the Ocean, ed. E.B. Kraus, Pergamon Press, Oxford.

Pollard, Raymond T., Peter B. Rhines and Rory O.R.Y. Thompson (1973), The deepening of the wind-mixed layer, Geophys. Fluid Dyn. 3, 381-404.

Por, F.D. (1970), Solar lakes on the shores of the Red Sea, Nature 218, 860-861.

Price, James F. (1979), On the scaling of stress-driven entrainment experiments, J. Fluid Mech. 90, 509, 529.

Rabl, Ari and Carl E. Nielsen (1974), Solar ponds for space heating, Solar Energy 17, 1-12.

Rothmeyer, M. (1980), The Soret effect and salt gradient solar ponds, Solar Energy 25, 567-568.

Rouse, H. and J. Dodu (1955), Turbulent diffusion across a density discontinuity, La Houille Blanche 4, 530-532.

Salhotra, A.M., E.E. Adams and D.R.F. Harleman (1984), Effect of Salinity and Ionic Composition on Evaporation: Analysis of Dead Sea Evaporation Pans, submitted to Water Res. Research Nov. 1984.

Shah, R.A., T.H. Short and R.P. Flynn (1981), Modeling and testing a salt gradient solar pond in Northeast Ohio, Solar Energy 27, 393-401.

Shelkovnikov, N.K. and G.I. Alyavdin (1982), Experimental study of turbulent entrainment in a two-layer fluid, Oceanology 22, 140-144.

Sherman, F.S., J. Imberger and G.M. Corcos (1978), Turbulence and mixing in stably stratified waters, Ann. Rev. Fluid Mech. 10, 267-288.

Shirtcliffe, T.G.L. (1969), An experimental investigation of thermosolutal convection at marginal stability, J. Fluid Mech. 35, 677-688.

Stefan, Heinz and Dennis E. Ford (1975), Temperature dynamics in dimictic lakes, J. Hyd. Div., A.S.C.E. 101, 97-114.

Steinhorn, Ilana, Ben-Zion Gershgoren and Gad Assaf (1979), Mixing of flood waters within the Dead Sea and its salt evaporation pond, Israel J. Earth Sci. 28, 77-85.

Stommel, H., A.B. Arons and D. Blanchard (1956), An oceanographical curiosity: The perpetual salt fountain, Deep Sea Res. 3, 152-153.

Swinbank, W.C. (1963), Longwave radiation from clear skies, Q.J. Roy. Met. Soc. London 89.

Tabor, H. (1963), Solar ponds: Large-area solar collectors for power production, Solar Energy 7, 189-194.

Tabor, H. (1980), Non-convecting solar ponds, Phil. Trans. R. Soc. Lond. A295, 423-433.

Tabor, H. (1981), Solar ponds, Solar Energy 27, 181-194.

Tabor, Harry and Zvi Weinberger (1981), Nonconvecting solar ponds, from Solar Energy Handbook, ed. Jan F. Kreider and Frank Kreith, McGraw-Hill, New York.

Takao, Shingo and Uichiro Narusawa (1980), An experimental study of heat and mass transfer across a diffusive interface, Int. J. Heat Mass Transf. 23, 1283-1285.

Tennekes, H. (1973), A model for the dynamics of the inversion above a convective boundary layer, J. Atmos. Sci. 30, 558-567.

Thompson, S.M. and J.S. Turner (1975), Mixing across an interface due to turbulence generated by an oscillating grid, J. Fluid Mech. 67, 349-368.

Tucker, W.A. and A.W. Green (1977), A time-dependent model of the lake-averaged vertical temperature distribution of lakes, Limnol. and Oceanog. 22, 687-699.

Turk, L.J. (1970), Evaporation of brine: A field study on the Bonneville Salt Flats, Utah, Water Res. Res. 6, 1209-1215.

Turner, J.S. (1965), The coupled turbulent transports of salt and heat across a sharp density interface, Int. J. Heat Mass Transf. 8, 759-767.

Turner, J.S. and E.B. Kraus (1967), A one-dimensional model of the seasonal thermocline, I: A laboratory experiment and its interpretation, Tellus 19, 88-97.

Turner, J.S. (1968a), The influence of molecular diffusivity on turbulent entrainment across a density interface, J. Fluid Mech. 33, 639-656.

Turner, J.S. (1968b), The behavior of a stable salinity gradient heated from below, J. Fluid Mech. 33, 183-200.

Turner, J.S. (1969), A note on wind-mixing at the seasonal thermocline, Deep Sea Res. 16, Suppl., 297-300.

Turner, J.S. (1973), Buoyancy Effects in Fluids, Cambridge Univ. Press, Cambridge.

Turner, J.S. (1974), Double-diffusive phenomena, Ann. Rev. Fluid Mech. 6, 37-56.

Turner, J.S. (1975), Double-diffusive processes in fluids, Int. Assoc. Hyd. Res. 16th Cong., Sao Paulo, Brazil, 10-28.

Turner, J.S. (1981), Small-scale mixing processes, from Evolution of Physical Oceanography, ed. Bruce A. Warren and Carl Wunsch, M.I.T. Press, Cambridge.

Tybout, R.A. (1966), A recursive alternative to Weinberger's model of the solar pond, Solar Energy 11, 109-111.

Veronis, G. (1965), On finite amplitude instability in thermohaline convection, J. Mar. Res. 23, 1-17.

Viskanta, R. and J.S. Toor (1972), Radiant energy transfer in waters, Water Res. Res. 8, 595-608.

Viskanta, R. and J.S. Toor (1978), Absorption of solar radiation in ponds, Solar Energy 21, 17-25.

Walton, I.C. (1982), Double-diffusive convection with large variable gradients, J. Fluid Mech. 125, 123-135.

Wang, Y.F. and A. Akbarzadeh (1983), A parametric study on solar ponds, Solar Energy 30, 555-562.

Weeks, D.D., S.M. Long, R.E. Emery and H.C. Bryant (1981), What happens when a solar pond boils?, Article 7, Int. Solar Pond Newsletter (4), Solar Energy Group, Los Alamos Nat. Laboratory, Los Alamos, NM.

Weinberger, Hershel (1964), The physics of the solar pond, Solar Energy 8, 45-56.

WESTEC Services, Inc. (1981), Final Report, Solar Pond Project, Salton Sea, California, prepared for Jet Propulsion Laboratory, Pasadena, CA.

Willis, G.E. and J.W. Deardorff (1974), A laboratory model of the unstable planetary boundary layer, J. Atmos. Sci. 31, 1297-1307.

Winsberg, Sandra (1980), Solar perspectives: Solar pond power, the Israel-California connection, Sunworld 4 (5).

Wittenberg, Layton J. and Don E. Etter (1982), Heat extraction from a large solar pond, proc. Winter Annual Meeting A.S.M.E., Phoenix, AZ.

Wolanski, E.J. and L.M. Brush, Jr. (1975), Turbulent entrainment across stable density step structures, Tellus 27, 259-268.

Worthem, Sylvia, E. Mollo-Christensen and F. Ostapoff (1983), Effects of rotation and shear on doubly-diffusive instability, J. Fluid Mech. 133, 297-319.

Wu, Jin (1973), Wind-induced turbulent entrainment across a stable density interface, J. Fluid Mech. 61, 275-287.

Wu, Jin (1978), An alternative analysis of entrainment data from a circular annular tank under constant stress, Tech. Rep. JW-7, College of Mar. Studies, Univ. of Del.

Wu, Jin (1980), Wind-stress coefficients over sea surface near neutral conditions - A revisit, J. Phys. Oceanog. 10, 727-740.

Wyatt, L.R. (1978), The entrainment interface in a stratified fluid, J. Fluid Mech. 86, 293-311.

Zaneveld, J.R.V. and R.W. Spinrod (1980), An arctangent model of irradiance in the sea, J. Geophys. Res. 85 (C9), 4919-4922.

Zangrando, F. and H.C. Bryant (1977), Heat extraction from a salt gradient solar pond, proc. Int. Conf. Alternate Energy Sources, vol. 6, 2935-2967.

Zangrando, Federica (1979), Observation and analysis of a full-scale salt gradient solar pond, Ph.D. Thesis, Dept. of Physics, Univ. of New Mexico.

Zangrando, F. (1980), A simple method to establish salt gradient solar ponds, Solar Energy 25, 467-470.

Zeman, O. and H. Tennekes (1977), Parameterization of the turbulent energy budget at the top of the daytime atmospheric boundary layer, J. Atmos. Sci. 34, 111-123.

Zilitinkevich, S.S. (1975), Comments on 'A Model For the Dynamics of the Inversion Above A Convective Boundary Layer', J. Atmos. Sci., 32, 991-992.

Appendix A

Nomenclature

a = wave amplitude

A = area

$\Delta b = -g \frac{\Delta \rho}{\rho_o}$ = buoyancy step across interface

B = width

B_f = buoyancy flux

C (with various subscripts) = proportionality coefficient

c_p = specific heat

CC = cloud cover

D = total depth

D_s = Dufour coefficient

e_s = saturated vapor pressure

e_z = vapor pressure at height z

$E = u_e/\hat{u}$ = normalized entrainment rate

f = grid oscillation frequency

f_s = data sampling frequency

F_s = salt flux

g = gravitational acceleration

$g' = g \frac{\Delta \rho}{\rho_o}$ = reduced gravity

h = upper (mixed) layer depth

$H = \rho c_p T$ = thermal energy concentration

H_f = heat flux

H_{SP} = "solid plane" heat flux

k_s = salt molecular diffusivity

$\hat{k}_s$ = effective double-diffusive salt diffusivity

k_t = thermal molecular diffusivity

$\hat{k}_T$ = effective double-diffusive thermal diffusivity

$\hat{\ell}$ = characteristic length scale

$L = \hat{u}^3/B_f$ = Monin-Obukhov length

L_v = latent heat of vaporization

M_f = mass flux

$N = (-g/\rho_o \Gamma)^{1/2}$ = Brunt-Vaisala frequency

p = pressure

R_h = relative humidity

R_t = autocorrelation for lag t

s = grid oscillation stroke

S = salinity (percent by weight)

S_T = Soret coefficient

t = time

$\hat{t}$ = characteristic time scale

T = temperature

T_a = air temperature

T_s = surface temperature

u_d = buoyancy-induced velocity due to double-diffusive convection

$u_e = dh/dt$ = entrainment velocity

u_g = grid-induced velocity

u_i = bulk horizontal inflow velocity

u_o = bulk horizontal outflow velocity

u_r = return velocity along interface

u_s = surface drift velocity

$u*$ = friction velocity

$u*_a$ = air friction velocity

$\hat{u}$ = characteristic velocity scale

$\bar{u}$ = mean velocity

w = vertical velocity

$w*$ = buoyancy-induced velocity

W = wind speed

X = fetch or longitudinal distance

z = vertical coordinate (positive downward)

z_b = bottom position

z_s = surface position

$\alpha_T = -\frac{1}{\rho_o}\frac{\partial \rho}{\partial T}$ = thermal expansion coefficient

$\alpha_S = \frac{1}{\rho_o}\frac{\partial \rho}{\partial S}$ = saline expansion coefficient

β = fraction of solar radiation absorbed at water surface

δ = interface thickness

Δz = layer thickness

$\Delta \rho$ = interfacial thickness

ε = emissivity

ε_1 = viscous dissipation

ε_2 = internal wave energy loss

$\Gamma = d\rho/dz$ = density gradient

κ = von Karmon constant

κ_T = thermal molecular conductivity

$\hat{\kappa}_T$ = effective double-diffusive thermal conductivity

λ = wavelength

$\lambda_C = u_g/u_d$ = Crapper mixing parameter

$\lambda_L = w^2/u_g^2$ = Linden mixing parameter

η = extinction coefficient

η_S = factor to account for effect of salinity on evaporation

ϕ_a = atmospheric radiation flux

ϕ_c = conduction

ϕ_e = evaporation heat flux

ϕ_n = net surface heat flux

ϕ_s = solar radiation flux

ψ = precipitation

μ = chemical potential

ν = kinematic viscosity

ρ = density

ρ_o = surface layer or reference density

$\rho_S = \rho S$ = salt concentration

$\Delta\rho$ = interfacial density step

$\sigma = (w_*^3 + C_v^3 u_*^3)^{1/3}$ = turbulence velocity scale

$\tau_s = \rho_o u_*^2$ = surface shear stress

Non-dimensional Numbers

$Fr = u/(g'\hat{\ell})1/2 =$ Froude number

$Nu = H_{SP}/\kappa_T \frac{\Delta T}{h} =$ Nusselt number

$Pe = \hat{u}\hat{\ell}/k =$ Peclet number (salt or heat)

$Pr = \nu/k_T =$ Prandtl number

$R_s = Nh/\sigma =$ inverse Froude number

$R_\rho = \alpha_S \Delta S/\alpha_T \Delta T =$ stability parameter

$$Ra = \frac{g\alpha_T \Delta T D^3}{\nu k_T} = \text{thermal Rayleigh number}$$

$$Ra_e = Ra - \frac{Pr+\tau}{Pr+1} Ra_S = \text{"effective" Rayleigh number}$$

$\tau = k_S/k_T =$ diffusivity ratio

$$Ra_S = \frac{g\alpha_S \Delta S D^3}{\nu k_T} = \text{saline Rayleigh number}$$

$Re = \hat{u}\hat{\ell}/\nu =$ Reynolds number

$Rf = \Delta PE/\Delta KE =$ flux Richardson number

$Ri = g' \hat{\ell}/u^2 =$ bulk Richardson number

$Ri_* = g' h/u_*^2 =$ bulk Richardson number

$$Ri_G = \left(\frac{N\lambda}{\hat{u}}\right)^2 = \text{gradient Richardson number}$$

$Sc = \nu/k_s =$ Schmidt number

Appendix B

The Soret Effect and Solar Ponds

Expressions for the diffusive flux of a solute and of heat may be derived from principles of non-equilibrium thermodynamics (Eckart, 1962; Fofonoff, 1962; Hurle and Jakeman, 1971). Diffusion is an irreversible process which tends to increase the entropy of the system in accordance with the second law of thermodynamics. Diffusive fluxes may be estimated by calculating the rate of change of entropy as the system proceeds towards well-mixed conditions (i.e., a state of maximum entropy). The simplest assumption for diffusion of a solute which is consistent with the non-negativity of entropy change for an irreversible process is that the diffusive mass flux is proportional to the gradient of the chemical potential of the solution,

$$M_f = -D\nabla\mu \tag{B.1}$$

where $D > 0$ is a proportionality constant and μ is the chemical potential. This expression is analogous to Fourier's Law of heat conduction. In general, μ is a function of pressure, temperature and salinity, so

$$M_f = -D[\frac{\partial\mu}{\partial p}\nabla p + \frac{\partial\mu}{DT}\nabla T + \frac{\partial\mu}{\partial S}\nabla S] \tag{B.2}$$

Fick's Law of diffusion is seen to be a special case of (B.2). For situations in which there are negligible temperature and pressure gradients, (B.2) reduces to

$$M_f = -D \frac{\partial \mu}{\partial S} \nabla S \ .$$

If a salinity diffusion coefficient is now defined as $k_S = D\, \partial\mu/\partial S$, then we have $M_f = -k_S \nabla S$, which is Fick's Law. The pressure and temperature terms in (B.2) may be defined similarly, so that

$$M_f = -k_p \nabla p - k_{TS} \nabla T - k_s \nabla S \ . \tag{B.3}$$

Not much is known about the coefficients k_p or k_{TS}, but the pressure effect is generally considered to be very small and may be ignored for most conditions. The temperature term is known as the Soret effect.

In a similar manner the heat flux may be assumed to be dependent on temperature, salinity and pressure gradients. From text books on non-equilibrium thermodynamics, the diffusive fluxes of heat and of a solute are expressed as follows, where the pressure terms are again ignored:

$$H_f = -K_T \nabla T - TS \frac{\partial \mu}{\partial S} D_S \nabla S \tag{B.4}$$

and

$$M_f = -k_s [\nabla S + S S_T \nabla T] \tag{B.5}$$

where K_T = thermal conductivity, D_S = Dufour coefficient, and S_T = Soret coefficient. In writing (B.5), it has been assumed that the

concentration of dissolved mass is small. Values for D_S in liquids are very small and usually neglected. The Soret effect will also usually be quite small. However, the Soret effect may be important when turbulent fluxes are sufficiently small so as not to dominate molecular effects and also when the thermal, Soret-driven diffusion is significant compared with the usual Fickian diffusion (Caldwell, 1973).

The strength of the Soret-driven diffusion has been examined by Caldwell (1973), who calculated limits for the Soret flux based on studies in double-diffusive convection. Experimental observations have shown that a series of layers will form when a stable salt gradient is heated from below. Mixing occurs when the stability parameter R_ρ becomes of order one. Layers will exist for $R_\rho > 1$ and Huppert (1971) has shown that a steady state may be achieved when $R_\rho > 2$. Caldwell's analysis shows that in double-diffusive layering under oceanic conditions, the Soret-driven flux is at most 50% of the Fickian flux and for steady layering the ratio is at most 25%. He concluded that the Soret transport of sodium chloride in oceans was not significant.

Rothmeyer (1980) has used Caldwell's data to evaluate the expected strength of the Soret-driven flux in comparison to the Fickean flux under solar pond conditions and concluded that the Soret term should be included in the salt diffusion equation so as not to underestimate the total molecular diffusive flux. His calculations show that the Soret flux is less than 10% of the Fickean flux for temperatures less than about 40°C, but average about 27% of the Fickean flux for temperatures greater than 40°C, with some values as high as 73%. It should be noted, however, that the data used to evaluate the Soret coefficient did not encompass the high temperature and salinity conditions of a SGSP, so

there is a large degree of uncertainty in applying these results. Meyer (1982) included the Soret term in his model, but did not indicate the values for the Soret coefficient. Considering the large degree of uncertainty for values of this parameter and also its relative unimportance in determining flux, it is neglected in the present model.

Appendix C

Evaluation of Effective Diffusivities for Interfacial Double-Diffusive Fluxes

Previous studies of fluxes across a diffusive interface have usually reported results in terms of H_F/H_{SP} vs. R_ρ and $R_F = \rho_o C_p \alpha_s F_s/\alpha_T H_f$ vs. R_ρ. H_{SP} is defined as the heat flux which would be observed across a thin, rigid, impermeable conducting plane. If this plane separates two regions each of depth h and there is a temperature difference ΔT, the heat flux is described by a Nusselt number,

$$H_{SP} = N_u \kappa_T \Delta T/h \tag{C.1}$$

and

$$Nu = C\ Ra^{1/3}\ , \tag{C.2}$$

where C is a constant. This form is chosen since h is eliminated as a factor determining H_{SP} (Turner, 1965). It is seen that Nu = 1 implies that the heat flux is carried entirely by molecular conduction and Nu > 1 implies some convection must be present. Therefore, the value of C must relate to a critical value of Ra at which instability would begin, i.e., $C = Ra_C^{-1/3}$. Turner suggested a value $Ra_C = 1600$, so C = 0.085. Thus, we have,

$$H_{SP} = 0.085\ \kappa_T \left(\frac{g\alpha_T}{\nu k_T}\right)^{1/3} \Delta T^{4/3}\ . \tag{C.3}$$

Let us now define an "effective" thermal conductivity $\hat{\kappa}_T$ for a diffusive interface which can be used to explain the observed heat flux, i.e.

$$H_f = \hat{\kappa}_T \, \Delta T / \delta \quad , \tag{C.4}$$

where δ = interface thickness. Then, dividing (C.4) by (C.3) and rearranging results in

$$\hat{\kappa}_T = 0.085 \, \kappa_T \frac{\delta}{h} \, Ra^{1/3} \left(\frac{H_f}{H_{SP}}\right) \quad . \tag{C.5}$$

Expressions for (H_f/H_{SP}) as a function of R_ρ obtained from the literature are summarized in Table C.1 and Figure C.1. Data from previous experiments is shown on Figure C.1 and a best fit curve is shown there and listed in Table C.1. Using the best fit a final expression for $\hat{\kappa}_T$ is obtained,

$$\hat{\kappa}_T = 0.092 \, \kappa_T \frac{\delta}{h} \, Ra^{1/3} (R_\rho - 1)^{-1.14} \quad . \tag{C.6}$$

This is similar to the expression derived by Meyer (1982), except he used Marmorino and Caldwell's (1976) result for H_f/H_{SP}.

An "effective" salt diffusivity $\hat{k}_S$ is now defined in a similar manner, i.e.,

$$F_S = \hat{k}_S \frac{\Delta S}{\delta} \quad . \tag{C.7}$$

Using the definition of R_F we find

$$\hat{k}_S = \hat{k}_T R_F / R_\rho \qquad (C.8)$$

where $\hat{k}_T = \hat{\kappa}_T / \rho_o c_p$ = "effective" thermal diffusivity.

Experimentally determined values of R_F show considerable scatter but there is some indication that there is a slight dependence on H_f (Figure C.2). Using a fit to this data (Meyer, 1982) results in

$$\hat{k}_S = 0.15 \frac{\hat{k}_T}{R_\rho} H_F^{-0.13} \quad , \qquad (C.9)$$

where H_f is measured in W/cm^2.

$\hat{k}_T$ and $\hat{k}_S$ were calculated from (C.6) and (C.9), using the following order-of-magnitude values:

$\rho_o c_p = 4.2$ J/cm^3°C, $\delta = 1$ cm, $\alpha_T = 2 \times 10^{-4}$ °C^{-1},

$\alpha_S = 7.6 \times 10^{-3}$ ‰$^{-1}$, $k_T = 1.4 \times 10^{-3}$ cm^2/S and

$\nu = 10^{-2}$ cm^2/S. The results are shown in Figure C.3 with ΔT as an independent variable. Note that ΔS is determined by choosing ΔT and R_ρ. It should be remembered that $\hat{k}_T$ and $\hat{k}_S$ are evaluated in terms of the interfacial fluxes measured by bulk changes in temperature and salinity of the mixed layer and the discussion in Section 3.2.3 explains why values less than molecular are calculated. This is a point of interest when modeling SGSPs, since there is concern over the fluxes of salt and heat into the UCZ.

Table C.1. Expressions for $H_f/H_{s\rho}$ (H_b = imposed bottom heat flux)

Reference	Range of Data	$H/H_{s\rho}$	Notes
Huppert (1971)	$1 < R_\rho < 7$ $H_b = 1.1, 1.7, 2.4, 3.3 \frac{cal}{cm^2\ min}$	$3.8\ R_\rho^{-2}$	data from Turner (1965)
Marmorino and Caldwell (1976)	$1 < R_\rho < 12$ $H_b \simeq 0.006 - 1 \frac{cal}{cm^2\ min}$	$0.10 \exp\{4.6 \exp[-0.54(R_\rho - 1)]\}$	
Shirtcliffe (1973)	$2 < R_\rho < 7$	$2.67\ R_\rho^{-1.79}$ $2.59\ R_\rho^{-12.6}$	data from Turner (1965) salt-sugar interface
Linden and Shirtcliffe (1978)	(theoretical model)	$\frac{1}{\pi^{1/3}} \frac{(1 - \tau^{1/2} R_\rho)^{4/3}}{(1 - \tau^{1/2})^{1/3}}$	based on boundary layer stability model for quasi-steady conditions

Table C.1. Expressions for $H_f/H_{s\rho}$ (H_b = imposed bottom heat flux) (continued).

Reference	Range of Data	$H/H_{s\rho}$	Notes
Takao and Narusawa (1980)	$1 < R_\rho < 7$	$4.38 \cdot 10^{-2}\ \tau^{-0.21} \exp\{4.6 \exp[-0.54(R_\rho - 1)]\}$	
Newell (1983)	$\tau^{-1/2} < R_\rho < 30$ $\Delta s = 1.5, 3, 4.5$	$[.085\ \pi^2\ h\ \tau\ \ln(\frac{R_\rho}{\tau^{-1/2}})]^{-1}\ (\frac{\nu k}{\tau})^{1/3}\ R_\rho{}^{1/3}$	extension of Linden and Shirtcliffe model by allowing interface to grow in time
Murota and Michioka (1983)	$R_\rho \geq 2.8$	$4.0\ R_\rho{}^{-2.8}$	

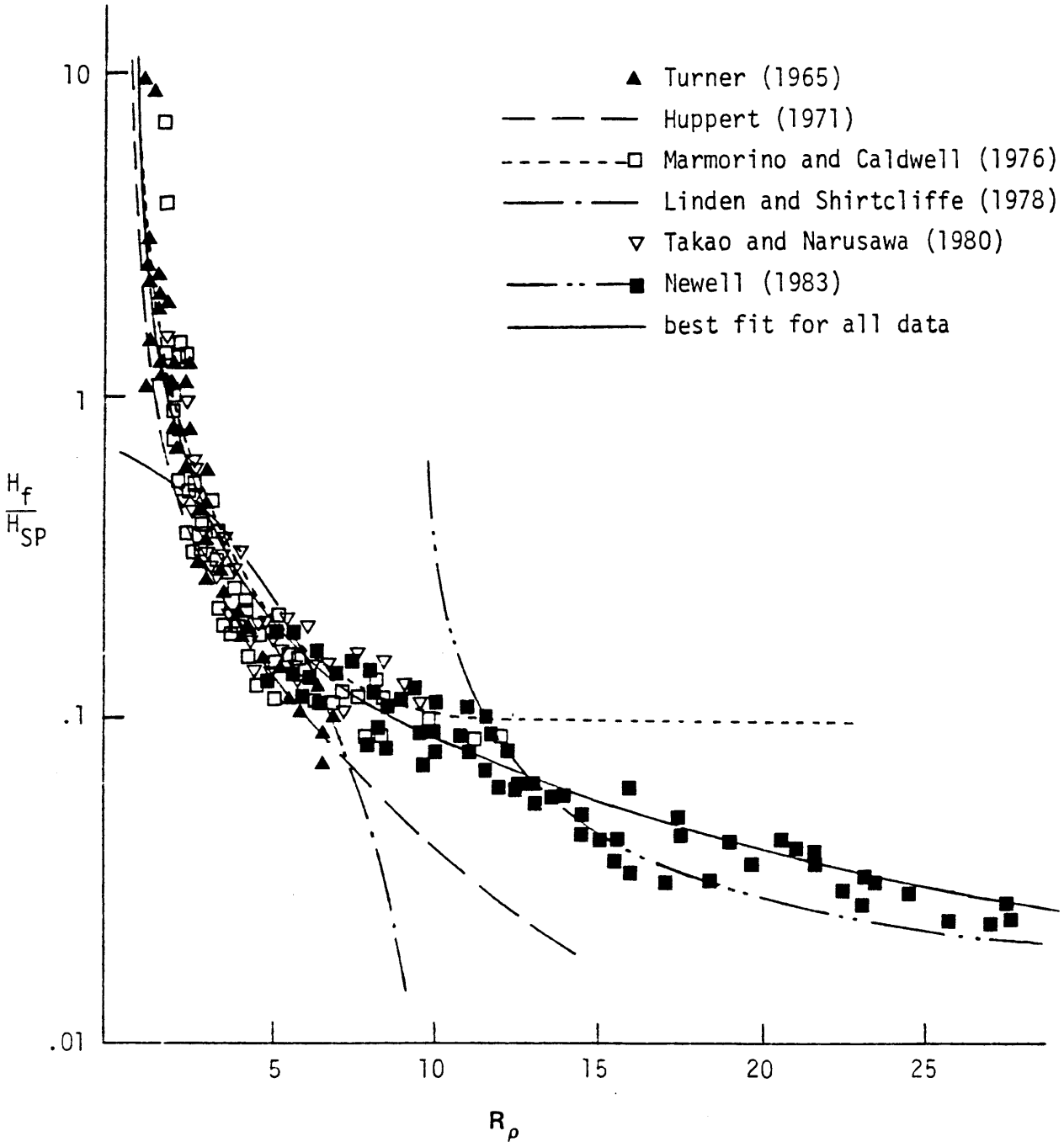

FIGURE C.1 H_f/H_{sp} vs. R_ρ; Data and Model Information Given in Table C.1

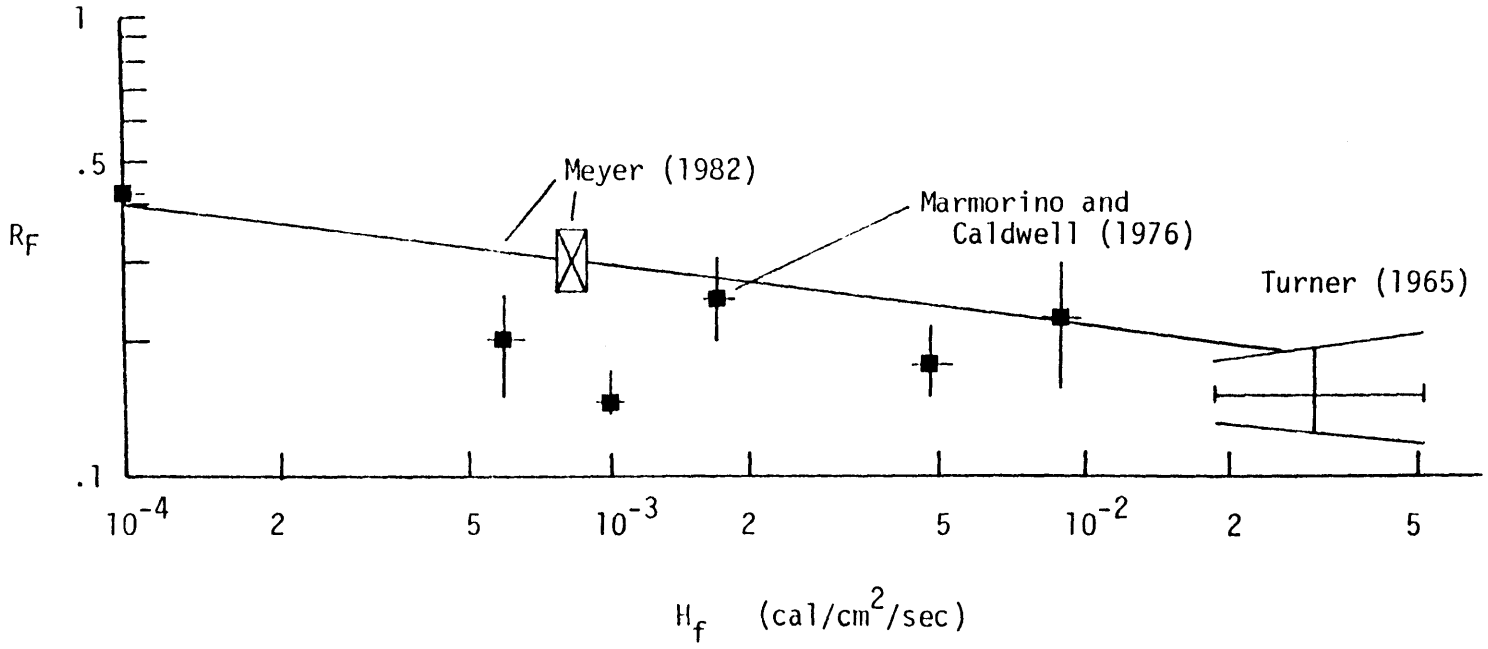

FIGURE C.2 R_F vs. R_ρ

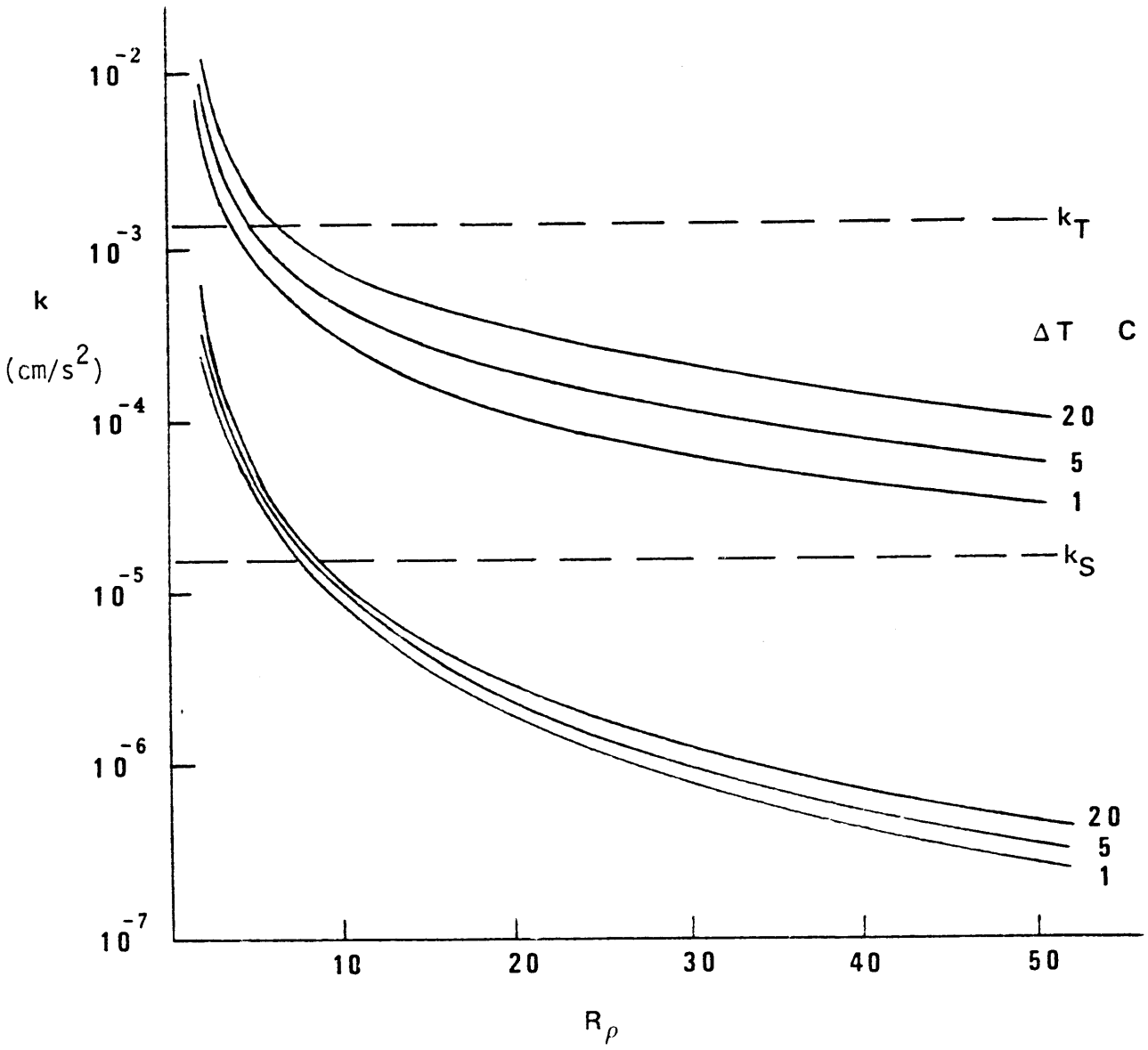

FIGURE C.3 Variation of k'_τ (Upper Curves) and k'_s (Lower Curves) With R_ρ

Appendix D

Probe Descriptions and Calibrations

Temperature measurements were made with a small thermistor mounted at the tip of a 6.5 cm long stainless steel tube 1 mm in diameter (Fenwal Electronics, model k5078). The time constant for this probe is 0.1 to 0.2 sec. A standard bridge arrangement was used and the voltage drop caused by the change in resistance of the thermistor material as a function of temperature was calibrated in the following manner. The probe was suspended over a 500 ml beaker so that the tip was positioned near the center of the beaker. A mercury thermometer with 0.1°C divisions was also positioned so that the probe tip was about 1 cm from the thermistor tip. The beaker was then placed on a flat plate heater equipped with a stirrer and voltage output from the probe was recorded as a function of temperature as the temperature was slowly varied over the range of interest for the experiments (approximately 15°C to 60°C).

Figure D.1 shows results from two calibration runs and it can be seen that the probe output was very steady and quite linear. A better approximation to the output was obtained by a series of three linear segments, as shown. Stability of the probe output was checked at three different temperatures, 20°C, 35°C and 50°C, by maintaining constant temperature in the beaker and recording the output with time. It was found that over a period of two hours the output voltage varied less than 0.5 percent of its initial reading. A calibration run was also done with the beaker containing a solution of 10 percent (by weight) salinity in order to check any possible dependence of the probe output on

salinity. This run produced virtually the same response as shown in Figure D.1 and it was assumed that there was no salinity dependence for the thermistor output. The accuracy and precision of the temperature data is 0.1°C, imposed by the mercury therometer.

Salinity values were obtained by measuring both temperature and conductivity. Conductivity was measured with a Head Designs (now Precision Engineering) micro scale conductivity instrument, model 106. This instrument consists of a four-electrode probe at the end of a small glass tip approximately 5.5 cm long. This tip is connected to a .25" (.64 cm) diameter stainless steel tube which leads into a preamplifier section. A very stable output was produced (checked by monitoring output for constant conditions - T and S - over several hours), but calibrations were required at frequent intervals since the probe response could shift by several percent whenever power was disconnected (i.e., between experiments).

Conductivity is a strong function of both salinity and temperature so that calibrations were required for both temperature and salinity dependence. A temperature calibration equation for the probe is suggested by the manufacturer which is a linearized version of the temperature dependence of the conductivity of NaCl solutions in water. This equation is based on a reference temperature of 18°C. However, after discussions with the manufacturer it was decided that due to the wide temperature and salinity ranges to be considered in the present experiments it would be better to calibrate the probe directly. The procedure for calibration was similar to the procedure followed for the thermistor calibration, except that solutions of different salinities

were used in addition to varying the temperature. These solutions were prepared by disolving a known quantity of salt (NaCl) in a known volume (mass) of water and were checked by a gravimetric method using a small sample of the solution. That is, a small aluminum pan was weighed, a small sample of solution was then placed in the pan and the pan was weighed again and then put into an oven to dry overnight. The pan was then weighed again the following day (with only residue) and salinity was determined by taking the ratio of residue weight to solution weight.

Figures D.2 to D.5 show results from calibration runs. Figure D.2 covers a wide range of salinities and was used for a preliminary set of experiments where S varied considerably. Figures D.3 to D.5 cover smaller salinity ranges in somewhat greater detail, each calibration being of interest for a particular set of experiments. It can be seen that for a given salinity the variation of conductivity with temperature was quite linear. When interpreting experimental data salinity was determined by looking at the intersection point for the temperature and voltage output from the conductivity probe. Salinity was then estimated by interpolating between the calibration curves. This procedure is illustrated on Figure D.1. Here, $T = 26^{o}C$ and $v = -3.5$ volts implies a salinity $S = 5.04$ percent. It should be noted that due to the manner in which the probes were installed in the tank and the relative fragility of the conductivity probe tip, it was practically impossible to run calibrations for every single experiment. However, calibrations were run for small sets of experiments where the conditions did not change very drastically. In addition, temperature and salinity for each layer were measured using the thermometer and gravimetric analysis noted above at

the beginning and end of each experiment to provide checks for the probe calibrations. The accuracy of the salinity measurements is estimated to be ± 0.1 percent (by weight).

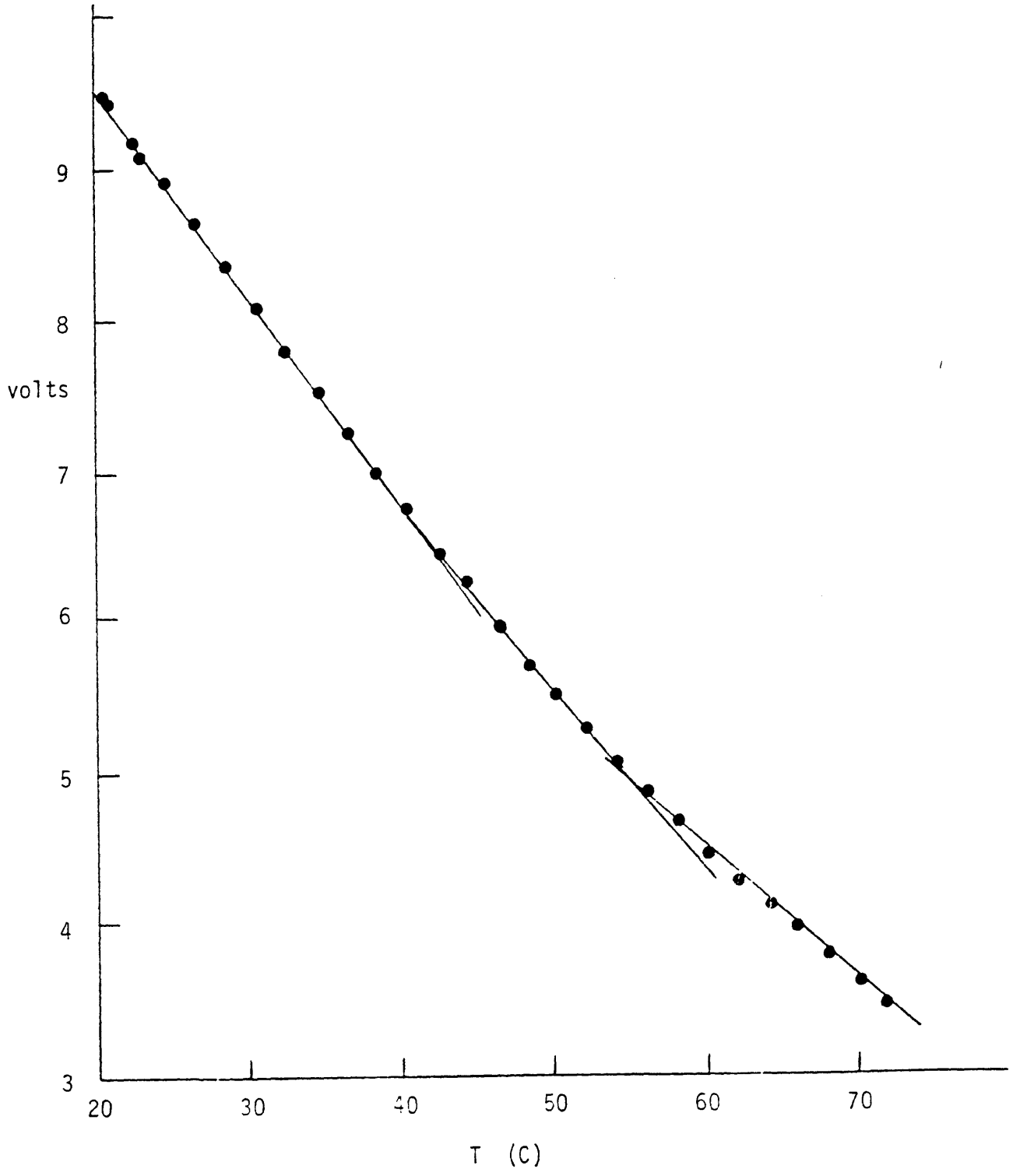

FIGURE D.1 Calibration Curve for Thermistor, Showing 3 Piecewise Linear Segments

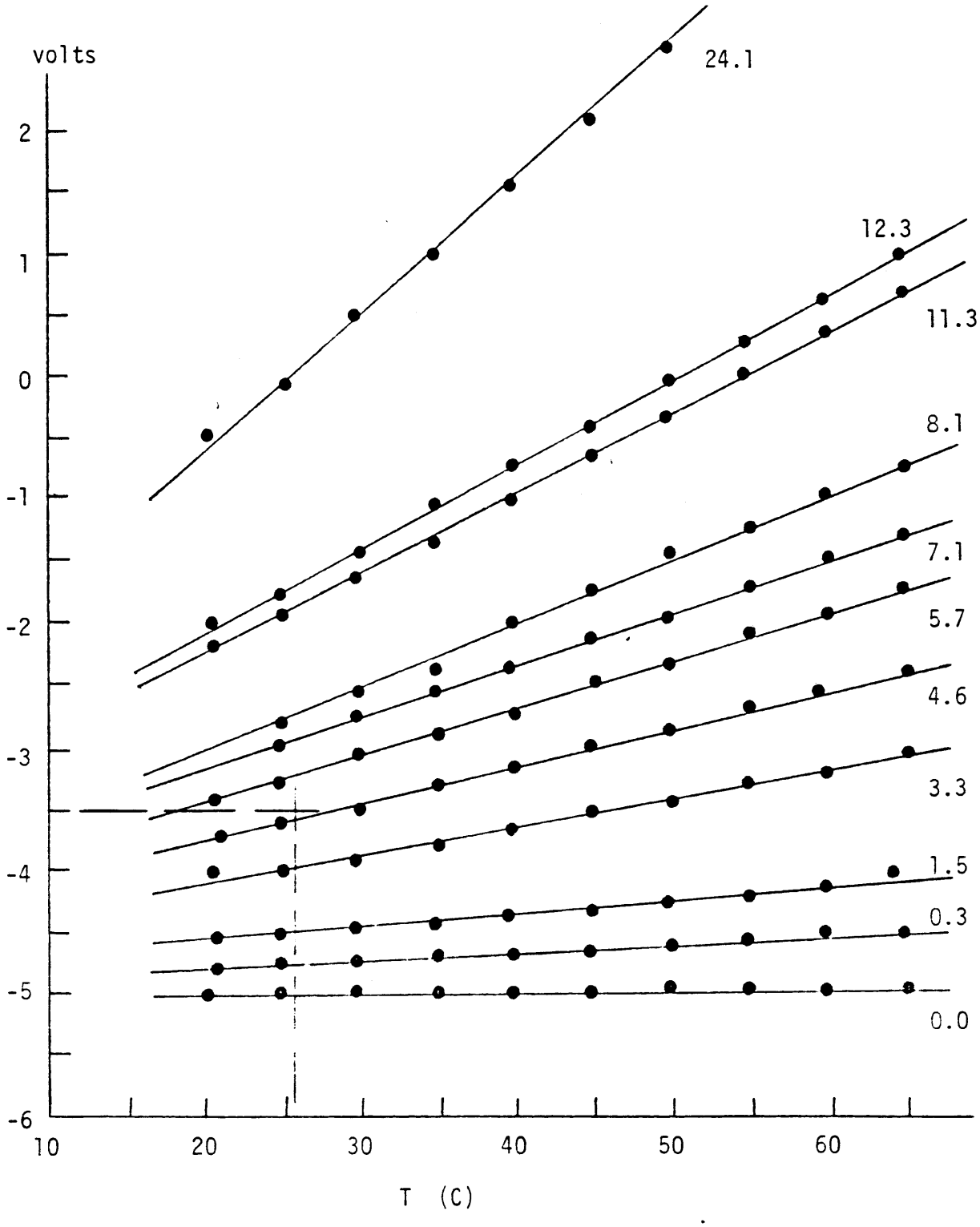

FIGURE D.2 Calibration Curves For Micro-Conductivity Probe; Values at The Right Indicate Salinity (%)

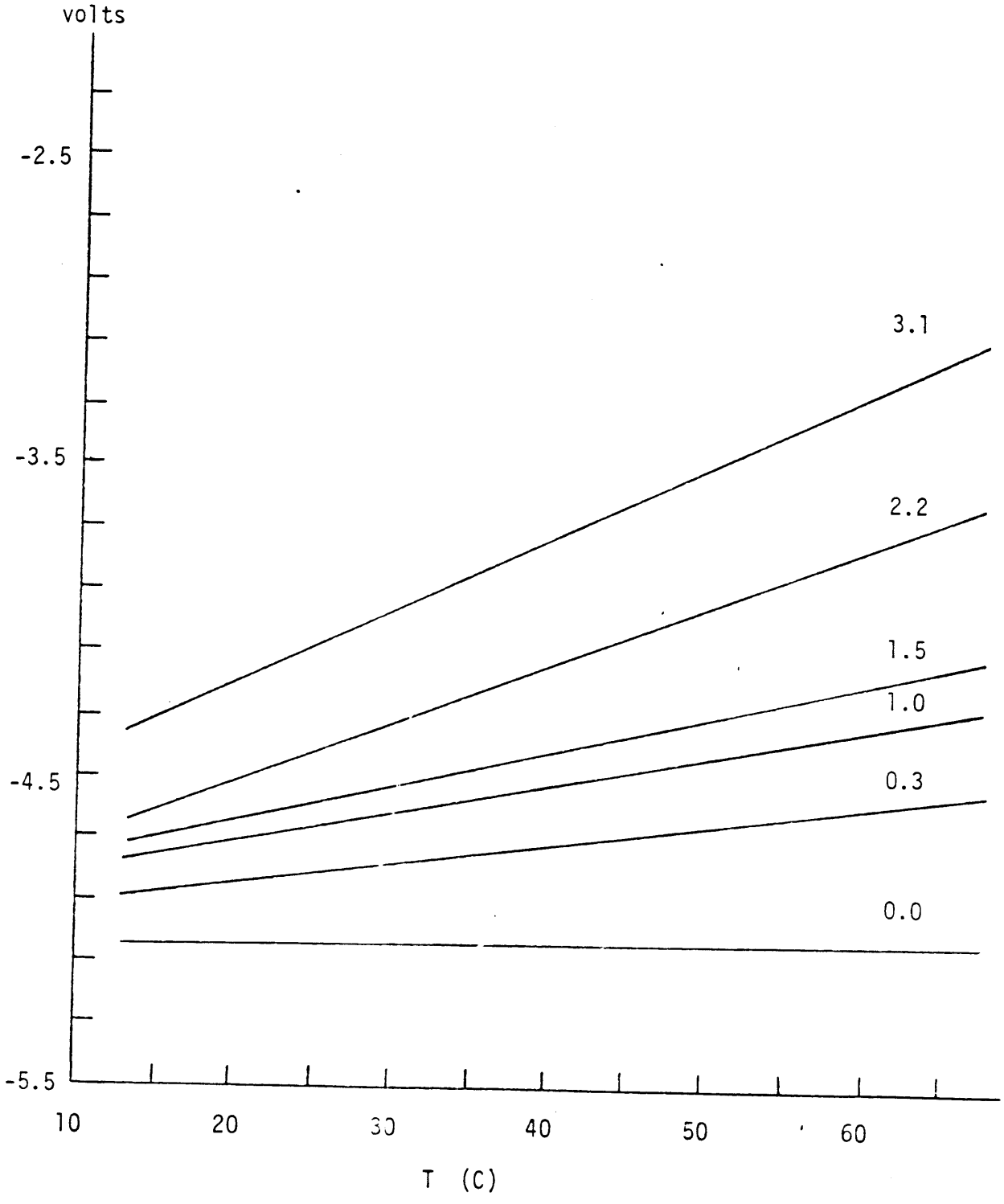

FIGURE D.3 Calibration Curves For Micro-Conductivity Probe; Values at The Right Indicate Salinity (%)

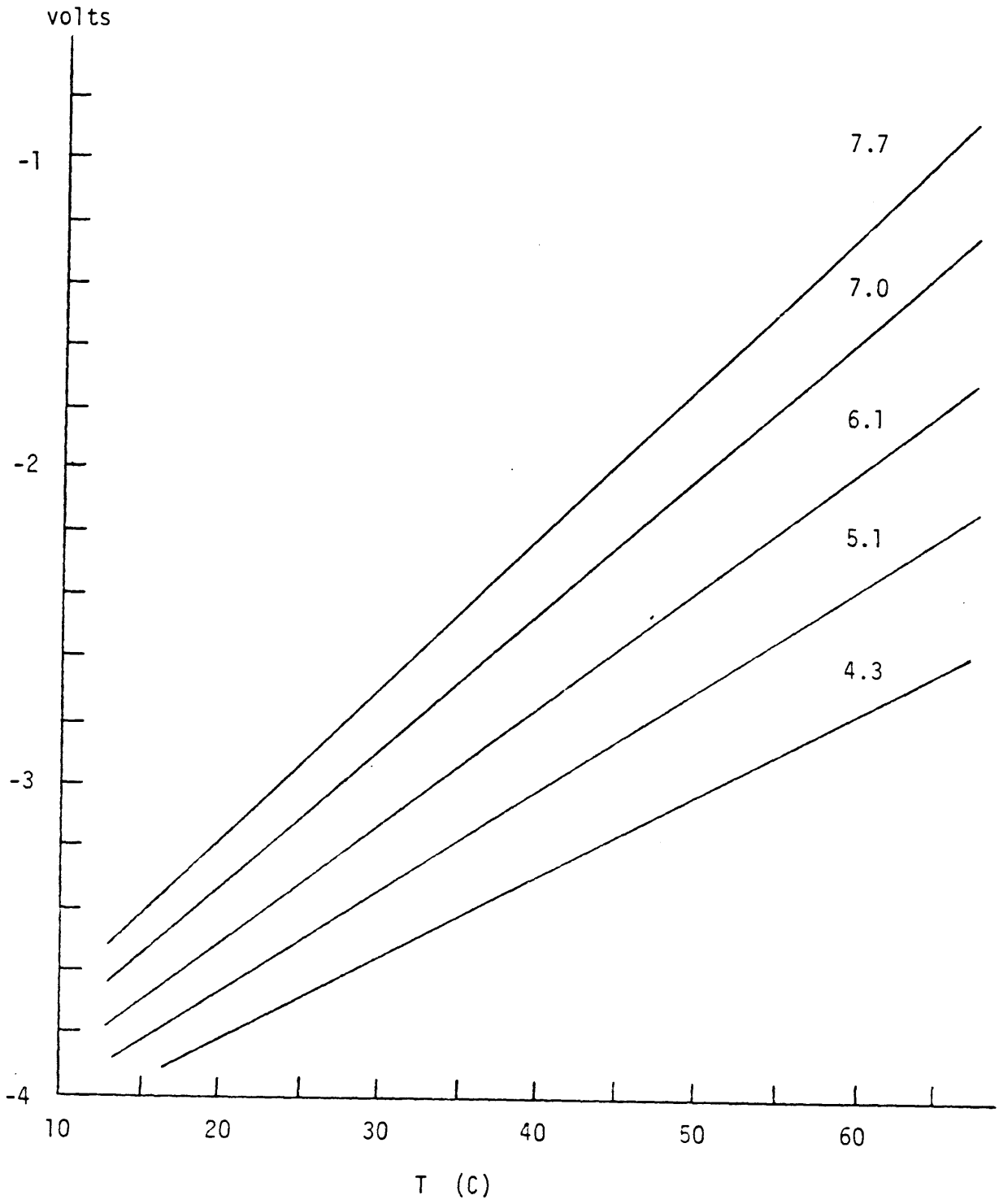

FIGURE D.4 Calibration Curves For Micro-Conductivity Probe; Values at The Right Indicate Salinity (%)

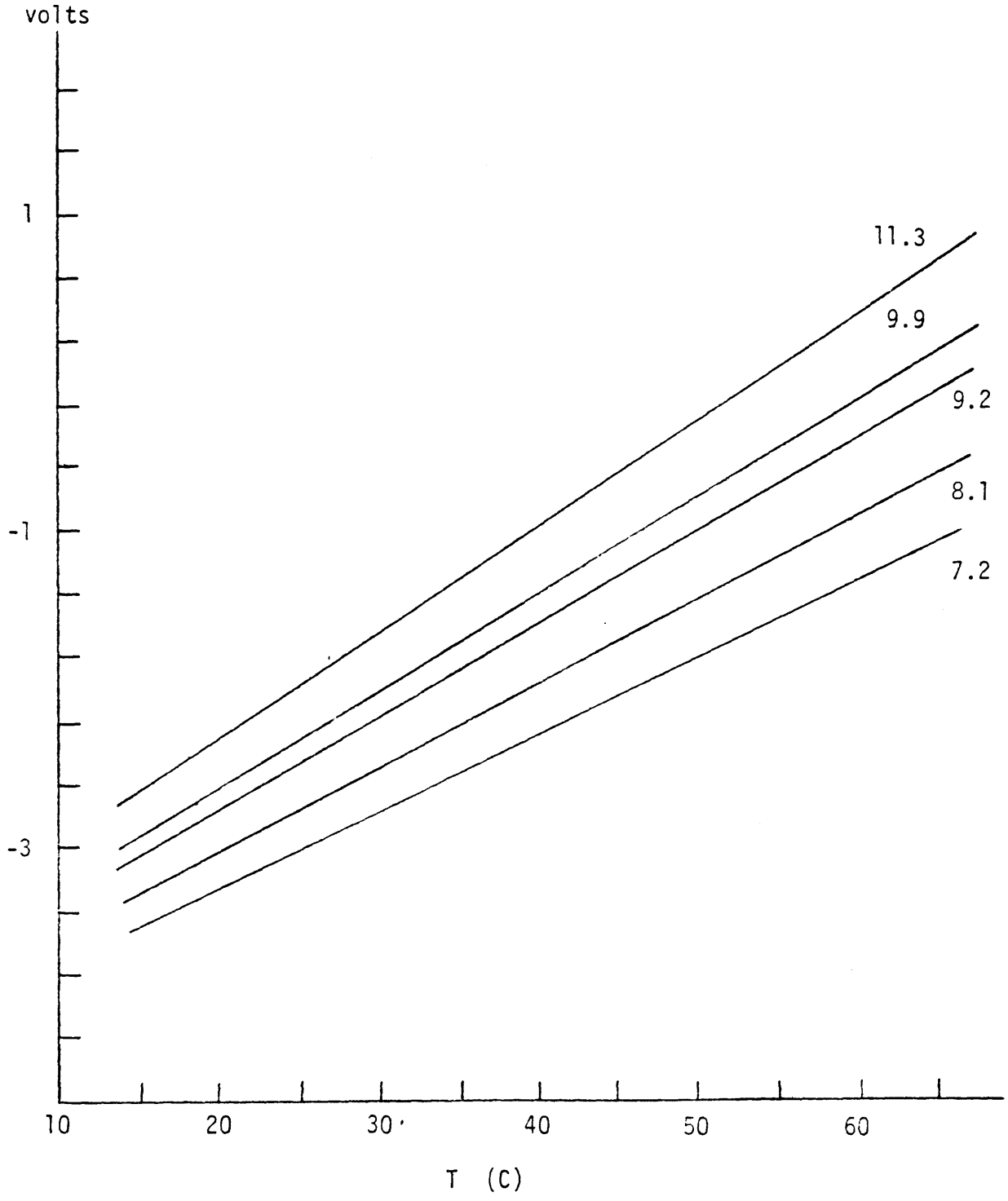

FIGURE D.5 Calibration Curves For Micro-Conductivity Probe; Values at The Right Indicate Salinity (%)